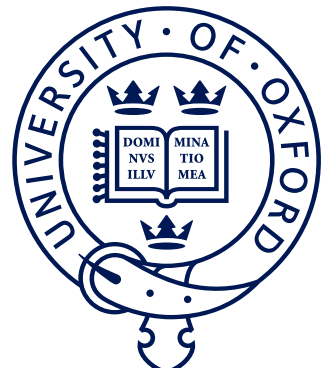


¹ **CP violation in $B^\pm \rightarrow Dh^\pm$ decays**
² **where $D \rightarrow K_S^0 h'^+ h'^-$**

³ *A measurement of the CKM angle γ at LHCb and understanding
⁴ the impact of neutral kaon CP violation*



⁶ Mikkel Bjørn
⁷ St. Anne's College
⁸ University of Oxford

⁹ A thesis submitted for the degree of
¹⁰ *Doctor of Philosophy*
¹¹ Trinity 2020

¹²

Acknowledgements

¹³ suitable thank you's

Abstract

14

¹⁵ World's best measurement of γ . Details to be added.

Contents

16

¹⁷	Preface	^{vii}
¹⁸	1 Introduction	1
¹⁹	1.1 Structure of the thesis	1
²⁰	2 Theoretical background	2
²¹	2.1 The C, P and T symmetries and their violation	2
²²	2.2 CP violation in the Standard Model	4
²³	2.2.1 The CKM matrix and the Unitarity Triangle	4
²⁴	2.2.2 Measuring γ in tree level decays	9
²⁵	2.3 Measuring γ using multi-body D final states	12
²⁶	2.3.1 Dalitz plots and the phase space of multi-body decays	12
²⁷	2.3.2 The GGSZ method to measure γ	14
²⁸	2.3.3 A model-independent approach	16
²⁹	2.3.4 Measuring strong-phase inputs at charm factories	18
³⁰	2.3.5 Global CP asymmetry and the relation to GLW and ADS measurements	22
³¹	2.4 Strategy for the LHCb measurement	26
³³	3 The LHCb experiment	29
³⁴	3.1 The LHCb subdetectors	31
³⁵	3.1.1 The VELO	32
³⁶	3.1.2 Magnet and tracking stations	34
³⁷	3.1.3 The RICH detectors	36
³⁸	3.1.4 Calorimeters	38
³⁹	3.1.5 Muon detectors	40
⁴⁰	3.2 Reconstruction	41
⁴¹	3.2.1 Track reconstruction	41
⁴²	3.2.2 Particle identification	43
⁴³	3.3 The LHCb trigger system	44
⁴⁴	3.3.1 The level-0 hardware trigger	45
⁴⁵	3.3.2 High-level triggers	46
⁴⁶	3.3.3 Offline data filtering: the LHCb stripping	47
⁴⁷	3.4 Simulation	48

48	4 Neutral kaon CP violation and material	49
49	interaction in BPGGSZ measurements	49
50	4.1 CP violation and material interaction of neutral kaons	49
51	4.1.1 A first look at the impact on γ measurements	53
52	4.2 Impact on BPGGSZ measurements of γ :	
53	principles	55
54	4.2.1 Modified symmetry relations	55
55	4.2.2 Relationship between the K_S^0 and K_L^0 amplitudes	56
56	4.2.3 Modification of the BPGGSZ yield equations	57
57	4.3 Impact on BPGGSZ measurements of γ :	
58	LHCb and Belle II measurements	60
59	4.3.1 Detector geometries	61
60	4.3.2 Kaon momentum distributions	62
61	4.3.3 Experimental time acceptance	63
62	4.3.4 Detector material budget	64
63	4.3.5 Calculation procedure	66
64	4.3.6 Results	67
65	4.3.7 Coupled $B^\pm \rightarrow DK^\pm$ and $B^\pm \rightarrow D\pi^\pm$ measurements	69
66	4.4 Concluding remarks	70
67	5 A BPGGSZ measurement of γ with $B^\pm \rightarrow Dh^\pm$ decays	72
68	5.1 Candidate reconstruction and selection	72
69	5.1.1 Initial requirements	73
70	5.1.2 Boosted decision tree	75
71	5.1.3 Particle-identification requirements	81
72	5.1.4 Final requirements	82
73	5.1.5 Selected candidates	82
74	5.2 Signal selection efficiencies	83
75	5.2.1 Efficiency of the PID requirements	86
76	5.2.2 Efficiency profile over the Dalitz plot	87
77	5.3 Background studies	89
78	5.3.1 Charmless decays	91
79	5.3.2 Background from four-body D decays	92
80	5.3.3 Semi-leptonic backgrounds	93
81	5.3.4 Cross-feed from other $D \rightarrow K_S^0 h^+ h^-$ decays	101
82	5.3.5 Swapped-track backgrounds	101
83	5.4 Signal and background mass shapes	103
84	5.4.1 Signal decays	104
85	5.4.2 Cross-feed between $B^\pm \rightarrow Dh^\pm$ channels	105

86	5.4.3	Partially reconstructed backgrounds	107
87	5.4.4	Combinatorial background	113
88	5.4.5	Fit results	113
89	5.5	Measurement of the CP-violation observables	115
90	5.5.1	Fit setup	116
91	5.5.2	Main results	126
92	5.5.3	Cross checks	128
93	5.6	Systematic uncertainties	136
94	5.6.1	Strong phase uncertainties	136
95	5.6.2	Efficiency-profile-related systematic uncertainties	137
96	5.6.3	Mass shapes	142
97	5.6.4	CP violation and material interaction of the K_S^0	148
98	5.6.5	Impact of D mixing	148
99	5.6.6	PID efficiencies	148
100	5.6.7	Dalitz-coordinate resolution	149
101	5.6.8	The fixed yield fractions	150
102	5.6.9	Systematic uncertainty due to backgrounds that are not modelled in fit	150
103	5.6.10	Bias correction	152
104	5.6.11	Charmless backgrounds	153
105	5.6.12	Summary of systematic uncertainties	153
106	5.7	Obtained constraints on γ	155
107	5.7.1	Statistical approach	155
108	5.7.2	Interpretation results	158
109	5.7.3	Compatibility with other measurements	160
110	6	Summary and outlook	164
111	Appendices		
112	A	Projections of the main fit to data	166

Preface

¹¹⁵ The work presented in this thesis has been resulted in two papers, either under
¹¹⁶ review or published in the Journal of High Energy Physics. These are

¹¹⁷ [?] *Measurement of the CKM angle γ using $B^\pm \rightarrow [K_S^0 h^+ h^-]_D h^\pm$ decays*,
¹¹⁸ submitted to JHEP.

¹¹⁹ This paper describes a measurement of the CKM angle γ using pp collision
¹²⁰ data taken with the LHCb experiment during the Run 1 of the LHC, in 2011
¹²¹ and 2012, and during the full Run 2, in 2015–2018. The measurement uses the
¹²² decay channels $B^\pm \rightarrow D h^\pm$ where $D \rightarrow K_S^0 h'^+ h'^-$, in which h and h' denotes
¹²³ pions or kaons. It obtains a value of $\gamma = (69 \pm 5)^\circ$, which constitutes the
¹²⁴ world’s best single-measurement determination of γ . The work is the main
¹²⁵ focus of this thesis and described in detail in Chapter 5.

¹²⁶ [?] *CP violation and material interaction of neutral kaons in measurements*
¹²⁷ *of the CKM angle γ using $B^\pm \rightarrow DK^\pm$ decays where $D \rightarrow K_S^0 \pi^+ \pi^-$* , JHEP
¹²⁸ 19 (2020) 106.

¹²⁹ This paper describes a phenomenological study of the impact of neutral-
¹³⁰ kaon CP violation and material interaction on measurements of γ . With the
¹³¹ increased measurement precision to come in the near future, an understanding
¹³² of these effects is crucial, especially in the context of $B \rightarrow D\pi$ decays; however
¹³³ no detailed study had been published at the start of this thesis. The study is
¹³⁴ the subject of Chapter 4. Some text excerpts and figures from the paper have
¹³⁵ been reproduced in the thesis.

¹³⁶ All of the work described in the thesis is my own, except where clearly referenced
¹³⁷ to others. Furthermore, I contributed significantly to an analysis of $B^\pm \rightarrow DK^\pm$
¹³⁸ decays with LHCb data taken in 2015 and 2016, now published in

¹³⁹ [?] *Measurement of the CKM angle γ using $B^\pm \rightarrow DK^\pm$ with $D \rightarrow K_S^0 \pi^+ \pi^-$,*
¹⁴⁰ *$K_S^0 K^+ K^-$ decays*, JHEP 08 (2018) 176.

¹⁴¹ I was responsible for the selection and analysis of the signal channel, studies of
¹⁴² systematic uncertainties, and the interpretation of the measured observables in
¹⁴³ terms of underlying physics parameters. The measurement is superseded by that
¹⁴⁴ of Ref. [?] and is not described in detail in the thesis.

145 Within the LHCb collaboration, I took part in the preparation for Run 3 by
146 working as a *migration coordinator* for the *B-decay-to-open-charm* (B2OC) physics
147 working group, responsible¹ for the migration of the working group's centralised,
148 offline selections (so called *stripping lines*) to the software-trigger framework being
149 developed for the LHCb Upgrade.² With more than 800 lines in the current B2OC
150 stripping module this is a major task; I took a leading role in the initial design and
151 testing of the upgraded B2OC module, and in helping the first analysts implement
152 their selections within it. I have also undertaken shift work as RICH piquet and
153 Data Manager, and acted as the liaison between the B2OC physics working group
154 and the *particle-identification* performance working group.

¹Along with Alessandro Bertolin and Shunan Shang.

²The current software trigger and *stripping* framework is presented in Section 3.3.

Le roi est mort, vive le roi!

— Traditional French proclamation at the death
of one monarch and the ascension of a new

1

155

156

Introduction

157 All the big picture stuff: constraints on New Physics from high precision measure-
158 ments, a small nod to matter-antimatter asymmetry questions etc.

159 This thesis places itself at the forefront of the latter effort, presenting the
160 World’s most precise measurement of the CP -violating phase γ ; a fundamental
161 parameter in the Standard Model, in which it describes the sole source of matter-
162 antimatter asymmetries.

163 Naturally, the work presented here is far from the last word on the value of
164 γ . In the very near future, several important results will be updated by the
165 LHCb collaboration, based on the full data set collected during Run 2 of the LHC.
166 In the slightly longer term, both the LHCb and Belle II collaborations expect
167 to collect data samples of B decays that are orders of magnitudes larger than
168 the current ones during the coming decade, pushing the obtainable precision on
169 γ towards, even below, one degree. An outlook towards this exciting future of
170 CP -violation measurements is given in Chapter 6, along with a summary of the
171 contributions made in the present thesis.

172 1.1 Structure of the thesis

2

173

174

Theoretical background

175 This chapter lays out the theoretical framework of the thesis. Section 2.1 introduces
176 charge and parity symmetry violation in general, while Section 2.2 covers the
177 description in the Standard Model and the general theory behind charge-parity
178 symmetry violation measurements in charged B decays. Section 2.3 focuses on
179 the theory of measurements using $B^\pm \rightarrow Dh^\pm$ decays with multi-body D final
180 states, after which the specific analysis strategy for the measurement described
181 in the thesis is outlined out in Section 2.4.

182 2.1 The C, P and T symmetries and their vio- 183 lation

184 The concept of symmetry play a fundamental role in modern physics. By Noether's
185 theorem [?], the simple assumption of invariance of our physical laws under universal
186 temporal and spatial translations leads to the very non-trivial prediction of conserved
187 energy and momentum; within the field of particle physics, the interactions and
188 dynamics of the Standard Model (SM) follow completely simply from requiring
189 the fundamental particle fields to satisfy a local $U(1) \times SU(2) \times SU(3)$ gauge
190 symmetry [?]; and one of the short-comings of the SM, is that it fails to explain
191 the apparent *lack* of symmetry in our matter-dominated universe [?]. Indeed, it is
192 important to experimentally establish the symmetries of our world at a fundamental
193 level, and the degree to which they are broken.

194 Three discrete symmetries of importance are the symmetries under

I'll
adjust
this para-
graph
when
I've
written
the intro-
duction.

- 195 1. The charge operator C , which conjugates all internal quantum numbers of a
 196 quantum state and thus converts particles into their anti-particle counter parts.
 197 For example, C transforms the electric charge of a particle state $Q \rightarrow -Q$.
- 198 2. The parity operator P , which inverts the spatial dimensions of space time:
 199 $\vec{x} \rightarrow -\vec{x}$. As such, it transforms left-handed particle fields into right-handed
 200 particle fields and vice versa.
- 201 3. The time-inversion operator T , which inverts the temporal dimension of space
 202 time: $t \rightarrow -t$.

203 These are fundamentally related by the *CPT* theorem [?], which states that any
 204 Lorentz-invariant Quantum Field Theory (QFT) must be symmetric under the
 205 simultaneous application of *all* three operators. However, any one of the symmetries
 206 can be broken individually, and experiments have shown the physical laws of our
 207 world to violate each of the C , P , and T symmetries.

208 Such a symmetry-breaking effect was established for the first time in 1956, when
 209 Chien-Shiung Wu observed parity violation in weak decays of Co-60 nuclei [?], after
 210 carrying out an experiment that was proposed by Yang Chen-Ning and Tsung-Dao
 211 Lee [?]. While this experiment established the breaking of P symmetry, it left open
 212 the possibility that the physical laws are invariant under a combination of a charge-
 213 and parity inversion; that they are CP symmetric. However, this was disproved in
 214 1964 when Kronin and Fitch observed that long-lived kaons, which predominantly
 215 decay to the CP -odd 3π state, could also decay to the CP -even $\pi\pi$ states [?].

216 Since then CP violation has been found in the B^0 system by the BaBar and Belle
 217 collaborations [?, ?] during the early 2000's; the B factories, along with CDF, also saw
 218 evidence for CP violation in B^\pm decays [?, ?, ?, ?, ?, ?, ?] later confirmed by LHCb [?],
 219 and CP violation was measured for the B_s^0 meson by LHCb in 2013 [?]; within the
 220 last year and a half, the first observation of CP -violation in D^0 decays has also been
 221 made by the LHCb collaboration [?], and most recently evidence for CP -violation in
 222 the neutrino sector has been reported by the T2K collaboration [?]. The observed
 223 effects can be divided into distinct classes. The conceptually simplest case is

- 224 1. *CP -violation in decay*, where $|A/\bar{A}| \neq 1$ for some decay amplitude A , and the
 225 amplitude \bar{A} of the CP -conjugate decay. The result is different decay rates in
 226 two CP -conjugate decays

$$\Gamma(M \rightarrow f) \neq \Gamma(\bar{M} \rightarrow \bar{f}). \quad (2.1)$$

227 This type of CP violation was not seen until the late 1980ies [?, ?], more than
 228 20 years after the first observation of CP violation, and only finally established
 229 around the year 2000 [?, ?]. Also this discovery was made in $K \rightarrow \pi\pi$ decays.

230 CP -violation in decay is the only type possible for charged initial states, and
231 it is thus the main focus of the thesis. Two additional CP -violating effect are
232 possible for neutral initial states (a situation that will be the main focus of
233 Chapter 4). These effects are

234 2. *CP -violation in mixing*, which denotes the case where the mixing rates between
235 the M^0 and \bar{M}^0 states differ

$$\Gamma(M^0 \rightarrow \bar{M}^0) \neq \Gamma(\bar{M}^0 \rightarrow M^0). \quad (2.2)$$

236 The CP violation first observed by Kronin and Fitch in the neutral kaon
237 sector [?] is (dominantly) of this type.

238 3. *CP -violation in interference between mixing and decay*, which can be present
239 for a neutral initial states M^0 decaying into a final state f common to both
240 M^0 and \bar{M}^0 . The decay rate includes an interference term between two
241 amplitudes: the amplitude for a direct $M^0 \rightarrow f$ decay and the amplitude
242 for a decay after mixing: $M^0 \rightarrow \bar{M}^0 \rightarrow f$. Even in the absence of the two
243 aforementioned effects, the rates $\Gamma(M^0 \rightarrow f)$ and $\Gamma(\bar{M}^0 \rightarrow \bar{f})$ can differ due
244 to the interference term. Such CP asymmetries have been measured in eg.
245 $B^0 \rightarrow J/\psi K$ by LHCb and the B factories, and in $B_s^0 \rightarrow J/\psi \phi$ decays by the
246 LHC and Tevatron experiments [?].

247 CP violation measurements thus have a long, rich, and still-developing history.

248 2.2 **CP violation in the Standard Model**

249 All existing measurements of CP violation in the quark sector are naturally explained
250 in the SM; indeed, the need to explain the observation CP violation in neutral
251 kaons was a driving force in the development of the model in the first place, when
252 it lead Kobayashi and Maskawa to predict the existence of then-unknown particles
253 in 1973 [?] (now known to be the third generation quarks).

254 2.2.1 **The CKM matrix and the Unitarity Triangle**

255 The SM contains three generations of quarks, each consisting of an up-type quark (u ,
256 c , and t) and a down-type quark (d , s , and b). The charged weak interaction of the
257 W^\pm boson couples up and down-type quarks. The quark states that couple to the W
258 are not (a priori) identical to the mass eigenstates, and can be denoted (u' , c' , and t')
259 and (d' , s' , and b'). A basis for the quark states can be chosen such that the weakly

260 coupling up-quark states are identical to the propagating quark states, $u = u'$, but
261 then the down-type quark state are different: $d' \neq d$. The two bases of the down-type
262 quarks are related via the Cabibbo-Kobayashi-Maskawa (CKM) matrix [?, ?]¹

$$\begin{pmatrix} d' \\ s' \\ t' \end{pmatrix} = V \begin{pmatrix} d \\ s \\ t \end{pmatrix} = \begin{pmatrix} V_{ud} & V_{us} & V_{ub} \\ V_{cd} & V_{cs} & V_{cb} \\ V_{td} & V_{ts} & V_{tb} \end{pmatrix} \begin{pmatrix} d \\ s \\ t \end{pmatrix}. \quad (2.3)$$

263 Thus the Lagrangian terms representing the coupling of a W^\pm boson with a u -
264 and a d -type quark is

$$\mathcal{L}_{W^+} = -\frac{g}{\sqrt{2}} V_{ud} (\bar{u} \gamma^\mu W_\mu^+ d) \quad \mathcal{L}_{W^-} = -\frac{g}{\sqrt{2}} V_{ud}^* (\bar{d} \gamma^\mu W_\mu^- u) \quad (2.4)$$

265 where g is the weak coupling constant, γ_u are the Dirac matrices, and u and d
266 represent the left-handed components of the physical quark states.

267 The CKM matrix is a unitary complex 3×3 matrix, and hence has $3^2 = 9$
268 independent, real parameters. However, 5 of these can be absorbed into non-physical
269 phases of the quark states (both mass and weak eigenstates) and hence the matrix
270 has 4 real, physical parameters: 3 mixing angles and a single phase. Chau and
271 Keung [?] proposed the parameterisation

$$\begin{aligned} V &= \begin{pmatrix} 1 & 0 & 0 \\ 0 & c_{23} & s_{23} \\ 0 & -s_{23} & c_{23} \end{pmatrix} \begin{pmatrix} c_{13} & 0 & s_{13}e^{-i\delta_{CP}} \\ 0 & 1 & 0 \\ -s_{13}e^{-i\delta_{CP}} & 0 & c_{13} \end{pmatrix} \begin{pmatrix} c_{12} & s_{12} & 0 \\ -s_{12} & c_{12} & 1 \\ 0 & 0 & 1 \end{pmatrix} \\ &= \begin{pmatrix} c_{12}c_{13} & s_{12}c_{13} & s_{13}e^{-i\delta_{CP}} \\ -s_{12}c_{23} - c_{12}s_{23}s_{13}e^{i\delta_{CP}} & c_{12}c_{23} - s_{12}s_{23}s_{13}e^{i\delta_{CP}} & s_{23}c_{13} \\ s_{12}s_{23} - c_{12}c_{23}s_{13}e^{i\delta_{CP}} & -c_{12}s_{23} - s_{12}c_{23}s_{13}e^{i\delta_{CP}} & c_{23}c_{13} \end{pmatrix} \end{aligned} \quad (2.5)$$

272 which is the preferred standard by the PDG [?]. Here, $s_{ij} \equiv \sin \theta_{ij}$ and $c_{ij} \equiv \cos \theta_{ij}$
273 denote the sine and cosine of three rotation angles in quark space; $\theta_{12} = \theta_C$ being
274 the usual Cabibbo angle [?].

275 The presence of the complex phase δ_{CP} in the Lagrangian term of the W coupling
276 causes CP violation because, as evident from Eq. (2.4), if δ_{CP} enters the amplitude
277 for some decay mediated by a W boson, $A = |A|e^{i(\delta_0 + \delta_{CP})}$, then it will enter the
278 CP conjugate decay amplitude with the opposite sign: $\bar{A} = |A|e^{i(\delta_0 - \delta_{CP})}$. In these
279 expressions, δ_0 denotes a CP conserving phase that is not caused by complex terms
280 in the Lagrangian, but arises due to potential intermediate states in the decay

¹ A basis for the quarks can of course be chosen, such that neither the up-quarks or the down-quarks are expressed in their mass eigenstates. In that case the CKM matrix is recovered as $V = U_u^* U_d$, where $U_{u/d}$ is the unitary transformation matrices that brings the u/d quarks into their mass eigenstates.

amplitude.² Usually the underlying mechanism is due to QCD effects, and these CP conserving phases are therefore generally dubbed *strong* phases, as opposed to the CP violating *weak* phase of the W coupling [?]. This terminology will be applied throughout the thesis.

Experimentally, it has been observed that the CKM matrix elements of Eq. (2.5) satisfy $s_{13} \ll s_{23} \ll s_{12}$. This motivates an often used, alternative parameterisation of the matrix, where the elements are expressed as power series in a parameter λ that naturally incorporates this hierarchy: the Wolfenstein parameterisation [?].

The definitions

$$\begin{aligned} s_{12} &\equiv \lambda \\ s_{23} &\equiv \lambda^2 A \\ s_{13} &\equiv \lambda^3(\rho - i\eta) \end{aligned} \tag{2.6}$$

are made, after which the unitarity conditions (or Eq. 2.5) determine the remaining elements to any order in λ .³ To $\mathcal{O}(\lambda^5)$ the Wolfenstein parameterisation of the CKM matrix is [?, ?]

$$V = \begin{pmatrix} 1 - \frac{\lambda^2}{2} - \frac{\lambda^4}{8} & \lambda & A\lambda^3(\rho - i\eta) \\ -\lambda + \frac{\lambda^5}{2}A^2(1 - 2(\rho + i\eta)) & 1 - \frac{\lambda^2}{2} - \frac{\lambda^4}{8}(1 + 4A^2) & A\lambda^2 \\ A\lambda^3(1 - (\rho + i\eta)(1 - \frac{\lambda^2}{2})) & -A\lambda^2(1 - \frac{\lambda^2}{2}(1 - 2(\rho + i\eta))) & 1 - \frac{1}{2}A^2\lambda^4 \end{pmatrix}. \tag{2.7}$$

293

294 The unitarity condition $V^\dagger V = \mathbb{1}$ of the CKM matrix defines 9 relations between
295 the CKM elements of the form

$$\sum_j V_{jq}^* V_{jq} = 1 \quad , \quad q \in \{d, s, b\} \quad \text{along the diagonal} \tag{2.8a}$$

$$\sum_j V_{jq}^* V_{jq'} = 0 \quad , \quad q, q' \in \{d, s, b\}, q \neq q' \quad \text{off-diagonal.} \tag{2.8b}$$

296 The off-diagonal conditions constrain three complex numbers to sum to zero, and
297 can thus be visualised as triangles in the complex plane, the so-called unitarity
298 triangles. Of these, the triangle corresponding to the (d, b) elements plays a
299 special role, because all three sides are of the same order of magnitude, $\mathcal{O}(\lambda^3)$.
300 When expressed in the form

$$\frac{V_{ud}^* V_{ub}}{V_{cd}^* V_{cb}} + \frac{V_{td}^* V_{tb}}{V_{cd}^* V_{cb}} + 1 = 0, \tag{2.9}$$

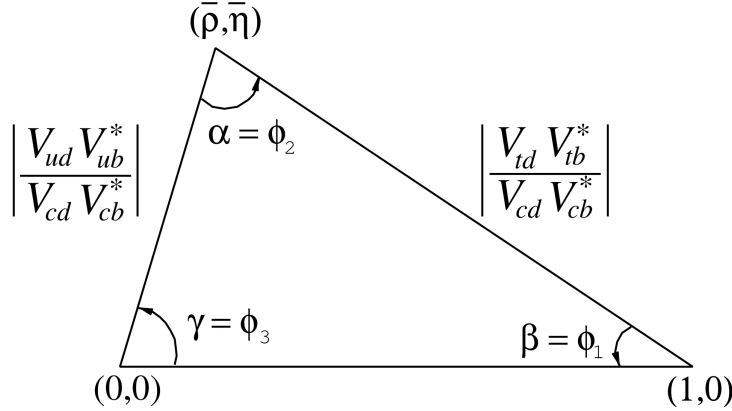


Figure 2.1: Definition of the lengths and sides of the Unitarity Triangle. Figure is taken from the *CKM Quark-Mixing Matrix* review of the PDG [?].

301 it is often referred to as the singular Unitarity Triangle, illustrated in Fig. 2.1 where
 302 the usual names for the three angles are also given.

303 Over-constraining the unitarity triangle by making separate measurements of all
 304 sides and angles, in as many different decay channels as possible, is an important,
 305 and non-trivial test of the SM. The current experimental constraints are in agreement
 306 with the SM predictions, as visualised in Fig. 2.2. The CKM angle

$$\gamma \equiv \arg(-V_{ud} V_{ub}^* / V_{cd} V_{cb}^*) = \arg(-V_{cb} V_{cd}^* / V_{ub} V_{ud}^*) \quad (2.10)$$

307 is unique among the CKM parameters, in that it can be measured in tree-level pro-
 308 cesses without significant theoretical uncertainty from lattice QCD calculations [?].
 309 Because tree-level processes are less likely to be affected by Beyond-Standard-Model
 310 (BSM) effects, direct measurements of γ can be considered a SM benchmark, which
 311 can be compared to estimates based on measurements of other CKM elements
 312 that are measured in loop-level processes, and thus are more likely to be affected
 313 by BSM effects [?]. The current, worldwide combination of direct measurements,
 314 published by the CKMFitter group, is $\gamma = (72.1^{+5.4}_{-5.7})^\circ$, to be compared with the
 315 estimate from loop-level observables of $\gamma = (65.66^{+0.90}_{-2.65})^\circ$ [?]. Other world averages
 316 exist [?, ?], but the overall picture is the same: the ability to constrain BSM physics
 317 is currently limited by the uncertainty of the direct measurements. Hence further
 318 precision measurements of γ are highly motivated. Presently, the precision is driven
 319 by time-integrated measurements of direct CP -violation in $B^\pm \rightarrow D K^\pm$ decays;

²It is generally true that all phases of a single term in a given amplitude will be convention dependent, but that the phase differences between terms are not.

³Other variants of the Wolfenstein parameterisation do exist [?]. They all agree at the lowest orders of λ .

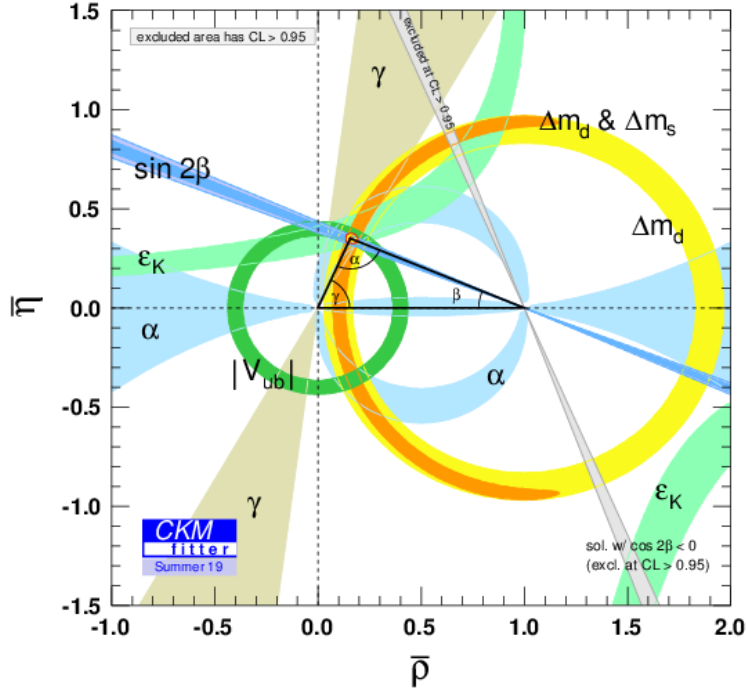


Figure 2.2: Current constraints on the Unitarity Triangle parameters as determined by the CKMFitter group for the EPS 2019 conference [?].

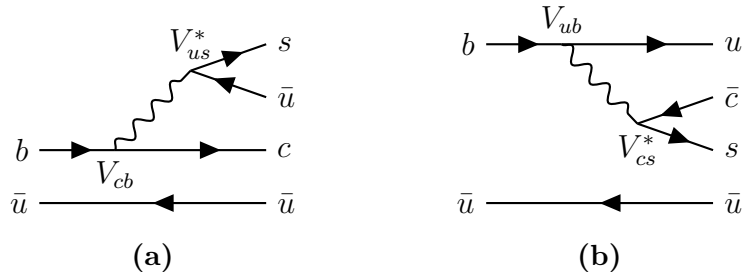


Figure 2.3: Tree level Feynman diagrams describing (a) $B^- \rightarrow D^0 K^-$ and (b) $B^- \rightarrow \bar{D}^0 K^-$ decays. The electro-weak phase difference between the two decays is $\Delta\phi = \arg(V_{cb}V_{us}^*/V_{ub}V_{cs}^*) \simeq \gamma$.

such a measurement is the topic of this thesis and the theory behind is treated in detail in the following section. It is also possible to measure γ in time-dependent mixing analyses of $B_s^0 \rightarrow D_s^\mp K^\pm$, $B^0 \rightarrow D^\mp \pi^\pm$ and related decays, by measuring CP violation in interference between mixing and decay. These modes are expected to provide competitive measurements in the future [?, ?].

2.2.2 Measuring γ in tree level decays

The phase γ can be measured in tree-level processes with interference between $b \rightarrow c\bar{s}u$ and $b \rightarrow \bar{c}s u$ transitions. The canonical example, also the subject of this thesis, is based on measurements sensitive to interference between the $B^\pm \rightarrow D^0 K^\pm$ and $B^\pm \rightarrow \bar{D}^0 K^\pm$ decay amplitudes. As illustrated in Fig. 2.3 for the case of B^- decays, the electro-weak phase difference between the two decays is $\Delta\phi = \arg(V_{cb}V_{us}^*/V_{ub}V_{cs}^*)$. While $\Delta\phi$ is not identical to the definition of γ in Eq. (2.10), the ratio of the involved CKM matrix elements is [?]

$$\begin{aligned} -\frac{V_{cd}^*/V_{ud}^*}{V_{us}^*/V_{cs}^*} &= -\frac{-\lambda[1 - \frac{\lambda^4}{2}A^2(1 - 2(\rho - i\eta))](1 - \frac{\lambda^2}{2} - \frac{\lambda^4}{8}(1 + 4A^2))}{\lambda(1 - \frac{\lambda^2}{2} - \frac{\lambda^4}{4})} \\ &= 1 - \lambda^4 A^2(1 - 2(\rho - i\eta)) + \mathcal{O}(\lambda^5). \end{aligned} \quad (2.11)$$

The ratio equals unity to $\mathcal{O}(\lambda^4) \simeq 2.6 \times 10^{-3}$, and thus $\Delta\phi \simeq \gamma$ is a good approximation within current experimental uncertainties. For the remainder of this thesis the approximation will be used without further comment. The diagrams in Fig. 2.3 describe the leading order contributions to the two amplitudes

$$\begin{aligned} A[B^- \rightarrow D^0 K^-] &\equiv A_B \\ A[B^- \rightarrow \bar{D}^0 K^-] &\equiv \bar{A}_B \equiv r_B A_B e^{i(\delta_B - \gamma)}, \end{aligned} \quad (2.12a)$$

where the last equality introduces two new parameters: the amplitude magnitude ratio $r_B \equiv |\bar{A}_B|/|A_B|$, and δ_B , the strong-phase difference between the decay amplitudes. Since all CP -violation is attributed to the electro-weak phase in the SM, the CP -conjugate decay amplitudes are [?]

$$\begin{aligned} A[B^+ \rightarrow \bar{D}^0 K^+] &= A_B \\ A[B^+ \rightarrow D^0 K^+] &= \bar{A}_B = r_B A_B e^{i(\delta_B + \gamma)}. \end{aligned} \quad (2.12b)$$

In an experimental setting, the D^0 and \bar{D}^0 mesons are reconstructed in some final state, f or its CP -conjugate \bar{f} . In analogy with the B^\pm decays, the D decay amplitude can be related⁴

$$\begin{aligned} A[D^0 \rightarrow f] &= A[\bar{D}^0 \rightarrow \bar{f}] = A_D \\ A[\bar{D}^0 \rightarrow f] &= A[D^0 \rightarrow \bar{f}] = r_D A_D e^{i\delta_D}. \end{aligned} \quad (2.13)$$

where the assumption has been made that CP violation in the D decays is negligible, and δ_D denotes a CP -conserving strong-phase difference. While CP -violation in

⁴In this notation δ_D is thus phase of the suppressed D -decay amplitude minus the phase of the favoured D -decay amplitude. This is the opposite convention to that used in the LHCb measurements with the ADS technique, but aligns with the notation used in the literature on γ measurements in $D \rightarrow K_S^0 \pi^+ \pi^-$ decays.

³⁴⁶ D decays has recently been measured [?], the size of the effect is small and it is
³⁴⁷ considered negligible in this thesis. Based on Eqs. 2.12 and (2.13), the decay rates
³⁴⁸ of B^+ and B^- mesons into the possible final states can be seen to satisfy

$$\Gamma(B^- \rightarrow D(\rightarrow f)K^-) \propto 1 + r_D^2 r_B^2 + 2r_B r_D \cos [\delta_B + \delta_D - \gamma], \quad (2.14a)$$

$$\Gamma(B^+ \rightarrow D(\rightarrow \bar{f})K^+) \propto 1 + r_D^2 r_B^2 + 2r_B r_D \cos [\delta_B + \delta_D + \gamma], \quad (2.14b)$$

$$\Gamma(B^- \rightarrow D(\rightarrow \bar{f})K^-) \propto r_D^2 + r_B^2 + 2r_B r_D \cos [\delta_B - \delta_D - \gamma], \quad (2.14c)$$

$$\Gamma(B^+ \rightarrow D(\rightarrow f)K^+) \propto r_D^2 + r_B^2 + 2r_B r_D \cos [\delta_B - \delta_D + \gamma]. \quad (2.14d)$$

³⁴⁹ The processes in Eqs. (2.14a) and (2.14b) are CP -conjugate and it is clear how, in the
³⁵⁰ general case where $\delta_B + \delta_D \neq 0$, a non-zero value of γ leads to CP violation in the form
³⁵¹ of differing decay rates. The same is true for the processes in Eqs. (2.14c) and (2.14d).
³⁵² Depending on the choice of D final state, these expressions can be used to relate
³⁵³ γ to various observables that are experimentally accessible. This thesis concerns
³⁵⁴ the choice $f = K_S^0 \pi^+ \pi^-$ or $f = K_S^0 K^+ K^-$, where the terms related to the D decay
³⁵⁵ all have a non-trivial variation over the phase space of the decay. However, it is
³⁵⁶ useful to first analyse the simpler case where f is a two-body state.

³⁵⁷ The simplest case is when f is chosen to be a CP eigenstate, so that $f = \pm \bar{f}$
³⁵⁸ and the rate equations of (2.14a)–(2.14d) simplify, because $r_D = 1$ and $\delta_D \in \{0, \pi\}$.
³⁵⁹ Measurements of γ in such decay modes are denoted GLW measurements, after
³⁶⁰ Gronau, London, and Wyler who described the approach in the early 90ies [?, ?].
³⁶¹ Experimentally it is preferable to measure yield ratios rather than absolute rates,
³⁶² and the observables of interest are thus the CP asymmetry

$$\begin{aligned} A_{CP=\pm 1} &= \frac{\Gamma[B^- \rightarrow D_{CP} K^-] - \Gamma[B^+ \rightarrow D_{CP} K^+]}{\Gamma[B^- \rightarrow D_{CP} K^-] + \Gamma[B^+ \rightarrow D_{CP} K^+]} \\ &= \frac{\pm r_B \sin \delta_B \sin \gamma}{1 + r_B^2 \pm 2r_B \cos \delta_B \cos \gamma}, \end{aligned} \quad (2.15a)$$

³⁶³ as well as the ratio

$$\begin{aligned} R_{CP=\pm 1} &= 2 \frac{\Gamma[B^- \rightarrow D_{CP} K^-] + \Gamma[B^+ \rightarrow D_{CP} K^+]}{\Gamma[B^- \rightarrow D^0 K^-] + \Gamma[B^+ \rightarrow \bar{D}^0 K^+]} \\ &= 1 + r_B^2 \pm 2r_B \cos \delta_B \cos \gamma. \end{aligned} \quad (2.15b)$$

³⁶⁴ In practice, A_{CP} and R_{CP} are obtained from measured yield ratios that are corrected
³⁶⁵ with appropriate branching fractions. A measurement of A_{CP} and R_{CP} alone is not
³⁶⁶ sufficient to determine the underlying physics parameters (γ, r_B, δ_B) , and this is
³⁶⁷ not solely due to the number of parameters exceeding the number of constraints:
³⁶⁸ the equations also allow for multiple, ambiguous solutions for (γ, δ_B) . One way
³⁶⁹ to break the ambiguity, first noted in the original paper [?], is to make further

370 measurements in additional B decays. These can be described with the formalism
 371 described above, but will not share the same ambiguous solutions because (r_B, δ_B)
 372 are unique to a given B decay. Another method is to analyse D decay final states
 373 that are not CP eigenstates.

374 A few years later, Atwood, Dunietz, and Sonis analysed an alternative choice of
 375 D final states: a simultaneous analysis of a Cabibbo-favoured (CF) decay $D^0 \rightarrow f$
 376 and the doubly-Cabibbo-suppressed (DCS) decay $D^0 \rightarrow \bar{f}$ into the CP conjugate
 377 final state [?, ?]. Their suggested method is named the ADS method after the
 378 authors. The classical example is to take $f = K^-\pi^+$ and $\bar{f} = \pi^-K^+$. The relative
 379 suppression means that the r_D of Eq. (2.14) is small, typically of the same order of
 380 magnitude as r_B , and thus the CP asymmetry of the suppressed decay is $\mathcal{O}(1)$:

$$\begin{aligned} A_{ADS(\bar{f})} &= \frac{\Gamma[B^- \rightarrow D(\rightarrow \bar{f})K^-] - \Gamma[B^+ \rightarrow D(\rightarrow f)K^+]}{\Gamma[B^- \rightarrow D(\rightarrow \bar{f})K^-] + \Gamma[B^+ \rightarrow D(\rightarrow f)K^+]} \\ &= \frac{r_D r_B \sin(\delta_B - \delta_D) \sin \gamma}{r_D^2 + r_B^2 + 2r_D r_B \cos(\delta_B - \delta_D) \cos \gamma}. \end{aligned} \quad (2.16a)$$

381 The large CP asymmetry is a prime feature of the ADS method. However, also the
 382 suppressed-to-favoured yield ratio is sensitive to the physics parameters of interest:

$$\begin{aligned} R_{ADS(\bar{f})} &= \frac{\Gamma[B^- \rightarrow D(\rightarrow \bar{f})K^-] + \Gamma[B^+ \rightarrow D(\rightarrow f)K^+]}{\Gamma[B^- \rightarrow D(\rightarrow f)K^-] + \Gamma[B^+ \rightarrow D(\rightarrow \bar{f})K^+]} \\ &= \frac{r_B^2 + r_D^2 + 2r_D r_B \cos(\delta_B - \delta_D) \cos \gamma}{1 + r_D^2 r_B^2 + 2r_D r_B \cos(\delta_B + \delta_D) \cos \gamma}. \end{aligned} \quad (2.16b)$$

383 The interpretation of A_{ADS} and R_{ADS} in terms of (γ, r_B, δ_B) requires knowledge of
 384 the r_D and δ_D parameters, but these can be measured independently. In general,
 385 the constraints from a single set of ADS observables suffer the same ambiguities as
 386 in the GLW case. However, unlike the GLW case, each D decay mode provides an
 387 independent set of constraints, because the parameters related to the D decay vary.

388 The discussion of this section has centred on the classical case of $B^\pm \rightarrow DK^\pm$
 389 decays with a two-body D final state. With minor modifications the techniques have
 390 been used to make measurements sensitive to γ in B^0 decays, with B decay final
 391 states including excited D mesons or kaons, and in $B^\pm \rightarrow D\pi^\pm$ decays (summaries of
 392 the measurements made by the B factories and LHCb can be found in Refs. [?, ?, ?, ?]).
 393 The $B^\pm \rightarrow D\pi^\pm$ decay is also CP -violating, although the effect is much smaller
 394 than in the $B^\pm \rightarrow DK^\pm$ decay because $r_B^{D\pi} \simeq 0.005$ [?], whereas $r_B^{DK} \simeq 0.1$.
 395 Furthermore, it is possible to use multi-body D final states. However, in some
 396 cases, a better precision can then be obtained by exploiting phase-space dependent
 397 decay rates. This is the topic of the next section.

398 2.3 Measuring γ using multi-body D final states

399 In multi-body D decays, the r_D and δ_D parameters of the fundamental rate equations
400 in Eq. (2.14) vary over the phase space of the D decay. This section describes
401 a model-independent approach to measure γ in $B \rightarrow D(\rightarrow K_S^0\pi^+\pi^-)h^\pm$ decays
402 by exploiting this variation. The theory is identical for $D \rightarrow K_S^0K^+K^-$ decays,
403 and similar ideas have been proposed for the $D \rightarrow K_S^0\pi^+\pi^-\pi^0$ [?] and $D \rightarrow$
404 $2\pi^+2\pi^-$ modes [?]. First, however, the formalism for describing amplitudes of
405 multi-body decays is briefly reviewed.

406 2.3.1 Dalitz plots and the phase space of multi-body decays

407 In general, the phase space of the n -body decay $P \rightarrow p_1 + p_2 + \dots + p_n$ consists of n
408 four momenta, with a total of $4n$ components. The requirement that each of the final
409 state particles is on-shell provides n constraints on these components, and energy-
410 momentum conservation removes a further 4 degrees of freedom. If the original
411 particle P is a scalar, the decay is isotropic, which removes an additional 3 degrees
412 of freedom, leaving the total number of degrees of freedom at $3n - 7$. For the specific
413 case of three-body decays, the available phase space can thus be parameterised with
414 only two parameters. A practical and often used choice is the invariant masses

$$s_{12} = m^2(p_1 p_2) = (p_1^\mu + p_2^\mu)^2, \quad s_{13} = m^2(p_1 p_3) = (p_1^\mu + p_3^\mu)^2. \quad (2.17)$$

415 The choice of particle pairs is arbitrary, and the coordinates easily related

$$m_P^2 + m_{p_1}^2 + m_{p_2}^2 + m_{p_3}^2 = m^2(p_1 p_2) + m^2(p_1 p_3) + m^2(p_2 p_3). \quad (2.18)$$

416 A scatter plot of (s_{12}, s_{13}) values for a sample of particle decays is denoted a Dalitz
417 plot [?]. It has the very useful feature that the presence of (narrow) resonances
418 in the decay leads to visible bands in the scatter plot. Figure 2.4 illustrates how
419 the limits of the Dalitz plot are defined by kinematic constraints, and shows an
420 example of a Dalitz plot for $D \rightarrow K_S^0\pi^+\pi^-$ decays in which the $K^*(892)^\pm$ and $\rho(770)$
421 resonances are clearly visible. The plot shows the sample of $B^+ \rightarrow D\pi^+$ decays
422 used to make the measurement described in Chapter 5 and thus the D meson is in
423 a superposition of D^0 and \bar{D}^0 states (as detailed in the following section).

424 In terms of the coordinates of Eq. (2.17) the differential decay rate is given by

$$d\Gamma = \frac{1}{32(2\pi)^3 m_P^3} |\mathcal{M}|^2 ds_{12} ds_{13}, \quad (2.19)$$

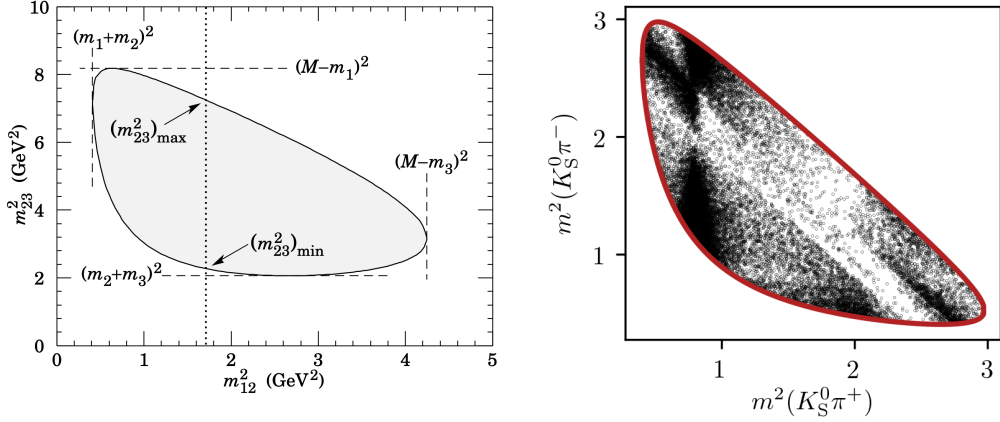


Figure 2.4: (Left) Schematic of a Dalitz plot and the limits of the kinematically allowed phase space limits. (Right) Example of a Dalitz plot for $D \rightarrow K_S^0 \pi^+ \pi^-$ decays where the D meson originates in a $B^+ \rightarrow D \pi^+$ decay; the decaying D meson is in a superposition of the D^0 and \bar{D}^0 states, but predominantly \bar{D}^0 -like.

where \mathcal{M} is the QFT matrix element, or total decay amplitude, corresponding to the decay. In general, it is not possible to calculate \mathcal{M} from first principles. Instead, a model is defined with an empirically well motivated form, in which a number of free parameters must be determined experimentally. The simplest case is that of an *isobar* model, where it is assumed that the full decay can be decomposed into consecutive two-body decays of the form $P \rightarrow R_{12}(\rightarrow p_1 + p_2)p_3$. Thus, \mathcal{M} is expressed as a non-resonant constant amplitude term, k_{NR} , plus a sum of resonance terms

$$\mathcal{M}(s_{12}, s_{13}) = k_{NR} + \sum_r k_r \mathcal{M}^r(s_{12}, s_{13}). \quad (2.20)$$

The exact form of the \mathcal{M}^r function depends on the resonance in question. An overview is given in the PDG review on resonances and references therein [?]. The isobar formalism breaks down when resonances in the decay are not well separated. In this case, models of the form in Eq. (4.27) can still be employed, if the contribution from overlapping resonances are collected in a single term. An example of such a model, is the amplitude model for $D^0 \rightarrow K_S^0 \pi^+ \pi^-$ decays developed by the Belle collaboration for a measurement of the CKM angle β in 2018 [?]. In this model, individual terms are included for $D^0 \rightarrow K^*(\rightarrow K_S^0 \pi^\pm)\pi^\mp$ decays, whereas the $\pi\pi$ and $K\pi$ S -wave contributions are modelled with the so-called K -matrix- and LASS formalisms [?, ?]. The amplitude and phase of \mathcal{M} as predicted by this model are shown in Fig. 2.5.

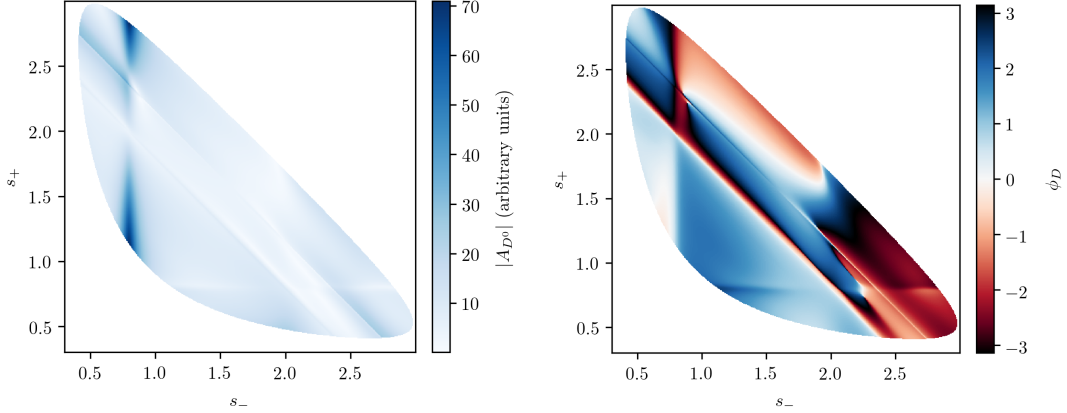


Figure 2.5: The (left) magnitude and (right) phase of the $D \rightarrow K_S^0 \pi^+ \pi^-$ amplitude in the Belle 2018 model [?].

2.3.2 The GGSZ method to measure γ

The non-trivial phase-space dependence of the $D \rightarrow K_S^0 \pi^+ \pi^-$ decay amplitude can be exploited to measure γ with $B^\pm \rightarrow DK^\pm$ or $B^\pm \rightarrow D\pi^\pm$ decays. This approach was proposed independently by Bondar [?], and by Giri, Grossman, Soffer, and Zupan [?] after whom it takes the commonly used acronym GGSZ. For this specific decay s_- and s_+ are used to describe the Dalitz coordinates $m^2(K_S^0 \pi^-)$ and $m^2(K_S^0 \pi^+)$, respectively, and the D decay amplitude is a function of these coordinates

$$A_S^{\bar{D}}(s_-, s_+) = A(\bar{D}^0 \rightarrow K_S^0 \pi^+ \pi^-). \quad (2.21)$$

To a good approximation the K_S^0 meson is a CP eigenstate, meaning that the $K_S^0 \pi^+ \pi^-$ state is self-conjugate. Assuming this approximation to be exact, and that CP violation in the D decay is negligible, the D decay amplitude satisfies the symmetry relation

$$A_S^{\bar{D}}(s_-, s_+) = A_S^D(s_+, s_-). \quad (2.22)$$

The impact of the K_S^0 meson *not* being an exact CP eigenstate is treated in detail in Chapter 4. In order to simplify equations, the short-hand notation

$$(s_{-+}) = (s_-, s_+), \quad (s_{+-}) = (s_+, s_-), \quad (2.23)$$

will be employed for the remainder of the thesis, so that the relation in Eq. (2.22) can be expressed as $A_S^{\bar{D}}(s_{-+}) = A_S^D(s_{+-})$. Thus, the rate equations of Eq. (2.14)

458 for the $D \rightarrow K_S^0\pi^+\pi^-$ decay mode are

$$\begin{aligned} d\Gamma^-(s_{-+}) &\propto |\mathcal{A}_S^-|^2 = |A_B|^2 |A_{K_S^0}|^2 \\ &\times [|A_S^D(s_{-+})|^2 + r_B^2 |A_S^D(s_{+-})|^2 + 2r_B |A_S^D(s_{-+})| |A_S^D(s_{+-})| \\ &\times (\cos[\delta_D(s_{-+})] \cos[\delta_B - \gamma] + \sin[\delta_D(s_{-+})] \sin[\delta_B - \gamma])], \end{aligned} \quad (2.24a)$$

$$\begin{aligned} d\Gamma^+(s_{-+}) &\propto |\mathcal{A}_S^+|^2 = |A_B|^2 |A_{K_S^0}|^2 \\ &\times [|A_S^D(s_{+-})|^2 + r_B^2 |A_S^D(s_{-+})|^2 + 2r_B |A_S^D(s_{-+})| |A_S^D(s_{+-})| \\ &\times (\cos[\delta_D(s_{-+})] \cos[\delta_B + \gamma] - \sin[\delta_D(s_{-+})] \sin[\delta_B + \gamma])]. \end{aligned} \quad (2.24b)$$

459 Here, $\delta_D(s_{-+}) = \phi_D(s_{-+}) - \phi_D(s_{+-}) = -\delta_D(s_{+-})$, where $\phi_D(s_{-+})$ denotes the
 460 complex phase of the $A_S^D(s_{-+})$ amplitude, and a standard trigonometric relation
 461 have been employed to factorise the terms depending on the complex phases of the B
 462 and D decays. It can be seen that in the case where $\gamma = 0$ the B^+ and B^- decay rates
 463 are symmetric if the Dalitz coordinates are exchanged: $\Gamma^+(s_-, s_+) = \Gamma^-(s_+, s_-)$.
 464 The presence of CP violation in the B decay breaks the symmetry. Therefore it is
 465 possible to measure γ (and the nuisance parameters r_B and δ_B) from the phase-space
 466 distribution of $B^\pm \rightarrow D(\rightarrow K_S^0\pi^+\pi^-)K^\pm$ decays, given knowledge of $A_S^D(s_{-+})$.

467 A series of measurements of γ have been made that use amplitude models of
 468 the D decay [?, ?, ?, ?, ?, ?, ?, ?, ?]. However, a model-independent approach has been
 469 proposed by Bondar and Poluektov [?, ?] that relies on binning phase-space, in
 470 which case the necessary information on the D decay amplitude can be summarised
 471 in a small set of coefficients that can be measured in a separate experiment. That is
 472 the approach followed in this thesis, and has been used previously by the Belle [?]
 473 and LHCb collaborations [?]. It is described in detail in the following section.

474 Such a model-independent approach is favourable for two reasons. Firstly,
 475 uncertainty estimates related to model inputs and the choice of parameterisation in
 476 an amplitude model are non-trivial, yet would become the leading systematic with
 477 the very high precision expected for γ measurements in the near future. Secondly,
 478 amplitude models are notoriously hard to reproduce, and in a high-precision era it is
 479 favourable that any experiment is easy to reinterpret in various extensions of the
 480 SM. This is a lot easier for an experiment that measures a small set of well-defined
 481 observables, than for an experiment that fits a complicated amplitude model.

482 An alternative model-independent approach has recently been proposed by
 483 Poluektov [?] where the externally measured input on the D -decay phase are Fourier
 484 expansion coefficients, and which therefore avoids binning phase space; this approach
 485 may have the potential to improve the obtainable precision in the future.

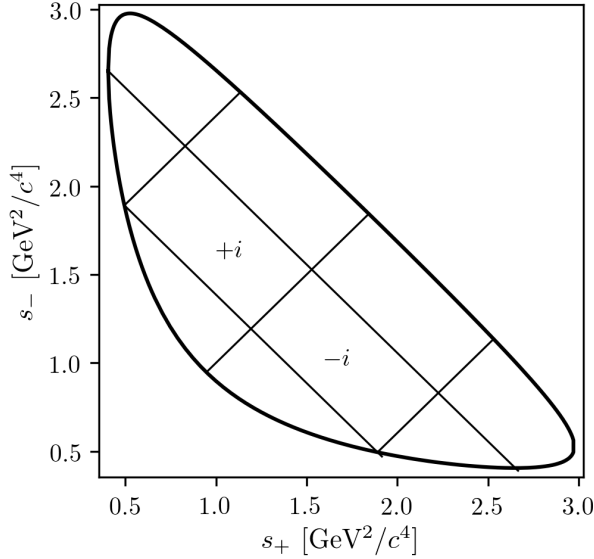


Figure 2.6: Illustration of the binning scheme used in GGSZ measurements: the bins are symmetric around the $m^2(K_S^0\pi^+) = m^2(K_S^0\pi^-)$ diagonal, and numbered so that opposite bins have the same number, but with opposite sign.

2.3.3 A model-independent approach

The phase-space distribution can be analysed in a model-independent way, if the D -decay phase space is split into regions, or bins, and the B decay yield in each bin determined experimentally. A measurement of γ using this approach is the main topic of the thesis. This section describes the fundamental principle, whereas the details pertaining to the exact experimental approach are delegated to Section 2.4.

The amplitude symmetry of Eq. (2.22) is exploited by defining $2N$ bins to be symmetric around the $s_- = s_+$ diagonal of the Dalitz plot, numbered $i = -N$ to N (omitting zero) such that if the point (s_-, s_+) is in bin i , then (s_+, s_-) is in bin $-i$, and by convention $i > 0$ for bins where $s_- > s_+$. The principle is illustrated in Fig. 2.6, but the binning schemes used in actual measurements are more complicated. The decay rates in Eq. (2.24) can be integrated over such bins, and give the bin yields

$$\begin{aligned} N_i^- &\propto h^- \left[K_i + r_B^2 K_{-i} + 2\sqrt{K_i K_{-i}} (c_i x_- + s_i y_-) \right], \\ N_i^+ &\propto h^+ \left[K_{-i} + r_B^2 K_i + 2\sqrt{K_i K_{-i}} (c_i x_+ - s_i y_+) \right], \end{aligned} \quad (2.25)$$

where the parameters describing the B decay have been expressed in terms of the observables

$$x_\pm = r_B \cos(\delta_B \pm \gamma), \quad y_\pm = r_B \sin(\delta_B \pm \gamma), \quad (2.26)$$

and a number of phase-space integrated quantities related to the D -decay have been introduced. The K_i parameters denote fractional yield of a flavour-tagged D^0 decaying into bin i , defined as

$$K_i = \frac{1}{N_K} \int_i ds^2 |A_S^D(s_{-+})|^2, \quad N_K = \int ds^2 |A_S^D(s_{-+})|^2, \quad (2.27)$$

where $\int_i ds^2$ denotes integration over bin i of the Dalitz plot. The c_i and s_i denote the amplitude-weighted average of $\cos \delta_D(s_{-+})$ and $\sin \delta_D(s_{-+})$ over bin i

$$\begin{aligned} c_i &= \frac{\int_i ds^2 |A_S^D(s_{-+})| |A_S^D(s_{+-})| \cos[\delta_D(s_{-+})]}{\sqrt{\int_i ds^2 |A_S^D(s_{-+})|^2} \sqrt{\int_i ds^2 |A_S^D(s_{+-})|^2}}, \\ s_i &= \frac{\int_i ds^2 |A_S^D(s_{-+})| |A_S^D(s_{+-})| \sin[\delta_D(s_{-+})]}{\sqrt{\int_i ds^2 |A_S^D(s_{-+})|^2} \sqrt{\int_i ds^2 |A_S^D(s_{+-})|^2}}. \end{aligned} \quad (2.28)$$

By the symmetry properties of $\delta_D(s_{-+})$ these parameters satisfy $c_i = c_{-i}$ and $s_i = -s_{-i}$. The normalisation constants h^+ and h^- are identical in the ideal case, but it is convenient to define them separately for practical reasons: depending on the experimental setup, there may be overall production and detection asymmetries that affect the total signal yields. An experimental analysis can be made insensitive to these effects because they can be absorbed into the normalisation constants, as long as they are constant over the D -decay phase space. This comes at the cost that the information on x_\pm and y_\pm from the overall CP asymmetry is lost, but Section 2.3.5 will show the loss in precision to be minimal.

Thus, for a set of $2N$ bins, the bin yields of Eqs. (2.25) provide $4N$ constraints on a total of $4N + 6$ parameters: $(h^\pm, K_i, c_i, s_i, x_\pm, y_\pm)$. However, the K_i , c_i , and s_i parameters relate only to the D decay, and can thus, in principle, be measured in independent experiments. With such external inputs, a measurement of the $B^\pm \rightarrow D(\rightarrow K_S^0 \pi^+ \pi^-) K^\pm$ yields in a set of bins can be used to constrain x_\pm and y_\pm , and thereby (γ, r_B, δ_B) . The measurement presented in this thesis determines the K_i parameters directly, but uses externally measured values of c_i and s_i as input, as measured in quantum correlated D decays by the CLEO [?] and BESIII [?] collaborations. Because these measurements are the foundation of the approach, they are described in some detail in the following section. In the future, it is possible that the c_i and s_i parameters may be measured in quantum-correlated D decays in LHCb [?], and in charm-mixing measurements [?].

2.3.4 Measuring strong-phase inputs at charm factories

The strong-phase parameters c_i and s_i have been measured by the CLEO and BESIII collaborations, using quantum correlated $D^0\bar{D}^0$ pairs from decays of the $\psi(3770)$ resonance state, itself produced in e^+e^- collisions at the resonance energy. The $\psi(3770)$ has quantum-number $C = -1$, which is conserved in the strong decay into two D mesons, and thus the two D mesons are produced in an anti-symmetric wave function. By observing the decay of one D meson into a specific final state, say a CP eigenstate, the quantum state of the other D meson can be determined. The measurement is based on decays where both D decays are reconstructed, one in the $K_S^0\pi^+\pi^-$ final state, the other in one of several different tag categories. The main principles are outlined below, but most experimental considerations and implementation details are left out for the sake of brevity.

The simplest case is when one D meson decays into a final state that uniquely tags the flavour, such as $\bar{D}^0 \rightarrow K^+e^-\bar{\nu}_e$. In that case, the D meson decaying to $K_S^0\pi^+\pi^-$ is known to be in the D^0 state and the decay rate is simply determined by $A_S^D : \Gamma(s_{-+}) \propto |A_S^D(s_{-+})|^2$. This allows for a measurement of the K_i parameters.

If one D meson is reconstructed in a CP -even state, eg. K^+K^- , or a CP -odd state, eg. $K_S^0\pi^0$, the D meson decaying to $K_S^0\pi^+\pi^-$ is known to be in a state of opposite CP . Thus, for a tag-decay of $CP = \pm 1$ the decay rate has the form

$$\Gamma_{CP=\pm 1} \propto |A_S^D(s_{-+}) \mp A_S^D(s_{+-})|^2 \quad (2.29a)$$

and the bin yields will be given by

$$M_i^\pm \propto K_i + K_{-i} \mp 2\sqrt{K_i K_{-i}} c_i. \quad (2.29b)$$

Thus a simultaneous analysis of flavour and CP tagged decays allow for a determination of the K_i and c_i parameter sets.

Finally, the case where both D mesons, for now denoted D and D' , decay into the $K_S^0\pi\pi$ final state can be considered. The total amplitudes have contributions from the case where D is in the D^0 state and D' is in the \bar{D}^0 state, as well as the opposite flavour assignment. Thus the decay rate satisfies

$$\Gamma_{CP=\pm 1} \propto |A_S^D(s_{-+})A_S^D(s'_{+-}) + A_S^D(s_{+-})A_S^D(s'_{-+})|^2 \quad (2.30a)$$

where s_{-+} denotes the Dalitz-plot coordinates of the D meson, and s'_{-+} those of the D' meson. Defining M_{ij} to be the yield of decays where the D decay is in bin i and the D' in bin j , the bin yields satisfy

$$M_{ij} \propto K_i K_{-j} + K_j K_{-i} - 2\sqrt{K_i K_{-i} K_j K_{-j}} (c_i c_j + s_i s_j). \quad (2.30b)$$

556 Thus, analysing these decays in addition to the CP and flavour tagged decays provide
 557 information on all of K_i , c_i , and s_i . Note, however, that Eqs. (2.29) and (2.30) are
 558 invariant under the transformation $\delta_D \rightarrow -\delta_D$. In practice, the analysis is extended
 559 in a number of ways to enhance the statistics: using "flavour-tag" states that are not
 560 exact flavour tags, such as $K^-\pi^+$, using self-conjugate multi-body D -decay final
 561 states that are not exact CP eigenstates, such as $\pi^+\pi^-\pi^0$, and using the $K_L^0\pi^+\pi^-$
 562 final state as well. However, the main principles are the same as described above.

563 The measurements of c_i and s_i are made for a range of different binning schemes.
 564 It was noted already in Ref. [?] that a rectangular binning scheme, such as the
 565 example in Fig. 2.6, does not provide the optimal sensitivity to γ . A better sensitivity
 566 can be obtained if the bins are defined such that δ_D is approximately constant over
 567 a given bin, by defining bin i out of N via the condition

$$\text{bin}_i = \{(s_-, s_+) \mid 2\pi(i - 3/2)/N < \delta_D(s_-, s_+) < 2\pi \times (i - 1/2)/N\}. \quad (2.31)$$

568 In practice, the binning scheme is defined by splitting the D -decay phase-space
 569 into quadratic *micro bins* with a width of $0.0054 \text{ (GeV}/c^2)^2$ and assigning a bin
 570 number to each micro bin via the condition in (2.31) as evaluated in an amplitude
 571 model of choice. The obtained binning scheme when using an amplitude model
 572 developed by the BaBar collaboration in 2008 [?] is shown in Fig. 2.7a. In Ref [?]
 573 it was also shown that the binning can be even further optimised for sensitivity.
 574 The suggested figure of merit is

$$Q^2 = \frac{\sum_i \left(\frac{1}{\sqrt{N_i^B}} \frac{dN_i^B}{dx} \right)^2 + \left(\frac{1}{\sqrt{N_i^B}} \frac{dN_i^B}{dy} \right)^2}{\int ds^2 \left[\left(\frac{1}{|\Gamma^B(s_-)|} \frac{d|\Gamma^B(s_-)|^2}{dx} \right)^2 + \left(\frac{1}{|\Gamma^B(s_-)|} \frac{d|\Gamma^B(s_-)|^2}{dy} \right)^2 \right]} \quad (2.32)$$

575 which quantifies the statistical sensitivity for a given binning, relative to the one
 576 achievable in an unbinned analysis. The CLEO collaboration defined an *optimal*
 577 binning scheme by an iterative procedure where, starting from the equal binning
 578 scheme, a micro-bin is randomly reassigned new bin numbers in each step, and a
 579 step accepted if Q^2 increases. The optimisation is done for the case where $x = y = 0$
 580 and thus Q^2 simplifies to $Q_{x=y=0}^2 = \sum_i N_i^{x=y=0} (c_i^2 + s_i^2) / N_{total}^{x=y=0}$. The resulting
 581 binning scheme is shown in Fig. 2.7b. An additional binning scheme is defined,
 582 denoted the *modified optimal* scheme and shown in Fig. 2.7c, where the Q^2 figure
 583 of merit is modified to take into account the presence of backgrounds [?]. The
 584 modified optimal binning scheme has proven beneficial to use in measurements with
 585 small signal yields [?], but is not employed in the present thesis.

Table 2.1: The experimentally measured c_i and s_i values used in the thesis. The $D \rightarrow K_S^0\pi^+\pi^-$ values are the combined values from the BESIII and CLEO measurements published by BESIII [?]. The $D \rightarrow K_S^0K^+K^-$ values are measured by CLEO [?].

Optimal binning scheme: $D \rightarrow K_S^0\pi^+\pi^-$		
Bin i	c_i	s_i
1	-0.037 ± 0.049	0.829 ± 0.097
2	0.837 ± 0.067	0.286 ± 0.152
3	0.147 ± 0.066	0.786 ± 0.154
4	-0.905 ± 0.021	0.079 ± 0.059
5	-0.291 ± 0.041	-1.022 ± 0.062
6	0.272 ± 0.082	-0.977 ± 0.176
7	0.918 ± 0.017	-0.184 ± 0.065
8	0.773 ± 0.033	0.277 ± 0.118

2-bins binning scheme: $D \rightarrow K_S^0K^+K^-$		
Bin i	c_i	s_i
1	0.818 ± 0.107	-0.445 ± 0.215
2	-0.746 ± 0.083	-0.229 ± 0.220

Both the CLEO and BESIII collaborations have measured the values of c_i and s_i for the equal, optimal, and modified optimal binning schemes. The results are also shown in Fig. 2.7, where they are compared to the expectation from the latest amplitude model [?]. The measurements presented in this thesis are based on a combination of the BESIII and CLEO results for the optimal binning scheme, made by the BESIII collaboration [?] and tabulated in Table 2.1.

While the *definition* and *optimisation* of these binning schemes depend on knowledge of $A_S^D(s_-, s_+)$ via an amplitude model, it is important to note that no model information is needed when the binning schemes are used in the subsequent measurements of strong-phases⁵ or CP -observables. Therefore the measurements will not be biased by any modelling imperfections, although the obtained precision might be lower than expected.

The preceding discussion has been focusing on the $D \rightarrow K_S^0\pi^+\pi^-$ channel, however the $D \rightarrow K_S^0K^+K^-$ channel can be analysed completely analogously. The CLEO collaboration measure c_i and s_i values for this mode as well, in three binning schemes [?]. These are all equal-phase binning schemes, with 2, 3, and 4 bins,

⁵With the exception of minimal model-dependence introduced when the $K_L^0\pi^+\pi^-$ final state is employed to constrain the s_i parameters by the D -factories [?, ?], the impact of which is well under control.

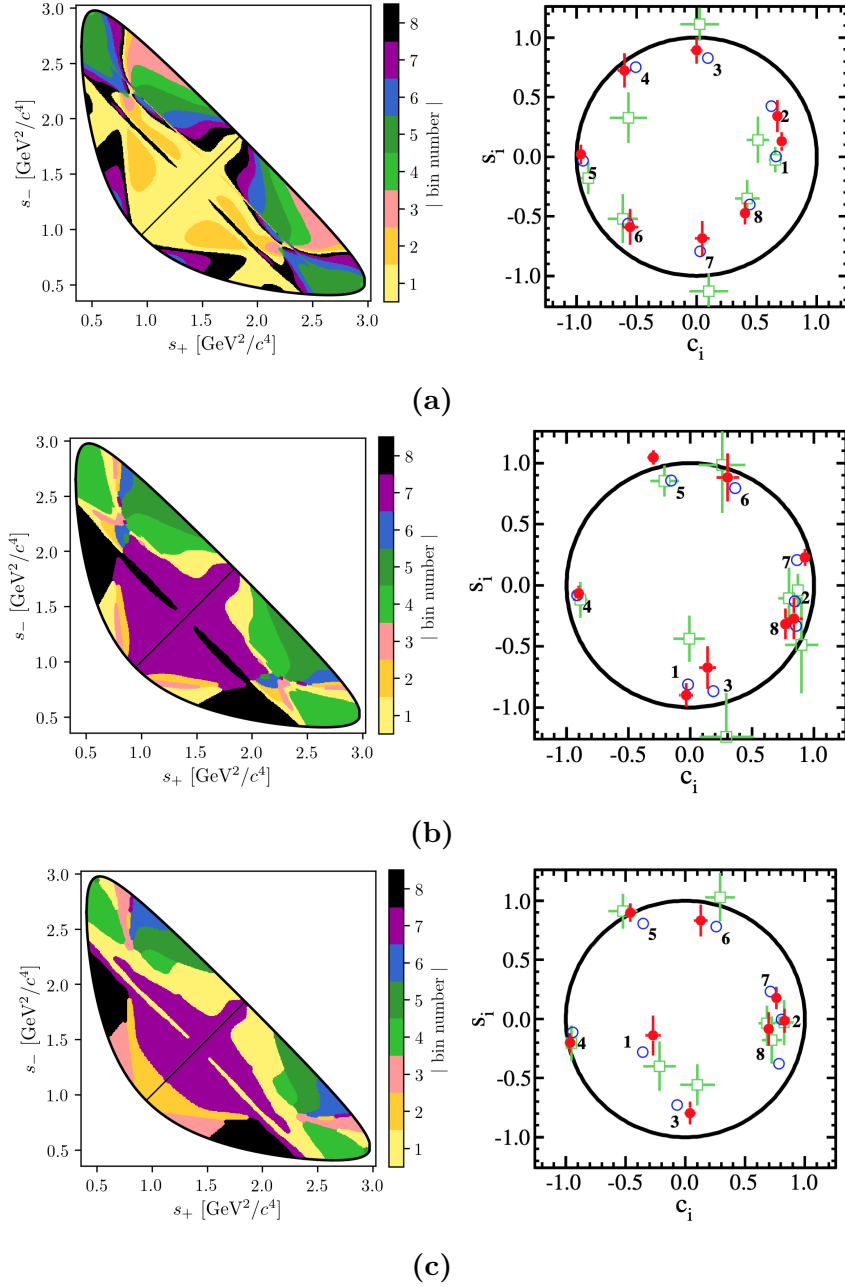


Figure 2.7: The (left) binning schemes and (right) measured values of (c_i, s_i) for (a) equal, (b) optimal, and (c) modified optimal binning schemes for $D \rightarrow K_S^0 \pi^+ \pi^-$ decays. The plots of the measured values are taken from Ref. [?] and show the results obtained by (red) BESIII, (green) CLEO, and (blue) the model expectation using the model from Ref. [?]. The measurement featured in this thesis used the optimal binning scheme.

respectively, shown in Fig. 2.8. The $D \rightarrow K_S^0 K^+ K^-$ decay amplitude is almost completely dominated by two $K^+ K^-$ resonances, the CP -odd $\phi(1020)$ and the CP -even $a_0(980)$, and this means that very little gain in sensitivity can be made by altering the equal-phase binning schemes. The measured c_i and s_i values are also shown in Fig. 2.8 and tabulated in Table 2.1 for the 2-bins scheme, which is used in this thesis. A BESIII measurement is in preparation, but has not been finished at the time of writing.

2.3.5 Global CP asymmetry and the relation to GLW and ADS measurements

The introduction of separate normalisation factors h^+ and h^- in Eq. (2.25) hides the fact that information on γ (in principle) can be obtained from the asymmetry in phase-space-integrated B^+ and B^- yields. In the ideal case where $h^- = h^+$ the total yield asymmetry is

$$\begin{aligned} A_{GGSZ} &= \frac{\sum_i N_- - N_i^+}{\sum_{i=-N}^N N_i - N_i^+} = \frac{\sum_{i=-N}^N \sqrt{K_i K_{-i}} c_i (x_- - x_+)}{1 + r_B^2 + 2 \sum_{i=-N}^N \sqrt{K_i K_{-i}} c_i (x_- + x_+)} \\ &= \frac{2 \sum_{i=1}^N \sqrt{K_i K_{-i}} c_i (x_- - x_+)}{1 + r_B^2 + 4 \sum_{i=1}^N \sqrt{K_i K_{-i}} c_i (x_- + x_+)}, \end{aligned} \quad (2.33)$$

where it has been exploited that $\sum_{i=-N}^N \sqrt{K_i K_{-i}} s_i = 0$ by definition. The size of the asymmetry is governed by the factor $\sum_{i=1}^N \sqrt{K_i K_{-i}} c_i$, which is small for $D \rightarrow K_S^0 \pi^+ \pi^-$ and $D \rightarrow K_S^0 K^+ K^-$ decays. The underlying reason is that $\delta_D(s_-, s_+)$ varies significantly across phase-space for these decays, as evident by the spread in the values of c_i in Table 2.1, which reduces the *average* of the asymmetry-generating $D^0 - \bar{D}^0$ interference term to being close to zero. The value of $\sum_{i=-N}^N \sqrt{K_i K_{-i}} c_i$ is closely related to the CP content of the final state in question: for a self-conjugate CP even (odd) final state

$$A_{D^0}(s_-, s_+) = {}^{(+)}_{(-)} A_{\bar{D}^0}(s_-, s_+) = {}^{(+)}_{(-)} A_{D^0}(s_+, s_-) \quad (2.34)$$

and thus $\sum_{i=1}^N \sqrt{K_i K_{-i}} c_i = {}^{(+)}_{(-)} 1$. This motivates the definition of the CP -even fraction of the decay

$$\mathcal{F}_+ \equiv \frac{1}{2} \left(1 + \sum_{i=1}^N \sqrt{K_i K_{-i}} c_i \right), \quad (2.35)$$

is equivalent to the definition in Ref. [?] for the case $N = 1$. With \mathcal{F}_+ in hand, the asymmetry in Eq. (2.33) can be rewritten

$$A_{GGSZ} = \frac{(2\mathcal{F}_+ - 1)r_B \sin \delta_B \sin \gamma}{1 + r_B^2(2\mathcal{F}_+ - 1)2r_B \cos \delta_B \cos \gamma}, \quad (2.36)$$

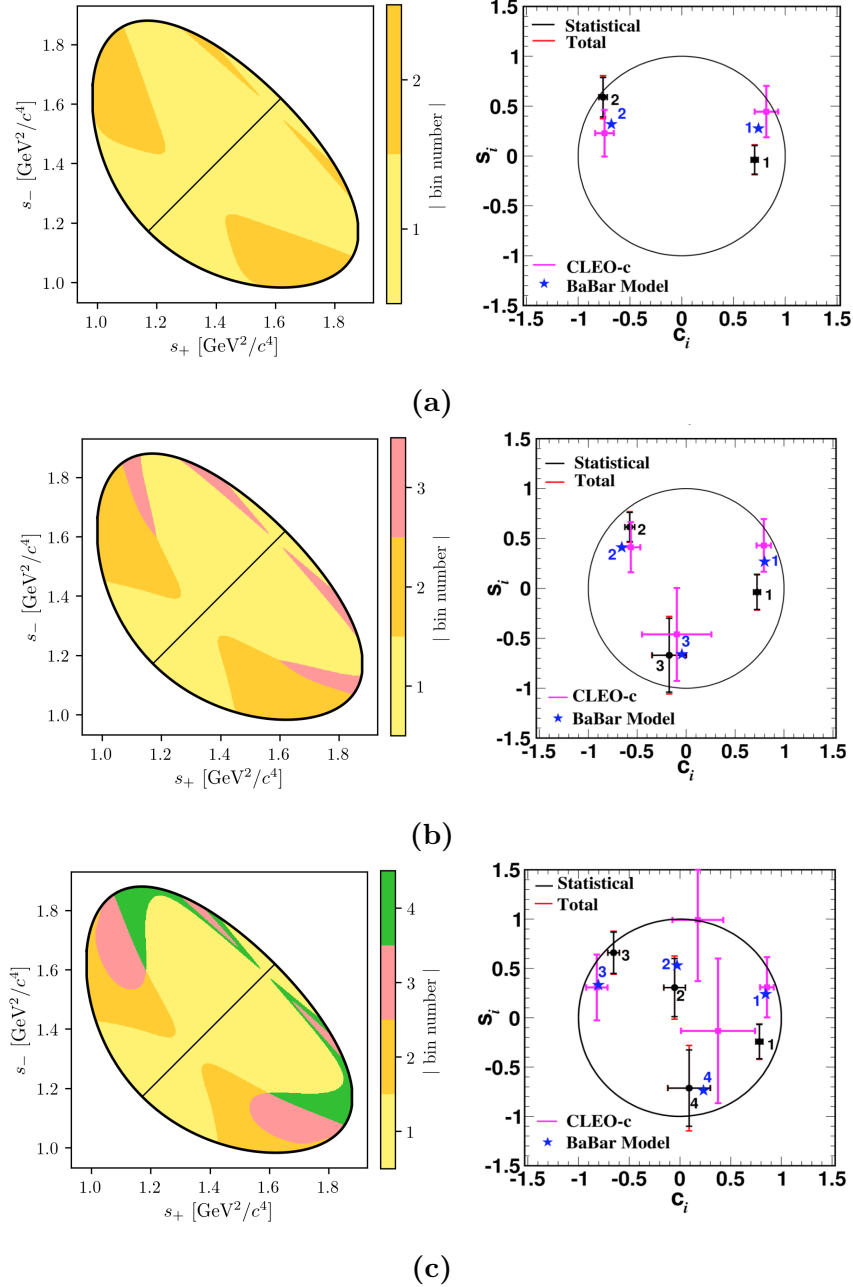


Figure 2.8: The (left) binning schemes and (right) measured values of (c_i, s_i) for the (a) 2-, (b) 3-, and (c) 4-bins binning schemes for $D \rightarrow K_S^0 K^+ K^-$ decays. The plots of the measured values are taken from Ref. [?] and show the (error bars) results obtained by (black) BESIII, (pink) CLEO, and (blue) the model expectation using the model from Ref. [?]. The measurement featured in this thesis uses the 2-bins scheme.

which is the usual form used in quasi-GLW measurements [?, ?]. The value of \mathcal{F}_+ is independent of the number and shape of bins in a given binning scheme, as long as the bin definitions follow the symmetry principles outlined in Section 2.3.3. For $D \rightarrow K_S^0\pi^+\pi^-$ and $D \rightarrow K_S^0K^+K^-$ decays the values of \mathcal{F}_+ are

$$\begin{aligned}\mathcal{F}_+(K_S^0\pi^+\pi^-) &= X? \\ \mathcal{F}_+(K_S^0K^+K^-) &= X?\end{aligned}\tag{2.37}$$

as evaluated with the Belle 2018 model for $D \rightarrow K_S^0\pi^+\pi^-$ decays and the BaBar 2010 model for $D \rightarrow K_S^0K^+K^-$ decays. Since $r_B^{DK^\pm} \sim 0.1$ the predicted global asymmetries are thus approximately 1–2 %, which is not resolvable with the current experimental yields. As shown in Chapter 4, CP violation in the K_S^0 sector leads to asymmetries of a similar size, further complicating the use of global asymmetries to constrain x_\pm and y_\pm . Thus these modes are ill-suited for quasi-GLW measurements, and ignoring global asymmetries leads to a negligible loss of information on γ in a GGSZ measurement. The reverse is true for a well-suited quasi-GLW mode, such as $D \rightarrow \pi^+\pi^-\pi^0$: if \mathcal{F}_+ is close to either zero or unity, it means that (c_i, s_i) will be close to $(\pm 1, 0)$ in all bins for *any* given binning scheme, and the set of bins will provide almost identical constraints on x_\pm and y_\pm . Thus, the binning of phase space leads to no significant gain in precision compared to a global analysis.

Indeed, a crucial quality of the GGSZ method, is that exactly because each bin-pair provides independent constraints on x_\pm and y_\pm , the method provides a single solution for (γ, r_B, δ_B) that does not suffer the ambiguities of the ADS and GLW approaches. In order to illustrate this further, it is useful to make one more comparison of the model-independent GGSZ formalism to the ADS and GLW formalisms. If there was no CP symmetry the B^+ yield in bin $+i$ would equal the B^- yield in bin $-i$. Therefore the relevant CP asymmetry for a given Dalitz bin is

$$\begin{aligned}A_{GGSZ}^i &\equiv \frac{N_i^- - N_{-i}^+}{N_i^- + N_{-i}^+} \\ &= \frac{\sqrt{K_i K_{-i}}(c_i(x_- - x_+) + s_i(y_- - y_+))}{K_i + r_B^2 K_{-i} + 2\sqrt{K_i K_{-i}}(c_i(x_- + x_+) + s_i(y_- + y_+)})\end{aligned}\tag{2.38}$$

This expression is identical to the ADS asymmetry in Eq. (2.16a) if the effective D -decay parameters r_D^i and δ_D^i are defined via

$$\kappa_i \cos \delta_D^i \equiv c_i \quad , \quad \kappa_i \sin \delta_D^i \equiv s_i \quad , \quad r_D^i \equiv \sqrt{K_i / K_{-i}},\tag{2.39}$$

and a coherence factor, κ , is included in the interference terms of the ADS expression, as is standard for multi-body D decays [?]. These parameters allow us to classify

Table 2.2: Classification of the bins used in model-independent GGSZ measurements, in terms of whether the interplay between the D^0 and \bar{D}^0 amplitudes in the bin resemble typical GLW or ADS behaviour. The parameters are calculated using the 2018 Belle model [?] for $D \rightarrow K_S^0\pi^+\pi^-$ decays and the 2010 BaBar model [?] for $D \rightarrow K_S^0K^+K^-$ decays.

Optimal binning scheme: $D \rightarrow K_S^0\pi^+\pi^-$					
Bin i	\hat{r}_D	$\hat{\delta}_D$	\mathcal{F}_+	κ	Bin type
1	0.473	91.9°	48.97 %	0.81	Odd-even
2	0.164	11.1°	63.38 %	0.85	ADS-like
3	0.157	79.4°	52.50 %	0.89	ADS-like
4	0.768	175.3°	5.85 %	0.92	GLW-odd-like
5	0.759	-99.9°	42.84 %	0.87	Odd-even
6	0.223	-64.5°	57.92 %	0.87	ADS-like
7	0.651	-13.3°	89.44 %	0.89	GLW-even-like
8	1.745	21.0°	87.08 %	0.92	GLW-even-like

2-bins binning scheme: $D \rightarrow K_S^0K^+K^-$					
Bin i	\hat{r}_D	$\hat{\delta}_D$	\mathcal{F}_+	κ	Bin type
1	0.816	19.8°	86.14 %	0.78	GLW-even-like
2	0.775	154.5°	16.23 %	0.77	GLW-odd-like

654 a given pair of bins with number $\pm i$ as either *GLW-like*, if δ_D^i is close to 0 or π
 655 and r_D^i is close to unity, or *ADS-like* if $0 < r_D^i \ll 1$. The *CP*-even fraction of the
 656 D -decay can also be defined for a given bin-pair:

$$\mathcal{F}_+^i = \mathcal{F}_+^{-i} \equiv \frac{1}{2} \left(1 + 2c_i \frac{\sqrt{K_i K_{-i}}}{K_i + K_{-i}} \right) = \frac{1}{2} \left(1 + 2c_i \frac{r_D^i}{1 + r_D^i} \right). \quad (2.40)$$

657 A GLW-even-like bin pair will have $\mathcal{F}_+^i \simeq 1$ and a GLW-odd-like bin pair will
 658 have $\mathcal{F}_+^i \simeq 0$.

659 Table 2.2 summarises a classification of the bins for the optimal $D \rightarrow K_S^0\pi^+\pi^-$
 660 binning scheme and the 2-bins $D \rightarrow K_S^0K^+K^-$ binning scheme following these
 661 principles. Two bins are classified as *Odd-even*; in these bins, r_D^i is not particularly
 662 small but \mathcal{F}_+^i is close to 0.5. The name refers to the fact that for these
 663 bins A_{GGSZ}^i , as defined in Eq (2.38), will be positive and A_{GGSZ}^{-i} negative (or vice
 664 versa). The fact that multiple bin types appear for both the $D \rightarrow K_S^0\pi^+\pi^-$ and
 665 $D \rightarrow K_S^0K^+K^-$ modes underline that each mode benefits from being analysed in
 666 the GGSZ formalism, and that the bins provide independent constraints, allowing
 667 for a non-ambiguous solution for (γ, r_B, δ_B) .

2.4 Strategy for the LHCb measurement

The main topic of the thesis is a model-independent GGSZ measurement using $B^\pm \rightarrow DK^\pm$ and $B^\pm \rightarrow D\pi^\pm$ decays, and the two D final states $K_S^0\pi^+\pi^-$ and $K_S^0K^+K^-$. The measurement uses the optimal binning scheme for the $D \rightarrow K_S^0\pi^+\pi^-$ mode, with the combined strong-phase inputs from the BESIII [?] and CLEO [?] collaborations published in Ref. [?]. For the $D \rightarrow K_S^0K^+K^-$ channel, the 2-bins scheme is used with the strong-phase parameters measured by the CLEO collaboration [?]. The details of the analysis are presented in Chapter (5), but the overall strategy and a few extensions of the formalism from the previous sections are given here.

Due to the geometry of the LHCb detector, the signal reconstruction efficiency for $B^\pm \rightarrow D(\rightarrow K_S^0h^+h^-)h'^\pm$ decays varies significantly across the D -decay phase space. Denoting the efficiency profile as $\eta(s_-, s_+)$, the yield equations of Eq. (2.25) are therefore modified slightly

$$\begin{aligned} N_i^- &= h^{B^-} \left[F_i + r_B^2 F_{-i} + 2\sqrt{F_i F_{-i}} (c'_i x_- + s'_i y_-) \right], \\ N_i^+ &= h^{B^+} \left[F_{-i} + r_B^2 F_i + 2\sqrt{F_i F_{-i}} (c'_i x_+ - s'_i y_+) \right], \end{aligned} \quad (2.41)$$

where the phase-space integrated quantities now include the efficiency profile

$$F_i = \frac{1}{N_F} \int ds^2 \eta(s_{-+}) |A_S^D(s_{-+})|^2, \quad N_F = \int ds^2 \eta(s_{-+}) |A_S^D(s_{-+})|^2, \quad (2.42)$$

$$c'_i = \frac{\int_i ds^2 \eta(s_{-+}) |A_S^D(s_{-+})| |A_S^D(s_{-+})| \cos[\delta_D(s_{-+})]}{\sqrt{\int_i ds^2 \eta(s_{-+}) |A_S^D(s_{-+})|^2} \sqrt{\int_i ds^2 \eta(s_{-+}) |A_S^D(s_{-+})|^2}}, \quad (2.43)$$

with an analogous definition of s'_i . At leading order, the strong-phase parameters are unaffected by the non-uniform efficiency, and, in addition, the bin definitions favour bins for which $\cos[\delta_D(s_{-+})]$ and $\sin[\delta_D(s_{-+})]$ take on similar values across each bin. Therefore, the c_i and s_i values reported by the charm factories are used directly in the measurement. The impact on the obtained central values is negligible, as described in detail in Section 5.6 where a systematic uncertainty is assigned.

The F_i are significantly different to the K_i due to the experimental acceptance profile in LHCb. Given external inputs for the strong-phase parameters, it is possible to fit the F_i parameters and x_\pm and y_\pm simultaneously in a fit to the LHCb $B^\pm \rightarrow DK^\pm$ data set, in which case the obtained F_i parameters incorporate the correct acceptance profile correction by construction. However, the obtainable precision for the CP observables measured by this procedure is suboptimal. As

an alternative, the first LHCb measurement [?] made a simultaneous analysis of $B^\pm \rightarrow DK^\pm$ and a much larger sample of $B^\pm \rightarrow D\pi^\pm$ decays; since the F_i parameters relate to the D decay, they can effectively be obtained in the $D\pi^\pm$ sample and shared between the two $B^\pm \rightarrow Dh^\pm$ channels. However, there is CP violation present in the $B^\pm \rightarrow D\pi^\pm$ decays, which led to a dominant systematic uncertainty. Later LHCb measurements [?, ?] instead relied on flavour tagged D mesons from $\bar{B}^0 \rightarrow D^{*+}(\rightarrow D^0\pi^+)\mu^-\bar{\nu}_\mu X$ decays to obtain F_i , where no CP violation is possible. However, due to necessarily different triggering paths and selections, the acceptance profile is not exactly identical between semi-leptonic decays and the $B^\pm \rightarrow Dh^\pm$ decays of interest. An efficiency correction based on simulation was therefore applied to obtain the correct F_i , and in this case, the uncertainty related to the correction constituted the largest systematic uncertainty on the measurement.

Both sources of systematic uncertainty can be avoided by making a simultaneous analysis of $B^\pm \rightarrow DK^\pm$ and $B^\pm \rightarrow D\pi^\pm$ decays, where CP -violating observables are measured in *both* channels and the F_i parameters are shared. It is a reasonable assumption that $F_i^{DK} = F_i^{D\pi}$ to a very good approximation, given the similar kinematics of the decays. The assumption is confirmed using simulated decays in Section 5.2.2, for the candidate selection used in the measurement of the thesis. Effectively, the F_i are determined in the high statistics $B^\pm \rightarrow D\pi^\pm$ channel, but with no systematic effect from CP -violation in that channel, since the CP -violation is incorporated in the yield description.

ADD SECTION ON INFORMATION ON GAMMA FROM DPI AND THE TWO SOLUTIONS IN THE LHCb COMBINATION?!

At the start of the work that lead to this thesis, it was not clear to what degree the measured CP -violating observables in $B^\pm \rightarrow D\pi^\pm$ decays were affected by CP violation in the neutral kaon sector. The impact had been shown to scale as $\mathcal{O}(|\epsilon|/r_B)$ [?], which is negligible for the $B^\pm \rightarrow DK^\pm$ channel but suggests potentially large biases in the $B^\pm \rightarrow D\pi^\pm$ channel, where r_B is 20 times smaller. However, the dedicated analysis presented in Chapter 4 has proved the effect on GGSZ measurements to be in fact be *smaller* than $\mathcal{O}(|\epsilon|/r_B)$ and the simultaneous measurement is indeed viable.

The measurement is performed by making extended maximum-likelihood fits to the m_B spectra of $B \rightarrow D(\rightarrow K_S^0 h^+ h^-)h'^\pm$ candidates split by charge and Dalitz bin. The $B^\pm \rightarrow DK^\pm$ signal yields are parameterised using the expressions in Eq. (2.41) directly, thus obtaining values for x_\pm^{DK} and y_\pm^{DK} directly. The Cartesian CP -violating observables x_\pm and y_\pm are employed because they lead to better statistical behaviour than fits to data where the underlying parameters $(\gamma, r_B^{DK^\pm}, \delta_B^{DK^\pm})$ are

determined, at the cost of introducing a fourth degree of freedom. With the addition of the $B^\pm \rightarrow D\pi^\pm$ mode as a true signal channel, two new underlying parameters are introduced, $r_B^{D\pi^\pm}$ and $\delta_B^{D\pi^\pm}$. There is a choice to be made, in terms of how to define the observables that are measured directly. One is to introduce an additional set of four observables, $(x_-^{D\pi}, y_-^{D\pi}, x_+^{D\pi}, y_+^{D\pi})$, that are analogous to the $B^\pm \rightarrow DK^\pm$ parameters. As an alternative, it is possible to introduce only two Cartesian parameters [?], by defining

$$\xi_{D\pi^\pm} = \left(\frac{r_B^{D\pi^\pm}}{r_B^{DK^\pm}} \right) \exp[i(\delta_B^{D\pi^\pm} - \delta_B^{DK^\pm})] \quad (2.44a)$$

and letting

$$x_\xi^{D\pi} = \text{Re}[\xi_{D\pi^\pm}] \quad y_\xi^{D\pi} = \text{Im}[\xi_{D\pi^\pm}]. \quad (2.44b)$$

In terms of these parameters, the usual Cartesian x_\pm and y_\pm are given by

$$x_\pm^{D\pi} = x_\xi^{D\pi} x_\pm^{DK} - y_\xi^{D\pi} y_\pm^{DK}, \quad y_\pm^{D\pi} = x_\xi^{D\pi} y_\pm^{DK} + y_\xi^{D\pi} x_\pm^{DK}. \quad (2.45)$$

Using this expression, the $B^\pm \rightarrow D\pi^\pm$ yields can also be defined via Eq. (2.41) in the maximum-likelihood fit. Note that ξ does not depend on γ : all information on CP asymmetries in both the $B^\pm \rightarrow DK^\pm$ and $B^\pm \rightarrow D\pi^\pm$ channels is encoded in x_\pm^{DK} and y_\pm^{DK} . In the thesis, the latter parameterisation is chosen, because it allows for a stable fit for all six x and y parameters and the shared F_i ; the choice is described in much greater detail in Section 5.5.1.

The combined analysis of $B^\pm \rightarrow DK^\pm$ and $B^\pm \rightarrow D\pi^\pm$ decays presents a significant step forward, because it solves the problem of obtaining F_i parameters for the appropriate acceptance profile in a manner that avoids leading systematic uncertainties, and almost all reliance on simulation. This is of great importance, if the large data samples that will be collected by LHCb in the future are to be exploited to their full potential.

3

754

755

The LHCb experiment

756 The LHCb experiment is one of the four large experiments at the Large Hadron
757 Collider (LHC), the World's most powerful accelerator, able to accelerate protons
758 to record centre-of-mass energies of $\sqrt{s} = 13$ TeV in a 27 km long tunnel underneath
759 Geneva. The LHCb experiment is specifically designed to study the large number
760 of particles containing b or c quarks produced in such collisions, which has led
761 to a number of design decisions that make the LHCb unique among the LHC
762 experiments. The LHCb detector is not a full-solid-angle detector like the other
763 three LHC experiments, CMS, ATLAS, and ALICE, but a single-arm spectrometer,
764 instrumented in the forward region where the majority of $b\bar{b}$ pairs are produced.
765 During data-taking the experiment is operated at a lower instantaneous luminosity
766 than the other experiments, leading to far fewer pp interactions. This, in combination
767 with a vertex detector located extremely close to the interaction point, allows for
768 excellent resolution in the reconstruction of primary and secondary vertex locations,
769 crucial to many of the central measurements of the experiment. Finally, dedicated
770 particle-identification detectors allow for very efficient separation of hadron species,
771 absolutely crucial to isolate a number important signal decays (including the
772 $B^\pm \rightarrow DK^\pm$ decay studied in the thesis). Each of these features is described in
773 much greater detail in the sections below.

774 During operation of the LHC, bunches of about $\mathcal{O}(10^{11})$ protons are accelerated
775 to the desired centre-of-mass energy in a series of linear and circular accelerators,
776 the final one being the LHC itself. This is illustrated in Fig. 3.1. The bunches
777 remain in the LHC for the duration of a *fill*, typically about 12 hours, where they are
778 made to collide at four distinct locations, the collision points, each home to one of

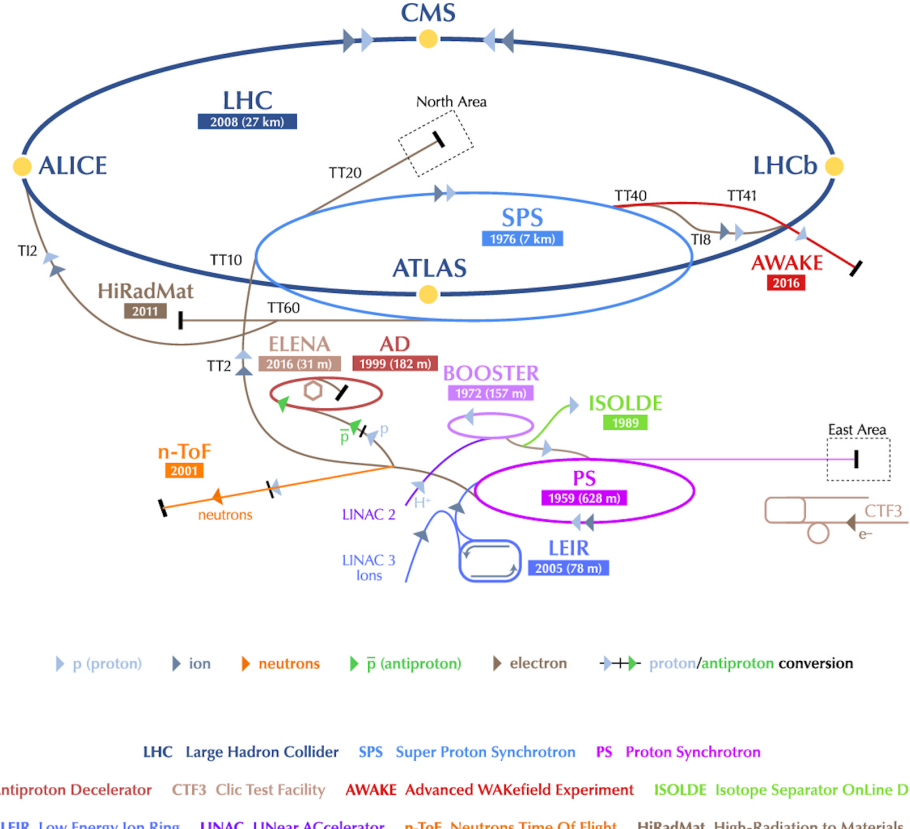


Figure 3.1: The CERN accelerator complex, including the length and construction year for a number of accelerators, not all of which are used in pp operations. During pp operation, the proton acceleration chain is: LINAC 2 → BOOSTER → PS → SPS → LHC. The figure is reproduced from Ref. [?].

the large experiments. The collisions occur with a frequency of up to 40 MHz. A fill ends when the beams are dumped, typically because the average number of protons in the bunches has become too low, after which the whole process begins again.

The LHC has been providing pp collisions during two periods so far: Run 1 during 2011 and 2012, where the centre-of mass energies were $\sqrt{s} = 7 \text{ TeV}$ and 8 TeV respectively, and Run 2 from 2015 to 2018, where $\sqrt{s} = 13 \text{ TeV}$. The instantaneous luminosity at the LHCb collision point has been $4 \times 10^{32} \text{ cm}^{-2} \text{ s}^{-1}$, and has allowed for the collection of data set corresponding to a total of 3 fb^{-1} during Run 1 and 6 fb^{-1} during Run 2. The full data set forms the basis of the thesis. This instantaneous luminosity is significantly lower than at other collision points, for example the peak instantaneous luminosity in the ATLAS detector was about $20 \times 10^{33} \text{ cm}^{-2} \text{ s}^{-1}$ in 2018 [?], 50 times higher than in LHCb. The lower luminosity is necessary to limit the number of pp interactions per bunch crossing to an average of about 1.1–1.4 (depending on the data taking period), necessary for a vertex reconstruction with the required precision. The lower luminosity is

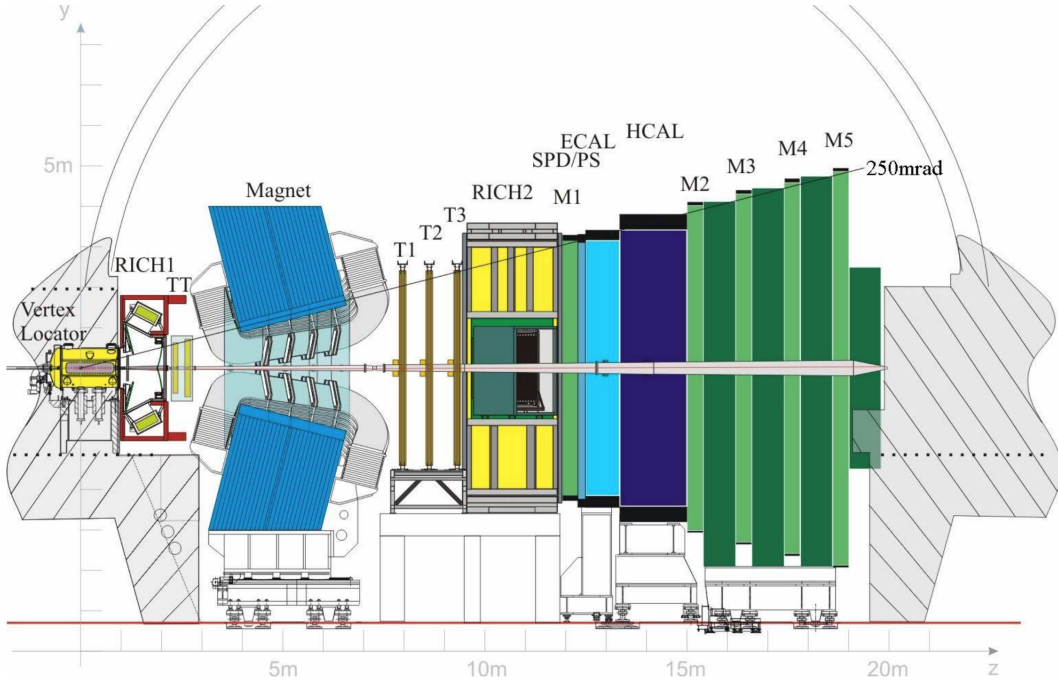


Figure 3.2: Overview of the LHCb detector reproduced from Ref. [?, ?]. The individual subdetectors are described in detail in the text.

794 achieved by colliding the proton beams with an off-set at the LHCb collision point.
 795 This has the added benefit that the offset can be continuously adjusted during a fill
 796 of the LHC, and thus all data can be taken at the same instantaneous luminosity,
 797 allowing for simpler trigger configuration, and simpler subsequent analysis because
 798 the detector occupancy is constant. The lower luminosity, of course, comes with
 799 the downside that the collected data sample is smaller.

800 3.1 The LHCb subdetectors

801 The LHCb detector, shown in Fig. 3.2, is able to detect particles in the forward
 802 region $\eta \in [2, 5]$, corresponding to an angle θ with respect to the beam line between
 803 15 and 300/250 mrad in the horizontal/vertical direction. As illustrated in Fig. 3.3,
 804 the $b\bar{b}$ production cross section is very large within the LHCb acceptance: even
 805 though the acceptance covers less than 2% of the solid angle, 24% of all $b\bar{b}$ pairs
 806 created at $\sqrt{s} = 14$ TeV are within the acceptance. The detector is described with
 807 a coordinate system, where the z -axis is along the beam line and the x (y) axis is
 808 in the horizontal (vertical) directions normal to the beam line. The origin is at the
 809 collision point. The experiment consists of a number of sub detectors, located in the
 810 region from around the interaction point, and up to a distance of $z = 20$ m along

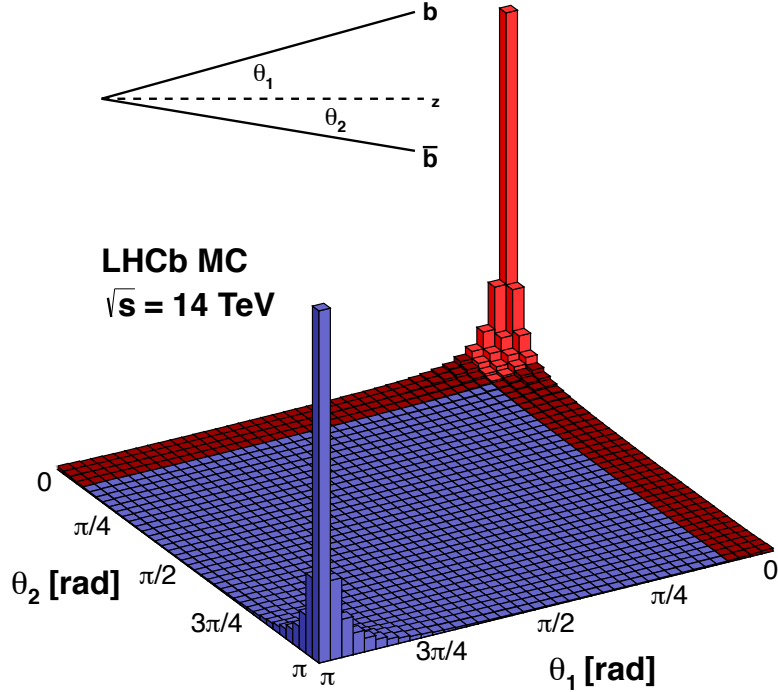


Figure 3.3: Production cross section of $b\bar{b}$ pairs at a centre-of-mass energy of $\sqrt{s} = 14$ TeV, as a function of θ_1 and θ_2 , the angle of the b and \bar{b} quark, respectively, with respect to the beam axis z . The LHCb acceptance is marked in red. The cross-section looks very similar for $\sqrt{s} = 7, 8$ TeV. The figure is taken from Ref. [?].

the beam line (in the following, the direction from the interaction point towards the sub detectors is denoted *downstream*, and the opposite direction *upstream*).
This section describes each of them in detail.

3.1.1 The VELO

The VErtex LOcator (VELO) [?] is a silicon detector located immediately around the collision point, used to provide precise measurements of the particle track coordinates in the interaction region. These are used to reconstruct the production and decay vertices of beauty and charm hadrons with a very high accuracy, allowing for an accurate reconstruction of their life times, and play an important role in the full track reconstruction. The ability to distinguish tracks originating in secondary vertices also plays a crucial role in efficient triggering, as described further below.

The detector consists of 21 VELO stations positioned along the beam line as illustrated in Fig. 3.4. Each station consists of two *modules*, mounted on each side

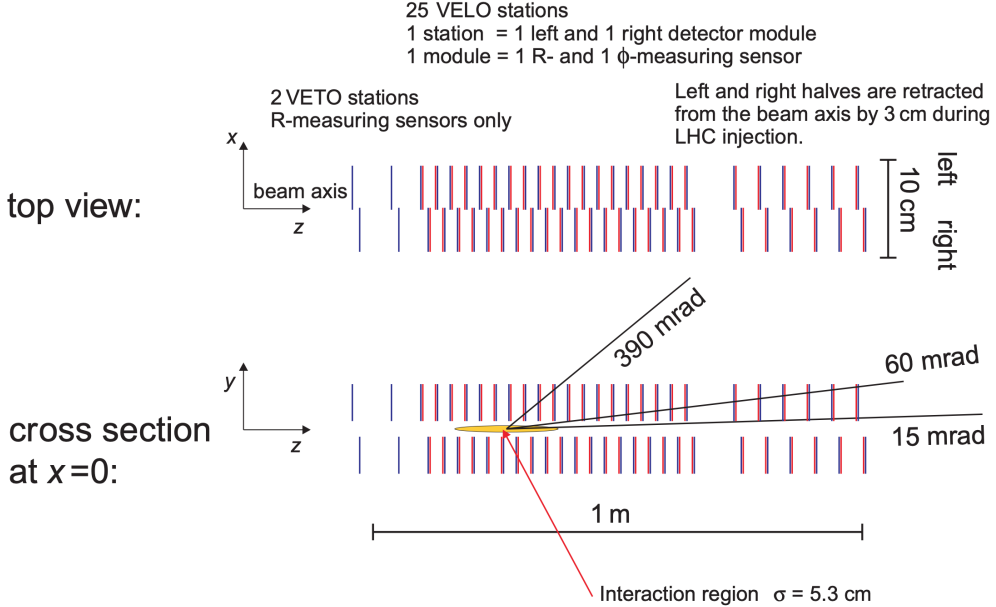


Figure 3.4: Overview of the arrangement of VELO stations from the VELO Technical Design Report (TDR) [?]. The actual detector includes 21 stations instead of 25, but the overall design is identical [?].

of the beam line; each module, in turn, consists of two silicon strip detectors, where the strips are oriented to provide a measurement of r , the radial distance from the beam line, and ϕ , the azimuthal angle, respectively. This is illustrated in Fig. 3.5. The strip pitch varies between 40 and 100 μm depending on the distance from the beam line. The stations are positioned such that all tracks that are within the acceptance region of the downstream detectors and originate at the interaction point are guaranteed to intersect 3 detector stations. During operation, the segments are located only 8 mm from the beam; this is achieved by mounting them on a moving frame that can be retracted during beam commissioning to avoid radiation damage. The detectors are kept in a vacuum, shielded from the beam vacuum by a 0.3 mm thick *RF foil* made of aluminium that also serves to screen the detector from electric fields induced by the proton beam. The silicon sensors were kept at an operating temperature of about -7 $^{\circ}\text{C}$, achieved with a liquid- CO_2 cooling system.

The primary vertex (PV) resolution of the VELO is typically $\sim 10 \mu\text{m}$ in the x and y directions and $\sim 50 \mu\text{m}$ in the z direction, improving with the number of tracks originating at the PV, and deteriorating with the overall number of PVs [?]. The typical uncertainty on the decay length of a B meson is about 230 μm , compared to a typical decay length $O(10)$ mm. The resolution of the *impact parameter*, IP, of a track is well-described by the formula $\sigma_{\text{IP}} = (15 + 29/[p_T/(\text{GeV}/c)]) \mu\text{m}$. This parameter excellently distinguished particles produced in secondary decays, from

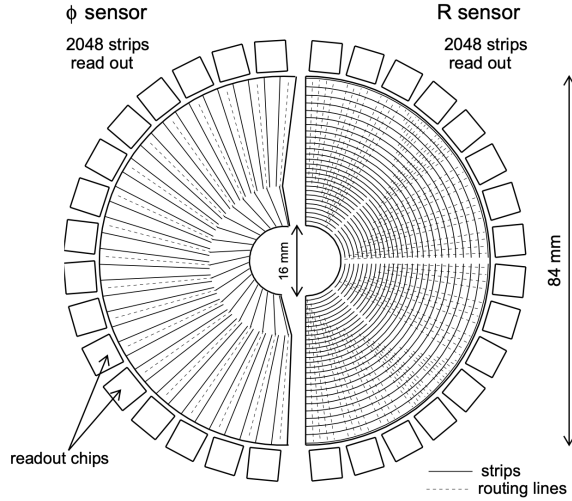


Figure 3.5: Illustration of the silicon strip layout in the VELO modules designed to measure (left) the azimuthal angle, ϕ , of a track, and (right) the radial distance from the beam, r . Reproduced from Ref. [?].

844 those produced in the primary interaction (for which the IP would be zero, were
845 it not for the experimental resolution).

846 3.1.2 Magnet and tracking stations

847 The LHCb experiments uses a warm (non-superconducting) dipole magnet to
848 measure the momentum of charged particles, by providing a maximum magnetic
849 field strength of approximate 1T and a total bending power of about 4 T m over
850 the region where $z \in [2.5, 8]$ m. The magnetic field has been measured to a relative
851 precision of about 4×10^{-4} and is uniform within a percent within the tracking
852 volume. The profile of the magnetic field along the z -axis is shown in Fig. 3.14 on
853 page 41, where the track types within LHCb are defined. The magnet can provide
854 a magnetic field in either vertical direction; over the span of a year of running the
855 experiment approximately equal amounts of data are collected with the magnet in
856 the "Up" and "Down" configurations; this leads to the cancellation of a number of
857 charge-asymmetry effects, significantly reducing potential systematic uncertainties.

858 The tracking system consists of the VELO, and four other tracking stations:
859 the Tracker Turicensis (TT) upstream of the magnet, and the tracking stations
860 1–3 (T1, T2, T3) downstream of the magnet. The downstream tracking stations
861 each consist of an Inner Tracker (IT) based on silicon strips, and an Outer Tracker
862 (OT) that employs drift tubes.

863 Both the TT and IT are based on silicon strip detectors with a pitch of about
864 200 μm ; they were developed as a single project and are collectively known as the

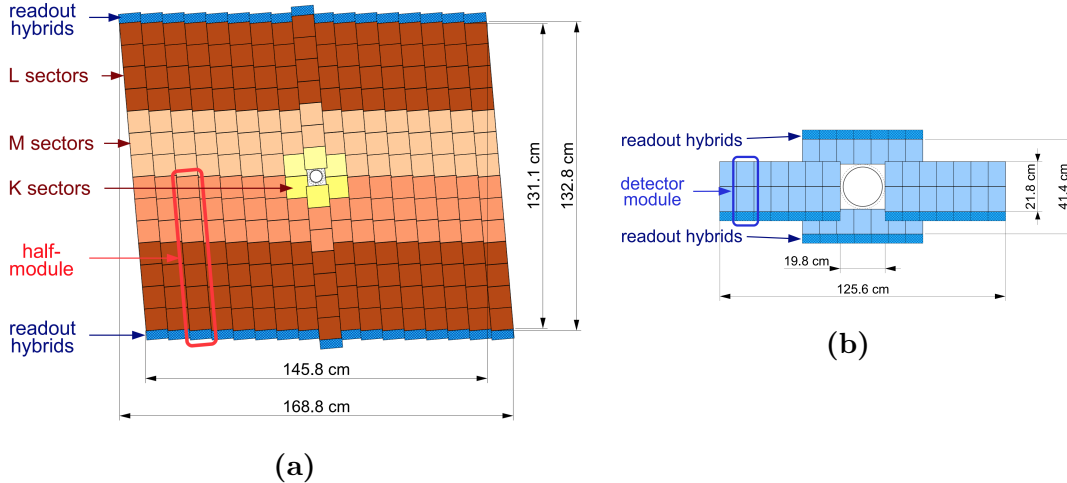


Figure 3.6: Overview of (a) a *v*-layer module of the IT and (b) an *x*-layer module of the IT. Reproduced from Ref. [?]

865 Silicon Tracker (ST). The TT is a 140 cm wide and 130 cm tall planar tracking
 866 station, covering the whole LHCb acceptance. It is shown in Fig. 3.6a. At each
 867 of the T1–T3 stations, the IT consist of four modules, arranged around the beam
 868 pipe as illustrated in Fig. 3.6b. They do now cover the full LHCb acceptance,
 869 only the very-forward region where the number of tracks is largest. Each TT or
 870 IT module comprises of four layers of silicon strips, where the central two layers
 871 are rotated $\pm 5^\circ$ with respect to the first and last layer (an *x-u-v-x* geometry).
 872 The ST has a spatial resolution for a given track of approximately 50 μm , chosen
 873 because the overall momentum resolution is then dominated by multiple-scattering
 874 effects for almost all reconstructed tracks.

875 At the T1–T3 stations, the OT covers the part of the overall acceptance of
 876 300 (250) mrad in the horizontal bending (vertical non-bending) plane that is not
 877 covered by the IT. The OT consists of arrays of gas-tight drift tubes with inner
 878 diameters of 4.9 mm. The OT is shown illustrated in Fig. 3.7. An Ar/CO₂/O₂
 879 (70/28.5/1.5) gas mixture is used to fill the tubes that ensures a drift time below
 880 50 ns and a drift coordinate resolution of 200 μm . The use of a drift-chamber
 881 detector is necessary, because it was not economically feasible to instrument the
 882 whole LHCb acceptance with silicon strip detectors in T1–T3. The condition that
 883 the OT occupancy should not be above 10 % in typical run conditions determined
 884 the boundary between the IT and the OT.

885 The overall relative momentum resolution achieved for most charged tracks in
 886 LHCb is less than a percent, as illustrated in Fig. 3.8, where it has been determined
 887 from a fit to the mass peak in $J/\psi \rightarrow \mu^+\mu^-$ decays in Run 1 data.

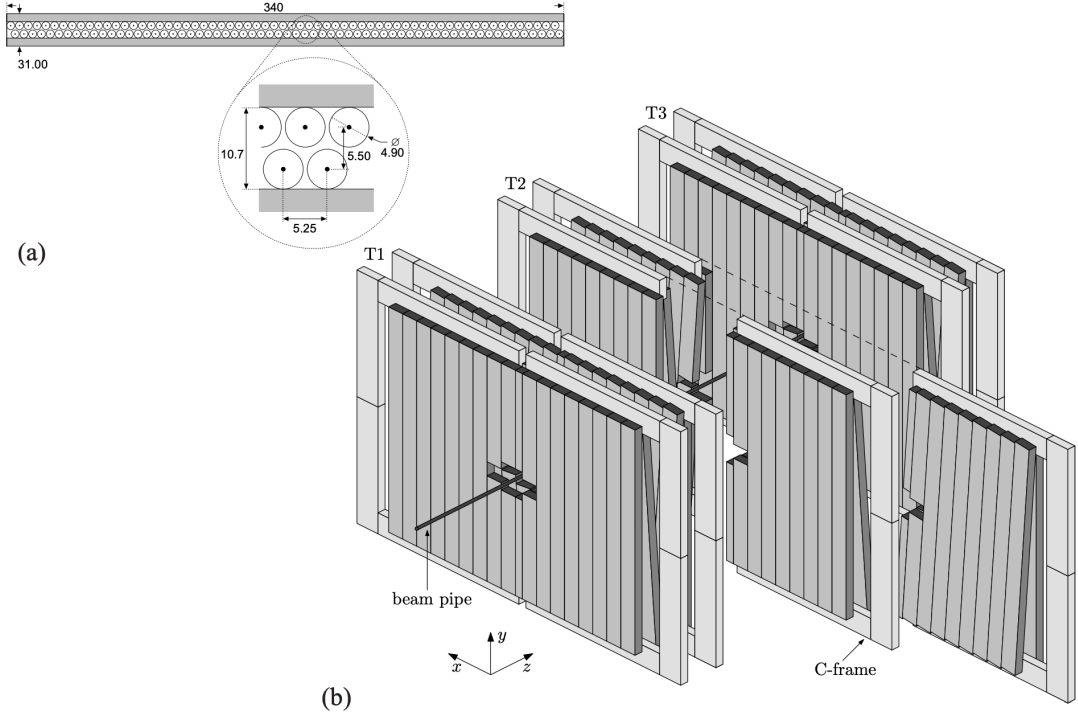


Figure 3.7: (a) Cross section of an OT module. (b) Arrangement of the OT modules in tracking stations. Reproduced from Ref. [?].

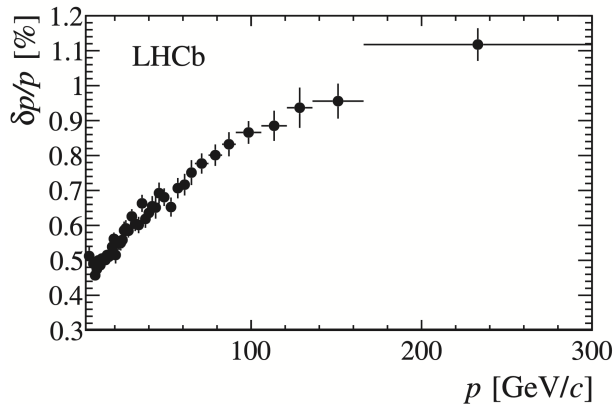


Figure 3.8: Relative uncertainty on the momentum of charged tracks (specifically long tracks, cf. the definitions in Section 3.2) in the LHCb detector, determined via the mass resolution obtained in $J/\psi \rightarrow \mu^+\mu^-$ decays in Run 1 data. Reproduced from Ref. [?]

3.1.3 The RICH detectors

Two Ring Imaging Cherenkov detectors (RICH) provide crucial information for particle identification (PID) in LHCb, in particular the ability to separate pions and kaons that is absolutely essential for the measurement presented in the thesis. The RICH 1 detector is located upstream of the magnet, in between the VELO and the TT tracking station. It is designed to provide PID capability for tracks

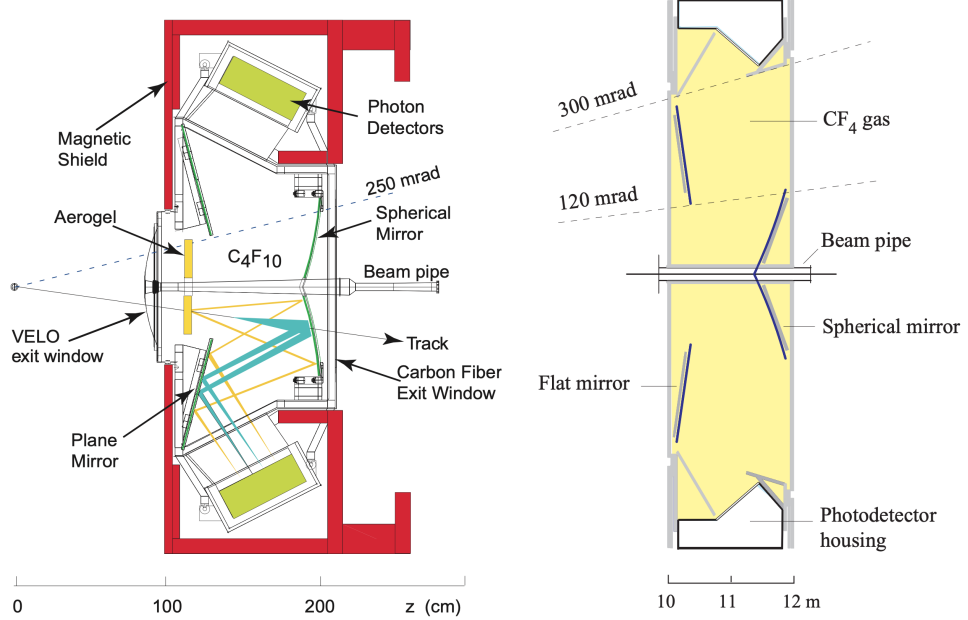


Figure 3.9: Overview of (left) the Rich 1 and (right) the RICH 2 detectors. Reproduced from Ref. [?, ?].

in the momentum range $p \in [1, 60] \text{ GeV}/c$ using a C_4F_{10} radiator, and covers the full LHCb acceptance. During Run 1 the RICH 1 detector also included an Aerogel radiator designed to provide PID for very low momentum particles; however, it was removed before Run 2 because it did not meet the performance requirements during Run 1 [?, ?]. The RICH 2 detector is located downstream of the T1–T3 tracking stations. It is designed to provide PID capabilities for higher momentum tracks in the range $p \in [15, 100] \text{ GeV}/c$ using a CF_4 radiator. It only covers the very forward region where $|\theta| < 120 \text{ mrad}(100 \text{ mrad})$ in the horizontal (vertical) directions, as high momentum particles are produced in that region. In both RICH detectors, mirrors are used to reflect the Cherenkov photons to arrays of Hybrid Photon Detectors (HPDs) located outside the LHCb acceptance. The optics are designed such that photons originating from a given track form rings in the HPD arrays, where the radius is determined by the Cherenkov angle θ_c . The detectors are illustrated in Fig. 3.9.

The resolution on θ_c can be measured by fitting the obtained θ_c distribution in high momentum tracks, where the Cherenkov angle is saturated. It is found to be $1.618 \pm 0.002 \text{ mrad}$ for RICH 1 and $0.68 \pm 0.02 \text{ mrad}$ for RICH 2 in Run 1 data [?], and was essentially unchanged in Run 2 [?]. Figure 3.10 shows the relation between track momentum and θ_c in RICH 1 for *isolated tracks* in Run 1 data; these are tracks where the Cherenkov ring does not overlap with any other

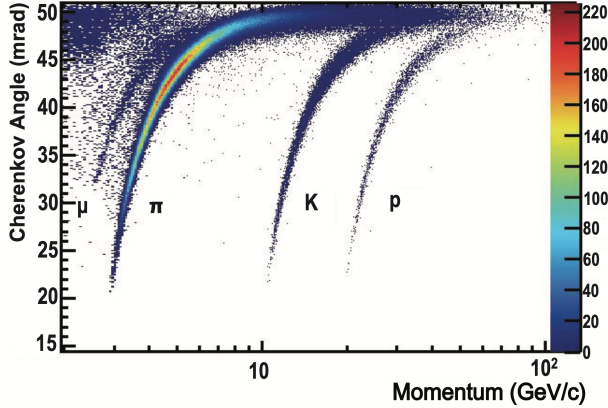


Figure 3.10: Cherenkov angle for isolated tracks in the RICH 1 radiator as a function of track momentum. Reproduced from Ref. [?].

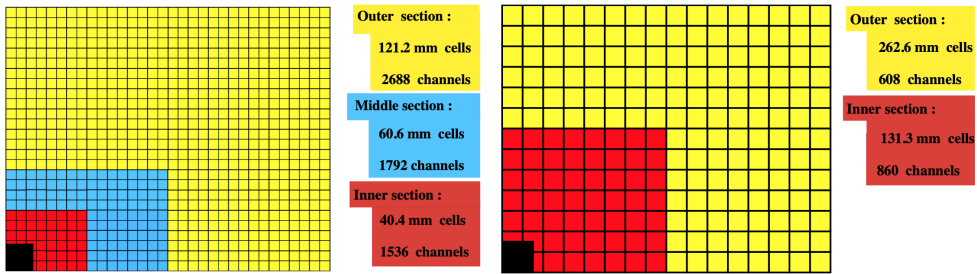


Figure 3.11: Illustration of the calorimeter cell size of (left) the ECAL and (right) the HCAL. Reproduced from Ref. [?].

Cherenkov rings. The bands for each hadron species are clearly visible, and it can be seen that the RICH detector also provide some ability to distinguish muons. The definition of the PID variables used in analysis is discussed in Section 3.2.2, along with the achieved PID performance.

3.1.4 Calorimeters

The calorimeter system of the LHCb detector has four components. Ordered from the interaction point, these are the Scintillating Pad Detector (SPD), the Pre-Shower (PS) detector, an Electromagnetic Calorimeter (ECAL), and a Hadron Calorimeter (HCAL). Information from the calorimeters also provide identification of electrons, photons, and hadrons, and measurements of their energies and positions, and also plays a crucial role in the triggering, as described below. In all four cases, light is produced in organic scintillators and transmitted to Photo Multiplier Tubes (PMTs) via optical fibres [?].

The SPD and PS detectors consist of almost identical planes of rectangular scintillator pads, with a 15 mm thick lead absorber located in between. The presence

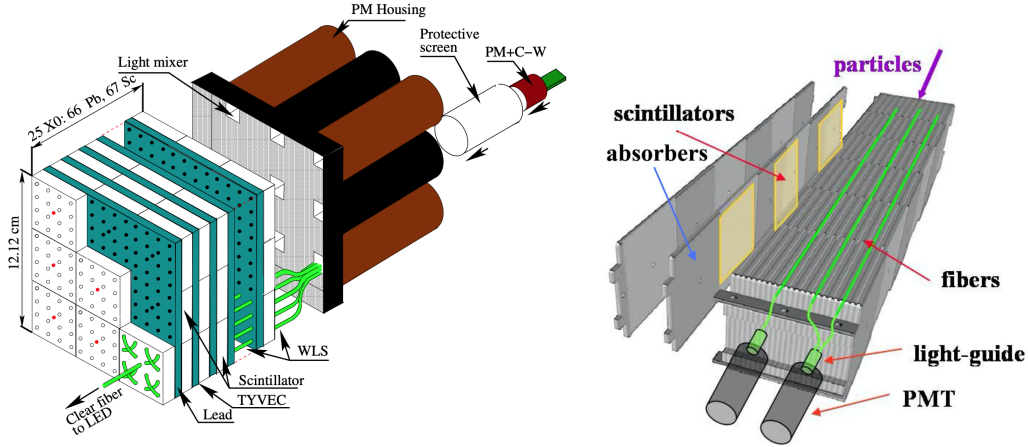


Figure 3.12: Illustration of (left) an ECAL and (right) a HCAL module. Reproduced from Ref. [?, ?].

of the SPD before the first absorption layer allows for the separation of photons and electrons in the trigger, because only electrons cause a signal in the SPD. The PS allows for the separation of pion and electron tracks, as only the latter interact significantly with the thin layer of lead. The cell divisions of the detectors closely follow that of the ECAL, shown in Fig. 3.11, to allow for the matching of energy deposits.

The ECAL has a Shashlik structure, with 66 layers consisting of 2 mm of lead absorber and 4 mm of scintillator; an example of a calorimeter module is shown in Fig. 3.12. Accurate energy measurements require that the full electronic shower is contained in the ECAL, which is achieved since the structure extends for 25 radiation lengths. The scintillators are divided into cells that allow for the determination of the location and shape of energy deposits; the cell dimensions vary as a function of radial distance from the beam pipe as shown in Fig. 3.11, to take into account the varying occupancy. The resolution of the ECAL has been measured to be $\Delta E/E \simeq (9/\sqrt{E} \oplus 0.8)\%$ (E in GeV/c^2) [?].

The HCAL is located downstream of the ECAL, designed to measure the energy of charged hadrons (which leave relatively little energy in the ECAL). It is constructed with layers of 1 cm iron absorbers inter-spaced with scintillators, oriented *along* the beam direction, such that a typical track will traverse 16 mm of iron per 4 mm of scintillator [?]. As for the ECAL, the cell size varies as a function of distance to the beam line, as shown in Fig. 3.11. An example of a module is shown in Fig. 3.12. The energy resolution required for efficient triggering is moderate; therefore, the HCAL only has a length of 5.6 interaction lengths and can measure the hadron energies at a resolution of $\Delta E/E \simeq (69/\sqrt{E} \oplus 9)\%$ (E in GeV/c^2) [?].

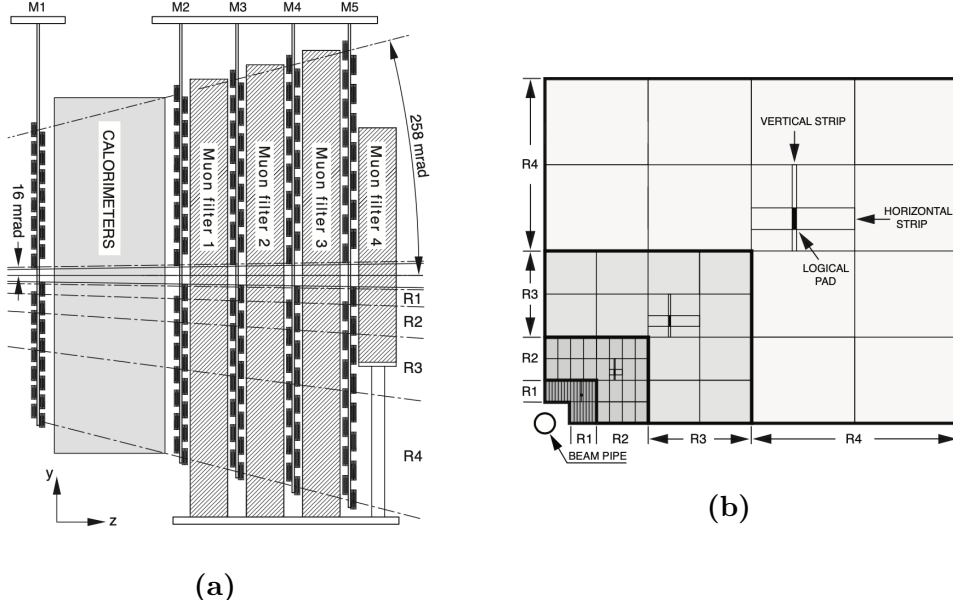


Figure 3.13: Illustration of (a) the location of the muon stations along the z -axis of the experiment, and (b) the geometry of the logical pads of the M3 muon station. Reproduced from Ref. [?].

3.1.5 Muon detectors

Muon identification and triggering is crucial for a range of high-profile LHCb measurements, such as lepton-universality tests [?, ?] or measurements of $B_{(s)}^0 \rightarrow \mu^+ \mu^-$ decays [?]. In the thesis, muon identification plays a role in suppressing a number of backgrounds. The LHCb muon system consists of 5 tracking stations, M1–M5, covering the full LHCb acceptance. M1 is located upstream of the ECAL, whereas M2–M5 are located downstream of the HCAL and inter-spaced with 80 cm thick ion absorbers in order to select penetrating muons. This is illustrated in Fig. 3.13a. The detectors are predominantly multiwire proportional chambers (MWPC), organised into logical pads, the dimensions of which define the (x, y) resolution of the measured spatial points. The exception is the central region of the M1 station, which is a triple gas-electron-multiplier detector, due to the higher track density in that region [?]. As for the calorimeters, the size of the pads vary as a function of the radial distance from the beam pipe, as illustrated in Fig. 3.13b. The resolution is significantly better in the bending plane (x) than in the non-bending plane (y). The resolution is also significantly better in the M1–3 stations than in M4 and M5, which are mostly used to identify penetrating tracks. The muon system can independently measure the p_T of a muon to within 20 %, which allows for efficient triggering.

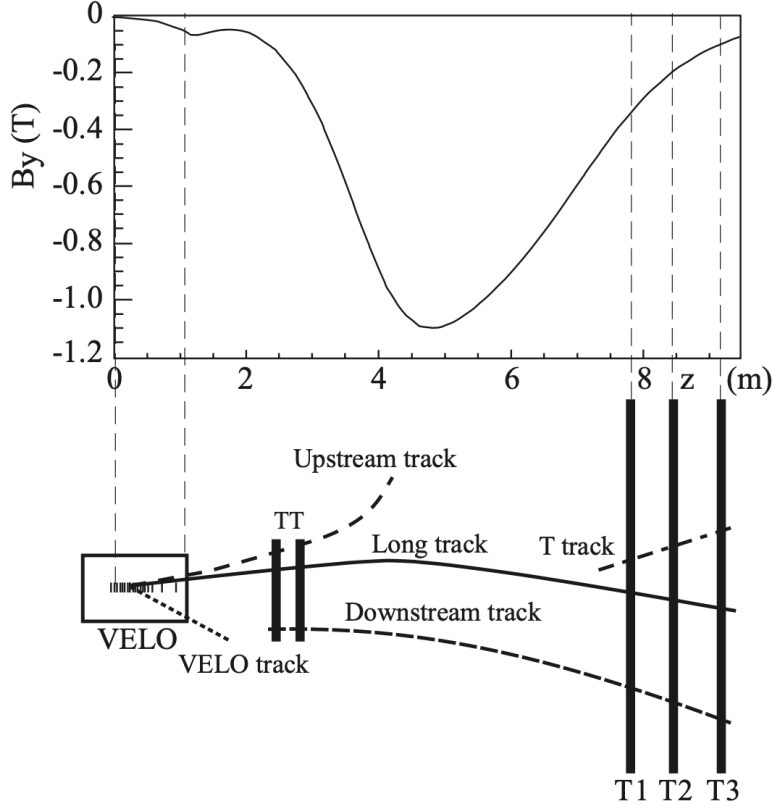


Figure 3.14: Definition of track types within the LHCb detector, depending on which set of tracking detectors the track intersects. The profile of the magnetic field is also shown. Reproduced from Ref. [?].

3.2 Reconstruction

This section describes the reconstruction algorithms that fit the detector hits in the tracking stations to form track candidates, as well as the algorithms used to identify the types of the particles that formed these tracks.

3.2.1 Track reconstruction

The LHCb experiments operates with a number of different particle track types, depending on which sub detectors a track intersects; these are summarised in Fig. 3.14. The two track types that are important for this thesis are *long* tracks, which have hits in the VELO and the TT and T1–T3 tracking stations, and *downstream* tracks that only have hits in the TT and T1–3 tracking stations. The analysis depends on both track types because a number of K_S^0 mesons produced in the signal decay leave the VELO before they decay into the $\pi^+\pi^-$ final state that is reconstructed; hence these pions necessarily form downstream tracks.

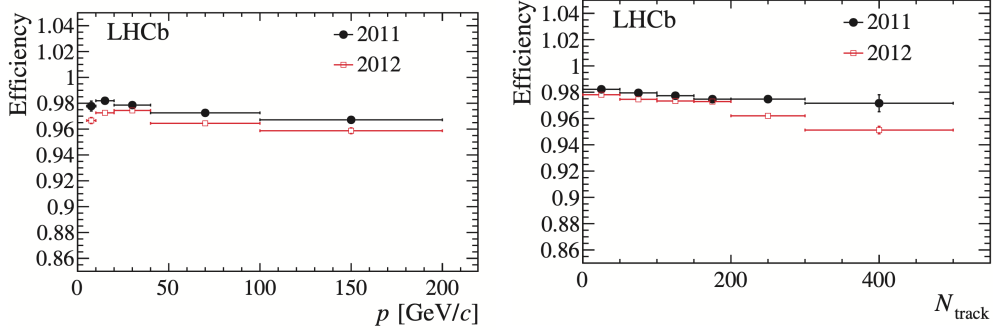


Figure 3.15: The long track reconstruction efficiency as a function of (left) track momentum and (right) the number of charged tracks in the event. The lower efficiency in 2012 than 2011 is partially due to the higher event multiplicity, given the higher centre-of-mass energy. The figure is reproduced from Ref. [?].

The first step is to form track candidates from hits in the VELO (VELO tracks) and T1–3 stations (T tracks) separately; because the magnetic field is low in the tracking detectors, these tracks are fairly straight. Long tracks are formed using two separate search strategies: in one, *forward tracking* [?], VELO tracks are used as seeds and matched with hits in the TT and T1–3 tracking stations by extrapolation. These are combined to form long tracks that are required to pass a set of quality conditions. An alternative approach, *track matching* [?, ?], matches VELO and T tracks by extrapolating both through the bending region, and deciding if they below together; finally TT hits are added. The union of tracks found via both approaches is saved, where only the track candidate with the best fit quality is kept in the case where a track appears twice. Downstream tracks are formed based on T tracks as seeds, matched with hits in the TT detector in a search region obtained by extrapolation of the seed [?]. Finally, each track is reprocessed using a Kalman filter that takes into account multiple scattering and corrects for energy loss due to ionisation [?, ?].

Many of the interesting signal decay channels of LHCb have 4–6 charged final state tracks, and therefore it is crucial to have a single-track reconstruction efficiency close to 100 %. The single-track reconstruction efficiency is shown in Fig. 3.15 as a function of track momentum and the number of tracks in an *event* (an *event* denotes a pp collision and all the particles produced therein and in subsequent decays). The efficiencies have been obtained in data, using a tag-and-probe method in $J/\psi \rightarrow \mu^+\mu^-$ decays [?]. One muon, the *tag*, is fully reconstructed, while the other, the *probe* is only partially reconstructed, allowing for the J/ψ invariant mass to be reconstructed with reasonable resolution. If the partially reconstructed probe track is matched to a full long track, the track is classified as efficient. Similar efficiencies have been achieved in Run 2.

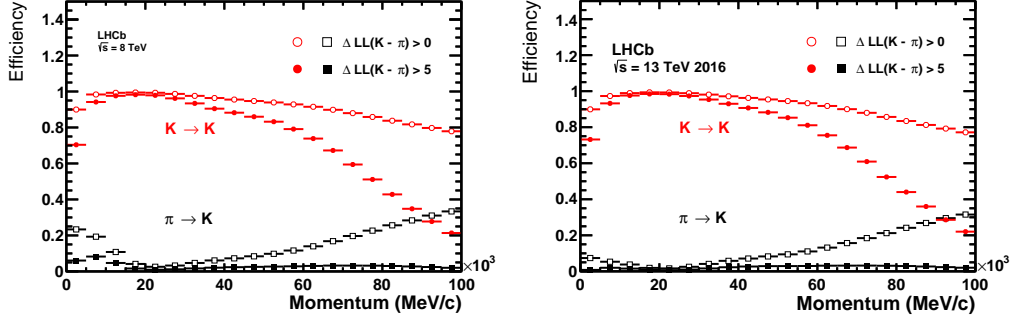


Figure 3.16: The probability to correctly identify a kaon/misidentify a pion as a kaon given two different requirements on $\Delta LL(K)$, as a function of track momentum in (left) Run 1 data from 2012 and (right) Run 2 data from 2016. Reproduced from Ref. [?].

3.2.2 Particle identification

The information from the RICH detectors, the calorimeters, and the muon system is combined for optimal identification of charged tracks as electrons, muons, pions, kaons, or protons. Photons and neutral pions are identified using the ECAL, but play no role in the thesis, and will not be discussed further.

The ability to separate $B^\pm \rightarrow DK^\pm$ and $B^\pm \rightarrow D\pi^\pm$ decays is essential to the measurement presented in this thesis. In LHCb, hadron separation is achieved via information from the RICH detectors, using a likelihood method where the observed pattern of hit pixels in the photo detectors is compared to the expected pattern, given all reconstructed tracks in an event under a given set of particle hypothesis. The likelihood is maximised by varying the particle hypotheses for each track being an electron, muon, pion, kaon, or proton [?]. It is necessary to consider all tracks of an event simultaneously because the Cherenkov rings of different tracks overlap. For each track, the maximum log likelihood of a particle hypothesis, say that the track is a kaon, relative to the hypothesis that it is a pion

$$\Delta LL_{\text{track}_i}(K) = \ln \mathcal{L}_{\max}^{\text{RICH}}(\text{pattern} | \text{track}_i = K) - \ln \mathcal{L}_{\max}^{\text{RICH}}(\text{pattern} | \text{track}_i = \pi), \quad (3.1)$$

is saved to inform PID decisions. In the case of pion-kaon separation, this variable alone is enough to achieve good separation power; in the remainder of the thesis it is denoted PIDK. The PID performance for pion-kaon separation has been measured in calibration data, following a procedure described in Section 5.2.1, and is illustrated in Fig. 3.16.

Muons are identified by extrapolating tracks to the muon stations to define fields-of-interest (FOI). A track is considered as a muon candidate when a minimum number of stations (2–4 depending on the track momentum) have hits in the

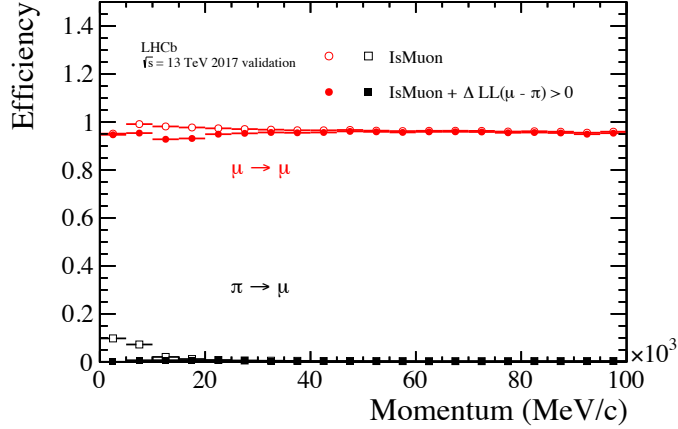


Figure 3.17: The probability to correctly identify a muon/misidentify a pion as a muon given requirements on either `isMuon` or $\Delta LL(\mu)$, as a function of track momentum in Run 2 data from 2017. Reproduced from Ref. [?].

corresponding FOI [?, ?]. This information is encoded in a variable denoted `isMuon` throughout the thesis. Additional information, such as a comparison of the slopes of the track in the main tracker and the muon stations, and the average track-hit distance in the FOI is used to form a $\Delta LL^{\text{muon}}(\mu)$ variable analogous to the one defined in Eq. (3.1) for the RICH detectors; it can be combined with $\Delta LL^{\text{RICH}}(\mu)$ to form a PID variable that takes information from both detectors into account, denoted `PIDmu`. The performance of the muon PID variables is shown in Fig. 3.17 as obtained in data. It can be seen that requiring `isMuon=0` rejects muon tracks efficiently at all momenta; this is used in the analysis to veto a number of semi-leptonic backgrounds.

In similar manner, a potential semi-leptonic background with electrons is also vetoed in the analysis presented in the thesis. In LHCb, electron PID is mainly based on the balance between deposited energy and track momentum in the ECAL [?]. This information is combined with information on photon energy deposits from brehmstrahlung, and energy deposits in the PS and HCAL, as well as information from the RICH and muon detectors, to form yet another ΔLL variable, denoted `PIDe`. As an example of the obtainable performance, an average electron selection efficiency of $(91.9 \pm 1.3\%)$ was achieved in displaced $J/\psi \rightarrow e^+e^-$ decays in Run 1, with a hadron misidentification rate of $(5.54 \pm 0.02)\%$ [?].

3.3 The LHCb trigger system

The collision rate in the LHC is up to 40 MHz, with a visible inelastic collision rate in LHCb of up to 30 MHz. The LHCb uses a multi-stage trigger to reduce rate with which events are stored to a manageable level (of eg. 12.5 kHz during Run 2). The

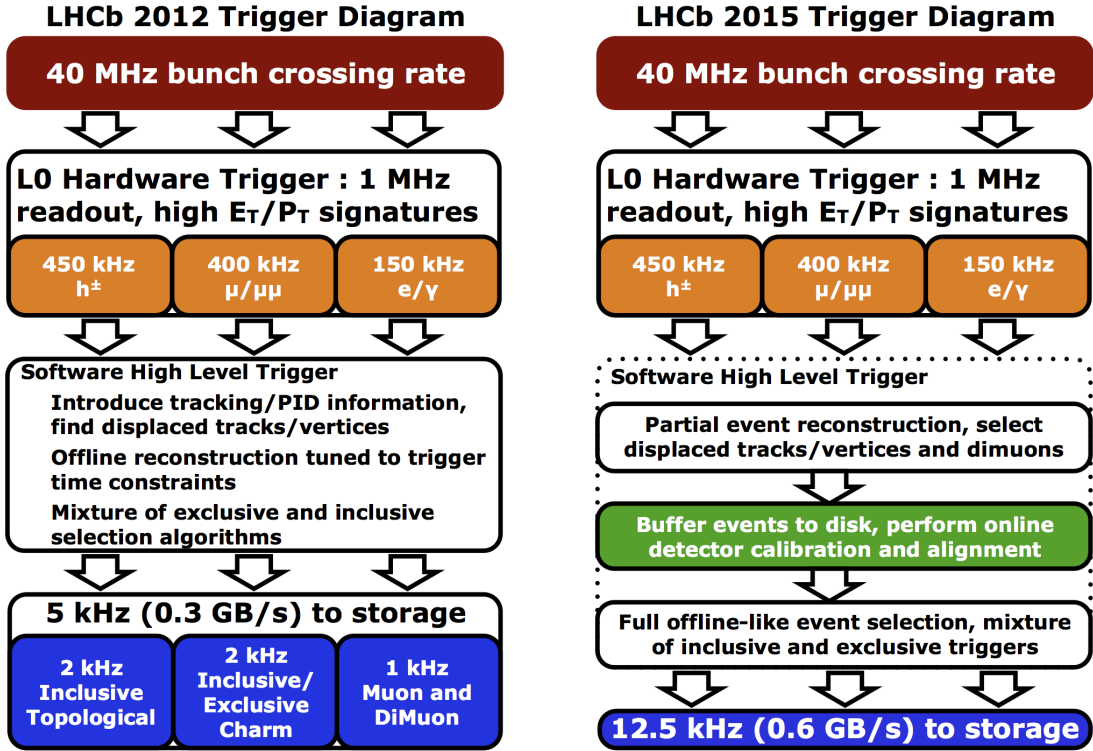


Figure 3.18: Illustration of stages and event processing rates in the LHCb trigger during (left) Run 1 and (right) Run 2.

1056 first stage consists of a hardware trigger that selects events with high transverse
 1057 energy in the calorimeters, or hits in the muon detectors. This is followed by two
 1058 software stages that rely on a reconstruction of tracks in the detector to select
 1059 events that are likely to include interesting physics. The overall trigger stages were
 1060 identical in Run 1 and Run 2, however the throughput rate was upgrade significantly
 1061 between the two data taking period, as was the quality of the reconstruction in the
 1062 software trigger stages; in Run 2, the final software trigger decisions are in fact based
 1063 on an event reconstruction that is fully equivalent to the one performed offline [?].
 1064 The stages are illustrated in Fig. 3.18, and described in detail in the following.

1065 A further, offline processing and reconstruction step is applied to all events
 1066 before they are made available to most LHCb analyses, commonly denoted as the
 1067 *stripping* step. Although the stripping does not form part of the LHCb trigger,
 1068 it does constitute an additional, centralised filter on the data, and a description
 1069 is included in Section 3.3.3.

1070 3.3.1 The level-0 hardware trigger

1071 The level-0 (L0) triggers that select physics events are based on the calorimeters
 1072 and the muon system. The ECAL and HCAL are divided into clusters of 2×2

1073 cells, for which the transverse energy is defined as

$$E_T = \sum_j E_j \sin \theta_j, \quad (3.2)$$

1074 where θ_j is the angle of cell j with respect to the beam axis and the average collision
1075 point. The trigger forms a L0Hadron candidate with the highest E_T found in the
1076 HCAL, combined with the ECAL cluster in front of it if such a cluster is present.
1077 Photon and electron candidates are formed based on clusters in the ECAL, identified
1078 by the presence (lack) of hits in the SPD for an electron (photon). The transverse
1079 energies of the candidates are compared to a fixed set of thresholds, and events
1080 where at least one candidate is above threshold are retained.

1081 The muon trigger searches for straight line tracks in the muon stations, estimating
1082 the associated muon p_T based on the track direction. An event is retained if either
1083 the largest muon p_T is above a given threshold, or the product of the two highest
1084 muon p_T values is above a different threshold.

1085 High-multiplicity events take a long time to process in the subsequent software
1086 stage; therefore it is favourable for the overall retention rate of interesting physics
1087 decays to put a maximum limit on the event multiplicity at the L0 stage. This
1088 is achieved by requiring the number of hits in the SPD detector to be below a
1089 threshold value in most L0 lines.

1090 3.3.2 High-level triggers

1091 The events that pass the L0 trigger are passed to a farm of multiprocessor computing
1092 node, the Event Filter Farm (EFF), tasked with bringing the rate down from
1093 approximately 1 MHz to the $\mathcal{O}(1 - 10)$ kHz rate that can be saved to disk. The EFF
1094 consisted of 900 (1700) nodes during Run 1 (Run 2). The software-based filtering
1095 proceeds in two stages: a first filter (HLT1) brings the rate down to approximately
1096 40 (110) kHz based on a limited reconstruction of the event, after which a second
1097 stage (HLT2) filters the events further based on a more complete reconstruction.
1098 Each step executes a number of different algorithms, each of which can allow an
1099 event to be accepted; these are denoted *trigger lines*.

1100 During both runs, the HLT1 performed a partial event reconstruction by building
1101 long tracks that satisfy a p_T requirement using the forward tracking approach
1102 described in Section 3.2.1, and determining the location of PVs using Velo tracks.
1103 In both runs, the HLT1 included an inclusive trigger that selected a high p_T track
1104 with significant displacement of all PVs (typical of a b or c decay). This line is denoted
1105 HLT1TrackAllL0 in Run 1 [?]; for Run 2 the track requirements were reoptimised

and it is denoted `Hlt1TrackMVA`. Further, an additional inclusive trigger was added that forms a two-prong vertex out of high p_T tracks inconsistent with originating in a PV, and applies a multivariate classifier to determine if it is signal-like based on a number of track and vertex properties. This line is denoted `Hlt1TwoTrackMVA` [?]. These lines triggered all events included in the analysis of the thesis; other lines exist for selecting events that include muons, calibration data, low-multiplicity events, and a number of exclusive lines, for a total of approximately 20 lines during Run 2 [?].

Because the rate of events is reduced significantly by HLT1, the HLT2 decisions can be based in a more complete reconstruction of the event. Indeed, during Run 2 it was based on a complete, fully aligned reconstruction equivalent to the offline reconstruction. During Run 1 the HLT2 reconstruction only included long tracks and did exclude some low momentum tracks; this was a main motivation for the upgrade of the EFF during the shutdown period. The need for full alignment in HLT2 means that it could not be run fully online in Run 2; instead the output events from HLT1 were saved to disk in the EFF, and processed with some delay [?]. The analysis presented in the thesis is based on a number of inclusive "topological" trigger lines, based on combinations of 2, 3, or 4 tracks that satisfy fit quality requirements, have high p_T , are separated from the PVs, and have a distance-of-closes-approach below 0.2 mm. A multivariate classifier [?] is applied to each formed n -body object, to determine if the event should be accepted based on the track momenta, invariant mass, a corrected invariant mass that takes into account missing transverse momentum, distance of closest approach, and the impact parameter and separation with the associated PV. The resulting trigger lines were denoted `Hlt2Topo{2, 3, 4}BodyBBDT` during Run 1 and `Hlt2Topo{2, 3, 4}Body` during Run 2. A large number of other HLT2 lines exist (more than 500 in Run 2), including a significant number of exclusive lines that aim to select specific decays and only save information on the signal decay, not the whole event. This was made possible by the full reconstruction within HLT2 [?], and have allowed for larger signal yields to be collected within the data storage limits.

3.3.3 Offline data filtering: the LHCb stripping

Events that are written to disk are processed with the full detector alignment and calibration. In a further, offline processing step denoted the *stripping*, hundreds of different, dedicated reconstructions are performed; decay candidates for various signal decays are built and a number of requirements are made to reject backgrounds from random track combinations. For example, the $B^\pm \rightarrow D(\rightarrow K_S^0 h^+ h^-) h^\pm$ candidates that are analysed in this thesis are built during the stripping stage, as

1142 described further in Section 5.1. The stripping is a centralised computing task,
1143 executed on the Worldwide LHC Computing Grid [?], and allows the analysts
1144 to process much smaller data sets during their individual analysis. Because the
1145 stripping is based on data saved to offline storage it can be repeated; however,
1146 the processing of data collected during a year of data taking takes many weeks,
1147 so this does not happen often.

1148 3.4 Simulation

1149 A centralised LHCb simulation is able to simulate pp collisions with the proper
1150 conditions within LHCb, model subsequent secondary decays and the full detector
1151 response, and process the output in the full LHCb reconstruction. In this thesis,
1152 simulated decays are used to determine the reconstructed invariant-mass distribution
1153 of a number of decay modes, as well as a number of relative selection efficiencies. The
1154 pp collisions are generated using PYTHIA [?] with a specific configuration specific
1155 to LHCb [?]. The time-dependent evolution and decays of unstable particles are
1156 described by the EVTGEN [?] package, designed specifically for B physics. Final-
1157 state radiation is generated using PHOTOS [?]. The interaction of the generated
1158 particles with the detector, and its response, are implemented using the GEANT4
1159 toolkit [?] as described in Ref. [?].

1160 The most significant computational cost of the simulation is due to the detector
1161 simulation. A single pp collision produces $\mathcal{O}(100)$ tracks in the detector, out of
1162 which only a handful belong to the signal decay under study. Therefore, significant
1163 computational resources can be saved by reusing the detector simulation of non-
1164 signal tracks a number of times, while redescaying the signal particle, say a B^+ , each
1165 time. This approach is called ReDecay [?], and has been relatively widely adopted
1166 within LHCb. ReDecay has been used to produce simulation samples corresponding
1167 to the conditions in 2017 and 2018 for this thesis. In some cases, the use of ReDecay
1168 necessitates special statistical treatment due the correlated detector occupancies
1169 between signal candidates, but for the analysis in this thesis the impact is negligible.

1170 A number of sub-dominant backgrounds are investigated using the fast-simulation
1171 package **RapidSim** [?]. This package can decay heavy b and c hadrons with kinematic
1172 distributions similar to those in LHCb pp collisions, or with user defined input
1173 distributions. The decays are typically evenly distributed over phase space, but can
1174 also be handled with EVTGEN [?] to take involved spins and resonant structure
1175 into account. Furthermore, a smearing of the obtained momenta can be applied
1176 that is based on the LHCb resolution.

4

1177

1178 Neutral kaon CP violation and material 1179 interaction in BPGGSZ measurements

1180 The presence of a K_S^0 meson in the $D \rightarrow K_S^0 h^+ h^-$ final states introduces a small
1181 bias in BPGGSZ measurements due to CP -violation in the neutral kaon sector
1182 and asymmetries caused by the interaction between the neutral kaons and detector
1183 material. These fundamental physics effects are reviewed in Section 4.1, after which
1184 the chapter presents a detailed analysis of the impact on the LHCb measurement
1185 that is the subject of the thesis, as well as future γ measurements with the Belle II
1186 experiment. Prior to this analysis, the only existing work on the effect on γ
1187 measurements suggested a small effect in $B^\pm \rightarrow D K^\pm$ measurements but potentially
1188 very significant effects in measurements based on $B^\pm \rightarrow D \pi^\pm$ decays [?]. However,
1189 as described in Section 4.1.1, the analysis in Ref. [?] does not take into account
1190 the fundamental aspect of the BPGGSZ method: that it relies on the phase-space
1191 distribution of signal decays, not phase-space integrated asymmetries. Furthermore,
1192 the study only considers the CP -violation effect, not material interaction. Therefore,
1193 a more detailed study was necessary before the $B^\pm \rightarrow D \pi^\pm$ decay mode could
1194 reliably be promoted to a signal channel.

1195 **4.1 CP violation and material interaction of neu-** 1196 **tral kaons**

1197 A brief review of the general phenomenology of mixing and CP violation in the
1198 neutral kaon system is useful, before analysing the impact on γ measurements.

1199 The presentation in this section follows the PDG review of *CP violation in the*
1200 *quark section [?]. The general theory considers any pair of neutral mesons* $|M^0\rangle$
1201 *and* $|\bar{M}^0\rangle$ *related by* CP *conjugation*

$$CP|M^0\rangle = e^{i\phi_M}|M^0\rangle \quad CP|\bar{M}^0\rangle = e^{-i\phi_M}|\bar{M}^0\rangle, \quad (4.1a)$$

1202 where ϕ_M is an arbitrary phase. In this thesis, the convention $\phi_M = 0$ is chosen
1203 to equal zero, so that

$$CP|M^0\rangle = |\bar{M}^0\rangle \quad CP|\bar{M}^0\rangle = |M^0\rangle. \quad (4.1b)$$

1204 A meson state that starts as a general superposition of $|M^0\rangle$ and $|\bar{M}^0\rangle$ states

$$\begin{aligned} \psi_M^0 &\equiv \psi_M(0) = a(0)|M^0\rangle + b(0)|\bar{M}^0\rangle \\ &\equiv \psi_{M^0}^0 + \psi_{\bar{M}^0}^0 \end{aligned} \quad (4.2)$$

1205 will, over time, involve into a state that consists of a different superposition of
1206 $|M^0\rangle$ and $|\bar{M}^0\rangle$, as well as components for all possible states the meson system
1207 can decay into

$$\begin{aligned} \psi_M(t) &= a(t)|M^0\rangle + b(t)|\bar{M}^0\rangle + \sum c_i(t)f_i \\ &\equiv \psi_{M^0}(t) + \psi_{\bar{M}^0}(t) + \sum c_i(t)f_i. \end{aligned} \quad (4.3)$$

1208 For time scales that are longer than the typical strong-interaction, the time evolution
1209 of the $M^0 - \bar{M}^0$ superposition can be described by a 2×2 Hamiltonian

$$\frac{d}{dt} \begin{pmatrix} \psi_{M^0}(t) \\ \psi_{\bar{M}^0}(t) \end{pmatrix} = -i\mathcal{H}_0 \begin{pmatrix} \psi_{M^0}(t) \\ \psi_{\bar{M}^0}(t) \end{pmatrix} \quad (4.4)$$

1210 that is *non-Hermitian* (to allow for decay) but can be parameterised in terms
1211 of two Hermitian matrices \mathcal{M} and Γ_0

$$\mathcal{H}_0 = \mathcal{M} - \frac{i}{2}\Gamma_0. \quad (4.5)$$

1212 The quantum states with well-defined (real) masses, m_j , and (real) decay widths,
1213 Γ_j , are the two eigenstates of \mathcal{H}_0 with eigenvalues $\lambda_j = m_j - \frac{i}{2}\Gamma_j$. The eigenstates
1214 (of course) evolve independently in time, so that

$$\psi_j(t) = e^{-i\lambda_j t}\psi_j^0 = e^{-im_j t - \frac{\Gamma_j}{2}t}\psi_j^0. \quad (4.6)$$

1215 The eigenstates are denoted H and L according to the size of m_j , the real part
1216 of the eigenvalues, such that $m_H > m_L$. Assuming that \mathcal{H}_0 conserves CPT the
1217 eigenstates have the general form

$$\begin{aligned} |M_H\rangle &\equiv p|M^0\rangle - q|\bar{M}^0\rangle \\ |M_L\rangle &\equiv p|M^0\rangle + q|\bar{M}^0\rangle \end{aligned} \quad (4.7)$$

where p and q are complex numbers that satisfy $|q|^2 + |p|^2 = 1$. With the convention in Eq. (4.1b) it follows that if \mathcal{H}_0 also conserves CP , so that $|M_H\rangle$ and $|M_L\rangle$ are CP eigenstates, then $p = \pm q$, where the sign depends on which of the heavy and the light meson states is CP even, and which is CP odd.

The eigenstates of the Hamiltonian governing the neutral kaon system are almost, but not exactly, equal to the CP eigenstates

$$|K_1\rangle = \frac{|K^0\rangle + |\bar{K}^0\rangle}{\sqrt{2}} \quad |K_2\rangle = \frac{|K^0\rangle - |\bar{K}^0\rangle}{\sqrt{2}}, \quad (4.8)$$

which are CP even and odd, respectively. This approximate equality leads to the most prominent feature of the neutral kaon system: the two eigenstates of \mathcal{H}_0 have lifetimes that differ by orders of magnitude. This is best understood by assuming, for a moment, that the states in Eq. (4.8) *do* equal the eigenstates with definite life times. The K_1 state can decay in the CP even $\pi^+\pi^-$ and $\pi^0\pi^0$ modes, and does so almost 100% of the time; these decay modes are not available to the K_2 (in the absence of direct CP violation) which results in a much lower decay rate and much longer life time. Therefore, the eigenstates in the kaon system are labelled the *short-lived* kaon, K_S^0 , which is almost CP even, and the *long-lived* kaon, K_L^0 , which is almost CP odd. The life times are [?]

$$\tau_{K_S^0} = (8.954 \pm 0.004) \times 10^{-11} \text{s} \quad \tau_{K_L^0} = (5.116 \pm 0.021) \times 10^{-8} \text{s}. \quad (4.9)$$

Experimentally, it is found that the K_S^0 corresponds to the light eigenstate, but that the mass splitting [?]

$$\begin{aligned} \Delta m = m_{K_L^0} - m_{K_S^0} &= (0.5289 \pm 0.0009) \times 10^{10} \hbar s^{-1} \\ &\simeq 3.5 \times 10^{-6} \text{ eV} \end{aligned} \quad (4.10)$$

is tiny compared to the neutral kaon masses of $m_{K_S^0} = 497.6 \text{ MeV}/c^2$ [?].

However, the discovery of $K_L^0 \rightarrow \pi\pi$ decays by Kronin and Fitch in 1964 established that the K_S^0 and K_L^0 are *not* exactly equal to the CP eigenstates in Eq. (4.8), because the \mathcal{H}_0 relevant to the kaon system is CP -violating. The CP violation in the kaon sector is conventionally parameterised in terms of the complex parameters ϵ and ϵ' , in terms of which

$$\frac{A(K_L^0 \rightarrow \pi^+\pi^-)}{A(K_S^0 \rightarrow \pi^+\pi^-)} = \epsilon + \epsilon' \quad \frac{A(K_L^0 \rightarrow \pi^0\pi^0)}{A(K_S^0 \rightarrow \pi^0\pi^0)} = \epsilon - 2\epsilon'. \quad (4.11)$$

In these expressions ϵ denotes the contribution from CP violation in mixing and ϵ' the contribution due to direct CP violation in the decays. The ϵ parameter has been measured to be [?]

$$|\epsilon| = (2.228 \pm 0.011) \times 10^{-3}, \quad \arg \epsilon = (43.52 \pm 0.05)^\circ. \quad (4.12)$$

1245 Direct CP violation is ignored for the remainder of the thesis, because ϵ' is measured
1246 to be three orders of magnitude smaller than ϵ . In terms of the CP eigenstates
1247 of Eq. (4.8), the mass eigenstates K_S^0 and K_L^0 are given by

$$\begin{aligned} |K_S^0\rangle &= \frac{|K_1\rangle + \epsilon|K_2\rangle}{\sqrt{1+|\epsilon|^2}} &= \frac{(1+\epsilon)|K^0\rangle + (1-\epsilon)|\bar{K}^0\rangle}{\sqrt{2(1+|\epsilon|^2)}} \\ |K_L^0\rangle &= \frac{|K_2\rangle + \epsilon|K_1\rangle}{\sqrt{1+|\epsilon|^2}} &= \frac{(1+\epsilon)|K^0\rangle - (1-\epsilon)|\bar{K}^0\rangle}{\sqrt{2(1+|\epsilon|^2)}}, \end{aligned} \quad (4.13)$$

1248 corresponding to the definition $p = (1+\epsilon)/\sqrt{2(1+|\epsilon|^2)}$ and $q = (1-\epsilon)/\sqrt{2(1+|\epsilon|^2)}$
1249 in Eq. (4.7).

1250 In an experimental setting, the time evolution of a neutral kaon state is affected
1251 by nuclear interactions with the detector. The interaction is governed by the strong
1252 force, and therefore sensitive to the *flavour* of the kaon state; the interaction
1253 strength is thus different for K^0 and \bar{K}^0 mesons. This difference introduces a
1254 non-zero $K_S^0 \leftrightarrow K_L^0$ transition amplitude for neutral kaons traversing a detector
1255 segment. This effect was predicted early in the history of kaon physics [?] and is
1256 commonly denoted *kaon regeneration*. The effect can be described by including a
1257 material-interaction term in the Hamiltonian that is diagonal in the $(|K^0\rangle, |\bar{K}^0\rangle)$
1258 basis, so that the equation governing the time evolution is [?, ?]

$$\frac{d}{dt} \begin{pmatrix} \psi_{K^0}(t) \\ \psi_{\bar{K}^0}(t) \end{pmatrix} = -i \left[\mathcal{H}_0 + \begin{pmatrix} \chi & 0 \\ 0 & \bar{\chi} \end{pmatrix} \right] \begin{pmatrix} \psi_{K^0}(t) \\ \psi_{\bar{K}^0}(t) \end{pmatrix}. \quad (4.14)$$

1259 The complex parameters χ and $\bar{\chi}$ describe the material interaction of the K^0
1260 and \bar{K}^0 flavour eigenstates and are related to their scattering cross section, as
1261 described further in Section 4.3.4. The solution of Eq. (4.14) for the time evolution
1262 in the K_S^0 and K_L^0 states is [?]

$$\begin{aligned} \psi_S(t) &= e^{-i\Sigma t} \left(\psi_S^0 \cos \Omega t + \frac{i}{2\Omega} (\Delta\lambda\psi_S^0 - \Delta\chi\psi_L^0) \sin \Omega t \right), \\ \psi_L(t) &= e^{-i\Sigma t} \left(\psi_L^0 \cos \Omega t - \frac{i}{2\Omega} (\Delta\lambda\psi_L^0 + \Delta\chi\psi_S^0) \sin \Omega t \right), \end{aligned} \quad (4.15)$$

1263 in terms of the parameters

$$\begin{aligned} \Delta\chi &= \chi - \bar{\chi}, \\ \Delta\lambda &= \lambda_L - \lambda_S = (m_L - m_S) - \frac{i}{2}(\Gamma_L - \Gamma_S), \\ \Sigma &= \frac{1}{2}(\lambda_S + \lambda_L + \chi + \bar{\chi}), \\ \Omega &= \frac{1}{2}\sqrt{\Delta\lambda^2 + \Delta\chi^2}. \end{aligned} \quad (4.16)$$

1264 In the vacuum limit where $\chi = \bar{\chi} = 0$, the expressions in Eq. (4.6) and Eq. (4.15) are
1265 equal.

4.1.1 A first look at the impact on γ measurements

The effects described above have an impact on measurements of CP asymmetries in modes with a neutral kaon in the final state. This was analysed for the first time in relation to γ measurements by Grossman and Savastio in 2014 [?]. The authors point out two sources of corrections to be included:

- the fact that K_S^0 is not an exact CP eigenstate can break potential symmetry relations employed in an analysis, and
- that when the neutral kaon is reconstructed in a $\pi\pi$ final state there will be contributions from both K_S^0 and K_L^0 decays.

The analysis in this chapter considers yet another effect, not treated by Grossman and Savastio, namely that

- material interaction can emulate the effect of neutral kaon CP violation, because it couples the almost- CP -even K_S^0 and the almost- CP -odd K_L^0 states.

Due to the presence of $K_L^0 \rightarrow \pi\pi$ decays, Grossman and Savastio point out that the relevant decay rates to consider in an experimental setting are of the form

$$d\Gamma(t) \propto |\psi_S(t) + \epsilon\psi_L(t)|^2. \quad (4.17)$$

The time dependence of the decay rates considered in Chapter 2 was left out because all terms shared a common time dependence. That is not the case in Eq. (4.17), due to the very different decay rates of the K_S^0 and K_L^0 components of the kaon state. As a consequence, the time-integrated yields have the form

$$N \propto \int dt \eta(t) |\psi_S(t) + \epsilon\psi_L(t)|^2, \quad (4.18)$$

where $\eta(t)$ is the time acceptance in a given experimental setting. Thus, the acceptance is crucial to model in order to correctly estimate the impact of kaon CP -violation effects on a given measurement.

Considering BPGBSZ measurements, the main effect of neutral kaon CP violation is a breakdown of the fundamental Dalitz-plot symmetry that is exploited in the derivation of the bin yield equations. Extending the amplitude definition of Eq. (2.21) to include K_L^0 decays

$$A_{S(L)}^{(\overline{D})}(s_-, s_+) = A((\overline{D})^0 \rightarrow K_{S(L)}^0 \pi^+ \pi^-), \quad (4.19)$$

the authors point out that CP -violation in the K_S^0 system means that the relation $A_S^{(\overline{D})}(s_{-+}) = A_S^D(s_{+-})$ is not exactly true; and in addition, there is now a

dependence on $A_L^D(s_{-+})$ which satisfies a different approximate symmetry, namely $A_L^{\bar{D}}(s_{-+}) \simeq -A_L^D(s_{+-})$. Grossman and Savastio describe these symmetry breaking effects in detail, but do not explicitly derive the corrections to the yield equations of Chapter 2, nor try to quantify the potential bias on γ in a measurement based on the binned yields. Instead, they derive expressions for the bias in a measurement obtained from phase-space integrated CP asymmetries. This is done for both GLW measurements that use $D \rightarrow K_S^0 X$ final states and for the $D \rightarrow K_S^0 h^+ h^-$ final states; however, for their quantitative estimate of $\Delta\gamma$ the authors make an approximation that corresponds to assuming that the $D \rightarrow K_S^0 h^+ h^-$ final state is a CP eigenstate, making the two results identical. The authors find that in this case, assuming a uniform experimental acceptance for all kaon decay times, the asymmetry has the form¹

$$A = \frac{2r_B \sin \gamma \sin \delta_B + 2\text{Re}[\epsilon]}{1 + r_B^2 - 2r_B \cos \gamma \cos \delta_B}, \quad (4.20)$$

If a measured value of A is interpreted to obtain γ without taking the ϵ term into account, it leads to a bias of

$$\Delta\gamma = -\frac{\text{Re}[\epsilon]}{r_B \cos \gamma \sin \delta_B} + O(|\epsilon|). \quad (4.21)$$

The scaling $\Delta\gamma \sim \mathcal{O}(r_B/|\epsilon|)$ is the main result of the analysis by Grossman and Savastio. For $B^\pm \rightarrow D K^\pm$ decays, where $r_B^{DK^\pm} \simeq 0.1$ this suggests a bias at the percent level, which is negligible compared to current experimental uncertainties. However, in the $B^\pm \rightarrow D \pi^\pm$ case, where $r_B^{D\pi^\pm} \simeq 0.005$ [?], their result suggests relative biases that are potentially of $\mathcal{O}(1)$.

The conclusions are lacking on two accounts, however. Firstly, as made clear in Section 2.3.5, the $K_S^0 \pi^+ \pi^-$ and $K_S^0 K^+ K^-$ states are *far from* CP eigenstates. From the asymmetry expression in that section, it is clear that the bias in a determination of γ based on phase-space asymmetries will in fact scale as

$$\Delta\gamma \sim \mathcal{O}\left(\frac{|\epsilon|}{(2\mathcal{F}_+ - 1)r_B}\right), \quad (4.22)$$

which suggests that Grossman and Savastio severely *underestimates* the potential impact. This is described in detail in Section 4.2.3. More importantly, the analysis of the phase-space integrated asymmetry is in fact *irrelevant* to BPGGSZ measurements as they are currently performed: as described in Section 2.3.5 the information from

¹In fact the expression in Eq. (4.20) is missing a term, as will be clear when an analogous expression is derived in detail in Section 4.2.3.

the global asymmetry is completely discarded. Therefore it is necessary to analyse the effects of kaon CP -violation on a full, binned analysis of $D \rightarrow K_S^0 h^+ h^-$ decays, which is done in detail in the following sections. While the aim is to extend the analysis if Grossman and Savastio, the treatment in the following sections is completely independent of that in Ref. [?].

4.2 Impact on BPGBSZ measurements of γ : principles

The analysis of the impact on BPGBSZ measurements is carried out in two stages. This section treats the leading order effects analytically, and derives the overall order of magnitude of the expected bias in a general setting. Then Section 4.3 presents a detailed numerical study of the expected effect in measurements with the LHCb and Belle II experiments specifically, because these will be crucial to constrain γ during the coming decade [?, ?].

4.2.1 Modified symmetry relations

In order to derive the corrections to the asymmetry relation $A_S^D(s_{-+}) \simeq A_S^{\bar{D}}(s_{+-})$, it is beneficial to express $A_{S(L)}^D$ in terms of the amplitudes

$$A_{1/2}^{\bar{D}} = A(\overline{D}^0 \rightarrow K_{1/2}^0 \pi^+ \pi^-), \quad (4.23)$$

because these amplitude satisfy the exact symmetries $A_1^D(s_{-+}) = A_1^{\bar{D}}(s_{+-})$ and $A_2^D(s_{-+}) = -A_2^{\bar{D}}(s_{+-})$. This approach is different to that of Grossman and Savastio, but the final results are equivalent. After the decay of a D^0 meson to a neutral kaon, the kaon state is

$$\begin{aligned} \psi^0 &= A_1^D |K_1\rangle + A_2^D |K_2\rangle \\ &= N \left[(A_1^D - \epsilon A_2^D) |K_S^0\rangle + (A_2^D - \epsilon A_1^D) |K_L^0\rangle \right], \end{aligned} \quad (4.24)$$

with the normalisation constant $N = \sqrt{1 + |\epsilon|^2}/(1 - \epsilon^2)$. Thus it can be seen that

$$\begin{aligned} A_S^D(s_{-+}) &= N \left[(A_1^D(s_{-+}) - \epsilon A_2^D(s_{-+})) \right], \\ A_L^D(s_{-+}) &= N \left[(A_2^D(s_{-+}) - \epsilon A_1^D(s_{-+})) \right], \end{aligned} \quad (4.25)$$

1342 with an analogous expression for the \bar{D}^0 decay amplitudes. Therefore, the generalised
1343 relations between the D^0 and \bar{D}^0 amplitudes are

$$\begin{aligned} A_S^{\bar{D}}(s_{+-}) &= N[A_1^{\bar{D}}(s_{+-}) - \epsilon A_2^{\bar{D}}(s_{+-})] \\ &= N[A_1^D(s_{-+}) + \epsilon A_2^D(s_{-+})] = A_S^D(s_{-+}) + 2N\epsilon A_2^D(s_{-+}), \\ A_L^{\bar{D}}(s_{+-}) &= N[A_2^{\bar{D}}(s_{+-}) - \epsilon A_1^{\bar{D}}(s_{+-})] \\ &= -N[A_2^D(s_{-+}) + \epsilon A_1^D(s_{-+})] = -A_L^D(s_{-+}) - 2N\epsilon A_1^D(s_{-+}). \end{aligned} \quad (4.26)$$

1344 4.2.2 Relationship between the K_S^0 and K_L^0 amplitudes

1345 The decay amplitude $A(D^0 \rightarrow K_S^0 \pi^+ \pi^-)$ has been carefully studied, and a number
1346 of amplitude models have been published [?, ?, ?, ?, ?]. No models have been
1347 published for $D^0 \rightarrow K_L^0 \pi^+ \pi^-$ decays. However, following an approach laid out by
1348 the CLEO collaboration [?], the two amplitudes can be related. Again, this is
1349 most easily done by relating the $A_1^D(s_{+-})$ and $A_2^D(s_{+-})$ amplitudes. In the isobar
1350 formalism, the decay amplitude $A(D^0 \rightarrow K_1 \pi^+ \pi^-)$ is expressed as a non-resonant
1351 constant amplitude plus a sum of resonances

$$A(D^0 \rightarrow K_1 \pi^+ \pi^-) = k_{NR} + \sum_{CF} k_i R^i(s_{K\pi^-}) + \sum_{DCS} k_j R^j(s_{K\pi^+}) + \sum_{R_{\pi\pi}} k_k R^k(s_{\pi^+\pi^-}). \quad (4.27)$$

1352 The resonances are split into Cabibbo-favoured (CF) K^{*-} resonances, doubly
1353 Cabibbo-suppressed (DCS) K^{*+} resonances and $\pi\pi$ resonances.² The CF resonances
1354 couple to the \bar{K}^0 component of $K_1 (\propto K^0 + \bar{K}^0)$, and therefore the corresponding
1355 k_i in the $K_2 (\propto K^0 - \bar{K}^0)$ amplitude will have a relative minus sign. The DCS
1356 resonances couple to the K^0 component of K_1 , and so the corresponding k_j in the
1357 K_2 amplitude will have a relative plus sign. For the $h^+ h^-$ resonances, there will be
1358 a coupling to both the K^0 and \bar{K}^0 components, however the coupling to the K^0
1359 component is expected to be suppressed with a Cabibbo suppression factor $r_k e^{i\delta_k}$,
1360 where $r_k \simeq \tan^2 \theta_C \simeq 0.05$ is determined by the Cabibbo angle θ_C and δ_k can take
1361 any value. Therefore, the k_k for these resonances have a relative $-(1 - 2r_k e^{i\delta_k})$
1362 factor in the K_2 amplitude. The same effect leads to the differences in decay rates
1363 between $D^0 \rightarrow K_S^0 \pi^0$ and $D^0 \rightarrow K_L^0 \pi^0$ decays [?, ?]. Thus, given a model of the

²In modern models, the $\pi\pi$ and $K\pi$ S -wave components are modelled via the K -matrix formalism and LASS parametrisations, respectively, instead of sums of individual resonances [?]. This does not alter the arguments below, as the R functions of Eq. (4.27) can equally well represent such terms.

¹³⁶⁴ form in Eq. (4.27), a model for the $A(D^0 \rightarrow K_2\pi^+\pi^-)$ amplitude will have the form

$$A(D^0 \rightarrow K_2\pi^+\pi^-) = k_{NR} + \sum_{CF} (-k_i) R^i(s_{K\pi^-}) + \sum_{DCS} (+k_j) R^j(s_{K\pi^+}) \\ + \sum_{R_{\pi\pi}} (-(1 - 2r_k e^{i\delta_k}) k_k) R^k(s_{\pi^+\pi^-}). \quad (4.28)$$

¹³⁶⁵ An important consequence of these substitution rules is that

$$A_2^D(s_{+-}) = -A_1^D(s_{+-}) + r_A \Delta A(s_{+-}), \quad (4.29)$$

¹³⁶⁶ where $r_A \simeq \tan^2 \theta_C$ and $\Delta A(s_{+-}) \sim A_1^D(s_{+-})$ are of the same order of magnitude
¹³⁶⁷ (at least when averaged over the bins used in γ measurements). This relation is
¹³⁶⁸ sufficient to make the qualitative arguments of this section, while the full set of
¹³⁶⁹ substitution rules above are used in the quantitative studies of Section 4.3.

¹³⁷⁰ 4.2.3 Modification of the BPGBSZ yield equations

¹³⁷¹ With suitable models to calculate $A_{S(L)}^{\bar{D}}$ (or $A_{1/2}^{\bar{D}}$) and knowledge of $\Delta\chi$ for the
¹³⁷² materials relevant to an experimental setting, the relations derived in the preceding
¹³⁷³ sections can be employed to calculate the expected phase-space bin yields, N_i^\pm ,
¹³⁷⁴ including the effects of kaon CP violation and material interaction. The decay
¹³⁷⁵ rates have additional terms compared to those in Eq. (2.24), because the K_L^0
¹³⁷⁶ contribution must be taken into account

$$d\Gamma(t, s_{+-}) \propto |\psi_S(t, s_{+-}) + \epsilon\psi_L(t, s_{+-})|^2, \quad (4.30)$$

¹³⁷⁷ where the time-dependence of $\psi_{S/L}(t, s_{+-})$ is governed by Eq. (4.15), and the phase-
¹³⁷⁸ space dependence is included in the state component, by defining $\psi_{S/L}^0$ in terms of
¹³⁷⁹ $A_{S(L)}^{\bar{D}}(s_{+-})$. For example, for the case of a $B^- \rightarrow DK^-$ decay, the definition is

$$\begin{aligned} \psi_{S/L}^{0,B^-}(s_{+-}) &= A_S^D(s_{+-}) + r_B e^{i(\delta_B - \gamma)} A_S^{\bar{D}}(s_{+-}) \\ &= A_1^D(s_{+-}) - \epsilon A_2^D(s_{+-}) + r_B e^{i(\delta_B - \gamma)} (A_1^{\bar{D}}(s_{+-}) - \epsilon A_2^{\bar{D}}(s_{+-})) \\ &= A_1^D(s_{+-}) - \epsilon A_2^D(s_{+-}) + r_B e^{i(\delta_B - \gamma)} (A_1^D(s_{+-}) + \epsilon A_2^D(s_{+-})). \end{aligned} \quad (4.31)$$

¹³⁸⁰ It is useful to look at the corrections to the BPGBSZ yield expressions in Eq. (2.25)
¹³⁸¹ to lowest order in ϵ and $r_\chi = \frac{1}{2} \frac{\Delta\chi}{\Delta\lambda}$, the dimensionless parameter governing material
¹³⁸² interactions. For LHCb and Belle II the average $|r_\chi| \simeq 10^{-3}$, as detailed in the
¹³⁸³ Section 4.3. To first order in r_χ , the time-dependent kaon states within a material,
¹³⁸⁴ given in Eq. (4.15), simplify to [?]

$$\begin{aligned} \psi_S(t, s_{+-}) &= e^{-\frac{i}{2}(x+\bar{x})t} e^{-i\lambda_S t} (\psi_S^0(s_{+-}) - r_\chi (1 - e^{-i\Delta\lambda t}) \psi_L^0(s_{+-})), \\ \psi_L(t, s_{+-}) &= e^{-\frac{i}{2}(x+\bar{x})t} e^{-i\lambda_L t} (\psi_L^0(s_{+-}) + r_\chi (1 - e^{+i\Delta\lambda t}) \psi_S^0(s_{+-})). \end{aligned} \quad (4.32)$$

1385 By inserting these expressions into Eq. (4.30) and employing the definition in
1386 Eq. (4.31) (and a similar definition for B^+ decays), the binned yields can be
1387 calculated by an integration over time and phase space. In the remainder of this
1388 section, it is assumed that the experimental time acceptance is $\eta(t) = 1$ for all times
1389 and that r_χ is constant at all times; more realistic assumptions are introduced in
1390 Section 4.3. In this case, the binned yields are given by the expression

$$N_i^- = h_B^{-'} \left(\hat{K}_{+i} + r_B^2 \hat{K}_{-i} + 2\sqrt{\hat{K}_{+i} \hat{K}_{-i}} (x_- \hat{c}_i + y_- \hat{s}_i) + O(r\epsilon) \right), \\ N_i^+ = h_B^{+'} \left(\hat{K}_{-i} + r_B^2 \hat{K}_{+i} + 2\sqrt{\hat{K}_{+i} \hat{K}_{-i}} (x_+ \hat{c}_i - y_+ \hat{s}_i) + O(r\epsilon) \right), \quad (4.33)$$

1391 where a number of new parameters have been defined, and where $O(r\epsilon)$ denotes terms
1392 of $O(r_A\epsilon)$, $O(r_B\epsilon)$, $O(r_A r_\chi)$, and $O(r_B r_\chi)$. Since $r_B \sim r_A \sim 10^{-1}$ (in $B^\pm \rightarrow D K^\pm$
1393 decays) and $r_\chi \sim \epsilon \sim 10^{-3}$, these terms are all of the same order of magnitude.

1394 The new normalisation constants $h_B^{\pm'} = h_B^\pm (1 + |\epsilon + r_\chi|^2 \frac{\Gamma_S}{\Gamma_L} \mp \Delta h)$ are de-
1395 fined in terms of

$$\Delta h = 2\text{Re}[\epsilon + r_\chi] - 4 \frac{\Gamma_S}{\Gamma_L + \Gamma_S} \frac{\text{Re}[\epsilon + r_\chi] + \mu \text{Im}[\epsilon + r_\chi]}{1 + \mu^2}, \quad \mu = 2 \frac{m_L - m_S}{\Gamma_L + \Gamma_S}. \quad (4.34)$$

1396 The \hat{K}_i parameters are defined to be

$$\hat{K}_i = \frac{1}{1 + |\epsilon + r_\chi|^2 \frac{\Gamma_S}{\Gamma_L}} \left(K_i^{(1)} + |\epsilon + r_\chi|^2 \frac{\Gamma_S}{\Gamma_L} K_i^{(2)} \right), \quad (4.35)$$

1397 in which the $K_i^{(1/2)}$ parameters are phase-space integrals, defined as in Eq. (2.27)
1398 but for $A_{1/2}^D$. To lowest order, the \hat{K}_i correspond to the fractional D^0 decay yield
1399 in each bin, as obtained in a measurement that averages D^0 and \bar{D}^0 decays, and
1400 assumes the $A_S^D(s_{-+}) = A_S^D(s_{+-})$ symmetry to be exact:

$$K_i^{\text{meas}} \equiv \frac{N_i^D + N_{-i}^{\bar{D}}}{\sum_j N_j^D + N_{-j}^{\bar{D}}} = \hat{K}_i + \mathcal{O}(r\epsilon). \quad (4.36)$$

1401 Here, N_i^D ($N_i^{\bar{D}}$) is the expected yield of flavour tagged D^0 (\bar{D}^0) mesons into bin
1402 i of the D decay phase-space.

1403 In similar fashion, the parameters (\hat{c}_i, \hat{s}_i) have been introduced to denote the
1404 *measured* average strong-phases, which are expected to differ from (c_i, s_i) at $O(\epsilon)$,
1405 since neutral kaon CP violation is not taken into account in the measurements
1406 by CLEO. Thus, any corrections arising if (\hat{c}_i, \hat{s}_i) and (c_i, s_i) are substituted in
1407 Eq. (4.33) will appear in the $O(r_B\epsilon)$ terms.

1408 Two observations can be made from the expression in (4.33). The first is that
1409 the phase-space *distribution* is only changed at $O(r\epsilon)$ compared to the expression in

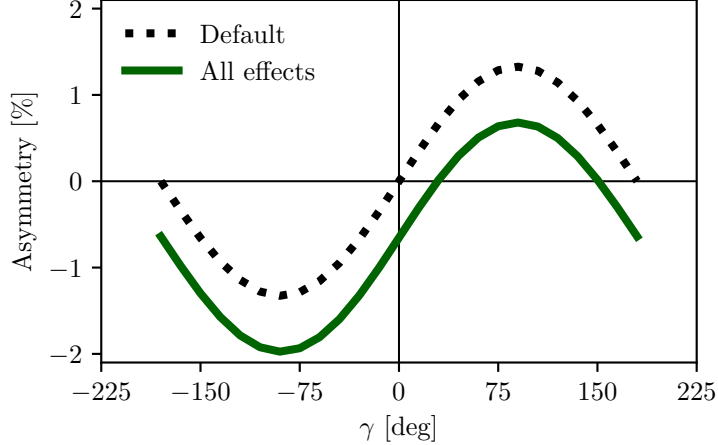


Figure 4.1: The asymmetry A_{total} as a function of γ calculated to $O(\epsilon)$ using Eq. (4.37). The calculation is made using for (black dotted line) the default case where $\Delta h = 0$ and (green) including neutral kaon CP -violation and material interaction with $r_\chi = \epsilon$.

Eq. (2.25), if the measured \hat{K}_i are used in the experimental analysis. This equally true whether the K_i are fitted in the signal channel along with x_\pm and y_\pm , as is the case in the measurement presented in the thesis, or if they are obtained in a control channel with flavour tagged D decays, according to Eq. (4.36). As the $D^0 - \bar{D}^0$ interference term that provides sensitivity to γ enters at order $O(r_B)$, the impact on γ measurements can be expected to be $\Delta\gamma/\gamma \sim O(r\epsilon/r_B)$. For $B \rightarrow DK$ analyses, where $r_B \simeq 0.1$, this is at the permille level, so the induced $\Delta\gamma$ bias can be expected to be smaller than 1° . Even in the case of $B^\pm \rightarrow D\pi^\pm$ decays, this suggests biases that are maximally a few percent. This is the main result of the chapter, because it means that the effect of neutral kaon CP violation and material interaction is small compared to the precision of the measurement that is the main subject of the thesis.

The second observation relates to potential future measurements of γ , which may also include sensitivity from the total, phase-space-integrated yield asymmetry

$$A_{\text{total}} = \frac{N^- - N^+}{N^- + N^+} = \frac{2(2\mathcal{F}_+ - 1)r_B \sin \delta_B \sin \gamma + \Delta h}{1 + r_B^2 + 2(2\mathcal{F}_+ - 1)r_B \cos \delta_B \cos \gamma} + O(r\epsilon), \quad (4.37)$$

where the definition of \mathcal{F}_+ from Section 2.3.5 has been employed. In the limit $r_B \rightarrow 0$ the expression agrees with the result for the analogous asymmetry in $D^\pm \rightarrow \pi^\pm K_S^0$ decays in Ref. [?], evaluated to $O(\epsilon)$ for an infinite and uniform time-acceptance. As hinted at above, the fact that $\mathcal{F}_+ \simeq 0.5$ means that the asymmetry due to γ being non-zero is not $\mathcal{O}(r_B)$, but of approximately the same order of magnitude as the asymmetry due to CP violation in the neutral kaon sector, governed by Δh . This is illustrated in Fig. 4.1, where the expression in Eq. (4.37) is plotted in the default

case where $\Delta h = 0$, using the model in Ref. [?] to calculate K_i and c_i , as well as including neutral kaon CP violation and material interaction effects, calculated using $r_\chi = \epsilon$, with ϵ taking the value in Eq. (4.12). The asymmetry changes significantly when including the latter effects. Therefore, measurements based only on the global asymmetry will suffer relative biases of tens of degrees, not a few degrees, if neutral kaon CP violation and material interaction is not taken into account.

4.3 Impact on BPGBSZ measurements of γ : LHCb and Belle II measurements

The previous section has established that the bias due to neutral kaon CP violation and material interaction is at the sub-percent level for measurements based on $B^\pm \rightarrow DK^\pm$ decays, and just a few percent in $B^\pm \rightarrow D\pi^\pm$ decays. Thus, the effects only contribute a manageable systematic uncertainty in the measurement that is the subject of the thesis. However, the expected precision on γ measurements will increase significantly in the coming decade, as both the LHCb [?] and Belle II [?] collaborations expect to make BPGBSZ measurements that measure γ with a precision of 1–3°. Therefore a deeper understanding of the expected bias for these specific experiments is important.

This section details a study, where the equations of the previous section are evaluated numerically to all orders, and care is taken to realistically model the experiment specific conditions. The scope of the original analysis, published in Ref. [?], was a stand-alone paper that covers both LHCb and Belle II, and which therefore does not rely on full detector simulation. Instead the following approaches are taken to model the necessary input

- the experimental time-acceptance is modelled based on the detector geometry and typical neutral kaon momentum spectrum
- the material interaction is included, using the material budget information available in the technical design reports on each experiment
- both the time-acceptance and material interaction depends on the neutral kaon momentum, for which realistic distributions are estimated using the `RapidSim` simulation package [?].

Each input is described in detail in the following sections. The study has been repeated to assign a systematic uncertainty to the LHCb measurement in Chapter 5, with slight adjustments to match the exact fit setup and with the inputs above extracted from full LHCb simulation. This is described further in Section 4.3.7.

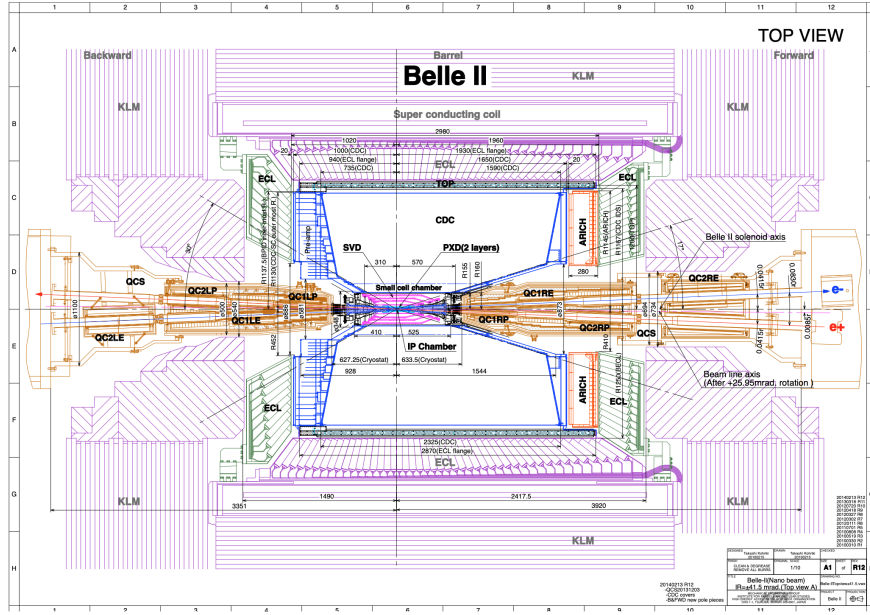


Figure 4.2: Schematic of the Belle II detector, reproduced from Ref. [?].

1464 4.3.1 Detector geometries

1465 The LHCb geometry and sub detectors are described in details in Chapter 3. In the
 1466 LHCb measurement discussed in Chapter 5, the K_S^0 mesons are reconstructed in
 1467 the $\pi^+\pi^-$ final state and two distinct categories of decay are considered, depending
 1468 on where in the detector the K_S^0 decay occurs. The categories have very different
 1469 decay-time acceptance, and therefore two scenarios are considered for LHCb: one
 1470 in which the decay products of the K_S^0 leave reconstructed tracks in both the silicon
 1471 vertex detector and downstream tracking detectors (denoted *long-long* or LL), and
 1472 one in which the decay products of the K_S^0 only leave tracks in the downstream
 1473 tracking detectors (denoted *down-down* or DD).

1474 The Belle II detector is a general purpose spectrometer, built to collect data from asymmetric e^+e^- collisions provided by the SuperKEKB accelerator in
 1475 Japan [?]. A schematic of the detector is shown in Fig. 4.2. The relevant sub
 1476 detectors for the present study are the tracking detectors: a central silicon vertex
 1477 detector, comprised of a total of six layers within 140 mm of the beam, and a large
 1478 volume drift chamber with 56 wire layers, extending to a radius of 1130 mm [?].
 1479 A single scenario is considered for Belle II, because essentially all the K_S^0 mesons
 1480 produced in signal decays in Belle II decay within the tracking volume, with more
 1481 than 90 % decaying in the vertex detector according to the studies described below.
 1482 Thus, three scenarios are considered in total: LL LHCb, DD LHCb, and Belle II.

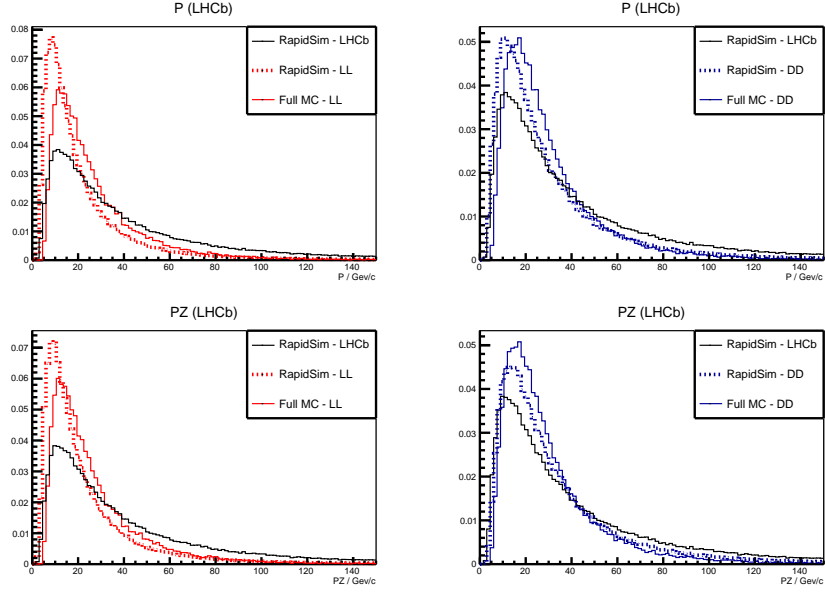


Figure 4.3: Momentum spectra for the K_S^0 meson in LHCb, as generated using **RapidSim** (black lines) directly, as well as reweighted to match decay time acceptance in the (red) LL and (blue) DD data categories of LHCb. The LHCb spectra are compared with the spectra in fully simulated signal decays, for both (dotted red lines) LL and (dotted blue lines) DD data categories.

1484 4.3.2 Kaon momentum distributions

1485 The neutral kaon momentum distributions are obtained using **RapidSim** [?], a simple
1486 tool to generate MC samples. **RapidSim** has an inbuilt capability to generate decays
1487 of B mesons with the kinematic distribution found in LHCb collisions and falling in
1488 the LHCb acceptance. However, the distributions need to be reweighted to take the
1489 kaon-decay-time acceptance into account. After being reweighted, the **RapidSim**
1490 momentum spectra are reasonably close to those found in full LHCb simulation
1491 samples of $B^\pm \rightarrow D(\rightarrow K_S^0\pi^+\pi^-)K^\pm$ decays, as seen in Fig. 4.3

1492 At Belle II, the signal B mesons stem from decays of $\Upsilon(4S)$ mesons produced in
1493 asymmetric electron-positron collisions. This leads to substantially different decay
1494 kinematics in comparison to those found at LHCb. The momentum distribution in
1495 Belle II is estimated by letting **RapidSim** decay B mesons with a momentum of 1.50
1496 GeV/ c along the z -axis using **RapidSim**, corresponding to the $\gamma\beta = 0.28$ boost of
1497 the centre-of-mass system in Belle II when operated at the $\Upsilon(4S)$ resonance [?]. A
1498 perfect 4π angular acceptance is assumed. It is not necessary to reweigh the Belle II
1499 momentum spectrum to account for the kaon-decay-time acceptance because all
1500 produced K_S^0 mesons decay in the tracking volume.

1501 The resulting momentum distributions for the three types of sample are shown in
1502 Fig. 4.4.

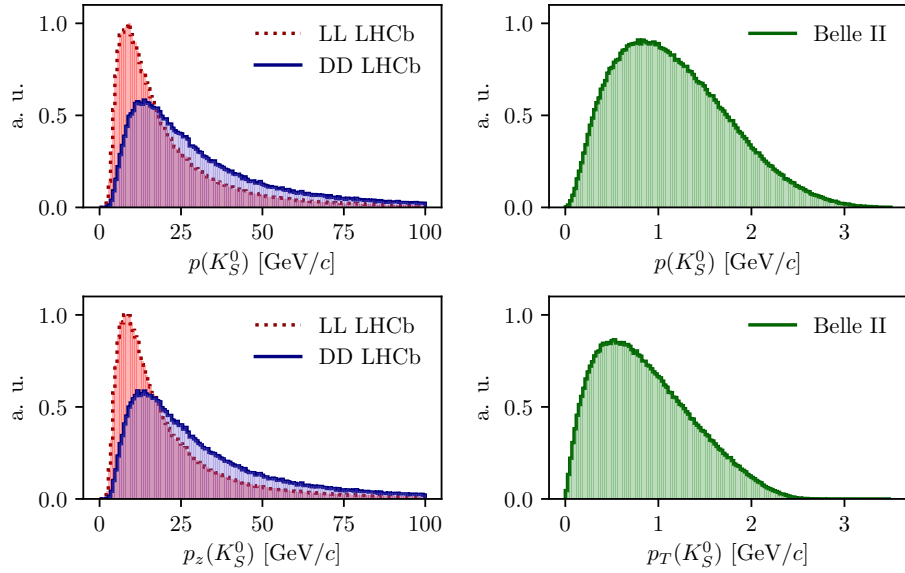


Figure 4.4: Momentum distributions for the LHCb (red dotted line) LL and (blue) DD categories, as well as (green) Belle II, obtained using `RapidSim`.

4.3.3 Experimental time acceptance

In order to model the experimental time acceptance, the time-dependent decay rates are only integrated over a finite time interval (τ_1, τ_2) . The intervals are defined for each of the three experimental categories, by requiring that a neutral kaon, if produced at $x = y = z = 0$ with momentum $p = (p_T, p_z)$, decays within the relevant part of the corresponding detector. For the LL LHCb category, it is required that the kaon decays before reaching $z_{max} = 280$ mm, corresponding to a decay where the decay products traverse at least 3 VELO segments (ignoring a number of widely spaced VELO segments placed at a distance of up to $z = 750$ mm from the interaction point) [?]. For the DD LHCb category a decay at $z \in [280, 2350]$ mm is required, corresponding to decay between the LL cut-off and the first downstream tracking station [?]. The time acceptance has a significant impact for the LHCb categories, where some 20 % of the kaons escape the tracking stations completely before decaying.

For Belle II, it is assumed that the K_S^0 reconstruction is similar to the Belle K_S^0 reconstruction, which is based on a neural network and reconstructs K_S^0 decays for which the decay product leave tracks in both the drift chamber and silicon vertex detectors, as well as decays that leave tracks in the drift chamber only [?, ?]. Therefore, the K_S^0 decay is required to be within $r_{max} = 1130$ mm of the beam axis, corresponding to a decay within the outer radius of the drift-chamber. In practice,

1523 most of the kaons decay inside the silicon vertex detector, and requiring a decay
1524 before 1130 mm is essentially equivalent to having no time cut-off.

1525 4.3.4 Detector material budget

1526 The effect of the material interaction is governed by parameter $\Delta\chi$ of Eq. (4.16). The
1527 parameter varies along a given kaon path, as the kaon intersects detector components
1528 made of different materials. In these studies, the calculations are simplified by
1529 using a single average material parameter for each experimental scenario. The
1530 average material parameters can be estimated for a given experimental scenario
1531 by considering the type and length of material traversed by a kaon in the relevant
1532 sub-detector(s). The average value is estimated, by exploiting that $\Delta\chi$ is related to
1533 the forward scattering amplitude f (\bar{f}) of K^0 (\bar{K}^0) mesons in a given material [?, ?]

$$\Delta\chi = -\frac{2\pi\mathcal{N}}{m_K}(f - \bar{f}) = -\frac{2\pi(N_A\rho/A)}{m_K}(f - \bar{f}), \quad (4.38)$$

1534 where $\mathcal{N} = N_A\rho/A$ is the scattering centre density of the material, m_K is the mass
1535 of the kaon state, A and ρ are the nucleon number and density of the material,
1536 and N_A is Avogadro's number. Measurements made for a range of nuclei [?] show
1537 that in the momentum range $p_K \in [20, 140] \text{ GeV}/c$

$$\left| \frac{f - \bar{f}}{p_K} \right| = 2.23 \frac{A^{0.758}}{p_K^{0.614}(\text{GeV}/c)} \text{ mb}, \quad \arg[f - \bar{f}] = -\frac{\pi}{2}(2 - 0.614), \quad (4.39)$$

1538 where the phase of Δf is determined via a phase-power relation [?]. In the numerical
1539 studies presented here, Eq. (4.39) is also used for the low momentum neutral kaons
1540 in the Belle II calculations, as a more detailed modelling of the low momentum $\Delta\chi$
1541 based on Ref. [?] is found to yield very similar results. The scattering centre density
1542 \mathcal{N} is approximated as being constant, equal to the average density along a neutral
1543 kaon path due to its intersection with different detector segments. This average
1544 is estimated using the simplifying assumption that the total detector material
1545 budget is due to silicon. In practice, $\mathcal{N} = N_A\rho/A$ is calculated using $A = 28$ and
1546 $\rho = f^{\text{Si}}\rho^{\text{Si}}$, where $f^{\text{Si}} < 1$ is the average fraction of a neutral kaon path length that
1547 is inside detector material, estimated via the known dimensions of the detector, the
1548 average nuclear interaction length seen by a track traversing it cf. the technical
1549 design reports [?, ?], and the nuclear interaction length of silicon $\lambda_I^{\text{Si}} = 465.2 \text{ mm}$ [?].
1550 The average value of $r_\chi = \frac{1}{2}\frac{\Delta\chi}{\Delta\lambda}$, which governs the size of the matter regeneration
1551 effect, can be calculated for the three considered experimental scenarios and satisfy
1552 $|r_\chi^{\text{LL}}| = 2.7 \times 10^{-3}$, $|r_\chi^{\text{DD}}| = 2.2 \times 10^{-3}$, and $|r_\chi^{\text{Belle II}}| = 1.0 \times 10^{-3}$.

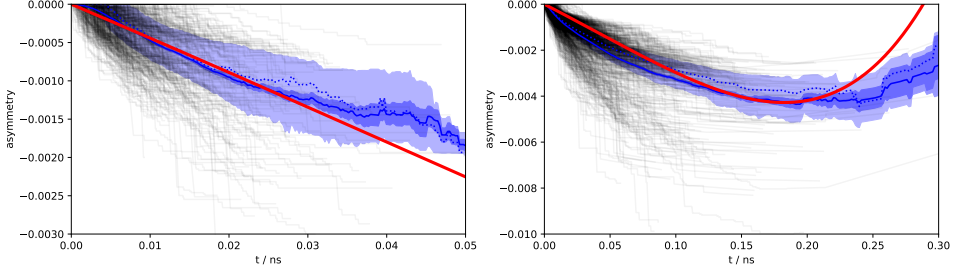


Figure 4.5: The asymmetry in Eq. (4.40) as a function of time for (left) LL and (right) DD K_S^0 tracks in a simulated LHCb sample. The black lines show individual tracks. The light blue area is the central 50 % quantile, the dark blue area is the 1σ uncertainty band on the mean. The red lines are calculated using the average $\Delta\chi$ values that are also used in the calculation of biases in BPGGSZ measurements.

1553 The neutral kaon tracks in LHCb generally pass through somewhere between
 1554 zero (for a significant amount of the LL tracks) and a hundred (for some DD tracks)
 1555 distinct detector segments. Therefore it is worth examining the degree to which
 1556 using a single average $\Delta\chi$ value, obtained following the procedure outlined above,
 1557 provides a reasonable description of the average material interaction. This can be
 1558 done using full LHCb simulation, where the kaon state for a simulated track can be
 1559 evaluated at all times, by applying Eq. (4.15) iteratively for each detector segment
 1560 the track traverses, using a $\Delta\chi$ value appropriate for that segment. This is done
 1561 in Fig. 4.5 for a simple observable: the yield asymmetry

$$A_{K^0} = \frac{|\psi_K^0(t)|^2 - |\psi_{\bar{K}^0}(t)|^2}{|\psi_K^0(t)|^2 + |\psi_{\bar{K}^0}(t)|^2}, \quad (4.40)$$

1562 where $\psi_K^0(t)$ ($\psi_{\bar{K}^0}(t)$) is the amplitude for an initial K^0 (\bar{K}^0) to decay to two pions at
 1563 time t . In this calculation, it is assumed that $\epsilon = 0$ to isolate the material effect with
 1564 no asymmetry contribution from the inherent CP -violation in the neutral kaon sector.
 1565 While the track-by-track asymmetries are found to differ significantly depending on
 1566 the exact detector segments a track intersects, the average asymmetry is seen to
 1567 evolve smoothly as a function of decay time, and in reasonable agreement with the
 1568 asymmetry value that is calculated using the average $\Delta\chi$ values estimated above.

1569 The LHCb detector is undergoing a significant upgrade prior to the start of
 1570 the LHC Run 3. However, the material budget and geometry of the relevant
 1571 sub-detectors will be similar to the sub-detectors used during Run 1 and 2 [?, ?].
 1572 Hence the results of this study will be valid for measurements during the upgrade
 1573 phases of LHCb, even though the detector parameters presented in this section
 1574 relate to the original LHCb detector.

¹⁵⁷⁵ **4.3.5 Calculation procedure**

¹⁵⁷⁶ The main idea in the bias study is to calculate the BPGBSZ bin yields including
¹⁵⁷⁷ the full effect of neutral kaon CP violation and material, fit them using the default
¹⁵⁷⁸ equations of Chapter 2, and obtain the bias $\Delta\gamma = \gamma - \gamma^0$ due to the kaon effects not
¹⁵⁷⁹ being considered in the parameter extraction. For the purpose of Ref. [?], a simple
¹⁵⁸⁰ fit setup of a single $B^\pm \rightarrow Dh^\pm$ mode is investigated, where the K_i parameters are
¹⁵⁸¹ determined in a control channel with the relevant experimental acceptance. This
¹⁵⁸² setup is modified in the study used to assign a systematic uncertainty on the LHCb
¹⁵⁸³ measurement of Chapter 5, as described in Section 4.3.7 below.

¹⁵⁸⁴ In practice, the amplitude model for $D^0 \rightarrow K_S^0 \pi^+ \pi^-$ decays in Ref. [?] is taken
¹⁵⁸⁵ to represent the $A_1(s_{+-})$ amplitude. Then $A_2(s_{+-})$ is obtained as described in
¹⁵⁸⁶ Section 4.2.2. In terms of A_1 and A_2 , the amplitudes $A_{S(L)}^{(\bar{D})}(s_{+-})$ can be expressed
¹⁵⁸⁷ and related via Eqs. (4.25) and (4.26), and the full signal decay amplitudes as a
¹⁵⁸⁸ function of phase-space coordinates, time, and the material interaction parameter
¹⁵⁸⁹ $\Delta\chi$ can be calculated for a given set of input parameters $(\gamma^0, r_B^0, \delta_B^0)$. The squared
¹⁵⁹⁰ decay amplitudes are then integrated over phase space and the kaon decay times
¹⁵⁹¹ to obtain the binned signal yield.

¹⁵⁹² The signal yields depend on the momentum via the time-acceptance parameters
¹⁵⁹³ τ_1 and τ_2 , and because the material interaction parameter $\Delta\chi$ is momentum
¹⁵⁹⁴ dependent. Therefore, the yields are averaged over the K_S^0 momentum distributions
¹⁵⁹⁵ of LHCb and Belle II.

¹⁵⁹⁶ The parameters x_\pm and y_\pm are determined by a maximum likelihood fit to the
¹⁵⁹⁷ calculated yields, after which the fit result and covariance matrix are interpreted in
¹⁵⁹⁸ terms of the physics parameters (γ, r_B, δ_B) using another maximum likelihood
¹⁵⁹⁹ fit [?]. In the fits, the K_i are obtained using the definition $K_i = K_i^{\text{meas}} =$
¹⁶⁰⁰ $(N_i^D + N_{-i}^{\bar{D}})/(\sum_j N_j^D + N_{-j}^{\bar{D}})$, in terms of the expected yields N_i^D ($N_i^{\bar{D}}$) of a flavour-
¹⁶⁰¹ tagged D^0 (\bar{D}^0) decays in bin i of the D decay phase space, calculated as described
¹⁶⁰² above for $r_B^0 = 0$. This corresponds to experimentally measuring the K_i in a control
¹⁶⁰³ channel, and takes the effect of neutral kaon CP violation and material interaction
¹⁶⁰⁴ on K_i measurements into account, as well the experimental time acceptance. The
¹⁶⁰⁵ (c_i, s_i) are calculated using $A_1(s_{+-})$ and the experimental time acceptance is taken
¹⁶⁰⁶ into account in this calculation as well.

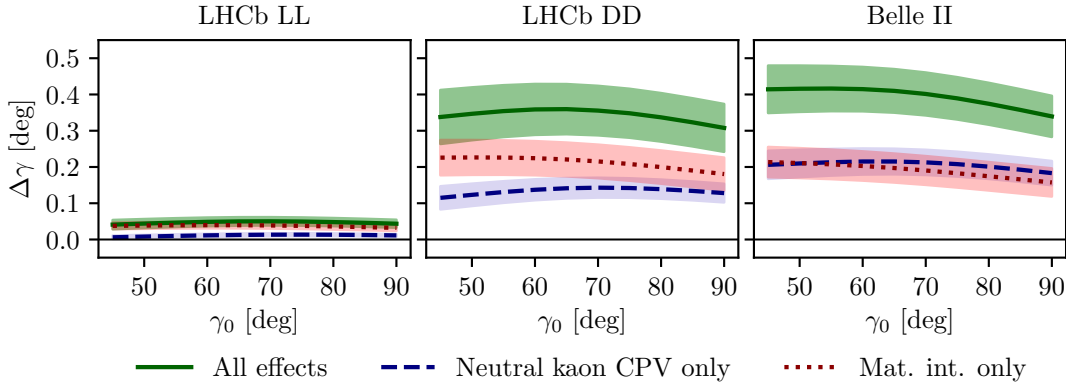


Figure 4.6: The bias $\Delta\gamma$ as a function of input γ_0 for (left) the LL LHCb category, (centre) the DD LHCb category, and (right) Belle II. The bias is calculated due to (blue, dashed line) neutral kaon CP violation alone, (red, dotted line) material interaction alone, and (green line) both effects. The shaded region shows the estimated 1σ uncertainty band.

4.3.6 Results

The obtained bias $\Delta\gamma$ is shown as a function of input γ^0 for the various experimental conditions in Fig. 4.6. The calculations are made using $(r_B^0, \delta_B^0) = (0.1, 130^\circ)$, approximately equal to the physics parameters relevant for $B^\pm \rightarrow DK^\pm$ decays [?, ?]. The bias does not vary significantly with γ^0 in the plotted range, which includes the world average value of direct γ measurements as well as the values obtained in full unitarity-triangle fits [?, ?, ?], and for all cases, the bias is found to be below 0.5° , corresponding to relative biases of about half a percent. Thus the biases are of $O(r\epsilon/r_B)$ as expected, given the arguments of Section 4.2.3. The contributions from the individual K_S^0 CPV and material interaction effects are also shown. It is seen that the neutral kaon CP violation and material interaction effects leads to approximately equal biases in all three cases.

Given the decay-time acceptance and momentum distribution for each experimental category, the mean life time, $\langle\tau\rangle$, of the reconstructed kaons can be calculated. In terms of the K_S^0 lifetime $\tau_{K_S^0} = (0.895 \pm 0.004) \times 10^{-11}$ s [?], $\langle\tau_{LL}\rangle \simeq 0.1\tau_{K_S^0}$ for the LHCb LL category, $\langle\tau_{DD}\rangle \simeq 0.8\tau_{K_S^0}$ for the LHCb DD category, and at Belle II $\langle\tau_{Belle\,II}\rangle \simeq \tau_{K_S^0}$. The difference in average kaon lifetime is reflected in the observed biases, which are found to be larger in the samples with longer lived kaons. The very small effect in the LL category is to be expected because the CP -violation effect due to K_S^0 not being CP -even is approximately cancelled by the CP -violation effect arising from $K_S^0 - K_L^0$ interference for kaons with decay times much smaller than $\tau_{K_S^0}$ [?].

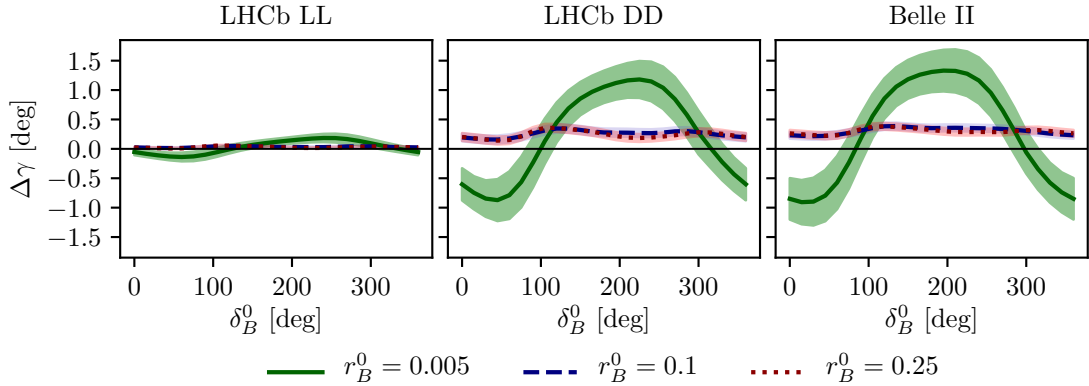


Figure 4.7: The bias $\Delta\gamma$ as a function of input δ_B for (left) the LL LHCb category, (centre) the DD LHCb category, and (right) Belle II. The bias is calculated for $\gamma = 75^\circ$ and (green line) $r_B = 0.005$, (blue, dashed line) $r_B = 0.1$, and (red, dotted line) $r_B = 0.25$. The shaded region shows the estimated 1σ uncertainty band.

1629 The uncertainty bands in Fig. 4.6 are calculated by repeating the study while
1630 varying some of the inputs. The model dependence of the predicted biases is
1631 probed by repeating the study using two other amplitude models as input for
1632 $A_1(s_{+-})$ and $A_2(s_{+-})$: the model published in Ref. [?] and the model included in
1633 EVTGEN [?]. hen defining $A_2(s_{+-})$ in terms of $A_1(s_{+-})$, there is an uncertainty
1634 due to the unknown (r_k, δ_k) parameters used to describe the $\pi\pi$ resonance terms.
1635 This uncertainty is assessed by making the study with several different random
1636 realisations of the parameter set. The studies are repeated while varying the time
1637 acceptances and material densities with $\pm 10\%$. There is an additional uncertainty
1638 due to the use of simulation samples generated with `RapidSim` to describe the kaon
1639 momentum distribution, in lieu of full detector simulations.

1640 There is also an uncertainty from the use of (c_i, s_i) as calculated using $A_1(s_{+-})$.
1641 It is to be expected that the measured values (\hat{c}_i, \hat{s}_i) from the CLEO collaboration
1642 differ by those calculated using $A_1^D(s_-, s_+)$ by terms of $O(\epsilon)$ due to neutral kaon
1643 CP violation, which is not taken into account in the measurement [?]. These
1644 corrections can be calculated via a procedure analogous to the one used to estimate
1645 the corrections on measurements of γ in this paper. However, as these corrections
1646 are much smaller than the experimental uncertainties in the measurement, they
1647 have not been studied further.

1648 For the purpose of this thesis, it is important to consider the bias in measurements
1649 that use $B^\pm \rightarrow D\pi^\pm$ decays as well, and other B decay modes can also be used in
1650 BPFGSZ measurements, such as $B^\pm \rightarrow D^*K^\pm$, $B^\pm \rightarrow DK^{*\pm}$, and $B^0 \rightarrow DK^{*0}$.
1651 For the purpose of the study presented here, the main difference between the decay

channels is that they have different values of r_B and δ_B . Figure 4.7 shows $\Delta\gamma$ as a function of input δ_B^0 , for $\gamma^0 = 75^\circ$ and three different values of r_B^0 . Aside from $r_B^0 = 0.1$, the results are shown for $r_B^0 = 0.005$, which corresponds to the expectation in $B^\pm \rightarrow D\pi^\pm$ decays [?] and $r_B^0 = 0.25$, which corresponds to $B^0 \rightarrow DK^{*0}$ decays [?]. The most notable feature is that the biases are significantly larger in the $B^\pm \rightarrow D\pi^\pm$ case. This is expected: the r_B^0 dependent behaviour is governed by the relative importance of different $O(r\epsilon)$ correction terms to the phase-space distribution. There are terms of both $O(r_A\epsilon)$ and $O(r_B\epsilon)^3$, which lead to expected biases of size $O(r_A\epsilon/r_B)$ and $O(r_B\epsilon/r_B) = O(\epsilon)$, respectively, cf. the discussion of Section 4.2.3. In the $B^\pm \rightarrow D\pi^\pm$ case, the $O(r_A\epsilon)$ correction terms dominate because $r_A/r_B \simeq (0.05/0.005) = 10$. This explains the relatively large bias, as $|r_A\epsilon/r_B^{D\pi}| \simeq 4\%$. The bias is seen to be up to $\pm 1.5^\circ$, but only about $+0.2^\circ$ with the expected value of $\delta_B^{D\pi} \simeq 300^\circ$ [?, ?]. These biases are *much smaller* than the precision on γ that is obtainable in a $B^\pm \rightarrow D\pi^\pm$ analysis with current experimental yields, and do thus not pose a problem. In the $r_B^0 = 0.1$ and $r_B^0 = 0.25$ cases the $O(r_B\epsilon)$ correction terms dominate, and the biases are of $O(\epsilon)$, independent of the r_B^0 value. Therefore both cases have biases of similar size.

Further, it is clear that the biases depend on δ_B^0 and that the oscillation period of the δ_B dependence is different between the $r_B^0 = 0.005$ case and the $r_B^0 \in \{0.1, 0.25\}$ cases. It is to be expected that $\Delta\gamma$ oscillates as a function of δ_B^0 , because δ_B^0 enters the yield equations via $\cos(\delta_B^0 \pm \gamma)$ and $\sin(\delta_B^0 \pm \gamma)$ terms. As explained above, the $O(r_A\epsilon)$ terms dominate the $B^\pm \rightarrow D\pi^\pm$ bias, and these are independent of δ_B^0 . The $O(r_B\epsilon)$ terms, however, are important for the bias corrections for larger r_B values, and the terms include factors of $\cos(\delta_B^0 \pm \gamma)$ and $\sin(\delta_B^0 \pm \gamma)$. This explains the different bias dependence on δ_B^0 .

While the input value of $\gamma^0 = 75^\circ$ was chosen for these studies, there is minimal variation in the results if another value of γ^0 in the range $[60^\circ, 85^\circ]$ is used.

4.3.7 Coupled $B^\pm \rightarrow DK^\pm$ and $B^\pm \rightarrow D\pi^\pm$ measurements

The studies presented above have been extended on two accounts in order to assign a systematic uncertainty to the LHCb measurement presented in Chapter 5. Firstly, full LHCb simulation has been used to obtain the momentum distributions, as well as to fit a better description of the time acceptance and the reconstruction efficiency profile over the D -decay phase space. Secondly, the fit setup is modified

³There are similar terms of $O(r_A r_\chi)$ and $O(r_B r_\chi)$, but as ϵ and r_χ are of the same order of magnitude, these terms can be treated completely analogously to the $O(r_A\epsilon)$ and $O(r_B\epsilon)$ terms, and have been left out of the discussion for brevity.

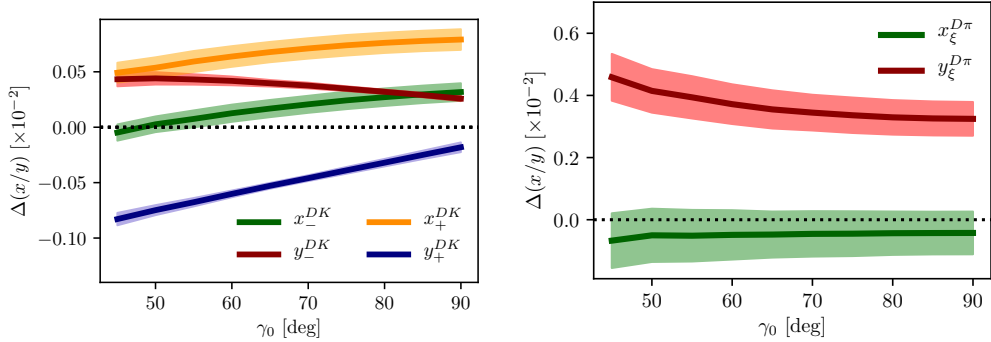


Figure 4.8: The bias on (left) the $B^\pm \rightarrow DK^\pm$ and (right) $B^\pm \rightarrow D\pi^\pm$ CP -violation observables in the LHCb DD category, evaluated in bias studies with inputs based on full LHCb simulation, calculated as a function of input γ_0 .

to correspond to the experimental approach described in Section 2.4 and Chapter 5: the signal yields are calculated for both the $B^\pm \rightarrow DK^\pm$ and $B^\pm \rightarrow D\pi^\pm$ channels, and fitted in a combined fit to obtain $(x_{\pm}^{DK}, y_{\pm}^{DK}, x_\xi^{D\pi}, y_\xi^{D\pi})$, where the F_i parameters are allowed to float in the fit. The biases obtained for each observable are shown in Fig. 4.8, evaluated using the time-acceptance, momentum distribution, and material budget relevant for the DD category (since the effect in the LL category is much smaller). As will be clear in Chapter 5, these biases are all significantly smaller than the corresponding statistical uncertainties. Thus, the effects of neutral kaon CP violation and material interactions contribute a manageable systematic uncertainty in current BPGGSZ measurements, even if the $B^\pm \rightarrow D\pi^\pm$ channel is promoted to a signal channel.

As the statistical uncertainty becomes comparable with the bias effects described in this chapter, the systematic uncertainty should be assigned by a more accurate study, incorporating the traversed material on a track-by-track basis in full detector simulation. Such a detailed calculations can also be used to apply a bias correction if desired.

4.4 Concluding remarks

The analysis presented in this chapter has shown the expected impact of neutral kaon CP violation and material interaction on current BPGGSZ measurements to be small compared to the statistical uncertainties; first by simple order-of-magnitude estimates and then by a detailed calculation of the expected effect in LHCb and Belle II.

While the calculations were made for the case of $D \rightarrow K_S^0 \pi^+ \pi^-$ decays, the BPGGSZ approach can of course also be applied in other D -decay final states,

such as $D \rightarrow K_S^0 K^+ K^-$ and $D \rightarrow K_S^0 \pi^+ \pi^- \pi^0$. The biases on measurements of γ based the D decay phase-space distributions should be of similar size in these decay channels. The impact on γ measurements based on the phase-space-integrated yield asymmetry can be expected to be tens of degrees for the $D \rightarrow K_S^0 K^+ K^-$ channel, where the yield asymmetry is expected to be around 2 %, for the reasons explained in Section 4.2.3. The $D \rightarrow K_S^0 \pi^+ \pi^- \pi^0$ decay, however, is dominantly CP -odd [?], and the bias in measurements based on the total asymmetry is therefore expected to be $O(\epsilon/r_B)$, ie. a few degrees [?]. More precise calculations of the biases would require a repeat of the study included here, with relevant amplitude models and binning schemes in place.

The chapter focuses on the model-independent, binned approach that is the subject of the thesis. However, the underlying mechanism that determines the scale of the bias, namely that the phase-space *distribution* of signal decays is unaffected at $\mathcal{O}(\epsilon)$ and $\mathcal{O}(r_\chi)$, is independent on the exact measurement approach. Therefore it is expected that amplitude-model-based measurements and measurements made with new unbinned methods such as those in Ref [?] will be similarly biased if kaon CP violation and regeneration are not accounted for.

5

1726

1727

1728

A BPGBGSZ measurement of γ with $B^\pm \rightarrow Dh^\pm$ decays

1729 This chapter describes a model-independent BPGBGSZ measurement of γ with
1730 $B^\pm \rightarrow DK^\pm$ and $B^\pm \rightarrow D\pi^\pm$ decays where $D \rightarrow K_S^0\pi^+\pi^-$ and $D \rightarrow K_S^0K^+K^-$,
1731 commonly denoted $B^\pm \rightarrow D(\rightarrow K_S^0h^+h^-)h'^\pm$ decays. The measurement is made
1732 with the full LHCb data set collected during Run 1 and 2 of the LHC, corresponding
1733 to an integrated luminosity of about 9 fb^{-1} . The analysis is under review for
1734 publication in the Journal of High Energy Physics at the time of writing [?]
1735 (one can hope).

1736 5.1 Candidate reconstruction and selection

1737 The $B^\pm \rightarrow D(\rightarrow K_S^0h^+h^-)h'^\pm$ candidates are constructed during the offline *stripping*
1738 stage described in Section 3.3.3. The candidates are defined by first combining
1739 tracks to form a $K_S^0 \rightarrow \pi^+\pi^-$ vertex, then a $D \rightarrow K_S^0h^+h^-$ vertex, and finally
1740 the $B^\pm \rightarrow Dh'^\pm$ candidate. Each final state track is required to satisfy certain
1741 momentum thresholds and track-quality requirements, and to be separated from all
1742 primary interaction vertices. Each decay vertex is required to satisfy a fit-quality
1743 threshold and to be separated from the primary vertex. Momentum thresholds
1744 are applied to the composite particles and they are required to have reconstructed
1745 invariant masses close to their known masses¹ except that the B candidate is
1746 required to have a reconstructed invariant mass in the interval $4750\text{--}7000\text{ MeV}/c^2$.

¹The exact mass window depends on the particle type and reconstruction category; narrower mass windows are applied at a later stage, as described below.

1747 The B candidate is required to satisfy $\chi^2_{\text{IP}} < 25$, where χ^2_{IP} is the difference in χ^2
1748 value of the primary vertex fit, when the vertex is formed with- and without the B
1749 candidate. As the final *stripping* stage, a multivariate algorithm is applied to the
1750 formed B candidate to reduce the amount of random track combinations, denoted
1751 combinatorial background, even further than the aforementioned requirements.

1752 Two data categories are defined, depending the tracks used to form the K_S^0
1753 candidate: the LL category where both pions are long tracks, and DD category where
1754 both pions are downstream tracks, using the track classifications of Section 3.2.1.

1755 Each candidate is re-analysed with the `DecayTreeFitter` (DTF) frame work [?],
1756 where a simultaneous fit of the full decay chain is made with a number of constraints
1757 applied: the momenta of the composite D and K_S^0 particles are required to form
1758 invariant masses exactly equal to the known particle masses [?], and the momentum
1759 of the B candidate is required to point in the direction defined by the B decay
1760 vertex and the primary vertex. This refit results in improved resolution of the
1761 invariant masses of the composite particles and, very importantly, of the Dalitz
1762 coordinates in the D -decay phase space. It also ensures that all candidates fall in the
1763 kinematically allowed region of the D -decay phase space. Unless otherwise specified,
1764 all results in this chapter are based on the refitted track momenta; for reasons
1765 explained below, some studies have to be based on parameters that are obtained
1766 without the constraints described above, or with only a subset of them applied.

1767 Following the stripping stage, the further selection of signal candidates is
1768 performed in three steps: an initial set of requirements to remove candidates
1769 that are very likely to be background and vetoes a number of specific backgrounds,
1770 the application of a multivariate analysis algorithm designed to reject combinatorial
1771 background decays, and finally a set of particle-identification requirements. The
1772 requirements are summarised in Table 5.1, and each step is described in detail
1773 in the following sections.

1774 5.1.1 Initial requirements

1775 At the hardware trigger level, it is required that a particle associated with the
1776 signal decay triggered the hadronic L0 trigger (classifying the event as *Trigger*
1777 *on Signal*, or TOS), or that the L0 decision was caused by a particle that is not
1778 associated with the signal decay (*Trigger Independent of Signal*, or TIS). The
1779 inclusion of the latter category increases the data sample about 50 %. At the
1780 software trigger level, a particle belonging to the signal decay is required to have
1781 caused one of each of the inclusive HLT1 and HLT2 lines to accept the events.
1782 Specifically, the Run 1 events are required to be TOS on the `HLT1TrackAllL0` and

Table 5.1: Summary of requirements applied to data. The base requirements are applied to all data samples before training or applying the BDT.

Base requirements		
Variable	Cut	Comment
Bachelor momentum, p	$< 100 \text{ GeV}/c$	
Bachelor has RICH	<i>true</i>	
K^\pm in D decay: momentum, p	$< 100 \text{ GeV}/c$	In $D \rightarrow K_S^0 K^+ K^-$
K^\pm in D decay: have RICH	<i>true</i>	In $D \rightarrow K_S^0 K^+ K^-$
DecayTreeFit converged	<i>true</i>	
D mass	$m_{D^0} \in m_{D^0}^{PDG} \pm 25 \text{ MeV}/c^2$	From DTF with constrained K_S^0 mass
K_S^0 mass	$m_{K_S^0} \in m_{K_S^0}^{PDG} \pm 15 \text{ MeV}/c^2$	From DTF with constrained D^0 mass

Background suppressing requirements		
Variable	Cut	Comment
K_S^0 flight distance χ^2	> 49	for LL only
$\Delta z_{\text{significance}}^{DB}$	> 0.5	for all candidates

PID requirements		
Channel	Cut	Comment
$B^\pm \rightarrow DK^\pm$	PIDK > 4	for bachelor
$B^\pm \rightarrow D\pi^\pm$	PIDK < 4	for bachelor
$B^\pm \rightarrow Dh^\pm$	IsMuon = 0	for bachelor
$B^\pm \rightarrow D(\rightarrow K_S^0 \pi^+ \pi^-)h^\pm$	PIDe < 0 & IsMuon = 0	for charged D decay products
$B^\pm \rightarrow D(\rightarrow K_S^0 K^+ K^-)h^\pm$	PIDK > -5 & IsMuon = 0	for charged D decay products

BDT requirements		
Channel	Cut	Comment
Run 1, DD	> 0.6	
Others	> 0.8	

1783 Hlt2Topo{2, 3, 4}BodyBBDT lines and the Run 2 events are required to be TOS on
1784 the Hlt1{Track, TwoTrack}MVA and Hlt2Topo{2, 3, 4}Body lines. These trigger
1785 lines were described in Section 3.3.

1786 Before any processing of the data, a loose preselection is applied to remove
1787 obvious background candidates. The reconstructed D (K_S^0) mass is required to
1788 be within 25 (15) MeV/c^2 of the known values [?]. The *companion* particle, the
1789 pion or kaon produced in the $B^\pm \rightarrow Dh^\pm$ decay, is required to have associated
1790 RICH information and a momentum less than $100 \text{ GeV}/c$; this ensures good particle-
1791 identification performance. Finally, all of the DTF fits of the full decay chain
1792 are required to have converged properly.

1793 Two additional requirements are made at this stage in order to suppress specific
1794 backgrounds. In order to suppress decays of the type $B^\pm \rightarrow K_S^0 h^+ h^- h'^\pm$ with
1795 no intermediate D meson, so called *charmless* decays, it is required that the
1796 significance of the z -separation of the D^0 decay vertex and the B^\pm decay vertex
1797 is above 0.5. The significance of the z -separation of the D^0 decay vertex and

1798 the B^\pm decay vertex is defined as

$$\Delta z_{\text{significance}}^{D-B} = \frac{z_{vtx}^D - z_{vtx}^B}{\sqrt{\sigma^2(z_{vtx}^D) + \sigma^2(z_{vtx}^B)}}. \quad (5.1)$$

1799 This source of background described further in section 5.3.1. In order to suppress
1800 a background from $D \rightarrow 4\pi$ and $D \rightarrow \pi\pi KK$ decays, it is required that the K_S^0
1801 flight distance χ_{FD}^2 is greater than 49, where

$$\chi_{\text{FD}}^2 = \left(\frac{\Delta r}{\sigma(\Delta r)} \right)^2, \quad (5.2)$$

1802 and Δr is the measured flight distance of the K_S^0 meson. This background is
1803 described in further detail in section 5.3.2.

1804 5.1.2 Boosted decision tree

1805 A Gradient Boosted Decision Tree [?] (abbreviated BDT in the following) is
1806 applied to classify each candidate on a scale from -1 to $+1$ as signal-like ($+1$)
1807 or combinatorial-background-like (-1), based on the values of a number of input
1808 parameters for a candidate in question. The BDT is implemented in the TMVA
1809 frame work [?].

1810 A boosted decision tree classifier consists of a number of sequentially trained
1811 decision trees, each of which classify events as either signal or background. Each tree
1812 bases the decision on an individual subset of variables, out of an overall set of input
1813 variables. At each training step, the input events are weighted when training a new
1814 tree, so that events that the already-trained trees classify incorrectly are given a
1815 higher weight; this is denoted boosting. The term *gradient boosting* denotes a specific
1816 weight calculation scheme [?]. The final score is the average over all decision trees.

1817 The full set of input variables are given in Table 5.2. It includes the momenta
1818 of particles in the decay; a number of geometric parameters such a absolute and
1819 relative vertex positions, and distances of closest approach between tracks; χ_{IP}^2
1820 values for a number of particles in the decay chain; the χ^2 per degree of freedom
1821 of the DTF refit; DIRA values, which denote the angle between the fitted particle
1822 momenta and the vector spanned by it's production ad decay vertices; and finally
1823 an isolation variable, defined as

$$A_{p_T} = \frac{p_T(B) - \sum p_T(\text{other})}{p_T(B) + \sum p_T(\text{other})} \quad (5.3)$$

1824 where the sum is over all other tracks in a cone around the B -candidate. The cone
1825 is defined as being within a circle with a radius of 1.5 units around the B candidate

1826 in the (η, ϕ_{azim}) -plane. This variable is highly efficient in rejecting combinatorial
1827 background. Two algorithms are trained, one for the LL category of K_S^0 mesons and
1828 one for the DD category, because some input parameters relate to the K_S^0 meson
1829 and have very different distributions between the two categories.

Table 5.2: Input parameter set used in BDT trained to separate signal and combinatorial background, sorted according to importance in the LL classifier.

Variable name	Importance LL/DD (Rank in DD)	Description
$\log(1-K_s_{DIRA_BPV})$	7.2 % / 3.5 % (16)	$\log \cos \theta_{DIRA}$ for K_S^0
$\log(B_u_{RHO_BPV})$	5.7 % / 5.5 % (5)	Radial distance of B vertex to beam line
$\log(Bach_PT)$	5.2 % / 6.9 % (1)	p_T of the bachelor particle
$\log(1-D_0_{DIRA_BPV})$	4.9 % / 5.8 % (4)	$\log \cos \theta_{DIRA}$ for D
$\log(1-B_u_{DIRA_BPV})$	4.9 % / 6.4 % (3)	$\log \cos \theta_{DIRA}$ for B^\pm
$\log(D_0_{RHO_BPV})$	4.8 % / 5.3 % (6)	Radial distance of D vertex to beam line
$Bu_PTASY_1.5$	4.7 % / 4.9 % (7)	Asymmetry parameters of B^\pm
$\log(D_0_PT)$	4.7 % / 6.6 % (2)	p_T of the D meson
$\log(Bu_constDOKSPV_CHI2NDOF)$	4.2 % / 4.5 % (9)	$\chi^2/d.o.f$ of kinematical refit with DecayTreeFitter
$\log(Bu_FDCHI2_OWNPV)$	3.9 % / 4.1 % (11)	Flight distance χ^2 of the B^\pm
$\log(\max_K s_{h1h2_IPCHI2_OWNPV})$	3.9 % / 3.0 % (20)	Largest χ^2_{IP} of the K_S^0 decay products
$\log(D_0_IPCHI2_OWNPV)$	3.8 % / 3.3 % (17)	χ^2_{IP} of the D
$\log(\min_K s_{h1h2_IPCHI2_OWNPV})$	3.7 % / 0.9 % (26)	Smallest χ^2_{IP} of the K_S^0 decay products
$\log(Bu_P)$	3.7 % / 3.9 % (12)	p of the B^\pm meson
$\log(Bu_IPCHI2_OWNPV)$	3.6 % / 4.6 % (8)	χ^2_{IP} of the B^\pm
$Bu_MAXDOCA$	3.6 % / 3.3 % (18)	"Distance of closest approach" for B^\pm vertex
$\log(Bach_IPCHI2_OWNPV)$	3.3 % / 4.3 % (10)	χ^2_{IP} of the bachelor particle
$\log(Bu_PT)$	3.3 % / 3.7 % (14)	p_T of the B^\pm meson
$\log(\max_h s_{h1h2_IPCHI2_OWNPV})$	3.1 % / 3.8 % (13)	Largest χ^2_{IP} of the D decay products
$\log(\min_h s_{h1h2_IPCHI2_OWNPV})$	3.0 % / 3.4 % (19)	Smallest χ^2_{IP} of the D decay products
$\log(Ks_VTXCHI2DOF)$	2.9 % / 2.3 % (21)	χ^2 of vertex fit for K_S^0
$D_0_MAXDOCA$	2.9 % / 1.0 % (25)	"Distance of closest approach" for D vertex
$\log(D_0_VTXCHI2DOF)$	2.7 % / 1.6 % (24)	χ^2 of vertex fit for D
$\log(D_0_P)$	2.7 % / 1.8 % (22)	p of the D meson
$\log(Bach_P)$	2.2 % / 3.6 % (15)	p of the bachelor particle
$\log(Bu_VTXCHI2DOF)$	1.8 % / 1.7 % (23)	χ^2 of vertex fit for B^\pm

The BDTs are trained and tested with input samples representing typical signal and background decay candidates: a signal sample that consists of simulated $B^\pm \rightarrow D(\rightarrow K_S^0\pi^+\pi^-)\pi^\pm$ decays corresponding to the LHCb running conditions for the years 2012–2018, and a sample of combinatorial background candidates from real data, where the reconstructed invariant mass of the B meson is larger than 5800 MeV/ c^2 . The candidates in both samples were required to have passed the initial requirements described in the preceding section. The input-parameter distributions in the signal and background training samples are shown in Figs. 5.1 and 5.2. The signal and background samples are each split into two before the training stage: one sub sample, the training sample, is used to train the BDT, after which the trained algorithm is applied to the other sub sample, the test sample. The classifier is found to perform well on the test sample, not just the training sample, which ensures that it does not suffer significant overtraining. The BDT output distribution are shown for both test and training samples in Fig. 5.3, where it is clear that the classifier very effectively separates signal and background candidates.

Each candidate in data is classified using the BDT, and candidates that are assigned a score below some threshold value are discarded. The threshold values are chosen in a set of pseudo experiments, such that the expected sensitivity to γ is maximised. This is done by performing preliminary fits to the data set for a range of different BDT threshold values, then generating many pseudo data sets with the obtained yields, and applying the full fit and interpretation procedure described in Sections 5.4–5.7 to each data set. Thus, the expected uncertainty on γ is obtained for a range of threshold values. The procedure is applied independently for the LL and DD categories, as well as for the Run 1 and Run 2 data sets, because some parameter distributions differ slightly between the two runs. The optimal threshold values are found to be 0.8 in all situations, except for LL candidates in Run 1 where it is 0.6. This is illustrated in Fig. 5.4 where the results of the threshold scans are shown. The same classifier is applied to both $B^\pm \rightarrow D\pi^\pm$ and $B^\pm \rightarrow DK^\pm$ candidates, and both D final state categories. While the classifiers were trained using samples of $B^\pm \rightarrow D(\rightarrow K_S^0\pi^+\pi^-)\pi^\pm$ simulation and data, the decays are similar enough that no significant improvement in performance was obtained when considering a more elaborate setup. Across all categories, the requirement on the BDT output is found to remove approximately 98 % of the combinatorial background, while being approximately 93 % efficient on signal.

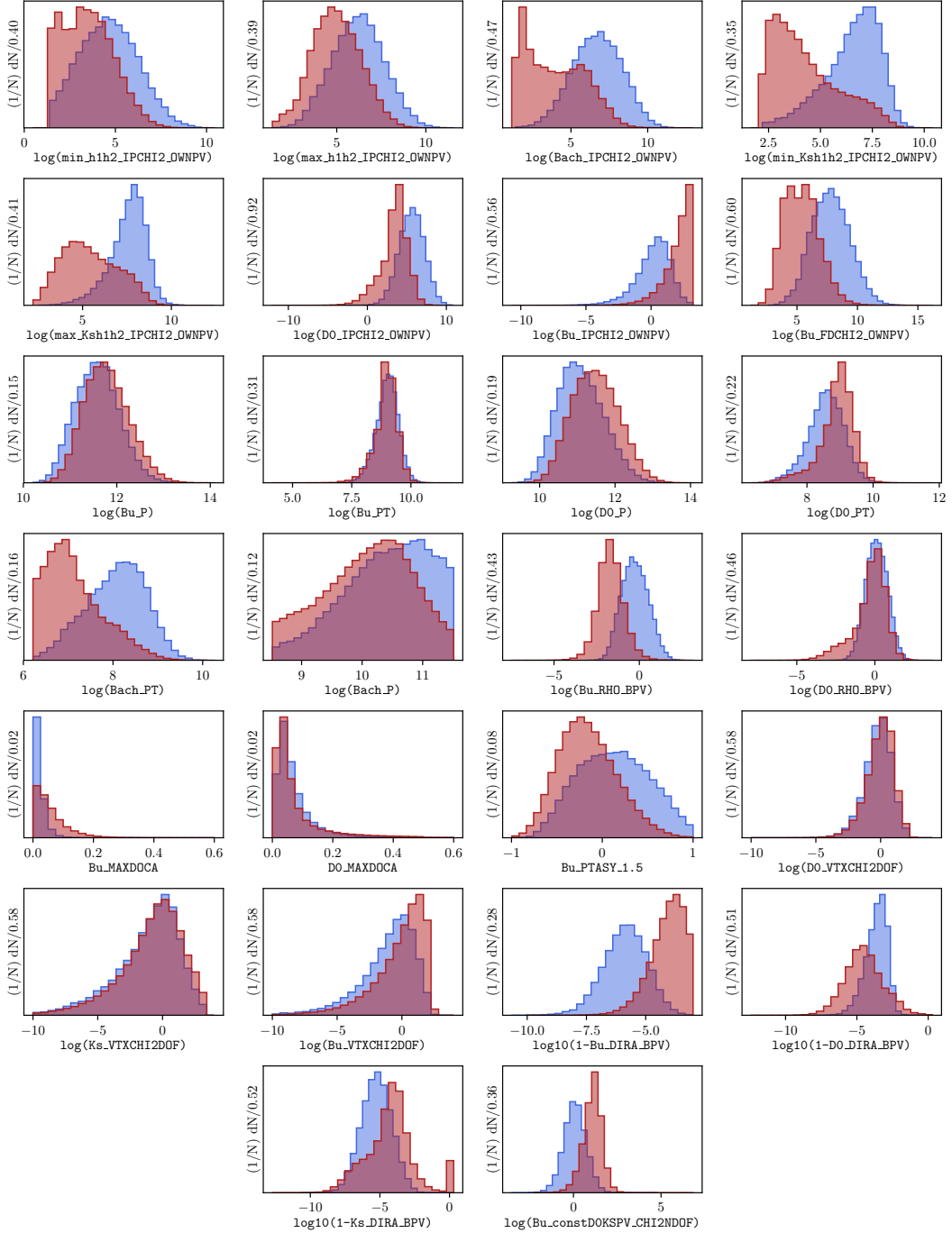


Figure 5.1: Distribution of input parameters in the LL training samples of (blue) signal decays from simulation and (red) background decays from the upper B sideband. The variable names are defined in Table 5.2.

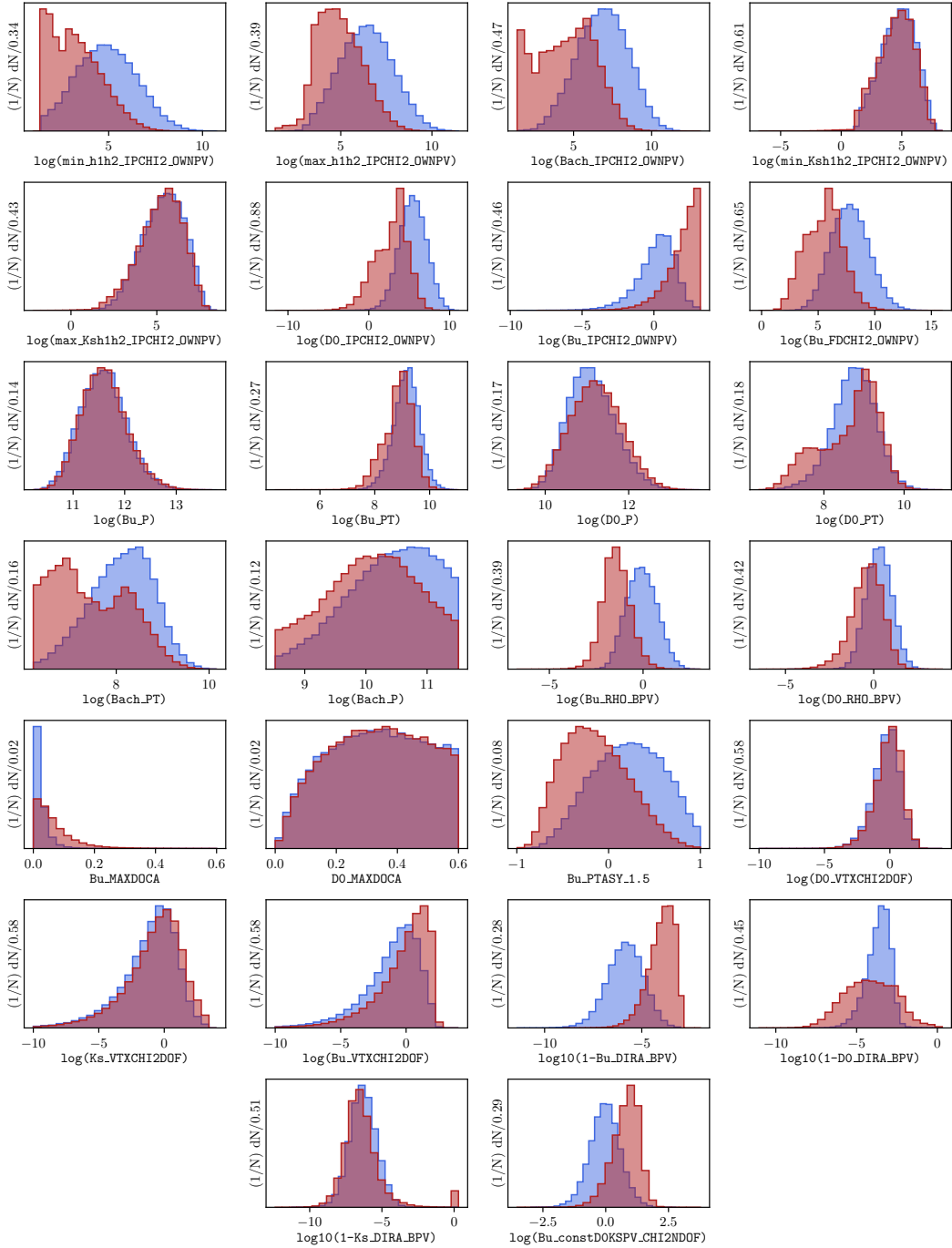


Figure 5.2: Distribution of input parameters in the DD training samples of (blue) signal decays from simulation and (red) background decays from the upper B sideband. The variable names are defined in Table 5.2.

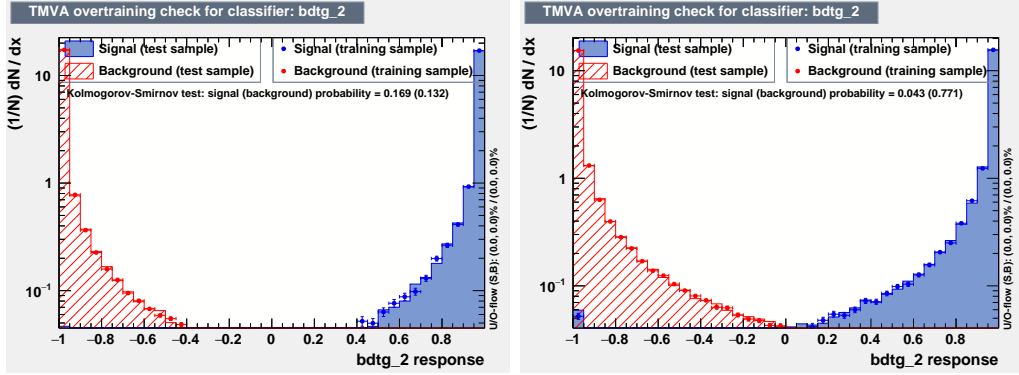


Figure 5.3: Distribution of BDT variable on test and training samples for (left) the LL and (right) the DD category, with logarithmic y -scale.

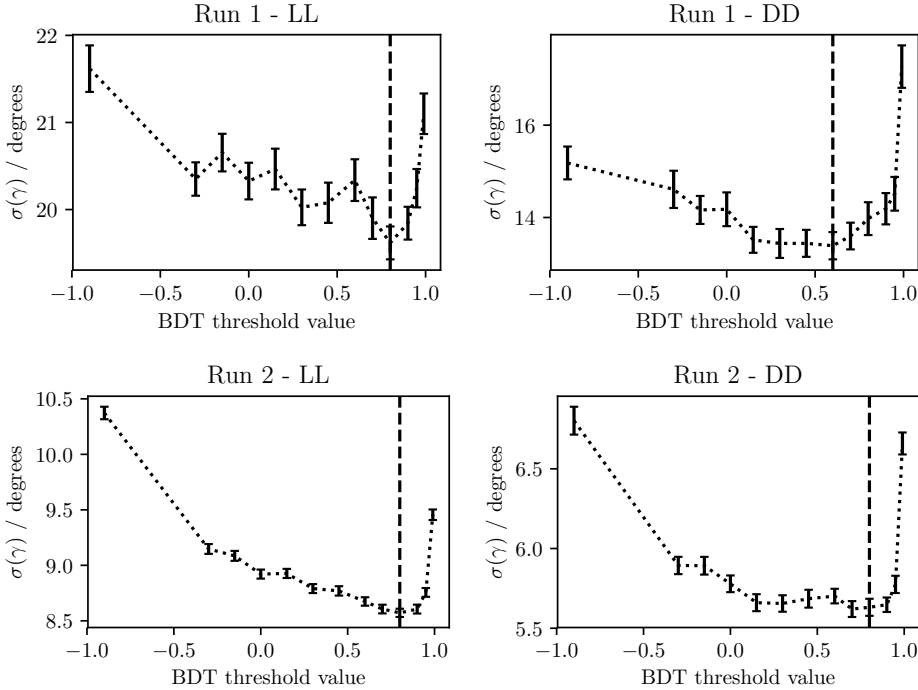


Figure 5.4: The mean uncertainty on γ in toy studies, performed with the signal and background yields corresponding to a given BDT requirement, using (top) the Run 1 and (bottom) Run 2 datasets, using only candidates in (left) the LL category and (right) the DD category. The dashed line shows the threshold value employed to discard background-like candidates in the selection.

5.1.3 Particle-identification requirements

A PID requirement is made to separate $B^\pm \rightarrow DK^\pm$ and $B^\pm \rightarrow D\pi^\pm$ candidates in the data sample, by requiring that the PIDK of the companion particle satisfies PIDK < 4 for $B^\pm \rightarrow D\pi^\pm$ candidates and PIDK > 4 for $B^\pm \rightarrow DK^\pm$ candidates. The PIDK variable was defined in Section 3.1.3. This ensures that any given candidates is selected into only one of these samples.

1870 Further to the requirement on the companion, PID requirements are made to
 1871 suppress semi-leptonic backgrounds as well as decays where a final state particle
 1872 decays in flight, and a loose PID requirement is made in the $D \rightarrow K_S^0 K^+ K^-$
 1873 channels where it leads to a higher signal purity:

- 1874 • the companion particle is required to satisfy `IsMuon` = 0.
- 1875 • For the $B \rightarrow D(\rightarrow K_S^0 \pi^+ \pi^-) h^\pm$ samples it is require that the charged pion
 1876 track from the D decay with opposite charge to the companion satisfies
 1877 $\text{PIDe} < 0 \& \text{IsMuon} = 0$, and for the other charged pion that `IsMuon` = 0. A
 1878 very loose requirement of $\text{PIDK} < 20$ is applied to both pions from the D -decay
 1879 in the stripping stage.
- 1880 • For the $B \rightarrow D(\rightarrow K_S^0 K^+ K^-) h^\pm$ samples it is required that the charged kaon
 1881 tracks from the D decay have RICH information, a momentum less than 100
 1882 GeV/c and $\text{PIDK} > -5 \& \text{IsMuon} = 0$.

1883 These backgrounds are described in Section 5.3.3.

1884 5.1.4 Final requirements

1885 For a small fraction of candidates in the final sample, it is the case that two
 1886 or more candidates originate in the same pp collision. In order to make sure
 1887 that all candidates are completely independent, a single, arbitrary candidate from
 1888 each pp collision is kept for these collisions, and the other candidates discarded.
 1889 This requirements results in the removal of less than 0.7% of candidates in
 1890 each data category.

1891 Furthermore, the D mass used to define the binning schemes described in Ref. [?]
 1892 differs slightly from the mass used in the DTF refit. Therefore a few of the decays are
 1893 reconstructed with Dalitz coordinates outside the allowed kinematic region. Because
 1894 this problem only concerns a handful of candidates, they are simply discarded.

1895 5.1.5 Selected candidates

1896 In total, about 47,000 $B^\pm \rightarrow DK^\pm$ candidates and 400,000 $B^\pm \rightarrow D\pi^\pm$ candidates
 1897 are selected, as summarised in Table 5.3. An example of the B mass distribution in
 1898 one of the data categories is shown in Fig. 5.5; it is clear that a significant number
 1899 of these candidates are background decays. The Dalitz plots for candidates in the
 1900 signal region where $m_B \in [5249, 5309] \text{ MeV}/c^2$ are shown in Fig. 5.6 and 5.7. Due to
 1901 the large yields in the full Run 1 and 2 LHCb data set, the asymmetries between
 1902 the B^+ and B^- distributions are visible to the eye in the $B^\pm \rightarrow DK^\pm$ plots.

Table 5.3: Final candidate yield in each data category after the full selection has been applied, including removing candidates outside the region $m_B \in [5080, 5800] \text{ MeV}/c^2$.

B Decay	D final state	K_S^0 type	Run 1	Run 2	Total
$B^\pm \rightarrow DK^\pm$	$K_S^0\pi^+\pi^-$	LL	2275	10525	12800
		DD	5097	23508	28605
	$K_S^0K^+K^-$	LL	383	1610	1993
		DD	772	3397	4169
$B^\pm \rightarrow D\pi^\pm$	$K_S^0\pi^+\pi^-$	LL	18209	90509	108718
		DD	40167	205807	245974
	$K_S^0K^+K^-$	LL	2879	13757	16636
		DD	6033	29790	35823

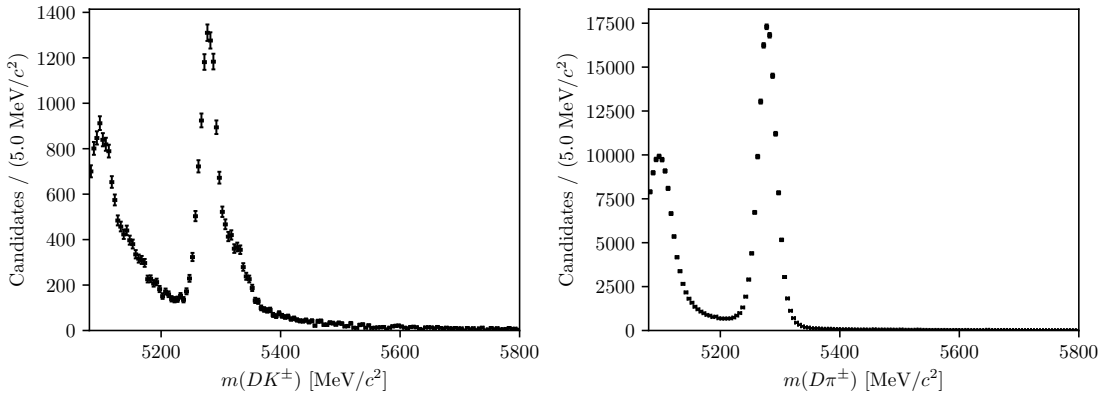


Figure 5.5: The spectrum of m_B in the (left) $B^\pm \rightarrow DK^\pm$ and (right) $B^\pm \rightarrow D\pi^\pm$ samples where $D \rightarrow K_S^0\pi^+\pi^-$ and the K_S^0 meson is reconstructed in the DD category, after the full selection has been applied.

1903 5.2 Signal selection efficiencies

1904 The efficiency of each step of the selection on signal decays can be investigated
 1905 using simulated decays. In the $B^\pm \rightarrow D\pi^\pm$ channel, only decays that were placed
 1906 in the "test" sample when training the BDT are used, in order to avoid over-
 1907 estimating the efficiency.

1908 In general, the total selection efficiency up until the PID requirements, including
 1909 the offline stage and the effect of the geometrical LHCb acceptance, is about 1
 1910 permille, slightly higher for $B^\pm \rightarrow DK^\pm$ than $B^\pm \rightarrow D\pi^\pm$ decays, slightly higher
 1911 for $D \rightarrow K_S^0K^+K^-$ than $D \rightarrow K_S^0\pi^+\pi^-$ decays, and somewhat higher in the Run 2
 1912 than in Run 1 due to improvements in the trigger. The PID requirements are
 1913 investigated separately in Section 5.2.1 below, using samples of calibration data.
 1914 The overall selection efficiency does not impact the measurement at all, because
 1915 the observables of interest are sensitive *only* to the distribution of decays over the

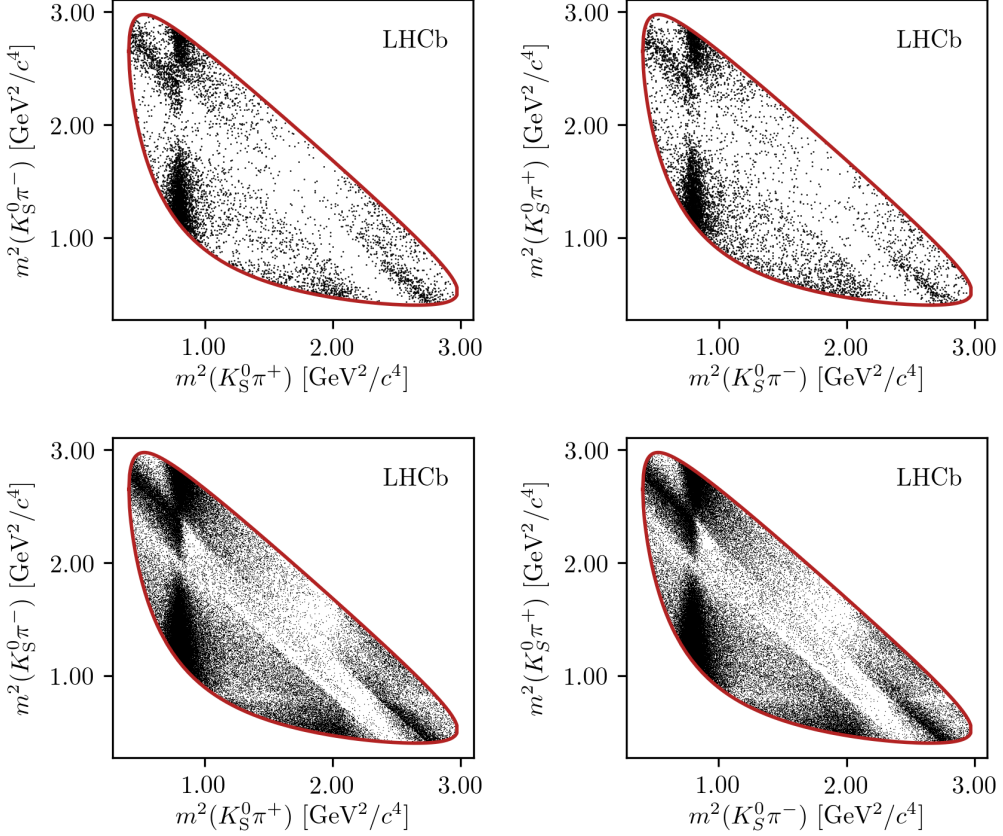


Figure 5.6: Dalitz plots of (left) $B^+ \rightarrow Dh^+$ and (right) $B^- \rightarrow Dh^-$ candidates in the signal region, in the (top) $B^\pm \rightarrow DK^\pm$ and (bottom) $B^\pm \rightarrow D\pi^\pm$ channels where $D \rightarrow K_S^0 \pi^+ \pi^-$. The LL and DD categories have been combined.

1916 Dalitz plot (except, of course, in the sense that a higher signal efficiency is desirable
 1917 because it leads to larger signal yields). Likewise, it makes no difference that the
 1918 overall selection efficiencies differ slightly between $B^\pm \rightarrow DK^\pm$ and $B^\pm \rightarrow D\pi^\pm$
 1919 decays, as long as the efficiency profile over the Dalitz plot is identical between the
 1920 two decay channels. This is confirmed separately in Section 5.2.2 below.

1921 The efficiencies of each individual selection step are shown in Fig. 5.8, obtained
 1922 using simulated $B^\pm \rightarrow D\pi^\pm$ decays. The main reason that some signal decays
 1923 do not survive the base requirement is the $p_{\text{companion}} < 100 \text{ GeV}/c$ requirement,
 1924 which is in place to ensure that the PID performance for the companion is good.
 1925 For decays with $p_{\text{companion}} > 100 \text{ GeV}/c$, only about 60 % of $B^\pm \rightarrow DK^\pm$ decays
 1926 survive the subsequent $\text{PIDK} > 4$ requirement and the cross-feed from misidentified
 1927 $B^\pm \rightarrow D\pi^\pm$ decays is 50 % larger than in the current selection. Thus, loosening
 1928 this requirement leads to little statistical gain, while leading to larger systematic
 1929 effects from the crossfeed background.

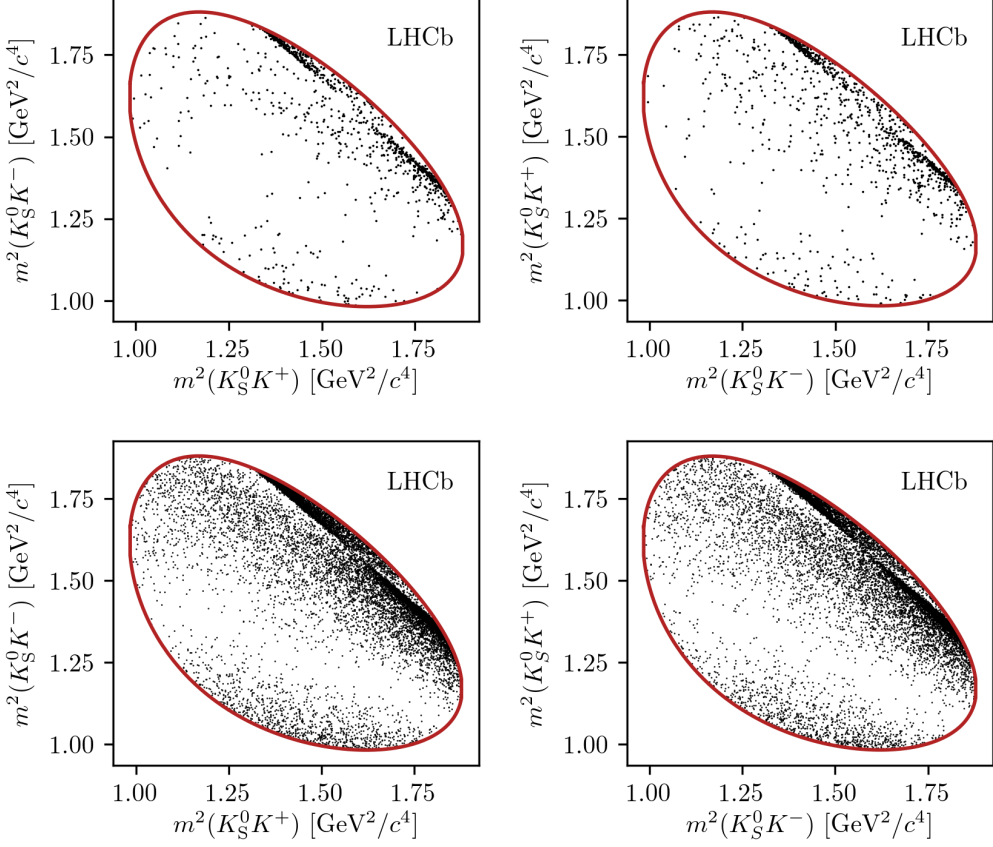


Figure 5.7: Dalitz plots of (left) $B^+ \rightarrow Dh^+$ and (right) $B^- \rightarrow Dh^-$ candidates in the signal region, in the (top) $B^\pm \rightarrow DK^\pm$ and (bottom) $B^\pm \rightarrow D\pi^\pm$ channels where $D \rightarrow K_S^0 K^\pm K^\mp$. The LL and DD categories have been combined.

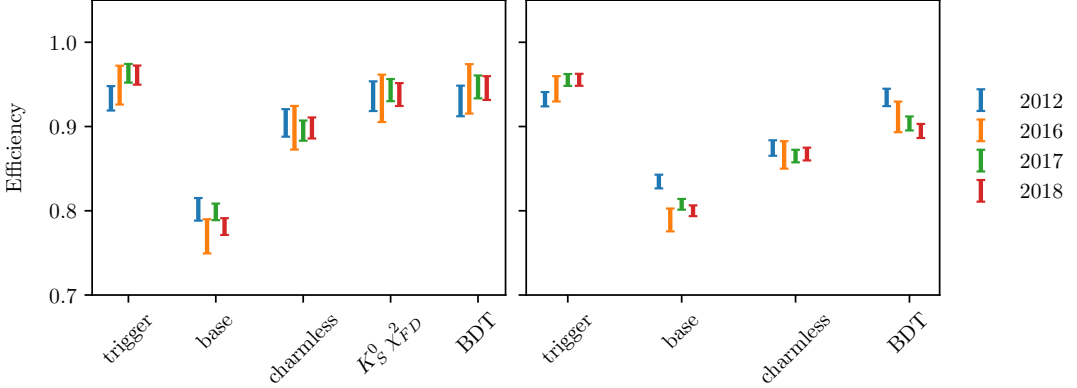


Figure 5.8: The efficiency of each selection step in samples of simulated $B^\pm \rightarrow D(\rightarrow K_S^0 \pi^+ \pi^-) \pi^\pm$ signal decays in the (left) LL and (right) DD categories. The selection steps are applied on top of each other, from left to right on the horizontal axis. The samples are split by year.

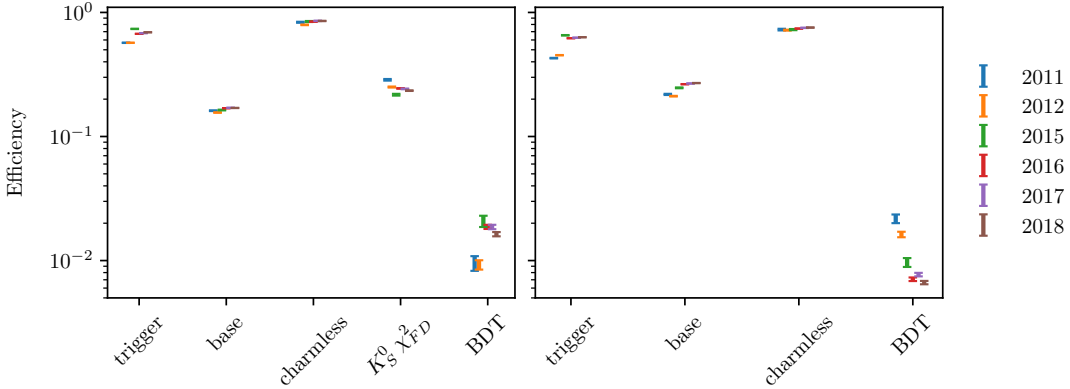


Figure 5.9: The efficiency of each selection step in samples of $B^\pm \rightarrow D(\rightarrow K_S^0 \pi^+ \pi^-) \pi^\pm$ candidates in data where the reconstructed B mass is above $5600 \text{ MeV}/c^2$, meaning the candidates stem from combinatorial background. The efficiency is shown for candidates in the (left) LL and (right) DD categories. The selection steps are applied on top of each other, from left to right on the horizontal axis. The samples are split by year. Notice the logarithmic scale on the vertical axis.

1930 An equivalent plot for the combinatorial background is shown in Fig. 5.9, using
 1931 $B^\pm \rightarrow D(\rightarrow K_S^0 \pi^+ \pi^-) \pi^\pm$ candidates in data with a reconstructed B mass above
 1932 $5600 \text{ MeV}/c^2$; it can be seen that the BDT is very efficient at rejecting combinatorial
 1933 background, but that the base requirements and the requirement on the K_S^0 flight
 1934 distance also remove a decent amount of background.

1935 5.2.1 Efficiency of the PID requirements

1936 The efficiencies of the PID requirements on the companion enter the yield parame-
 1937 terisations of the mass fits in Section 5.4 and 5.5 and must therefore be known.
 1938 They are determined using samples of calibration data selected without relying on
 1939 PID variables, as implemented in the `PIDCalib` frame work [?]. Reasonably pure
 1940 samples of pion and kaon tracks are obtained from $D^0 \rightarrow K^- \pi^+$ decays, where the
 1941 D meson originates in a $D^{*+} \rightarrow D^0 \pi^+$ decay and can therefore be flavour tagged.
 1942 The remaining background is subtracted via the *sPlot* [?] procedure, based on a
 1943 two-dimensional fit of the $m(K^- \pi^+)$ and $m(D^0 \pi^+) - m(D^0)$ distributions. The
 1944 obtained weights are employed to calculate the average efficiency of the requirement
 1945 on `PIDK` for a number of bins in the momentum and pseudorapidity of the calibration
 1946 tracks, and the number of charged tracks in the detector, thus constructing a three-
 1947 dimensional efficiency lookup table. The procedure is carried out for each PID
 1948 requirement, companion species, data-taking year, track charge, and magnet polarity.
 1949 Based on these tables, expected PID efficiencies for the $B^\pm \rightarrow D\pi^\pm$ and $B^\pm \rightarrow DK^\pm$
 1950 signal decays are calculated that take the kinematical distribution and detector

Table 5.4: PID efficiencies obtained with the `PIDCalib` tool. The uncertainty incorporates statistical uncertainty due to the size of the reference sample, the systematic uncertainty due to the choice of binning scheme in `PIDCalib`, and a systematic uncertainty due to the `sWeight` calculation in `PIDCalib` of 0.1 %.

Efficiency	Particle	D final state	$\varepsilon_{\text{PID}} (\%)$	
			LL	DD
Run I and II				
Correct ID	Kaon	$D \rightarrow K_S^0 \pi^+ \pi^-$	86.74 ± 0.13	86.90 ± 0.22
		$D \rightarrow K_S^0 K^+ K^-$	86.22 ± 0.26	86.56 ± 0.30
	Pion	$D \rightarrow K_S^0 \pi^+ \pi^-$	97.11 ± 0.11	97.17 ± 0.13
		$D \rightarrow K_S^0 K^+ K^-$	97.07 ± 0.11	97.16 ± 0.14

occupancy in the *BPGGSZ* data samples into account, by using the high-purity sample of $B^\pm \rightarrow D\pi^\pm$ candidates in the signal region as a reference. The dominating uncertainty on the efficiencies is statistical in nature, due to the finite size of the reference sample. In addition, systematic uncertainties are included due to the `sPlot` procedure, estimated at 0.1 % [?], and due to the choice of binning scheme, estimated by repeating the procedure using a number of alternative binning schemes. The final estimates of the correct-ID efficiencies, ε_{PID} , are shown in Table 5.4, including all sources of uncertainty. Note that the probability to misidentify a decay satisfies $\varepsilon_{\text{mis-ID}} = 1 - \varepsilon_{\text{PID}}$ by construction, due to the definition of the `PIDK` variable (given in Section 3.2.2) and the chosen PID requirement.

5.2.2 Efficiency profile over the Dalitz plot

The analysis strategy depends on sharing the F_i parameters between the $B \rightarrow D\pi$ and $B \rightarrow DK$ channels. This is reasonable, since the phase-space dependence of the reconstruction efficiency is expected to be very similar between the two decays, given the similar kinematics; an assumption that is verified using samples of simulated decays. The full selection is applied to the samples. The $B \rightarrow D\pi$ sample of LL (DD) candidates includes about 63,000 (146,000) simulated decays, and the $B \rightarrow DK$ samples include 60,000 (142,000) simulated decays. For the $B \rightarrow D\pi$ mode, this is approximately equal to the number of decays in the full Run 1+2 data sample, and for $B \rightarrow DK$ this is a factor of about 12 larger than the data sample. The decays were simulated with an equal decay probability across the D -decay phase space, so that any non-uniform distribution of reconstructed decays is completely determined by a phase-space dependent reconstruction and selection efficiency. Therefore the assumption that the phase-space dependence is identical between the $B \rightarrow D\pi$ and

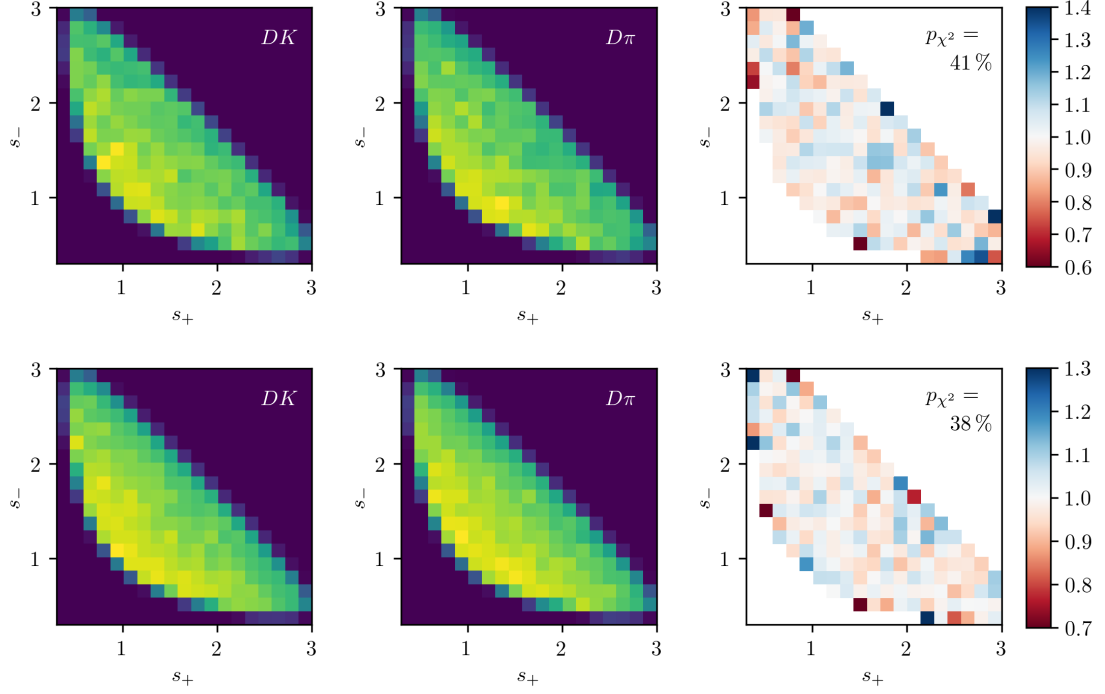


Figure 5.10: The (s_+, s_-) distribution in simulated samples of (left) $B \rightarrow DK$ decays and (center) $B \rightarrow D\pi$ decays where $D \rightarrow K_S^0 \pi^+ \pi^-$, as well as (right) the ratio between the two histograms (corrected for differences in sample sizes). The plots are shown for candidates in the (top) LL and (bottom) DD categories. The p values are the results of χ^2 compatibility tests between the two histograms.

1975 $B \rightarrow DK$ channels is verified by seeing if the Dalitz coordinates are distributed
 1976 differently between the samples of simulated $B \rightarrow D\pi$ and $B \rightarrow DK$ decays.

1977 This is investigated with two statistical tests. The first is a χ^2 comparison
 1978 of 2D histograms of the distribution of $m^2(K_S^0 h^+)$ and $m^2(K_S^0 h^-)$ in the different
 1979 $B \rightarrow D\pi$ and $B \rightarrow DK$ channels. These histograms, and the ratio between them,
 1980 are shown in Figs. 5.10 and 5.11, along with the p -values from the χ^2 tests. It can
 1981 be seen that, in all cases, the probability of obtaining the two histograms assuming
 1982 that they share the same underlying distribution has a reasonable value, and that
 1983 there is no clear trend in the ratio plots. The second test is a Kolmogorov-Smirnov
 1984 test [?] of the compatibility of the one-dimensional distributions of $m^2(K_S^0 h^+)$,
 1985 $m^2(K_S^0 h^-)$, and $m^2(h^+ h^-)$. These distributions, and the corresponding p -values,
 1986 are shown in Fig. 5.12 and 5.13. Again, all the p values are reasonable. Therefore,
 1987 it is concluded that there are no statistically significant differences between the
 1988 phase-space dependence of the reconstruction and selection efficiency between the
 1989 $B \rightarrow D\pi$ and $B \rightarrow DK$ channels, given the present sample sizes. Because the
 1990 simulation samples have approximately the same amount of decays as data (or
 1991 significantly more, in the $B \rightarrow DK$ case), any potential differences will be negligible

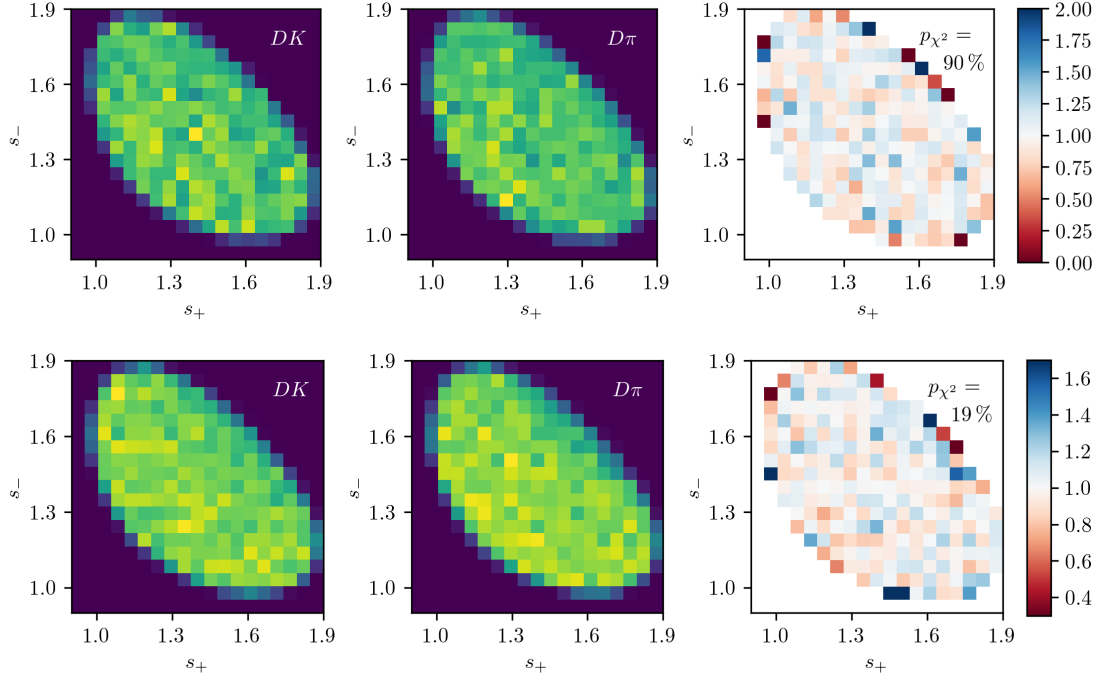


Figure 5.11: The (s_+, s_-) distribution in simulated samples of (left) $B \rightarrow DK$ decays and (center) $B \rightarrow D\pi$ decays where $D \rightarrow K_S^0 K^+ K^-$, as well as (right) the ratio between the two histograms (corrected for differences in sample sizes). The plots are shown for candidates in the (top) LL and (bottom) DD categories. The p values are the results of χ^2 compatibility tests between the two histograms.

with data yields. Thus, sharing the F_i parameters between the $B \rightarrow D\pi$ and $B \rightarrow DK$ channels is viable, and no efficiency correction is necessary.

5.3 Background studies

A wide range of backgrounds can potentially pollute the sample of signal candidates. The backgrounds group into three categories depending on how they are treated in the analysis:

- Backgrounds that can be effectively removed in the selection
 - Backgrounds that are only present at a level where the impact on the measurement result is small, and which do therefore not have to be modelled
 - Backgrounds that are present at a level where they have to be modelled in the fit to data, and cannot effectively be rejected further in the selection
- The latter category comprises of combinatorial background, which remains present at a non-negligible level after the application of the BDT described in Section 5.1.2;

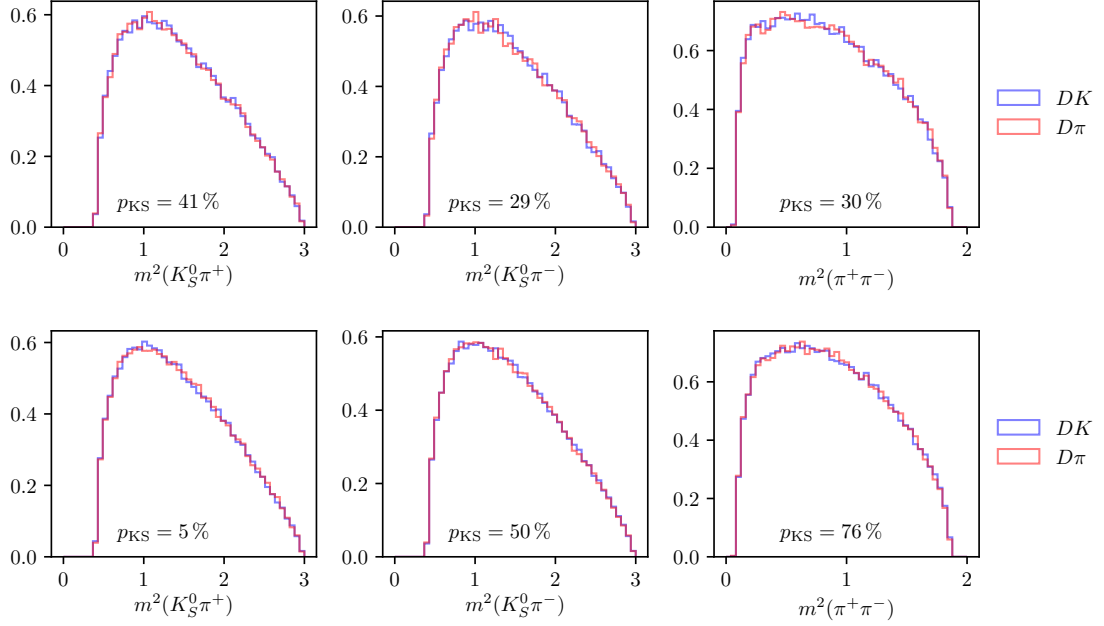


Figure 5.12: One-dimensional distributions of $m^2(K_S^0\pi^+)$, $m^2(K_S^0\pi^-)$, and $m^2(\pi^+\pi^-)$ in simulated (blue) $B^\pm \rightarrow DK^\pm$ and (red) $B^\pm \rightarrow D\pi^\pm$ decays where $D \rightarrow K_S^0\pi^+\pi^-$ in the (top) LL and (bottom) DD categories. The p values are the results of Kolmogorov-Smirnov compatibility tests between the distributions.

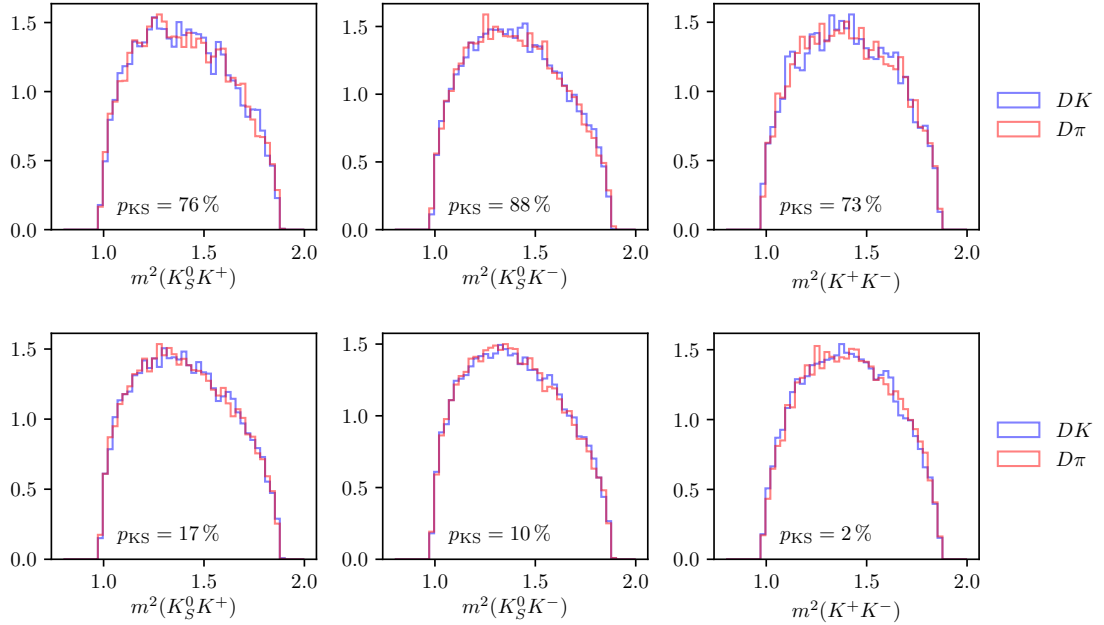


Figure 5.13: One-dimensional distributions of $m^2(K_S^0K^+)$, $m^2(K_S^0K^-)$, and $m^2(\pi^+\pi^-)$ in simulated (blue) $B^\pm \rightarrow DK^\pm$ and (red) $B^\pm \rightarrow D\pi^\pm$ decays where $D \rightarrow K_S^0K^+K^-$ in the (top) LL and (bottom) DD categories. The p values are the results of Kolmogorov-Smirnov compatibility tests between the distributions.

2005 contributions from a number of partly reconstructed $B \rightarrow Dh^\pm X$ decays, where
 2006 X denotes a pion or photon that is not included in the reconstructed decay, and
 2007 which can only be separated from signal decays by their $m(Dh)$ distribution; and
 2008 finally $B^\pm \rightarrow D\pi^\pm$ decays that are categorised as $B^\pm \rightarrow DK^\pm$ decays in the particle-
 2009 identification step and vice-versa. These background sources are described in detail
 2010 in Section 5.4. This section focuses on backgrounds that led to specific requirements
 2011 in the selection or proved to be small enough to not merit special treatment.

2012 5.3.1 Charmless decays

2013 There is potentially a so-called *charmless* background present in data, consisting
 2014 of $B^\pm \rightarrow K_S^0 h^+ h^- h'^\pm$ decays. These have the same final state as the signal decay,
 2015 but no intermediate D meson. Because all final state particles are reconstructed,
 2016 this background peaks in the B mass spectrum. This background is suppressed
 2017 by requiring the reconstructed B and D decay vertices to be separated in the
 2018 z direction; specifically by requiring that $\Delta z_{\text{significance}}^{D-B} > 0.5$, where $\Delta z_{\text{significance}}^{D-B}$
 2019 was defined in Eq. (5.1). The remaining background level can be investigated
 2020 by investigating the D mass sidebands.

2021 However, the use of the `DecayTreeFitter` χ^2_{DTF} as an input variable in the BDT
 2022 removes essentially all of the D (and K_S^0) sideband, due to the mass constraints in
 2023 the decay chain fit. Therefore separate BDT's are trained for LL and DD candidates
 2024 without the χ^2_{DTF} as an input variable, and used when selecting candidates for
 2025 the background studies presented in this section, and the following. In a similar
 2026 manner, all mass window requirements are made on the *default* reconstructed
 2027 masses, obtained with no use of `DecayTreeFitter`. The overlap of the two sets
 2028 of selected candidates in the signal B -mass window is above 95 %.

2029 The reconstructed B mass spectrum is shown for $B^\pm \rightarrow D\pi^\pm$ candidates in
 2030 the D sidebands in Fig. 5.14, both before and after making a requirement on
 2031 $\Delta z_{\text{significance}}^{D-B}$. The check is based on the upper D sideband for $D \rightarrow K_S^0 \pi^+ \pi^-$ decays
 2032 and the lower D sideband for $D \rightarrow K_S^0 K^+ K^-$ decays to avoid contamination
 2033 from real $B^\pm \rightarrow Dh^\pm$ decays with subsequent $D \rightarrow K_S^0 K^\pm \pi^\mp$ decays, or crossfeed
 2034 between the two signal D -decay modes. A peak is clearly visible, the size of
 2035 which is reduced by the requirement. This peak is partly due to a contribution
 2036 from $B^\pm \rightarrow K_S^0 \pi^+ \pi^- \pi^\pm$ decays ($B^\pm \rightarrow K_S^0 K^+ K^- \pi^\pm$ decays) in the $D \rightarrow K_S^0 \pi^+ \pi^-$
 2037 ($D \rightarrow K_S^0 K^+ K^-$) channel, and partly due to real signal decays that leak into the
 2038 D sidebands. The number of real signal decays can be calculated from the yield
 2039 obtained in the fit of Section 5.4, and the reconstructed m_D distribution in simulated
 2040 signal decays. Subtracting this contribution, it is estimated that approximately 450

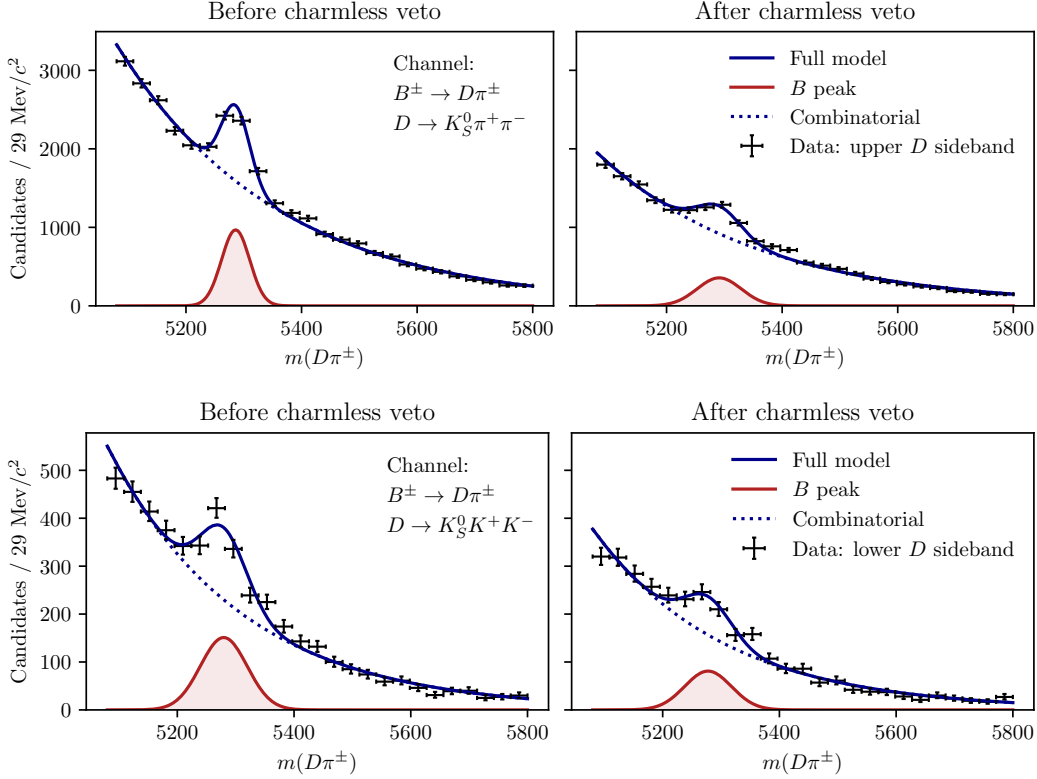


Figure 5.14: The B mass distribution of (top) $B^\pm \rightarrow D(\rightarrow K_S^0 \pi^+ \pi^-)\pi^\pm$ and (bottom) $B^\pm \rightarrow D(\rightarrow K_S^0 K^+ K^-)\pi^\pm$ candidates reconstructed in both the LL and DD categories, residing in the upper D mass sideband $m_D \in [1910, 1960] \text{ MeV}/c^2$ for $D \rightarrow K_S^0 \pi^+ \pi^-$ and in the lower sideband $m_D \in [1910, 1960] \text{ MeV}/c^2$ for $D \rightarrow K_S^0 K^+ K^-$, with (left) no requirement on $\Delta z_{\text{significance}}^{BD}$ and (right) after a requirement of $\Delta z_{\text{significance}}^{BD} > 0.5$.

(200) charmless decays are present in the $K_S^0 \pi^+ \pi^-$ ($K_S^0 K^+ K^-$) data samples. In similar fashion, Fig. 5.15 shows the m_B spectra for $B^\pm \rightarrow DK^\pm$ candidates in the D sidebands. In these plots, the peaks are at m_B values that are lower (higher) than the B mass in the $K_S^0 \pi^+ \pi^-$ ($K_S^0 K^+ K^-$) categories, because they stem from real $B^\pm \rightarrow K_S^0 K^+ K^- \pi^\pm$ decays where a kaon is mis-reconstructed as a pion or a pion is misreconstructed as a kaon, respectively. The total contribution of charmless decays in the $B^\pm \rightarrow DK^\pm$ data samples is estimated to be about 200 decays. As described further in Section 5.6.11, the presence of a charmless background at these levels has a negligible impact on the measurement results. It is not favourable to tighten the requirement further, as it does remove some real signal decays.

5.3.2 Background from four-body D decays

A similar potential background is from real $B^\pm \rightarrow Dh^\pm$ decays where the D meson decays directly to the $\pi^+ \pi^- h^+ h^-$ final state, without an intermediate K_S^0 meson.

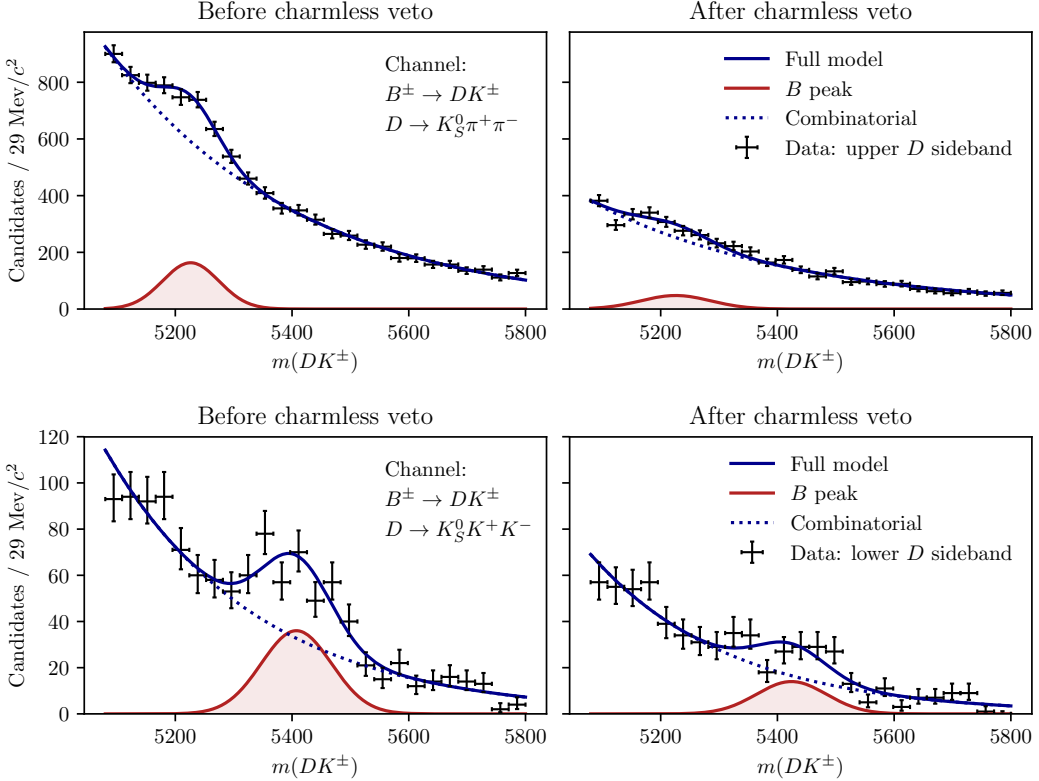


Figure 5.15: The B mass distribution of (top) $B^\pm \rightarrow D(\rightarrow K_S^0 \pi^+ \pi^-)K^\pm$ and (bottom) $B^\pm \rightarrow D(\rightarrow K_S^0 K^+ K^-)K^\pm$ candidates reconstructed in both the LL and DD categories, residing in the upper D mass sideband $m_D \in [1910, 1960] \text{ MeV}/c^2$ for $D \rightarrow K_S^0 \pi^+ \pi^-$ and in the lower sideband $m_D \in [1910, 1960] \text{ MeV}/c^2$ for $D \rightarrow K_S^0 K^+ K^-$, with (left) no requirement on $\Delta z_{\text{significance}}^{BD}$ and (right) after a requirement of $\Delta z_{\text{significance}}^{BD} > 0.5$.

This background can be investigated by looking for a peak in the B mass spectrum for candidates in the K_S^0 sideband, as illustrated in Fig. 5.16. The figure shows the spectrum in the final data sample, illustrating the significant effect of making the requirement on the K_S^0 flight distance that was discussed in Section 5.1.1. The BDT that does *not* rely on the DTF χ^2 has been used to suppress combinatorial background. The remaining peak after requiring $\chi_{\text{FD}}^2 > 49$ is completely accounted for by real signal decays that leak into the K_S^0 sideband. The requirement is made for candidates in the LL category only; if the pions stemming from a K_S^0 candidate are reconstructed as downstream tracks it implies that the K_S^0 has travelled from the interaction region.

5.3.3 Semi-leptonic backgrounds

The data sample has a minor background from $B \rightarrow D\mu\nu_\mu X$ decays, visible in the B mass spectrum when the companion is required to satisfy `isMuon=1`.

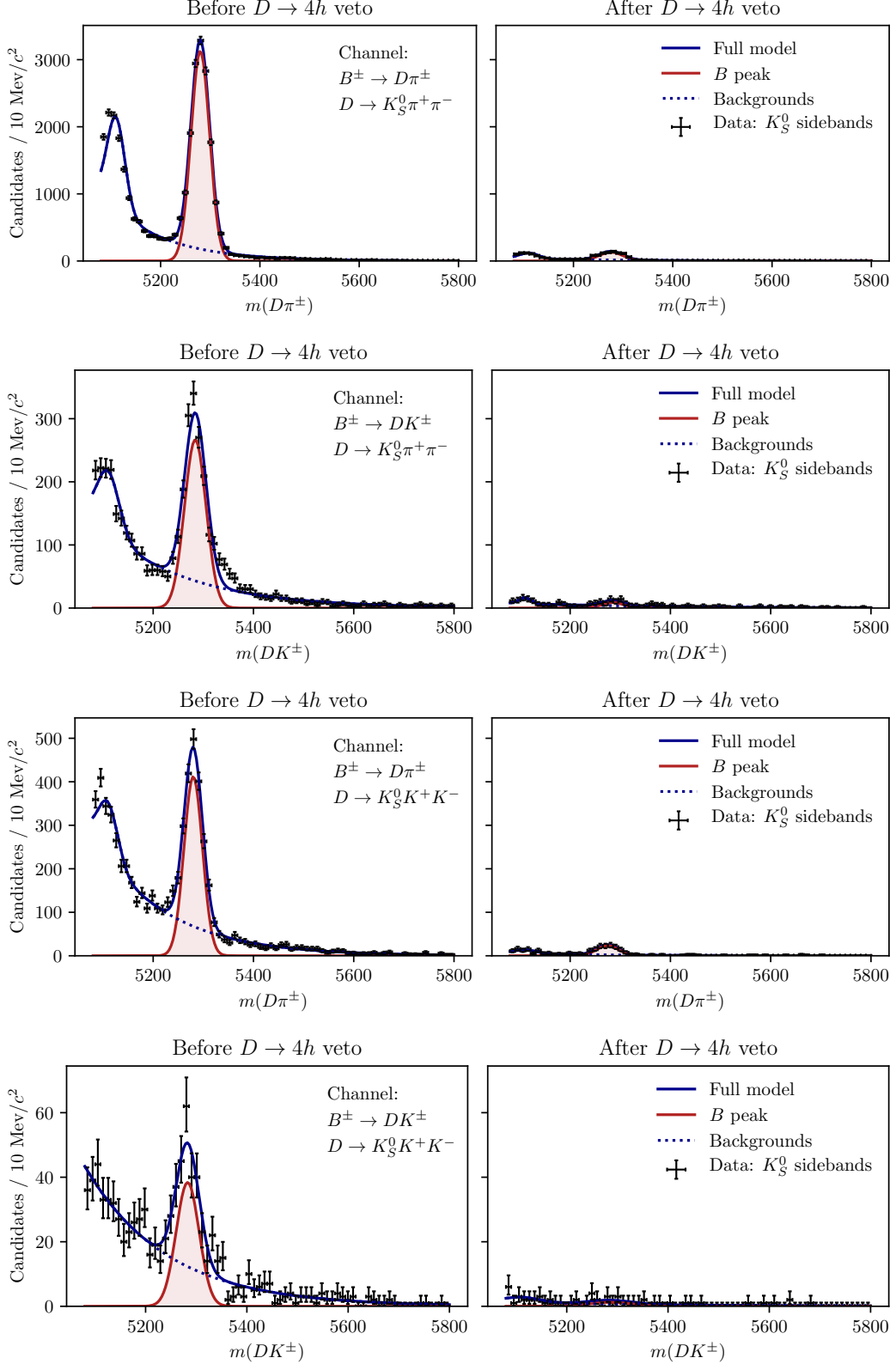


Figure 5.16: The B mass spectrum in the K_S^0 sideband where $m_{K_S^0} \in [467, 482] \text{ MeV}/c^2$ or $m_{K_S^0} \in [512, 527] \text{ MeV}/c^2$ (left) without a requirement on the K_S^0 flight distance significance, and (right) after the requirement implemented in the analysis.

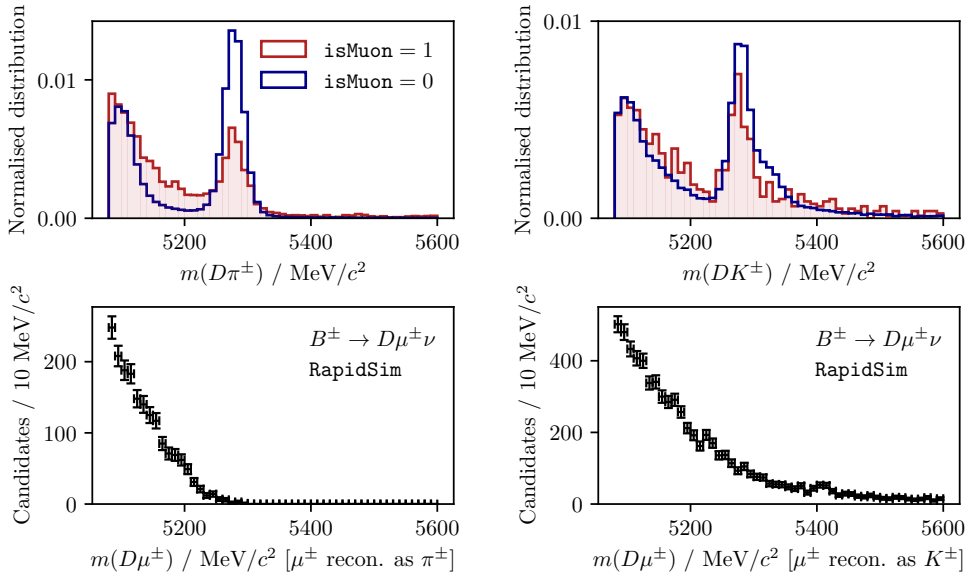


Figure 5.17: (Top) The m_B spectra in data split by the value of `isMuon` for the companion particle, in (left) the $D\pi^\pm$ and (right) the DK^\pm samples where $D \rightarrow K_S^0\pi^+\pi^-$. The two histograms are normalised independently, so that the distributions can be compared. The fractions of candidates in data (with $m_B \in [5080, 5800] \text{ MeV}/c^2$) where the companion satisfies `isMuon=1` are 1.6 % and 1.8 % for the $D\pi^\pm$ and DK^\pm channels respectively. (Bottom) the RapidSim mass spectra for $B^\pm \rightarrow D^0\mu^\pm\nu_\mu$ decays reconstructed in the (left) $D\pi^\pm$ and (right) DK^\pm categories.

This is shown in Fig. 5.17 for both the $B^\pm \rightarrow DK^\pm$ and $B^\pm \rightarrow D\pi^\pm$ channels where $D \rightarrow K_S^0\pi^+\pi^-$. The B mass spectra for simulated $B^\pm \rightarrow D\mu^\pm\nu_\mu$ decays reconstructed in each category are also shown, from simulation samples produced via RapidSim. The background is very efficiently vetoed by requiring `IsMuon=0` on the companion. This requirement removes approximately 85 % of the background decays, as estimated using the `PIDCalib` calibration samples and the (p, p_T) distribution for the muon in the RapidSim samples. The fraction of signal candidates for which the companion satisfies `IsMuon=1` in simulated signal samples is $\leq 0.9\%$ so the impact on signal yield is small.

The analogous $B \rightarrow D e \nu_e X$ background is investigated by inspecting the B mass spectra after making requirements on `PIDe` for the companion candidate, but a presence of the semi-leptonic background in data is not visible and no electron veto is applied to the companion.

Background from semi-leptonic D decays

There is a potential background from real $B^\pm \rightarrow Dh^\pm$ decays where the D meson decays semi-leptonically: $D^0 \rightarrow K_S^0\pi^-\ell^+\nu_\ell$. This background is particularly

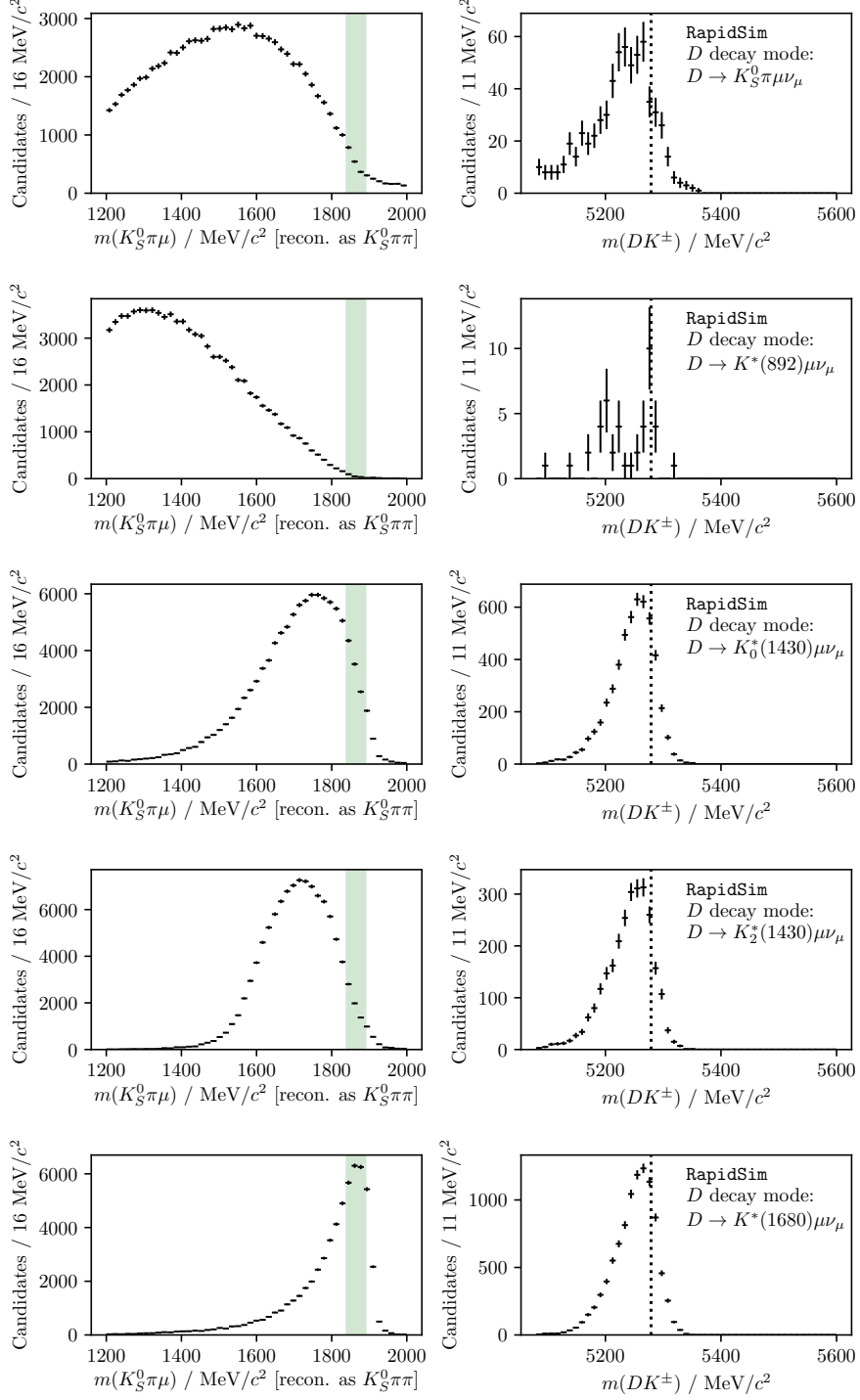


Figure 5.18: The reconstructed (left) $m(K_S^0 \pi^+ \pi^-)$ and (right) $m(Dh)$ distributions in RapidSim samples of $B^\pm \rightarrow DK^\pm$ decays where $D^0 \rightarrow K_S^0 \pi^- \mu^+ \nu_\mu$. The top plot is for decays that were uniformly distributed over phase space, and the following plots show the distribution where the $K_S^0 \pi^-$ originate in the resonances $K^{*-}(892)$, $K_0^{*-}(1430)$, $K_2^{*-}(1430)$, and $K^{*-}(1680)$. The shapes for the $D^0 \rightarrow K_S^0 \pi^- e^+ \nu_e$ case are almost identical.

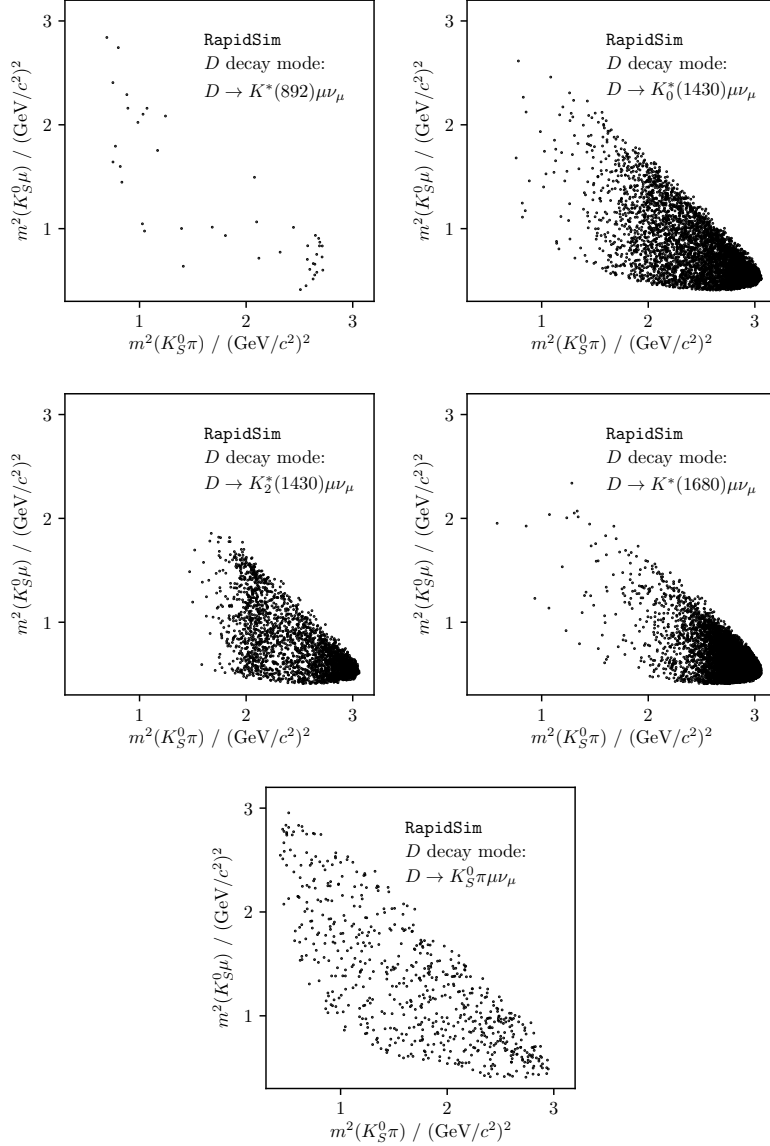


Figure 5.19: Dalitz distribution for $D \rightarrow K_S^0 \pi \mu \nu_\mu$ decays in RapidSim, where the $K_S^0 \pi^-$ originate in the resonances $K^{*-}(892)$, $K^{*-}_0(1430)$, $K^{*-}_2(1430)$, and $K^{*-}(1680)$, as well as for a uniform distribution over phase space.

dangerous because is peaks at the B mass, when the D -mass requirement is applied and it is reconstructed in the $D \rightarrow K_S^0 \pi^+ \pi^-$ category. This is illustrated in Fig. 5.18 using RapidSim samples of $B^\pm \rightarrow D(\rightarrow K^{*-}(\rightarrow K_S^0 \pi^-) \ell^+ \nu_\ell) h^\pm$ decays for $K^* \in \{K^*(892), K_0^*(1430), K_2^*(1430), K^*(1680)\}$. The respective spin of each resonance is taken into account in generation, by handling the decay via EVTGEN. The expected background yields relative to signal can be estimated by applying the B and D mass cuts to decays in the RapidSim samples, and using the relative branching ratios. Only the $D^0 \rightarrow K^{*-}(892) \ell \nu_\ell$ branching fractions have been measured [?],

Table 5.5: The selection efficiencies of $B^\pm \rightarrow DK^\pm$ decays where $D^0 \rightarrow K_S^0\pi^-\ell^+\nu_\ell$ when reconstructed in the $D \rightarrow K_S^0\pi^+\pi^-$ mode in RapidSim relative to the signal selection efficiencies, for a number of decay modes: PHSP as well as resonant production where the $K_S^0\pi^-$ pair originates in one of several K^* resonances. The relative branching ratios are also shown, calculated as explained in the main text, as well as the predicted relative yields.

Mode	$\epsilon_{bkg}/\epsilon_{signal}$ (%)	$\Gamma_{bkg}/\Gamma_{signal}$ (%)	N_{bkg}/N_{signal} (%)
$D \rightarrow K_S^0\pi^-\mu^+\nu_\mu$ (PHSP)	0.92 ± 0.05	18.3 ± 14.8	0.17 ± 0.14
$D \rightarrow (K_S^0\pi^-)_{K^{*-}(892)}\mu^+\nu_\mu$	0.06 ± 0.01	22.3 ± 3.2	0.013 ± 0.003
$D \rightarrow (K_S^0\pi^-)_{K_0^{*-}(1430)}\mu^+\nu_\mu$	7.3 ± 0.1	3.7 ± 0.8	0.27 ± 0.06
$D \rightarrow (K_S^0\pi^-)_{K_2^{*-}(1430)}\mu^+\nu_\mu$	3.7 ± 0.1	0.5 ± 0.3	0.02 ± 0.01
$D \rightarrow (K_S^0\pi^-)_{K^{*-}(1680)}\mu^+\nu_\mu$	24.4 ± 0.3	0.6 ± 0.5	0.15 ± 0.12
$D \rightarrow K_S^0\pi^-e^+\nu_e$ (PHSP)	0.53 ± 0.02	20.8 ± 16.3	0.11 ± 0.09
$D \rightarrow (K_S^0\pi^-)_{K^{*-}(892)}e^+\nu_e$	0.15 ± 0.02	25.6 ± 2.5	0.04 ± 0.01
$D \rightarrow (K_S^0\pi^-)_{K_0^{*-}(1430)}e^+\nu_e$	6.3 ± 0.1	4.2 ± 0.8	0.26 ± 0.05
$D \rightarrow (K_S^0\pi^-)_{K_2^{*-}(1430)}e^+\nu_e$	4.12 ± 0.08	0.5 ± 0.3	0.02 ± 0.01
$D \rightarrow (K_S^0\pi^-)_{K^{*-}(1680)}e^+\nu_e$	10.0 ± 0.2	0.7 ± 0.5	0.07 ± 0.05
Total	-	-	1.1 ± 0.4

but there is no reason to expect that higher K^* resonances should not contribute. To estimate their potential contribution, the branching ratios are approximated by

$$\text{BR}[D^0 \rightarrow K^{*-}(X)(\rightarrow K_S^0\pi^-)\ell\nu_\ell] \simeq \frac{\text{BR}[D^0 \rightarrow K^{*-}(X)(\rightarrow K_S^0\pi^-)\pi^+]}{\text{BR}[D^0 \rightarrow K^{*-}(892)(\rightarrow K_S^0\pi^-)\pi^+]} \text{BR}[D^0 \rightarrow K^{*-}(892)(\rightarrow K_S^0\pi^-)\ell\nu_\ell]$$

because all the relevant $D^0 \rightarrow K^{*-}(\rightarrow K_S^0\pi^-)\pi^+$ branching fractions are known [?]. The efficiencies and branching ratios relative to the signal channel are given in Table 5.5. It is clear that the higher K^* resonances are important: the smaller branching ratios are compensated for by a higher selection efficiency, due to the smaller phase-space of the missed neutrino. The total background yield is 1.1% of the signal yield in both the $B^\pm \rightarrow D\pi^\pm$ and $B^\pm \rightarrow DK^\pm$ channels. However, there will be an additional contribution in the $B^\pm \rightarrow DK^\pm$ channel from real $B^\pm \rightarrow D\pi^\pm$ decays with semi-leptonic D decays and a mis-identification of the companion. This background also peaks, and the yield is approximately 0.4% of the $B^\pm \rightarrow DK^\pm$ signal yield.

The potential impact from the presence of the background is estimated by

1. calculating the expected $B^\pm \rightarrow D\pi^\pm$ and $B^\pm \rightarrow DK^\pm$ signal yields in each bin for physics parameters similar to the world average values

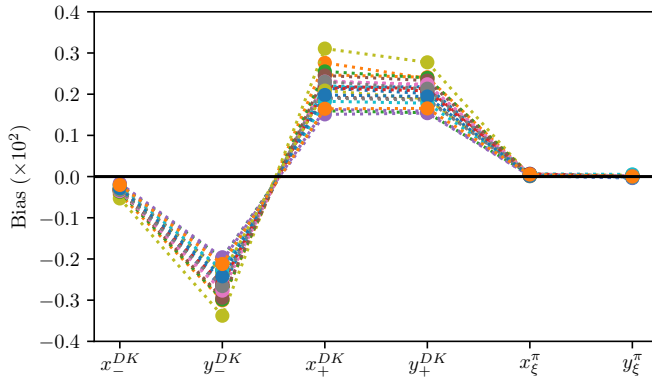


Figure 5.20: Estimated biases on the measured observables due to the presence of $D \rightarrow K_S^0 \pi^\pm \ell \nu_\ell$ backgrounds, calculated while varying efficiencies and branching ratios within uncertainties.

- 2106 2. then calculating the background bin yields in each bin, using the relative
2107 branching fractions and efficiencies described above and taking the bin-
2108 distribution from the RapidSim samples. The RapidSim samples are produced
2109 using the **ISGW2** model in EvtGen [?], yielding the Dalitz distributions in
2110 Fig. 5.19.
- 2111 3. adding the signal and background yields, and fitting the new $B^\pm \rightarrow D\pi^\pm$ and
2112 $B^\pm \rightarrow DK^\pm$ yields back with the default signal-yield expressions (including a
2113 fit of the F_i parameters)

2114 The obtained biases are shown in Fig. 5.20, where they are calculated a number
2115 of times, each time varying the efficiencies within statistical uncertainties and the
2116 relevant branching fractions within the measurement uncertainties. The systematic
2117 uncertainty due to the unknown branching fractions and the use of RapidSim in
2118 lieu of full simulation is not included, but is of course significant. Nevertheless
2119 it is clear that the potential biases are significant compared to the size of the
2120 systematic uncertainties of the analysis presented in Section 5.6. Therefore the
2121 backgrounds are vetoed by requiring **IsMuon=0** and **PIDe < 0** on the pions from
2122 the D -decay with opposite charge to the bachelor in the $D \rightarrow K_S^0 \pi^+ \pi^-$ channel.
2123 This requirement removes 88 % of the muonic background and 99 % of the electron
2124 background, according to PID efficiencies obtained via the **PIDCalib** package,
2125 using the (p, p_T) distribution for the muon/electron in the RapidSim samples. The
2126 survival rate for signal decays in full simulation is 94 %, so the impact on the
2127 obtainable precision is only about 3 %. A systematic uncertainty is assigned to
2128 account for the potential remaining background.

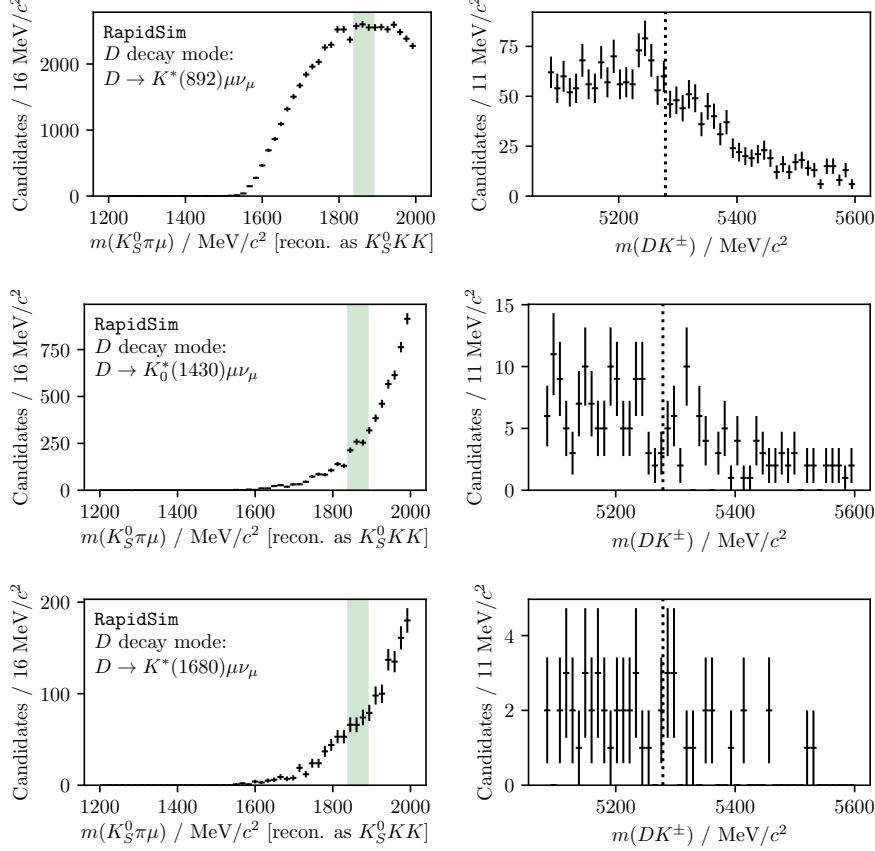


Figure 5.21: The reconstructed (left) $m(K_S^0 K^+ K^-)$ and (right) $m(Dh)$ distributions in RapidSim samples of $B^\pm \rightarrow DK^\pm$ decays where $D^0 \rightarrow K_S^0 \pi^- \mu^+ \nu_\mu$, where the $K_S^0 \pi^-$ originate in (top to bottom) the resonances $K^{*-}(892)$, $K_0^{*-}(1430)$, and $K^{*-}(1680)$. The shapes for the $D^0 \rightarrow K_S^0 \pi^- e^+ \nu_e$ case are almost identical.

In the $D \rightarrow K_S^0 K^+ K^-$ channel an analogous study shows the relative yields to be similar. The selection efficiencies are higher, as are the relative branching ratios due to the lower $D \rightarrow K_S^0 K^+ K^-$ branching fraction, but in this mode the PIDK > -5 requirement placed on the pion and lepton removes approximately 90 % of the background, leaving the relative rate similar to in $D \rightarrow K_S^0 \pi^+ \pi^-$. However, importantly, *the background is not peaking*, as shown in Fig. 5.21. The presence of a percent-level, *non-peaking* background in the $D \rightarrow K_S^0 K^+ K^-$ channel is safe to ignore and thus no veto is applied in the $D \rightarrow K_S^0 K^+ K^-$ channel.

The muon-veto for the semi-leptonic background does remove some signal decays, where an original pion or kaon results in hits in the muon detectors. A significant contribution is from particles that decay in flight. The track quality of these decays is worse than for nominal decays, which affects the resolution on the reconstructed Dalitz coordinates. In simulated signal decays the standard deviation of $\Delta m_{\pm}^2 = m_{reco}^2(K_S^0 \pi^\pm) - m_{TRUE}^2(K_S^0 \pi^\pm)$ is 50 % larger for decays where

one of the D -decay products has `IsMuon=1` than in decays where this is not the case. This can lead to systematic biases on the observables, as described further in Section 5.6.7. The overall effect is small, as evidenced by the systematic uncertainty described in that section; nevertheless this fact motivates removing decay-in-flight decays of the D -decay products. Therefore it is also required that `IsMuon=0` for the D -decay pion with the same charge as the companion in the $D \rightarrow K_S^0\pi^+\pi^-$ channels, and on the D -decay kaons in the $D \rightarrow K_S^0K^+K^-$ channels. This veto removes about 2 % of signal candidates in simulation that survive the lepton vetoes described in the previous sections.

5.3.4 Cross-feed from other $D \rightarrow K_S^0h^+h^-$ decays

Misidentification of a D decay product can lead to background from cross-feed between the $B^\pm \rightarrow D(\rightarrow K_S^0\pi^+\pi^-)h^\pm$ and $B^\pm \rightarrow D(\rightarrow K_S^0K^+K^-)h^\pm$ signal channels, or cross-feed from $B^\pm \rightarrow D(\rightarrow K_S^0K\pi)h^\pm$ decays into either of the signal channels. However, this background is very highly suppressed by the employed requirement on the D mass. This is illustrated in Fig. 5.22, where the D mass distribution in samples of simulated $B^\pm \rightarrow D(\rightarrow K_S^0K\pi)K^\pm$ decays are shown, when reconstructed as $D \rightarrow K_S^0\pi^+\pi^-$ and $D \rightarrow K_S^0K^+K^-$ decays. Essentially no decays that fall in the selected D mass window survive the full selection. Therefore this background is not considered further. Neither is the background due to cross-feed between $B^\pm \rightarrow D(\rightarrow K_S^0\pi^+\pi^-)h^\pm$ and $B^\pm \rightarrow D(\rightarrow K_S^0K^+K^-)h^\pm$, since it involves two misidentified particles, and therefore will result in reconstructed D masses even further away from the selected mass window. A very loose PID requirement on the charged D decay products is nonetheless included in the $D \rightarrow K_S^0K^+K^-$ channel, because it helps reduce the level of combinatorial background.

5.3.5 Swapped-track backgrounds

A possible peaking background stems from real $B \rightarrow DhX$ decays with the same final state tracks as in the signal case, but where some tracks are misassigned in the reconstruction. Examples are $B^+ \rightarrow (K_S^0h^+h^-)_D h^+$ decays where the companion and the D -decay product with the same charge are swapped, or $B^\pm \rightarrow (K^-\pi^+)_D K_S^0 h^\pm$ decays, where the K_S^0 is assigned to the D decay and the real companion is swapped with the D -decay product of the same charge. The signature of this background type is a peak at the D mass, when the invariant mass corresponding to the companion track and some subset of the D -decay tracks is formed. The presence of the background has been investigated by forming all

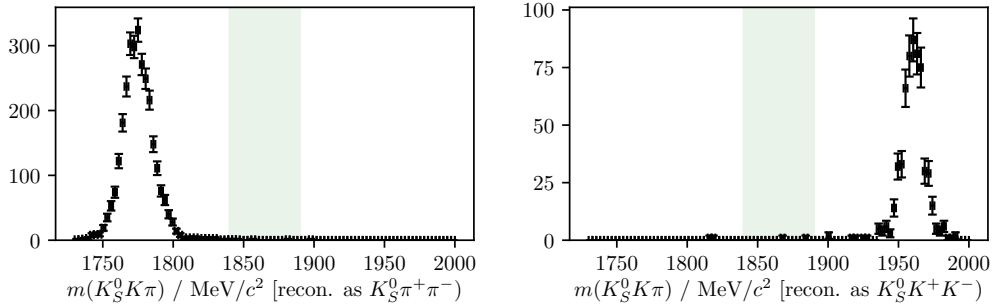


Figure 5.22: Simulated samples of $B^\pm \rightarrow D(\rightarrow K_S^0 K\pi)\pi^\pm$ decays reconstructed in the (left) $D \rightarrow K_S^0 \pi^+\pi^-$ and (right) $D \rightarrow K_S^0 K^+K^-$ channels, combining the LL and DD categories. The D -mass region included in the selection of signal decays is illustrated with the green band. The plots in the $B^\pm \rightarrow DK^\pm$ channels look almost identical.

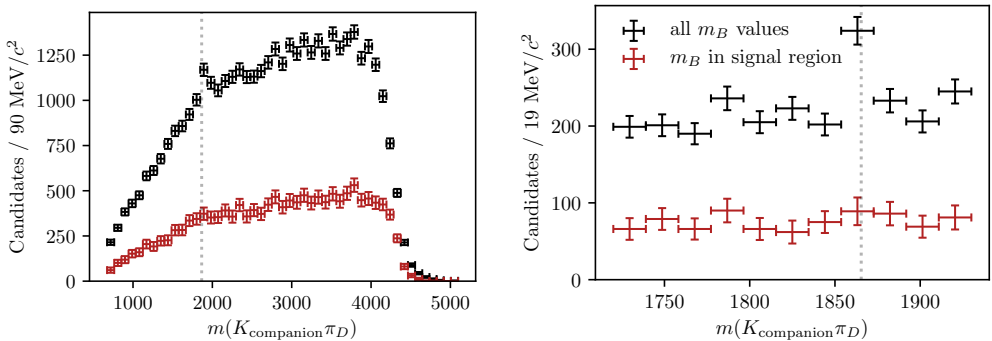


Figure 5.23: Invariant mass spectrum of the $m^2(K^\pm\pi^\mp)$ combination in the $B^\pm \rightarrow (K_S^0\pi^+\pi^-)K^\pm$ data sample for (black) all candidates and (red) candidates for which $m_B \in m_B^{PDG} \pm 30 \text{ MeV}/c^2$. The LL and DD categories are combined. The only difference between the left and right plots is the $m(K\pi)$ mass range on the horizontal axis. The dotted line indicated the known D mass [?].

such combinations, for all data categories, after the full selection has been applied. Only in a single channel is a peak visible: the $B^\pm \rightarrow (K_S^0\pi^+\pi^-)K^\pm$ channel, where $m(K^\pm\pi^\pm)$ has a peak, as shown in Fig. 5.23. Thus, a background is present from the favoured two-body D decay $B^\pm \rightarrow (K^\pm\pi^\mp)_D K_S^0\pi^\pm$, where the K^\mp is reconstructed as the companion, and the K_S^0 meson and both pions are assigned to the D decay. Is is not favourable to veto this background, because a requirement on the invariant mass of a track combination that includes the companion track would impact the Dalitz-plot acceptance differently in the DK^\pm and $D\pi^\pm$ channels. Thus it would break a fundamental underlying feature of the measurement: the identical selection efficiency profile between these modes. However, the yield excess in the $m(K^\pm_{\text{companion}}\pi^\mp_D)$ range around m_D , attributed to the background, corresponds to only about 0.5 % of the signal yield. A background at this level does not lead to a limiting systematic uncertainty on the measurement, as described in Section 5.6.9.

2190 5.4 Signal and background mass shapes

2191 The measurement employs *extended maximum-likelihood fits* [?] to the $m(Dh^\pm)$
 2192 distribution of signal candidates to determine the observables of interest. The
 2193 analysis implements a two-step fit procedure: first the data samples are analysed
 2194 without separating the candidates by B charge or Dalitz bin, in order to determine
 2195 appropriate parametrisations of the $m(Dh^\pm)$ distribution of the signal and relevant
 2196 background components. The parameterisations are then kept fixed in a subsequent
 2197 fit of the observables of interest, where the candidates are split by B charge
 2198 and Dalitz bin. This section describes the first step, whereas the latter fit is
 2199 the subject of Section 5.5.

2200 In both steps, the candidates are split in 8 categories depending on whether the
 2201 companion is categorised as a kaon or pion, whether the K_S^0 meson is in the LL
 2202 or DD category, and by whether the D meson is reconstructed in the $K_S^0\pi^+\pi^-$ or
 2203 $K_S^0K^+K^-$ final state. In the remainder of this text, these categories are indexed
 2204 with the letter c . For each category, c , the expected number of observed decays
 2205 at a given B mass, $F^c(m)$, is given by the sum of a signal contribution and a
 2206 number of background distributions

$$F^c(m|\theta) = N_s^c(\theta)f_s^c(m|\theta) + \sum_b N_b^c(\theta)f_b^c(m|\theta), \quad (5.4)$$

2207 where θ denotes a set of parameters that describe the mass shapes and expected
 2208 yields, in which some parameters are shared between categories. The distributions
 2209 $f_{s/b}^c$ are normalised to integrate to unity, and the expected signal (background)
 2210 yields are denoted N_s^c (N_b^c). A total, normalised distribution can then be defined

$$f^c(m|\theta) = \frac{1}{N_{\text{tot}}^c(\theta)} F^c(m|\theta), \quad N_{\text{tot}}^c(\theta) = N_s^c(\theta) + \sum_b N_b^c(\theta). \quad (5.5)$$

2211 Given a set of N_{observed}^c measured B masses, $\{m_i^c\}$, in a given category, the extended
 2212 log-likelihood function is defined

$$\ln \mathcal{L}_c(\theta|\{m_i^c\}) \equiv \sum_i \ln f^c(m_i^c|\theta) + \ln \text{Poisson}(N_{\text{tot}}^c(\theta), N_{\text{observed}}^c) \quad (5.6)$$

2213 In a simultaneous fit the total, negative log-likelihood is $-\ln \mathcal{L} = -\sum_c \mathcal{L}_c$, and
 2214 this function can be minimised to find the maximum-likelihood estimates of the
 2215 parameters in θ , as well as their confidence regions and correlation coefficients.
 2216 This is handled with the `RooFit` package [?].

2217 Apart from signal decays, the fit includes components that describe combinatorial
 2218 background, backgrounds from decays where a companion pion is misidentified
 2219 as a kaon or vice versa, and partially reconstructed backgrounds. Each of these
 2220 components are described in detail in the following, before the results of the
 2221 first-stage fit are presented in Section 5.4.5.

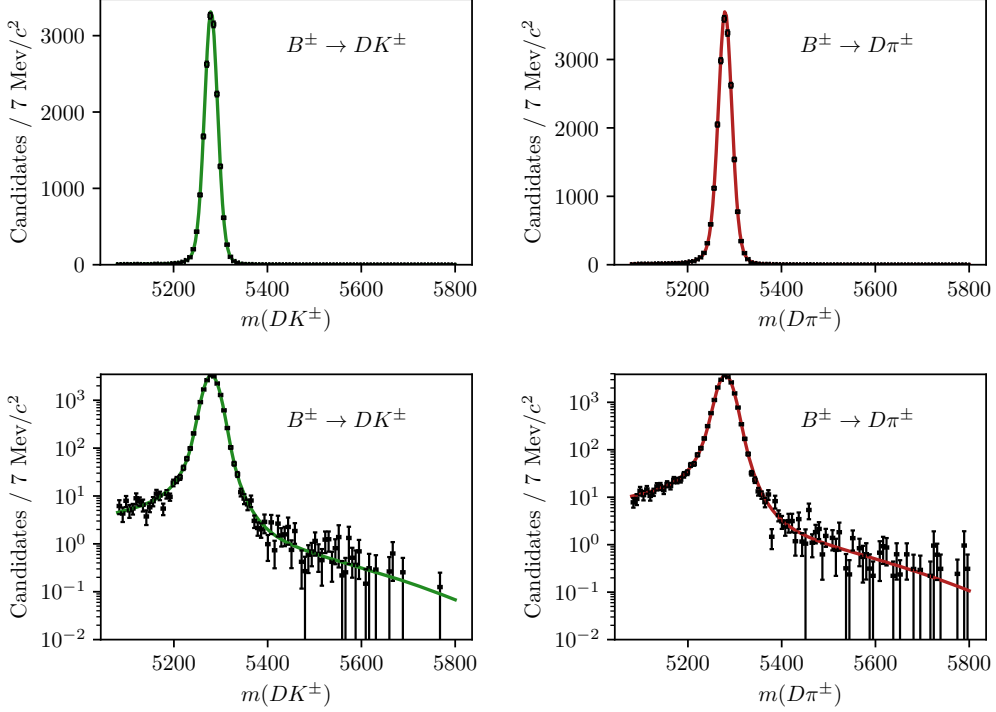


Figure 5.24: Fit projection of the signal shape to simulated $B^\pm \rightarrow D(\rightarrow K_S^0 \pi^+ \pi^-)h^\pm$ samples reconstructed in the LL category. (Left) shows DK shapes, and (right) shows $D\pi$ shapes. The shapes are shown with both linear and logarithmic y -axis scales.

5.4.1 Signal decays

The signal component is modelled with a sum of a Gaussian density function, $f_G(m|m_B, \sigma)$, and a modified Gaussian distribution with the parameterisation

$$f_C(m|m_B, \sigma, \alpha_L, \alpha_R, \beta) \propto \begin{cases} \exp\left[\frac{-\Delta m^2(1+\beta\Delta m^2)}{2\sigma^2+\alpha_L\Delta m^2}\right], & \Delta m = m - m_B < 0 \\ \exp\left[\frac{-\Delta m^2(1+\beta\Delta m^2)}{2\sigma^2+\alpha_R\Delta m^2}\right], & \Delta m = m - m_B > 0, \end{cases} \quad (5.7)$$

which is Gaussian when $\Delta m^2 \ll \sigma^2/\alpha_{L/R}$ or $\Delta m^2 \gg \beta^{-1}$ (with widths of σ and $\sqrt{\alpha_{L/R}/\beta}$ respectively), with an exponential-like transition that is able to model the effect of the experimental resolution of LHCb very well. For the case $\beta = 0$ the shape is denoted the *Cruijff* shape; however, in this case it tends to a uniform distribution for large Δm^2 values, and cannot model the tails of the signal distribution. Thus, the full density function is

$$f_s(m|m_B, \sigma, \alpha_L, \alpha_R, \beta) = k_C f_C(m|m_B, \sigma, \alpha_L, \alpha_R, \beta) + (1 - k_C) f_G(m|m_B, \sigma). \quad (5.8)$$

The tail parameters $(\alpha_{L/R}, \beta)$ and the constant k_C are determined in fits to simulated signal decays that have passed the full selection. The parameters are shared

2233 between the $K_S^0\pi^+\pi^-$ and $K_S^0K^+K^-$ channels, but otherwise independent in the
 2234 fit categories. An example of a fit to simulated $B^\pm \rightarrow D(\rightarrow K_S^0\pi^+\pi^-)h^\pm$ decays
 2235 is given in Fig. 5.24. The resolution parameters σ are determined in the fit to
 2236 actual data. Separate parameters are determined in the LL and DD categories,
 2237 because the LL category has a better resolution on the K_S^0 momentum, and
 2238 therefore a narrow peak in reconstructed B mass. Likewise, separate resolution
 2239 parameters are used for $B^\pm \rightarrow D\pi^\pm$ and $B^\pm \rightarrow DK^\pm$ decays, because the smaller
 2240 Q value in the latter case leads to smaller momenta of the decay products, and
 2241 a correspondingly better resolution.

2242 The signal yields are determined independently in each $B^\pm \rightarrow D\pi^\pm$ category.
 2243 The yields in the $B^\pm \rightarrow DK^\pm$ categories are then parameterised in terms of a single
 2244 yield-ratio $\mathcal{R}_{K/\pi}$, and ϵ^c , the corresponding selection efficiency for a given category

$$N_{DK^\pm}^c = \mathcal{R}_{K/\pi} \times N_{D\pi^\pm}^c \times \frac{\epsilon_{DK^\pm}^c}{\epsilon_{D\pi^\pm}^c}. \quad (5.9)$$

2245 The selection efficiency is obtained in simulation, except for the PID efficiencies
 2246 which are obtained in calibration data as described in Section 5.1.3. The parameter
 2247 $\mathcal{R}_{K/\pi}$ is shared between all categories, and corresponds to the branching ratio
 2248 between $B^\pm \rightarrow DK^\pm$ and $B^\pm \rightarrow D\pi^\pm$ decays. Therefore, it can be compared to
 2249 the known branching ratio [?], which serves as an important cross check of the
 2250 determination of relative efficiencies.

2251 5.4.2 Cross-feed between $B^\pm \rightarrow Dh^\pm$ channels

2252 There is a cross-feed between the $B^\pm \rightarrow D\pi^\pm$ and $B^\pm \rightarrow DK^\pm$ channels, where real
 2253 $B^\pm \rightarrow D\pi^\pm$ decays are reconstructed as $B^\pm \rightarrow DK^\pm$ decays, or where $B^\pm \rightarrow DK^\pm$
 2254 decays are reconstructed as $B^\pm \rightarrow D\pi^\pm$ decays. Due to relative branching fractions
 2255 the former contribution is by far the most important, but both are modelled.

2256 The cross-feed shapes are obtained in a data-driven manner using the sPlot
 2257 method [?], and fixed in the fit to data. Separate shapes are determined for each
 2258 category, using the following steps:

- 2259 • The procedure is based on the reasonably pure $B^\pm \rightarrow D\pi^\pm$ sample obtained
 2260 when the full selection is applied. A simple mass fit is performed to the
 2261 invariant mass spectrum and the sPlot method [?] is used to obtain the
 2262 sWeights, w_s , for the signal component. The mass fit uses the same components
 2263 for signal, low mass shape, and combinatorial background as described in this
 2264 section.

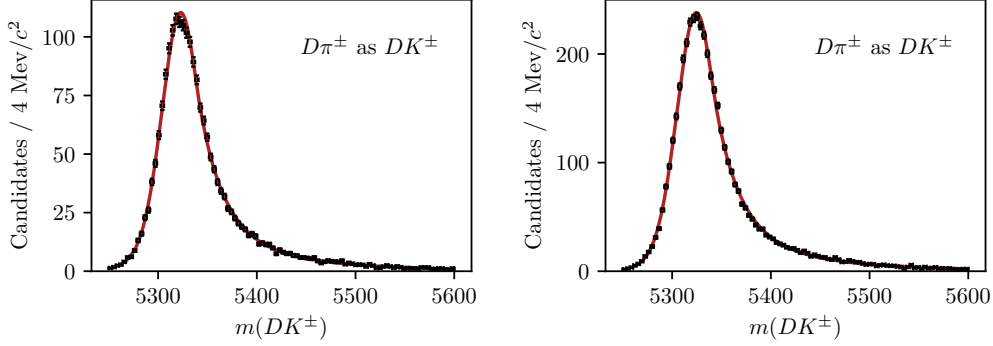


Figure 5.25: Fitted shape of the B^\pm invariant mass spectrum for $B^\pm \rightarrow D\pi^\pm$ decays misidentified as $B^\pm \rightarrow DK^\pm$ decays for (left) LL and (right) DD candidates in the $D \rightarrow K_S^0 \pi^+ \pi^-$ mode.

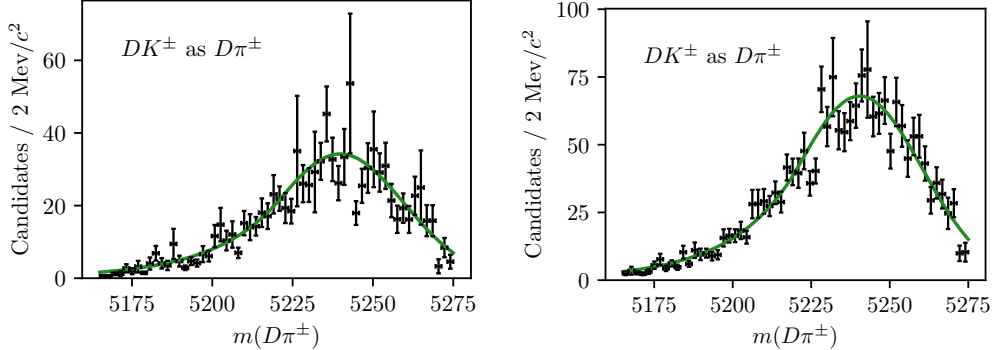


Figure 5.26: Fitted shape of the B^\pm invariant mass spectrum for $B^\pm \rightarrow DK^\pm$ decays misidentified as $B^\pm \rightarrow D\pi^\pm$ decays for (left) LL and (right) DD candidates in the $D \rightarrow K_S^0 \pi^+ \pi^-$ mode.

- 2265 • A set of weights are defined, based on the candidate-by-candidate PID
2266 efficiencies obtained as described in Section 5.1.3:

 2267 – The extracted PID efficiencies of the $\text{PIDK} < 4$ cut $\epsilon_{D\pi \rightarrow D\pi}(p, \eta, n_{\text{tracks}})$
2268 are used to reverse-weight the $B^\pm \rightarrow D\pi^\pm$ sample, in order to obtain the
2269 bachelor kinematic distributions before the $\text{PIDK} < 4$ cut is applied.

 2270 – The extracted PID efficiencies of the $\text{PIDK} > 4$ cut $\epsilon_{D\pi \rightarrow DK}(p, \eta, n_{\text{tracks}})$
2271 are used to obtain the bachelor kinematic distribution of the $B^\pm \rightarrow D\pi^\pm$
2272 candidates mis-identified as $B^\pm \rightarrow DK^\pm$.

 2273 • The raw distribution of the invariant mass of B^\pm particles with a misidentified
2274 bachelor, m_B^{mis-ID} , is produced by also doing the DecayTreeFit kinematic refit
2275 while swapping the companion mass hypothesis of each $B^\pm \rightarrow D\pi^\pm$ candidate
2276 to a kaon hypothesis.

- 2277 • Each candidate is reweighted by the overall weight $w = w_s^{cand.}/\epsilon_{D\pi \rightarrow D\pi}^{cand.} \cdot$
 2278 $\epsilon_{D\pi \rightarrow DK}^{cand.}$, and the reweighed m_B^{mis-ID} distribution is fitted to obtain the cross-
 2279 feed mass distribution function.

2280 The distributions are modelled with a sum of two Crystal Ball density functions,
 2281 each defined by the parameterisation [?]

$$f_{CB}(m, \mu, \sigma, \alpha, n) \propto \begin{cases} \exp \left[-\frac{1}{2} \left(\frac{m-\mu}{\sigma} \right)^2 \right] & \text{if } (m-\mu)/\sigma > -\alpha \\ A \left(B - \frac{m-\mu}{\sigma} \right)^{-n} & \text{otherwise,} \end{cases} \quad (5.10)$$

2282 where $\alpha > 0$, and

$$A = \left(\frac{n}{\alpha} \right)^n \exp[-\alpha^2/2], \quad B = \frac{n}{\alpha} - \alpha. \quad (5.11)$$

2283 The obtained m_B^{mis-ID} spectrum and obtained mass shape is given in Fig. 5.25
 2284 for the $D \rightarrow K_S^0 \pi^+ \pi^-$ category; the $D \rightarrow K_S^0 K^+ K^-$ shapes are very similar. An
 2285 analogous procedure is used to obtain the mass distribution of $B^\pm \rightarrow DK^\pm$ decays
 2286 reconstructed in the $B^\pm \rightarrow D\pi^\pm$ category. In the first stage where sPlots are
 2287 extracted by a fit to the $B^\pm \rightarrow DK^\pm$ mass spectrum, the cross-feed component
 2288 determined as described above is included. An example of one of the resulting
 2289 shapes is given in Fig. 5.26. The shape obtained in this manner performs better
 2290 than one obtained using simulated decays, because the precision of the momentum
 2291 determination is slightly overestimated in simulation.

2292 The yield of cross-feed from $B^\pm \rightarrow D\pi^\pm$ decays in a given $B^\pm \rightarrow DK^\pm$ category
 2293 is parameterised in terms of the yield of correctly identified $B^\pm \rightarrow D\pi^\pm$ decays and
 2294 the mis-identification probability extracted from calibration samples as described
 2295 in Section 5.1.3. Denoting the rate at which a pion is reconstructed as a kaon
 2296 by $\epsilon_{\pi \rightarrow K}^c$ in a given category, c , the yield is

$$N_{\pi \rightarrow K}^c = N_{D\pi^\pm}^c \frac{\epsilon_{\pi \rightarrow K}^c}{1 - \epsilon_{\pi \rightarrow K}^c}, \quad (5.12)$$

2297 with an analogous definition of the yield of the cross-feed component from
 2298 $B^\pm \rightarrow DK^\pm$ decays in the $B^\pm \rightarrow D\pi^\pm$ spectrum.

2299 5.4.3 Partially reconstructed backgrounds

2300 A number of background candidates stem from partly reconstructed B decays of the
 2301 type $B \rightarrow DhX$, where X denotes a photon or a pion that is not reconstructed. It
 2302 is not possible to reject these decays in the selection, due to the similarity to signal
 2303 decays. The missing momentum results in reconstructed B masses below the actual

2304 B mass, and therefore the backgrounds are also denoted *lowmass* backgrounds.
2305 These mass distributions are modelled with analytic shapes, derived based on two
2306 principles. Firstly, the kinematic endpoints of the distributions are fully defined by
2307 the particle masses in the decay. Secondly, the angular distribution of the missing
2308 particle has a one-to-one relation to the missing momentum, and therefore to the
2309 reconstructed B mass. Depending on the spin-parity of the particles and resonances
2310 involved in the decay, two different mass distributions arise.

2311 In B decays where the missing particle is a scalar that is produced in the
2312 decay of a vector resonance (eg. $B^\pm \rightarrow D^{*0}(\rightarrow D^0\pi^0)\pi^\pm$ decays where the π^0 is
2313 not reconstructed), the $m(D^0\pi^\pm)$ distribution has a double-peak structure. The
2314 D^{*0} helicity angle θ is defined as the angle between the π^0 momentum vector in
2315 the D^{*0} rest frame and the D^{*0} boost vector in the B rest frame. The helicity
2316 of the D^{*0} meson means that the π^0 will travel predominantly in the direction
2317 where $\theta = 0$ or $\theta = \pi$. When $\theta = 0$ the fraction of momentum carried by the
2318 missing π^0 is lower, leading to a higher reconstructed $m(D^0\pi^\pm)$. When $\theta = \pi$
2319 the converse occurs. The resulting B mass distribution is a parabola $f_{\text{HORNS}}^0(m)$
2320 peaking near both kinematic endpoints a and b

$$f_{\text{HORNS}}^0(m) = \begin{cases} (m - \frac{a+b}{2})^2, & \text{if } a < m < b \\ 0, & \text{otherwise.} \end{cases} \quad (5.13)$$

2321 Due to the double-peaking structure, and the fact that was developed by
2322 Paolo Gandini for the two-body ADS/GLW analyses [?], this shape is denoted a
2323 *HORNSdini* shape when convolved with a resolution function as described below.

2324 The second relevant decay situation is where the missing particle is a vector,
2325 again produced via the intermediate decay of a vector resonance (eg. $B^\pm \rightarrow$
2326 $D^{*0}(\rightarrow D^0\gamma)\pi^\pm$ decays where the photon is not reconstructed). In this case, the
2327 spin-parity of the photon (1^-) means that it will decay preferentially in the $\theta = \frac{\pi}{2}$
2328 or $\theta = \frac{3\pi}{2}$ directions, and so a double-peak structure is not seen. In this case
2329 the parabolic distribution $f_{\text{HILL}}^0(m)$ with kinematic endpoints a, b has negative
2330 curvature and can be described by

$$f_{\text{HILL}}^0(m) = \begin{cases} -(m - a)(m - b), & \text{if } a < m < b \\ 0, & \text{otherwise.} \end{cases} \quad (5.14)$$

2331 This shape is denoted a *HILLdini* shape when convolved with a resolution function.
2332 A convolution is applied to take into the non-perfect resolution in the momentum
2333 determination. The resolution function is chosen to be a sum of two Gaussians.

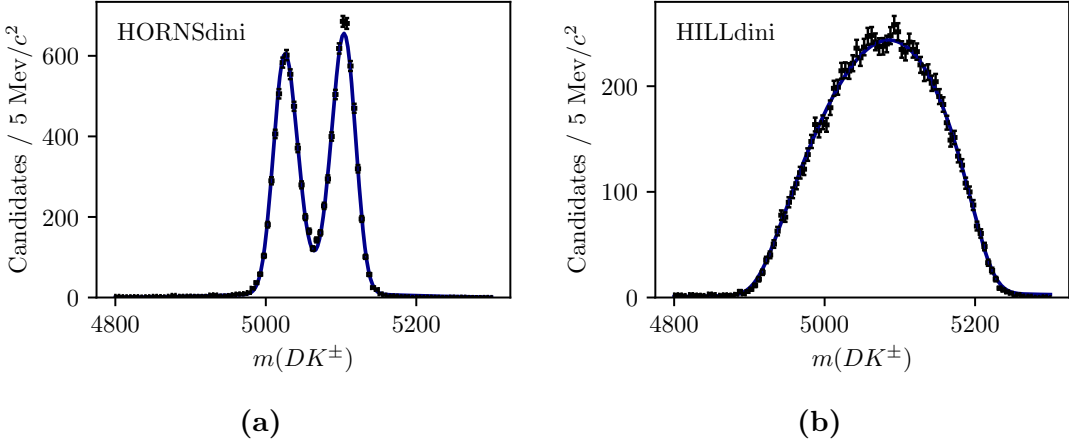


Figure 5.27: Examples of (a) the *HORN**sini* distribution fit to simulated $B^\pm \rightarrow (D^{*0} \rightarrow D^0[\pi^0])K^\pm$ decays, and (b) the *HILL**sini* distribution fit to simulated $B^\pm \rightarrow (D^{*0} \rightarrow D^0[\gamma])K^\pm$ decays. The fits in this figure are made to illustrate the features of each shape, but do not enter the actual fit to data.

For a single Gaussian shape $f_G(x|\mu, \sigma)$ with mean μ and width σ , the double Gaussian is expressed as

$$f_{DG}(x) = f_G(x|\mu, \sigma) + k_G f_G(x|\mu, R_\sigma \sigma). \quad (5.15)$$

where σ is the width of the first Gaussian, k_G is the relative fractions between the two Gaussians, and R_σ is their relative widths. Further, selection effects can distort the horns shape such that one of the peaks is higher than the other. This is taken into account by introducing a linear polynomial with slope parameter ξ . As $\xi \rightarrow 0$, the left hand peak decreases in size relative to the right hand peak. The resulting *HORNSdini* and *HILLdini* distributions are therefore

$$f_{\text{HORNS/HILL}}(m) = \int_a^b dx f_{\text{HORNS/HILL}}^0(x) f_{DG}(m|x, \sigma, k_G, R_\sigma) \left(\frac{1-\xi}{b-a}x + \frac{b\xi - a}{b-a} \right). \quad (5.16)$$

²³⁴² Examples of the shapes are given in Fig. 5.27. These shapes are used to fit all
²³⁴³ partially reconstructed backgrounds, as described in the following section.

Determination of the partially reconstructed background distributions

In both the $B^\pm \rightarrow DK^\pm$ and $B^\pm \rightarrow D\pi^\pm$ categories, components are included to describe contributions from the partially reconstructed decays

- $B^\pm \rightarrow (D^{*0} \rightarrow D^0[\pi^0])h^\pm$, described using a *HORN**Sdini* distribution,
 - $B^\pm \rightarrow (D^{*0} \rightarrow D^0[\gamma])h^\pm$, described using a *HILL**dini* distribution

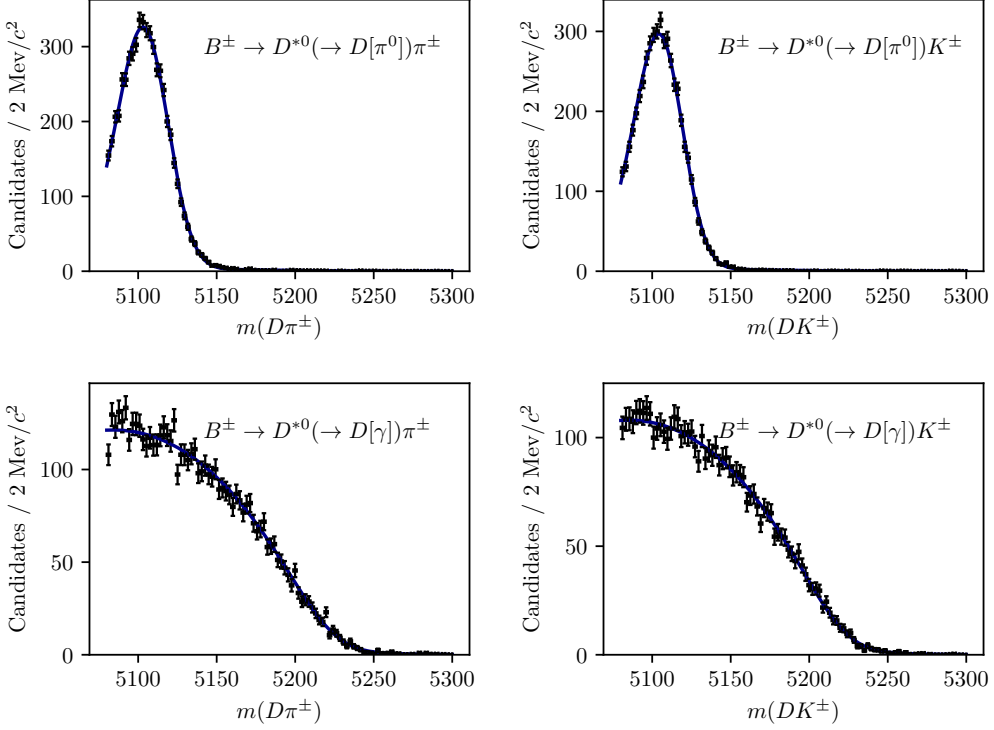


Figure 5.28: Fit projection of the fit to (top) simulated $B^+ \rightarrow D^{*0}(\rightarrow D^0[\pi^0])h^\pm$ decays and (bottom) simulated $B^+ \rightarrow D^{*0}(\rightarrow D^0[\gamma])h^\pm$ decays, all reconstructed in the DD category. Both the (left) DK and (right) $D\pi$ shapes are shown.

- 2349 $B^0 \rightarrow (D^{*\pm} \rightarrow D^0[\pi^\pm])h^\mp$, described using a *HORNsdini* distribution,
- 2350 $B^{\pm(0)} \rightarrow D^0 h^\pm [\pi^{0(\mp)}]$, described using a *HORNsdini* distribution,

2351 where the particle in square brackets is not reconstructed. The mass distributions
 2352 of all the $B \rightarrow D^* h^\pm$ contributions are obtained from fits to samples of full LHCb
 2353 simulation. Examples of these fits are shown in Fig. 5.28. All shape parameters are
 2354 kept fixed in the fit to data, except for the parameter σ of the resolution function
 2355 in Eq. (5.15) which is allowed to obtain the value preferred by data.

2356 The mass distribution of $B^\pm \rightarrow D^0 h^\pm [\pi^0]$ and $B^0 \rightarrow D^0 h^\pm [\pi^\mp]$ decays recon-
 2357 structed in the $B^\pm \rightarrow D\pi^\pm$ categories is obtained from full LHCb simulation samples
 2358 of $B^\pm \rightarrow D^0 \rho^\pm$ and $B^0 \rightarrow D^0 \rho^0$ decays. The shapes were compared to those
 2359 predicted by an amplitude model for $B^0 \rightarrow D^0 \pi^\pm \pi^\mp$ decays developed by LHCb [?],
 2360 but found to be very similar for the $m(D\pi^\pm)$ range relevant to this analysis. The
 2361 obtained shapes are shown in Fig. 5.29.

2362 The mass distribution of $B^\pm \rightarrow D^0 K^\pm [\pi^0]$ and $B^0 \rightarrow D^0 K^+ [\pi^-]$ decays recon-
 2363 structed in the $B^\pm \rightarrow DK^\pm$ categories, on the other hand, is obtained from a
 2364 sample of signal decays, generated via a an amplitude model for $B^0 \rightarrow D^0 K^+ \pi^-$

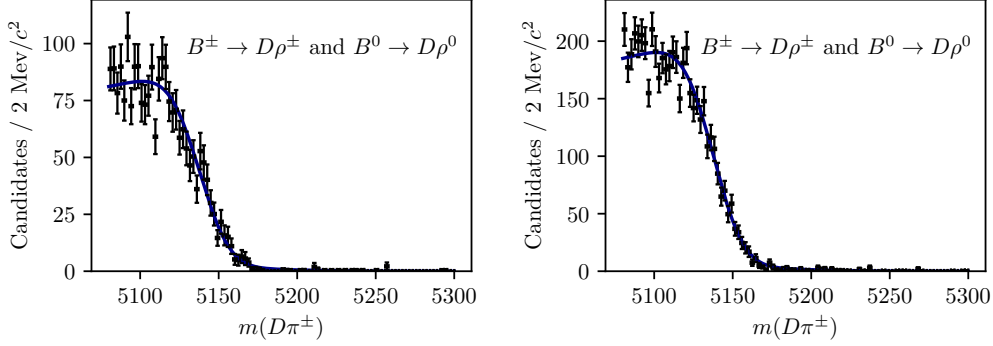


Figure 5.29: Projections of the fit to simulated $B^\pm \rightarrow D\rho^\pm$ and $B^0 \rightarrow D\rho^0$ samples reconstructed as $B^\pm \rightarrow D\pi^\pm$ decays for the (left) LL and (right) DD categories.

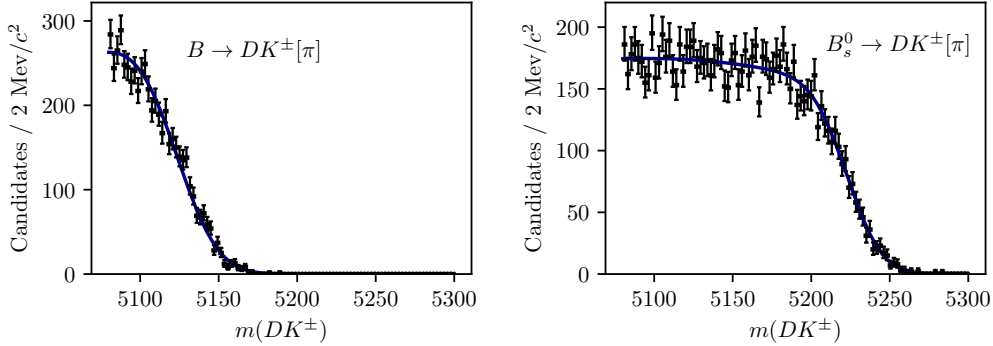


Figure 5.30: Fit projection for the fit used to obtain a shape for the partly reconstructed background from (left) $B \rightarrow DK\pi$ decays and (right) $B_s^0 \rightarrow DK^+\pi^-$ decays where a pion is not reconstructed.

decays developed by LHCb [?] and smeared to take the LHCb resolution into account. This follows an approach developed in the context of a GLW analysis based on partially reconstructed decays made within LHCb [?]. The obtained shape is shown in Fig. 5.30.

The background yields of these backgrounds are parameterised in terms of one total yield parameter, accounting for all partially reconstructed B^\pm and B^0 decays, and a number of parameters that describe the relative rates of the different contributions. In the $B^\pm \rightarrow D\pi^\pm$ channels, the relative rates of the $B^\pm \rightarrow (D^{*0} \rightarrow D^0[\pi^0])h^\pm$ and $B^0 \rightarrow (D^{*\pm} \rightarrow D^0[\pi^\pm])h^\mp$ backgrounds are fixed from the known branching fractions, and relative selection efficiencies in simulation. These backgrounds have almost identical mass distributions and it is not possible to determine the ratio in the fit to data. The relative yield of $B^\pm \rightarrow D^*(\rightarrow D^0[\gamma])\pi^\pm$ compared to the $B \rightarrow D^*(\rightarrow D^0[\pi])\pi^\pm$ is denoted $f_{D^*\gamma}^{D\pi}$ and is floated in the fit to data, as is the relative yield of $B \rightarrow D^0\pi^\pm[\pi]$ decays compared to the $B \rightarrow D^*\pi$

2379 modes, denoted $f_{D\pi\pi}^{D\pi}$. In the $B^\pm \rightarrow DK^\pm$ channels, all the relative background
2380 rates are fixed via known branching fractions and relative selection efficiencies; this
2381 is necessary to obtain a stable fit, due to the lower yields.

2382 In the $B^\pm \rightarrow DK^\pm$ categories, an additional partially reconstructed background
2383 is considered from $B_s^0 \rightarrow \bar{D}^0[\pi^+]K^-$ (and conjugate) decays. The mass shape is
2384 obtained from simulated decays, generated using an amplitude model published by
2385 LHCb [?] and smeared to account for the experimental resolution. The obtained
2386 shape is shown in Fig. 5.30. The yield of this background component is fixed relative
2387 to the signal yields in the corresponding $B^\pm \rightarrow D\pi^\pm$ category, taking the relative
2388 efficiencies, branching ratios and hadronisation factors into account [?, ?].

2389 In the $B^\pm \rightarrow DK^\pm$ channels there is a contribution from partially reconstructed
2390 $B \rightarrow D^*\pi^\pm X$ decays where the companion pion is misidentified as a kaon. The
2391 reverse contribution is negligible due to the relative branching fractions, and the
2392 fact that the $K \rightarrow \pi$ misidentification shifts most of these background decays
2393 below the mass range of the fit. These are modelled using analytic, empirical
2394 mass distributions (essentially sums of a number of regular *HORN*/*HILLdini*
2395 distributions), with parameters that are determined in fits to simulated $B \rightarrow D^*\pi^\pm$
2396 and $B \rightarrow D\rho$ decays where the pion is reconstructed with the kaon mass hypothesis.
2397 The shapes are fixed in the fit to data.

2398

2399 Partially reconstructed backgrounds that are not modelled

2400 It was considered whether a background from $\Lambda_b^0 \rightarrow D^0 p \pi^-$ decays where a pion is
2401 not reconstructed, and the proton is misidentified as the companion, can be expected
2402 to contribute significantly. This background has been investigated using full LHCb
2403 simulation samples for the D final state $K_S^0 \pi^+ \pi^-$. Taking into account the selection
2404 efficiencies, branching fractions, and hadronisation fraction of this background, the
2405 expected relative yield of the Λ_b^0 background compared to signal of 0.03 % in the
2406 $B^\pm \rightarrow D\pi^\pm$ channel, which is completely negligible. In the $B^\pm \rightarrow DK^\pm$ channel
2407 the yield relative to signal is about 1.2 %, for total of about 200 decays. However,
2408 most of these lie at B masses smaller than the signal peak, and their impact is
2409 small. Therefore it is not necessary to model the background in the nominal fit; a
2410 systematic uncertainty is assigned that accounts for the small potential impact.

2411 In the analogous case of $\Lambda_b^0 \rightarrow D^0 p K^-$ decays, the missing energy of the non-
2412 reconstructed kaon results in a reconstructed B mass below the fit range.

2413 It has also been investigated whether a background from $\Lambda_b^0 \rightarrow \Lambda_c^+ \pi^-$ or
2414 $\Lambda_b^0 \rightarrow \Lambda_c^+ K^-$ decays can be expected, where $\Lambda_c^+ \rightarrow p K_S^0 \pi^+ \pi^-$, a pion is missed

and the proton is misidentified as a pion or kaon from the D decay. In practice, the background is sufficiently suppressed from the applied D mass requirement to have no significant impact, and is therefore not modelled. A systematic uncertainty is assigned that accounts for any potential impact on the measurement due to this choice.

5.4.4 Combinatorial background

The combinatorial background is modelled with an exponentially falling density function, where both the yield and exponential slope are determined independently for each category. This shape is found to model the combinatorial well in all categories, most evident in the high- m_B regions where this background dominates.

5.4.5 Fit results

The fit range is chosen to be $m_B \in [5080, 5800] \text{ MeV}/c^2$. The low end of this interval includes the higher mass peak of the double-peak structure in the partially reconstructed background, which helps the fit constrain the relative contributions of backgrounds in the lowmass region. A number of additional backgrounds exist at even lower m_B values, thus extending the fit range to lower masses would necessitates an extended model, but not benefit the description of the signal region. The high end of the interval includes enough combinatorial background to allow the fit to determine the exponential slope parameter accurately.

A large number of pseudoexperiments are carried out to verify that the fit procedure is self-consistent, in which toy data sets are generated according to the expected B mass distributions, and then fitted. None of the parameters obtained in the fit exhibit a mean bias different from zero. For most parameters the uncertainties are well estimated. This is the case for the signal yields, and the DK^\pm - $D\pi^\pm$ yield ratio \mathcal{R} , as evidenced by the pull plots in Fig. 5.31. The fit underestimates the uncertainty by 10-20 % for some of the parameters related to the partly reconstructed backgrounds, as shown in Fig. 5.32, but this is taken into account when the uncertainties are propagated to the observables in the second-stage fit, as described in Section 5.6.3.

The projections of the fit to data are shown in Figs. 5.33 and 5.34, for the $D \rightarrow K_S^0 \pi^+ \pi^-$ and $D \rightarrow K_S^0 K^+ K^-$ data sets, respectively. The obtained yields for each fit component are given in Table 5.6. The total yield of $B^\pm \rightarrow D\pi^\pm$ decays is approximately 230,000 across all channels. The obtained value of the yield ratio is $\mathcal{R}_{K/\pi} = (7.7 \pm 0.1) \%$, corresponding to a total $B^\pm \rightarrow DK^\pm$ yield of 16,500, of which

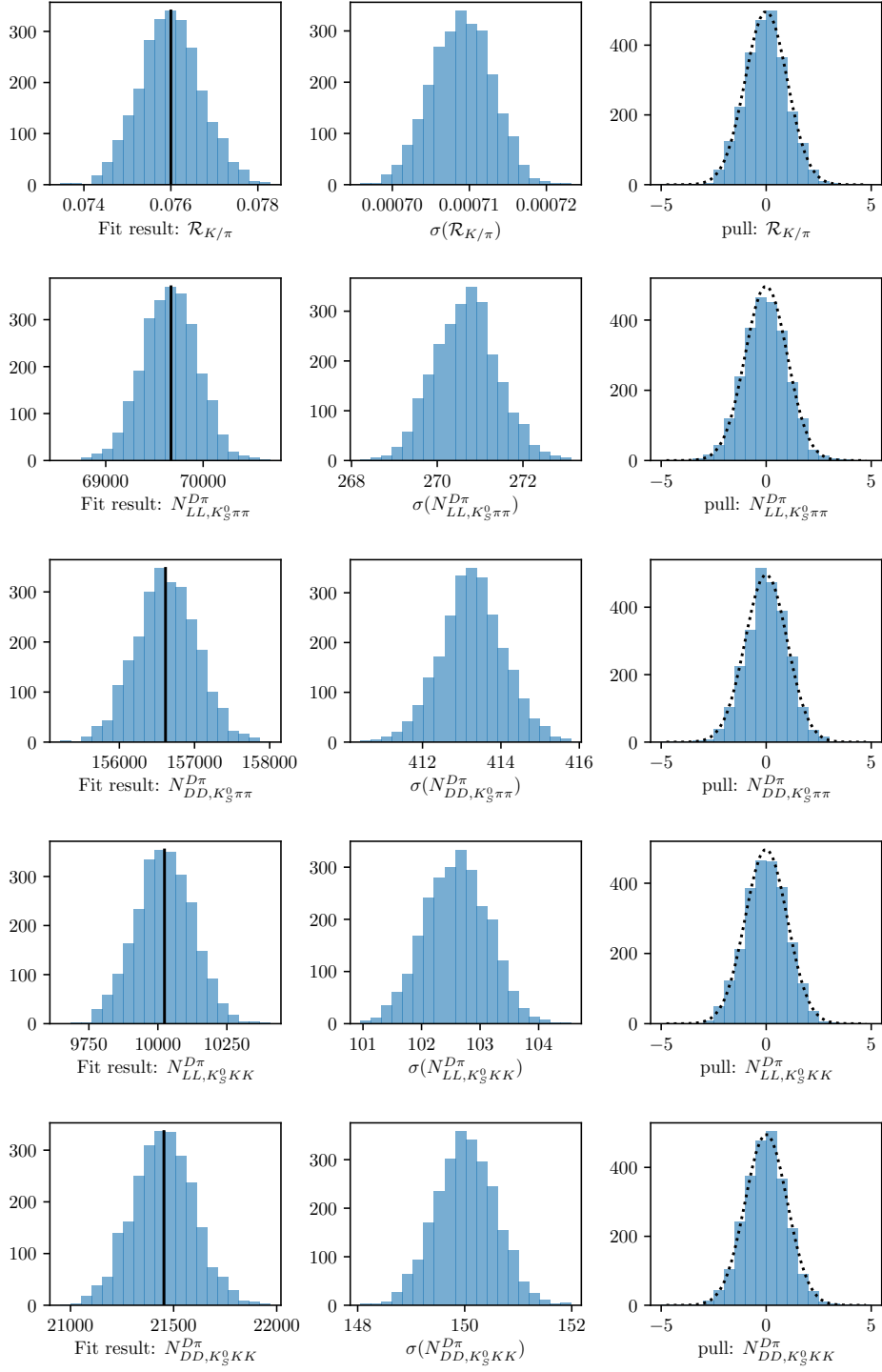


Figure 5.31: The (left) fitted value, (centre) estimated statistical uncertainty, and (right) pull plots for the signal yield parameters, as obtained in a number of pseudo experiments. The black line on the left shows the value used to generate the pseudo data sets; the dotted line on the right shows a Gaussian distribution with mean equal to zero and a standard deviation equal to unity.

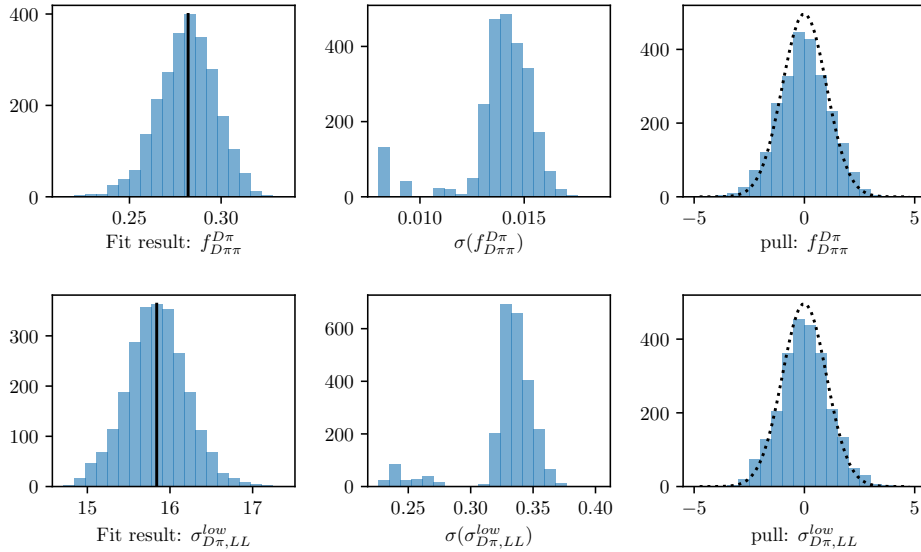


Figure 5.32: The (left) fitted value, (centre) estimated statistical uncertainty, and (right) pulls obtained in a number of pseudo experiments for two examples of parameters relating to the partially reconstructed backgrounds, where the uncertainties are slightly underestimated on average. The standard deviation of the pull distributions is approximately 1.15 in both cases.

about 14,300 pass the PID requirement and are reconstructed in the $B^\pm \rightarrow DK^\pm$ category. This value of \mathcal{R} is in excellent agreement with expectation from the known branching fractions [?], which predict $\mathcal{R}_{K/\pi}^{\text{PDG}} = (7.8 \pm 0.3)\%$.² The shape parameters determined in the fit to data are summarised in Table 5.7.

5.5 Measurement of the CP-violation observables

The section describes the second fit stage, in which the *CP*-violation observables of interest are determined. Compared to the first fit stage, the candidates are further split by B charge, and by the assigned Dalitz bin number, making for a total of 160 subcategories.³ Another extended maximum-likelihood fit is carried out, in which shape parameters of all signal and background components are fixed to those determined in the first fit stage, and all floating parameters relate to the signal and background yields. The signal yields are expressed in terms of the

²While it would seem this measurement thus determines the yield ratio $\mathcal{R}_{K/\pi}$ with a much better precision than the current world average uncertainty, that is because the result quoted here does not include any systematic uncertainties; it is only included to serve as a, successfully passed, cross check.

³In the thesis, the word *category* is used for the 8-way split of data by companion species, K_S^0 track type, and D -decay mode, indexed with a c ; the word *bin* denotes the 16 (4) regions of the $D \rightarrow K_S^0 \pi^+ \pi^-$ ($D \rightarrow K_S^0 K^+ K^-$) Dalitz plots, indexed with an i ; the simultaneous grouping by *category*, *bin*, and B charge is denoted a *subcategory*, of which there are $4 \times 2 \times (16 + 4) = 160$.

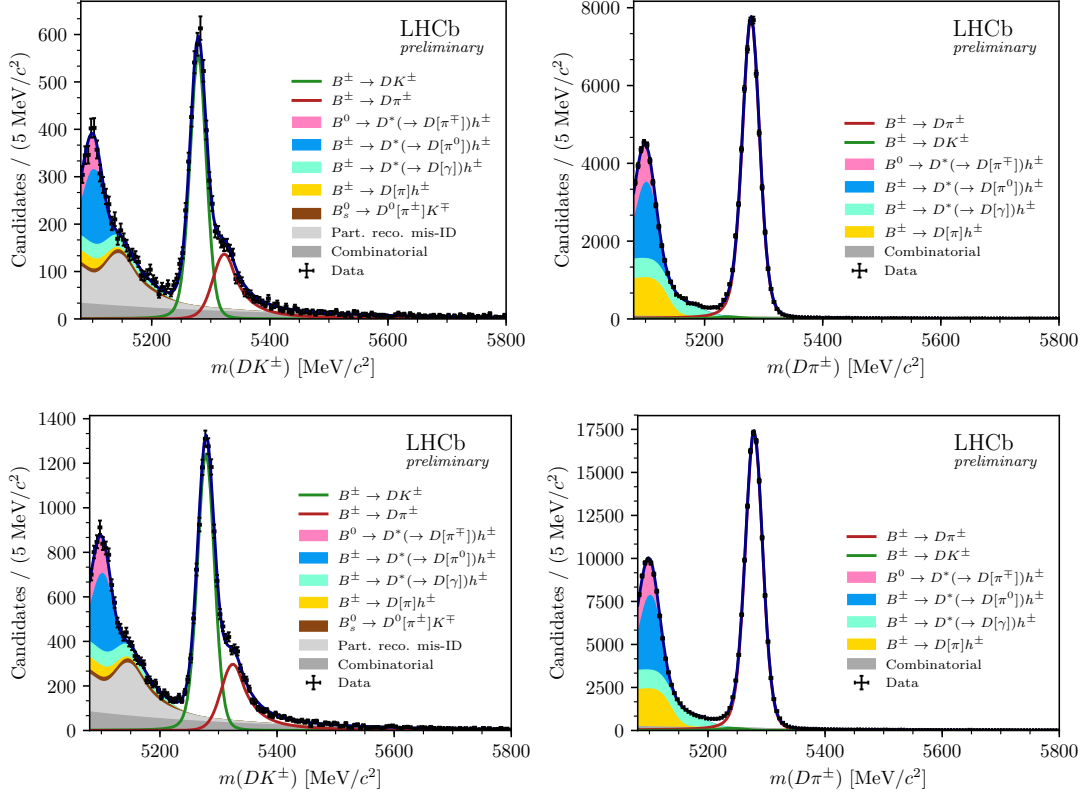


Figure 5.33: The invariant mass distribution for the (left) $B^\pm \rightarrow DK^\pm$ channel and (right) $B^\pm \rightarrow D\pi^\pm$ channel, where $D \rightarrow K_S^0\pi^+\pi^-$ and the K_S^0 is in the (top) LL and (bottom) the DD categories. The particle within square brackets in the legend denotes the particle that has not been reconstructed.

observables of interest, $(x_\pm^{DK}, y_\pm^{DK}, x_\xi^{D\pi}, y_\xi^{D\pi})$, allowing the fit to determine their optimal values. The details of the fit setup are summarised in the following section, along with a number of studies that lead to the specific setup being chosen. The results are presented in Section 5.5.2, and a wide range of consistency checks are described in Section 5.5.3.

5.5.1 Fit setup

The basic principle of the measurement is that the signal yields in each bin (in a given category) are defined using the equations of Chapter 2, in order to allow for the determination of the CP -violation observables. In practice, a set of variables are defined

$$Y_{c,i}^- = F_{c,-i} + [(x_-^c)^2 + (y_-^c)^2]F_{c,-i} + 2\sqrt{F_{c,i}F_{c,-i}}(c_i^c x_-^c + s_i^c y_-^c), \quad (5.17)$$

$$Y_{c,i}^+ = F_{c,-i} + [(x_+^c)^2 + (y_+^c)^2]F_{c,-i} + 2\sqrt{F_{c,i}F_{c,-i}}(c_i^c x_+^c - s_i^c y_+^c), \quad (5.18)$$

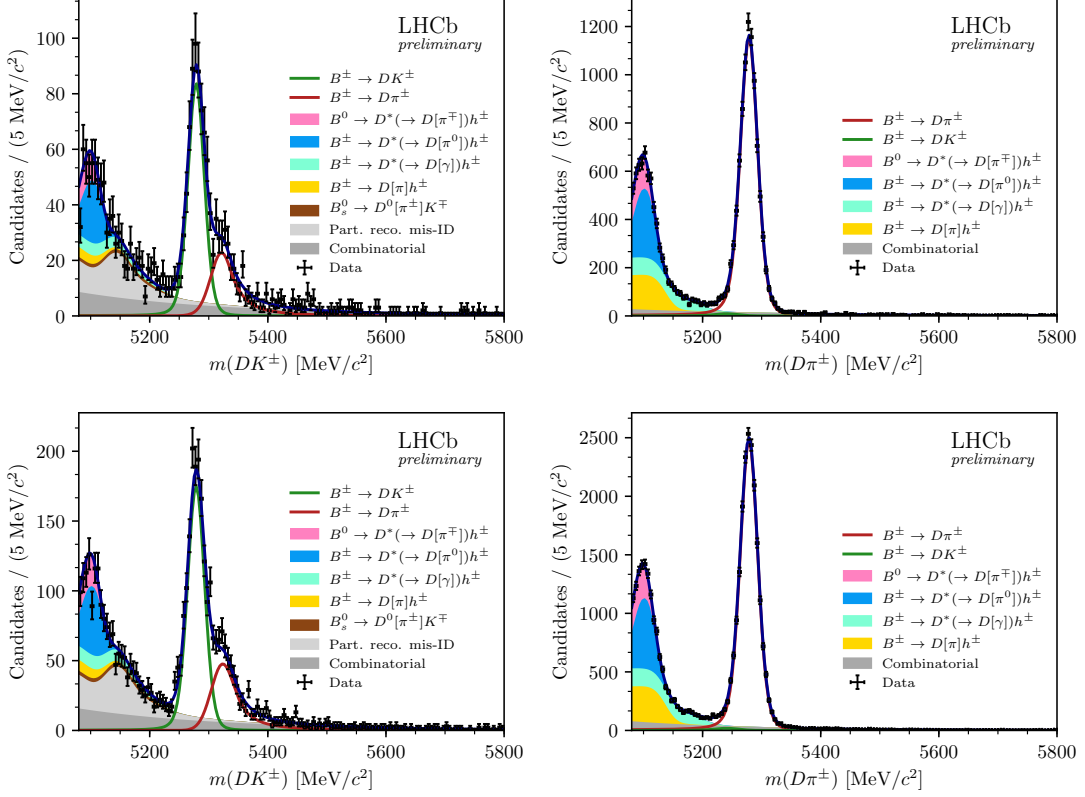


Figure 5.34: The invariant mass distribution for the (left) $B^\pm \rightarrow DK^\pm$ channel and (right) $B^\pm \rightarrow D\pi^\pm$ channel, where $D \rightarrow K_S^0 K^+ K^-$ and the K_S^0 is in the (top) LL and (bottom) the DD categories. The particle within square brackets in the legend denotes the particle that has not been reconstructed.

for each data category, c , in terms of which the bin yields that enter the likelihood are given by

$$N_{c,i}^\pm = \frac{Y_{c,i}^\pm}{\sum_j Y_{c,j}^\pm} \times N_{c,\text{total}}^\pm. \quad (5.19)$$

This parameterisation is essentially identical to the expressions in Section 2.4, slightly modified so that the phase-space-integrated yields of B^+ and B^- decays in a given category are determined directly, in lieu of the normalisation constants h^\pm of that section. As discussed briefly in Section 2.4, there are choices to be made in terms of how the x and y are parameterised in the $B^\pm \rightarrow D\pi^\pm$ channel, and how the F_i parameters are determined. A series of feasibility studies were carried out to determine the optimal setup; these are presented in the following section, before the final fit setup is described in detail.

Table 5.6: Fitted total candidate yields. The quoted signal yields are for the number of candidates that survive the respective PID cut, whereas the DK^\pm - $D\pi^\pm$ ratio is corrected for PID and selection efficiencies so that it corresponds to the branching ratio.

Component	LL	DD
Signal		
$B^\pm \rightarrow D(\rightarrow K_S^0\pi^+\pi^-)\pi^\pm$	$61,573 \pm 254$	$139,080 \pm 389$
$B^\pm \rightarrow D(\rightarrow K_S^0K^+K^-)\pi^\pm$	$9,160 \pm 98$	$19,910 \pm 144$
$R_{K/\pi} = n(DK)/n(D\pi)$ (%)		7.72 ± 0.08
Combinatorial background		
$B^\pm \rightarrow D(\rightarrow K_S^0\pi^+\pi^-)\pi^\pm$	$3,479 \pm 198$	$9,928 \pm 376$
$B^\pm \rightarrow D(\rightarrow K_S^0K^+K^-)\pi^\pm$	$1,103 \pm 94$	$2,545 \pm 155$
$B^\pm \rightarrow D(\rightarrow K_S^0\pi^+\pi^-)K^\pm$	$1,826 \pm 107$	$3,987 \pm 177$
$B^\pm \rightarrow D(\rightarrow K_S^0K^+K^-)K^\pm$	380 ± 39	655 ± 58
Partially reconstructed background		
$B^\pm \rightarrow D(\rightarrow K_S^0\pi^+\pi^-)\pi^\pm$	$43,004 \pm 242$	$95,452 \pm 403$
$B^\pm \rightarrow D(\rightarrow K_S^0K^+K^-)\pi^\pm$	$6,247 \pm 99$	$13,241 \pm 157$
$R_{K/\pi}^{low} = n_{low}(DK)/n_{low}(D\pi)$ (%)		6.65 ± 0.12

2481 Feasibility of alternative fit setups

2482 The motivation for promoting the $B^\pm \rightarrow D\pi^\pm$ channel to a signal channel is two-fold:
 2483 one aim is to extract the information on γ from the $B^\pm \rightarrow D\pi^\pm$ data, even the
 2484 precision gain is limited, and another is to be able to the F_i parameters directly
 2485 from the $B^\pm \rightarrow Dh^\pm$ channels, to avoid the need for a control channel and a
 2486 simulation-reliant efficiency correction. Two different sets of observables can be
 2487 defined to describe the CP -violation effects in the $B^\pm \rightarrow D\pi^\pm$ channel:

- 2488 • one option, defined the 8-parameters setup below, is to define a new set of four
 2489 Cartesian for the $B^\pm \rightarrow D\pi^\pm$ mode, $(x_-^{D\pi}, y_-^{D\pi}, x_+^{D\pi}, y_+^{D\pi})$, defined analogously
 2490 to the $B^\pm \rightarrow DK^\pm$ observables

$$x_\pm^{D\pi} = r_B^{D\pi} \cos(\delta_B^{D\pi} \pm \gamma), \quad y_\pm^{D\pi} = r_B^{D\pi} \sin(\delta_B^{D\pi} \pm \gamma), \quad (5.20)$$

- 2491 • another, proposed in Refs. [?, ?], is to introduce the parameter

$$\xi_{D\pi^\pm} = \left(\frac{r_B^{D\pi^\pm}}{r_B^{DK^\pm}} \right) \exp[i(\delta_B^{D\pi^\pm} - \delta_B^{DK^\pm})] \quad (5.21a)$$

Table 5.7: Fitted parameter values.

	LL	DD
$\sigma_{D\pi}$ (MeV/ c^2)	14.27 ± 0.05	14.58 ± 0.04
σ_{DK} (MeV/ c^2)	13.61 ± 0.24	14.19 ± 0.17
μ (MeV/ c^2)		5278.60 ± 0.04
Combinatorial Slopes		
Decay mode	Slope ($10 \times 10^{-3} GeV^{-1}c^2$)	
$B^\pm \rightarrow D(\rightarrow K_S^0\pi^+\pi^-)\pi^\pm$	-3.1 ± 0.2	-4.0 ± 0.1
$B^\pm \rightarrow D(\rightarrow K_S^0K^+K^-)\pi^\pm$	-4.1 ± 0.4	-5.5 ± 0.3
$B^\pm \rightarrow D(\rightarrow K_S^0\pi^+\pi^-)K^\pm$	-3.2 ± 0.2	-3.9 ± 0.2
$B^\pm \rightarrow D(\rightarrow K_S^0K^+K^-)K^\pm$	-4.2 ± 0.4	-4.3 ± 0.4
Part. Reco.		
$\sigma_{D\pi}^{low}$ (MeV/ c^2)	13.73 ± 0.33	13.78 ± 0.28
$f_{D\pi\pi}^{D\pi}$		0.268 ± 0.013
$f_{D^*\gamma}^{D\pi}$		0.317 ± 0.005

and then determine the observables

$$x_\xi^{D\pi} = \text{Re}[\xi_{D\pi^\pm}] \quad y_\xi^{D\pi} = \text{Im}[\xi_{D\pi^\pm}]. \quad (5.21b)$$

This is denoted the 6-parameters setup below. In terms of $x_\xi^{D\pi}$ and $y_\xi^{D\pi}$, the usual Cartesian x_\pm and y_\pm are given by

$$x_\pm^{D\pi} = x_\xi^{D\pi} x_\pm^{DK} - y_\xi^{D\pi} y_\pm^{DK}, \quad y_\pm^{D\pi} = x_\xi^{D\pi} y_\pm^{DK} + y_\xi^{D\pi} x_\pm^{DK}. \quad (5.22)$$

The former parameterisation has the benefit that information on γ from the $B^\pm \rightarrow DK^\pm$ and $B^\pm \rightarrow D\pi^\pm$ channels is encoded in separate sets of observables, whereas the latter parameterisation encodes information on CP violation from both channel in the (x_\pm^{DK}, y_\pm^{DK}) parameters. In combinations of many measurements, it is a useful cross check to be able to compare constraints obtained from individual decay modes; a good example is the LHCb combination from 2016 [?] where both $B^\pm \rightarrow DK^\pm$ and $B^\pm \rightarrow Dh^\pm$ combinations are made and compared in detail. This is only possible with the former parameterisation. On the other hand, the latter parameterisation avoids the introduction of two non-physical degrees of freedom, which, as seen below, leads to better statistical behaviour.

In order to inform the choice of parameterisation, a series of pseudo experiments has been carried out to compare the obtainable precision on γ (these studies were

performed, and discussed within LHCb, prior to the publication of Ref. [?]; thus, the results presented here constitute independent work, even if there is some overlap in scope and conclusions with that reference). Many simulated data sets were generated, constituting of a number signal yields approximately equal to the expected yields in the full Run 1 and 2 LHCb data set: approximately 15,000 $B^\pm \rightarrow DK^\pm$ decays and 210,000 $B^\pm \rightarrow D\pi^\pm$ decays.⁴ The signal decays were distributed between Dalitz bins according to $(\gamma, r_B^{DK}, \delta_B^{DK}) = (75^\circ, 0.1, 130^\circ)$ in the $B^\pm \rightarrow DK^\pm$ mode, which is to the world average values of direct γ measurements at the time. In the $B^\pm \rightarrow D\pi^\pm$ mode, the behaviour is investigated for different sets of input values; of most importance is the case $(r_B^{D\pi}, \delta_B^{D\pi}) = (0.005, 300^\circ)$, because it corresponds to the solution in the LHCb combination [?] that is in agreement with the theoretical expectation $r_B^{D\pi} \simeq 0.005$ [?]. The behaviour at larger $r_B^{D\pi}$ values is also investigated. The generated data sets are fitted using both parameterisations, and the observables are interpreted in terms of the underlying physics parameters using a maximum-likelihood fit, essentially following the procedure outlined in Section 5.7.1. In the 8-parameter setup it is possible to determine γ using the results in either the $B^\pm \rightarrow DK^\pm$ or $B^\pm \rightarrow D\pi^\pm$ channels separately, or consider the combined results; in the 6-parameter setup only the latter option is available. The studies are performed in two modes: with the F_i floating in the fit, emulating a realistic fit to data, as well as with the F_i fixed to the input values used in data generation. The latter studies emulate a setup where the F_i parameters are determined in an ultra-high statistics control channel, and perfect efficiency corrections are applied. In all cases, a single set of F_i parameters is shared between the $B^\pm \rightarrow DK^\pm$ and $B^\pm \rightarrow D\pi^\pm$ modes.

The 6-parameter setup shows significantly better statistical performance than the 8-parameter setup in the realistic case where the F_i parameters are determined in the fit and $r_B^{D\pi} \sim 0.005$.⁵ The fits that employ the 6-parameter setup behave well in this case, whereas the additional degrees of freedom in the 8-parameter fit leads to essentially all parameters being 100 % (anti-)correlated, and a significant number of fits not converging. For the fits that do converge, the uncertainties on the observables are significantly larger due to the large correlations, as shown exemplified with the case of y_+^{DK} in Fig. 5.35. This essentially determines the choice of parameterisation: it is possible to reliably model *CP* violation in the $B^\pm \rightarrow D\pi^\pm$ channel and simultaneously determine the F_i parameters by using the 6-parameter setup, but not by using the 8-parameter setup.

⁴No backgrounds were included in these studies, and thus the quoted uncertainties on γ are better than what is obtainable in the final measurement; a similar study including realistic backgrounds is presented for the final setup below.

⁵For larger, non-physical values of $r_B^{D\pi} > 0.03$ both fit setups behave well.

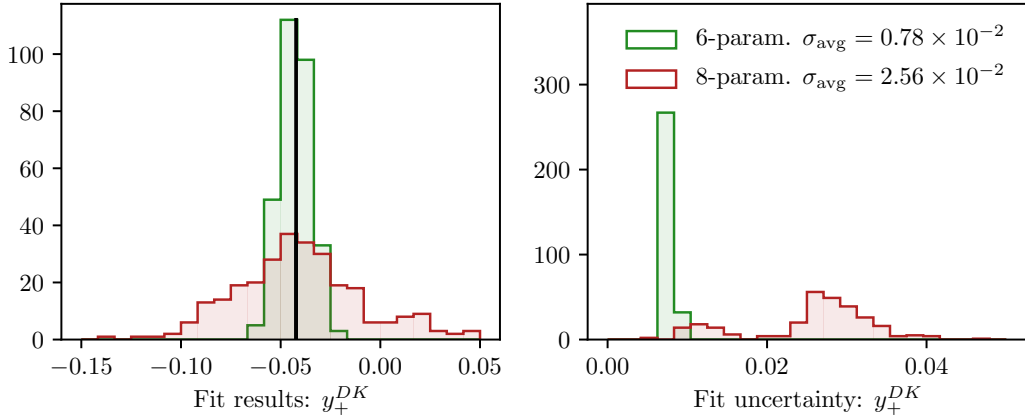


Figure 5.35: Caption here

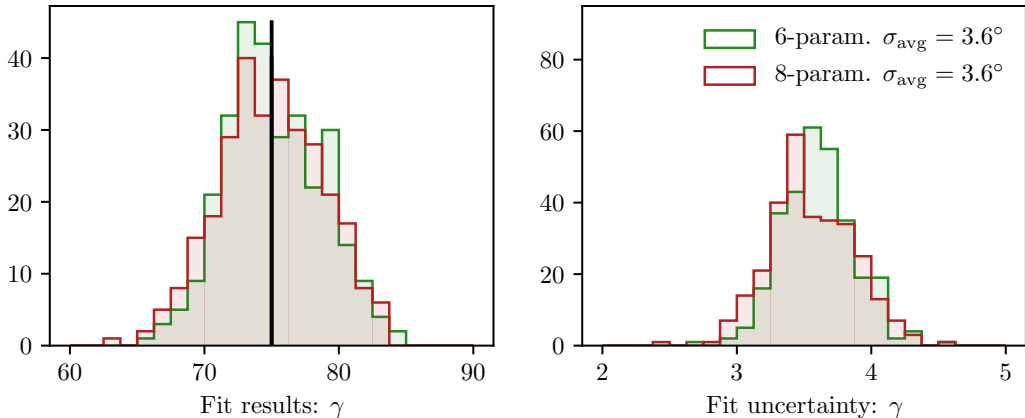


Figure 5.36: Caption here

Interestingly, when constraints on γ are . This is illustrated in Fig. ??

Furthermore, both the 6- and 8-parameter setups lead to fits that behave well in the studies where the F_i parameters are kept fixed, and the resulting uncertainties on the Cartesian observables and γ are essentially identical. Thus, the 6-parameter setup does not inherently lead to a gain in precision over the 8-parameter setup; the strength of the parameterisation is that it allows for a reliable, simultaneous determination of the F_i parameters and the observables of interest. This conclusion differs somewhat from the one drawn in Ref. [?].

The fixed- F_i studies allow for an assessment of the gain in precision on γ due to the inclusion of the $B^\pm \rightarrow D\pi^\pm$ mode, by comparing the precision obtained in the simultaneous fits with that obtained when γ is constrained using only information from the $B^\pm \rightarrow DK^\pm$ channel. In the realistic case where $r_B^{D\pi} = 0.005$, the gain in precision is about 0.1° . The reason for the small impact, in spite of the yield being

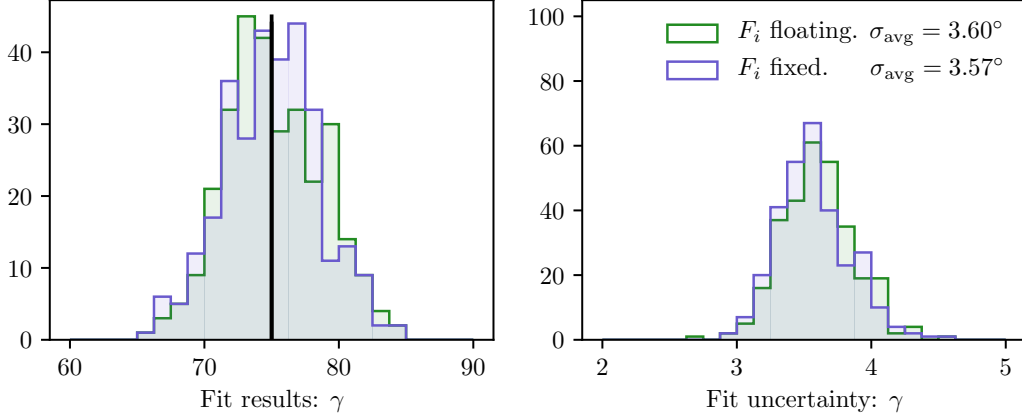


Figure 5.37: Caption here

approximately 14 times larger in the $B^\pm \rightarrow D\pi^\pm$ channel than in the $B^\pm \rightarrow DK^\pm$ channel, is that r_B is 20 times smaller, and the CP asymmetries are proportional to r_B . Thus, the main improvement to the analysis from including $B^\pm \rightarrow D\pi^\pm$ as a signal channel comes from the ability to determine the F_i parameters without adding a large systematic uncertainty.⁶

Finally, it is worth considering whether any precision can be gained by including information on the F_i parameters from a control channel, even if the fit is well behaved without external information. The potential yield in the $\bar{B}^0 \rightarrow D^{*+}(\rightarrow D^0\pi^+) \mu^- \bar{\nu}_\mu X$ control channel is approximately three times larger than in the $B^\pm \rightarrow D\pi^\pm$ channel, and it does therefore offer a better statistical handle on the F_i values (at the significant cost of having to worry about efficiency corrections). This question can be answered by comparing the obtained precision on γ in the fits where F_i parameters were floating, to the precision in the case where they were kept fixed. Such a comparison is shown for the 6-parameter setup in Fig. 5.37 for the realistic scenario where $r_B^{D\pi} = 0.005$. The difference in the average $\sigma(\gamma)$ is *less than* 0.05° , which is of course completely negligible. Therefore, no gain in precision can be obtained by including the control channel in the analysis, and it is not considered further.

Final choice of observables and the determination of the F_i parameters

In the chosen setup, a single set of four parameters, $(x_-^{DK}, y_-^{DK}, x_+^{DK}, y_+^{DK})$, are shared between *all* $B^\pm \rightarrow DK^\pm$ categories; they enter the expressions of Eq. (5.17)

⁶If this comparison is made using the parameter set $(r_B^{D\pi}, \delta_B^{D\pi}) = (0.03, 330^\circ)$, which corresponds to the alternative, non-physical solution in the LHCb combination [?], the gain in precision is 1.3° instead; this fact made the statistical interpretation of the $B^\pm \rightarrow Dh^\pm$ combination in Ref. [?] non-trivial.

2575 directly, and are thus determined in the fit. In the $B^\pm \rightarrow D\pi^\pm$ categories, the
 2576 four corresponding parameters, $(x_-^{D\pi}, y_-^{D\pi}, x_+^{D\pi}, y_+^{D\pi})$, are parameterised in terms
 2577 of (x_\pm^{DK}, y_\pm^{DK}) and the additional two observables $(x_\xi^{D\pi}, y_\xi^{D\pi})$. The F_i parameters
 2578 are determined in the fit, being shared between the $B^\pm \rightarrow DK^\pm$ and $B^\pm \rightarrow D\pi^\pm$
 2579 channels. However, separate parameter sets are determined for the LL and DD
 2580 categories because the acceptance profile over the Dalitz plot differs between them.

2581 The F_i parameters are subject to the constraint that $\sum_{i=-\mathcal{N}}^{\mathcal{N}} F_i^c = 1$, for each
 2582 category, c . Therefore, it is beneficial to introduce a reparameterisation in the
 2583 likelihood function, where the F_i parameters are expressed in terms of a set of
 2584 recursive fractions

$$\mathcal{R}_i = \begin{cases} F_i & , \quad i = -\mathcal{N} \\ F_i / (\sum_{j \geq i} F_j) & , \quad -\mathcal{N} < i < +\mathcal{N} \end{cases} , \quad (5.23)$$

2585 for which the constraint is much simpler, namely that each individual \mathcal{R}_i parameter
 2586 lies in the interval $[0, 1]$. This parameterisation leads to well behaved fits, where
 2587 the \mathcal{R}_i parameters do not suffer from significant correlations.

2588 Strong-phase inputs

2589 The strong-phase parameters (c_i, s_i) are fixed in the fit to data. In the $D \rightarrow K_S^0 \pi^+ \pi^-$
 2590 channels, the combined CLEO [?] and BESIII [?] measurement results are used, as
 2591 reported in Ref. [?]. The $D \rightarrow K_S^0 K^+ K^-$ categories also use combined CLEO [?]
 2592 and BESIII results [?], which are reported in Ref. [?]. The experimental uncertainty
 2593 on these measurements is propagated to the measured CP -violation observables
 2594 as part of the systematic uncertainties in Section 5.6.1.

2595 Treatment of backgrounds

2596 The yield of combinatorial background decays is determined independently in each
 2597 bin. A single, overall bin yield of partially reconstructed background from B^\pm and
 2598 B^0 decays is determined in each of the 160 subcategories; the relative contribution
 2599 from each individual background is fixed from the results of the first-stage fit,
 2600 corrected for the different fit region (a systematic uncertainty is assigned due to this
 2601 choice). In the $B^\pm \rightarrow DK^\pm$ channels, the bin yields of the partially reconstructed
 2602 background from $B_s^0 \rightarrow \bar{D}^0 [\pi^+] K^-$ decays are expressed via the F_i , exploiting that
 2603 a positive companion particle is always produced along with a \bar{D}^0 meson (and vice
 2604 versa). The overall yield is fixed from the results of the first stage fit. Finally,
 2605 the yield of the $D\pi^\pm \leftrightarrow DK^\pm$ cross-feed components in each bin are determined
 2606 via the obtained yield of correctly identified decays in the corresponding bin, and
 2607 the known PID efficiencies. This is true for both fully and partially reconstructed
 2608 decays, although only a $D\pi^\pm \rightarrow DK^\pm$ component is included in the latter case.

Table 5.8: Mean biases and pulls for the observables of interest in the final, binned fit, obtained in a large number of pseudoexperiments.

Parameter	Name in code	Mean bias ($\times 10^{-2}$)	Mean pull	Pull width
x_-^{DK}	A_xm_dk	-0.018 ± 0.022	-0.01 ± 0.02	1.01 ± 0.02
y_-^{DK}	A_ym_dk	-0.014 ± 0.026	-0.00 ± 0.02	0.99 ± 0.02
x_+^{DK}	A_xp_dk	-0.018 ± 0.022	-0.01 ± 0.02	1.00 ± 0.02
y_+^{DK}	A_yp_dk	-0.016 ± 0.028	0.01 ± 0.02	1.00 ± 0.02
$x_\xi^{D\pi}$	A_Re_xi_dpi	0.029 ± 0.052	0.06 ± 0.02	1.00 ± 0.02
$y_\xi^{D\pi}$	A_Im_xi_dpi	0.000 ± 0.060	0.01 ± 0.02	1.00 ± 0.02

2609 The choice of fit range

2610 The fit range is decreased to $m_B \in [5150, 5800] \text{ MeV}/c^2$. The information from
 2611 candidates with lower reconstructed B masses was useful in determining the relative
 2612 rates and free mass shape parameters of the partially reconstructed background
 2613 components in the first-stage fit; however, with these fixed in the second-stage
 2614 fit, this is no longer the case. Furthermore, the setup assumes that the shape of
 2615 the partially reconstructed background is identical across the Dalitz bins. This
 2616 assumption is not perfectly true, but the impact is minimal when the lower limit of
 2617 the fit range is taken to be $5150 \text{ MeV}/c^2$, as described further in Section 5.6.3.

2618 Self-consistency check

2619 In order to establish the fit stability and investigate a potential bias, a series of
 2620 pseudo experiments are run, in which data sets are generated using the model, and
 2621 then fitted back. The total yields are taken from the first-stage fit. The signal
 2622 yields are distributed between Dalitz bins using input physics parameters that
 2623 approximately equal the values obtained in Section 5.5.2 from the results of the fit
 2624 to data. The F_i parameters are taken from a fit to data. The partly reconstructed
 2625 background is distributed as " D^0 -like", ie. in the B^\pm channels $N_i^\pm \propto F_{\mp i}$, except for
 2626 the B_s^0 background, which is " \bar{D}^0 -like" ($N_i^\pm \propto F_{\pm i}$). The combinatorial background
 2627 includes real D mesons paired with a random bachelor, as well as fake D mesons
 2628 that are themselves made up of random tracks. The former is distributed as 50/50
 2629 D^0 -like and \bar{D}^0 -like in the toy generation, whereas the latter is assumed to be evenly
 2630 distributed over the Dalitz plot (ie. the bin yield is proportional to the bin area).

2631 A set of 2000 pseudo experiments has been run, out of which 98.8% con-
 2632 verged properly. The pull plots for the observables of interest are shown in
 2633 Figs. 5.38 and 5.39; the mean biases and pulls are summarised in Table 5.8. No
 2634 biases are statistically significant, and the uncertainties are seen to be well estimated.

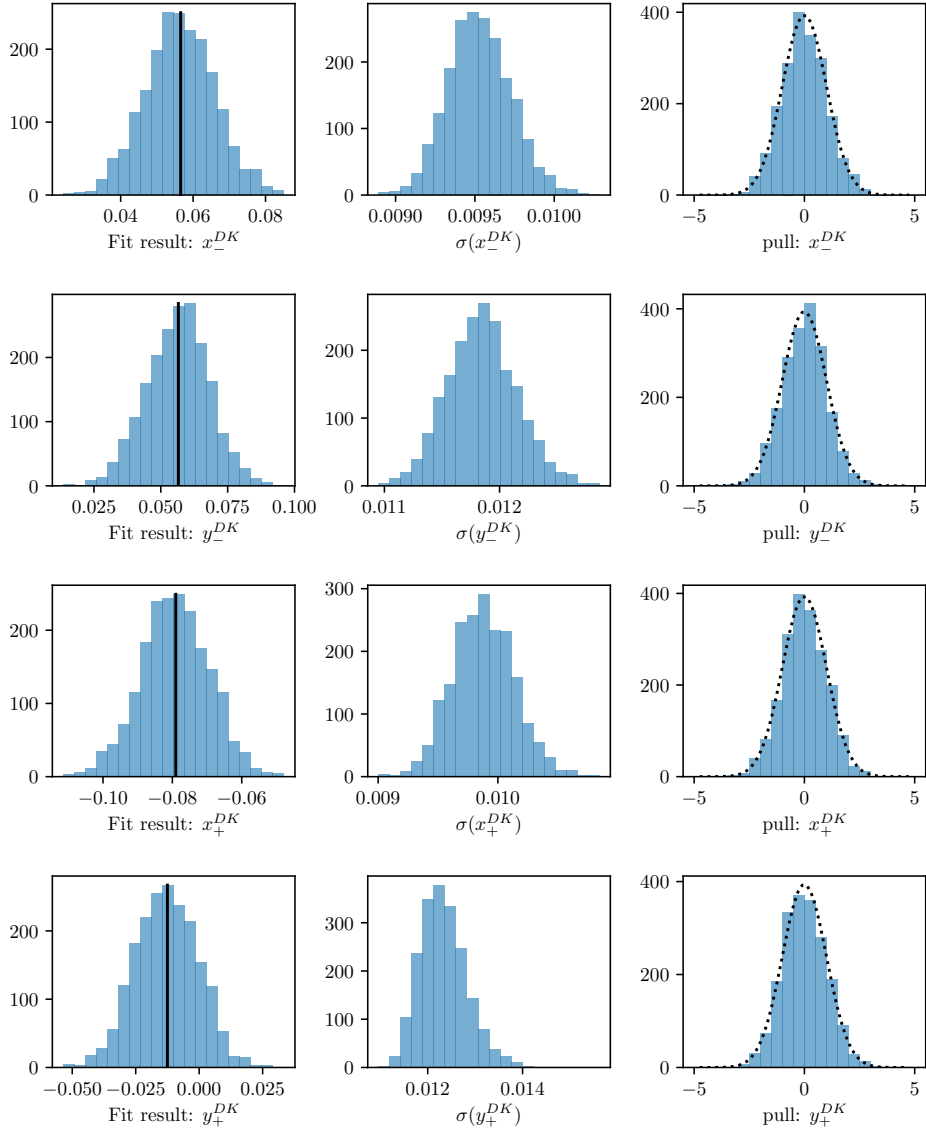


Figure 5.38: The (left) fitted value, (centre) estimated statistical uncertainty, and (right) pulls for the $B^\pm \rightarrow DK^\pm$ observables, as obtained in a number of pseudo experiments. The black line on the left shows the value used to generate the pseudo data sets; the dotted line on the right shows a Gaussian distribution with mean equal to zero and a standard deviation equal to unity.

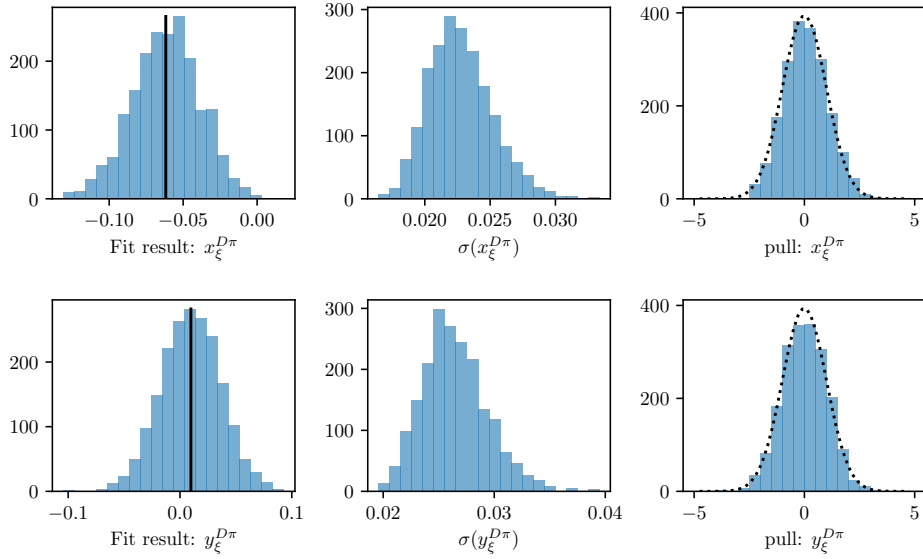


Figure 5.39: The (left) fitted value, (centre) estimated statistical uncertainty, and (right) pulls for the $B^\pm \rightarrow D\pi^\pm$ observables, as obtained in a number of pseudo experiments. The black line on the left shows the value used to generate the pseudo data sets; the dotted line on the right shows a Gaussian distribution with mean equal to zero and a standard deviation equal to unity.

5.5.2 Main results

The values and statistical uncertainties of observables obtained in the fit are

$$\begin{aligned} x_-^{DK} &= (-5.68 \pm 0.96) \times 10^{-2}, & y_-^{DK} &= (-6.55 \pm 1.14) \times 10^{-2}, \\ x_+^{DK} &= (-9.30 \pm 0.98) \times 10^{-2}, & y_+^{DK} &= (-1.25 \pm 1.23) \times 10^{-2}, \\ x_\xi^{D\pi} &= (-5.47 \pm 1.99) \times 10^{-2}, & y_\xi^{D\pi} &= (0.71 \pm 2.33) \times 10^{-2}. \end{aligned} \quad (5.24)$$

The statistical correlation matrix for the observables is given in Table 5.9. None of the correlations are larger than 15 % and the values of both uncertainties and correlation coefficients are similar to those obtained in the feasibility studies. The 2D log-likelihood profile for the observables is shown in Fig. 5.40, based on a full likelihood scan, where the fit is repeated with the observables fixed to a range of values around the optimal solution. It can be seen that the likelihood profile obtained in the scan is very well modelled by the Gaussian approximation, based on the Hessian matrix at maximum likelihood.

The full set of fit projections in all 160 subcategories is included in Appendix A. While the CP asymmetry of the phase-space integrated yield is small, this is not the case for all individual bin-pairs. This is shown in Fig. 5.41 where, as an example, the fit projections for the $B^+ \rightarrow DK^+$ decays in bin +2 and the $B^- \rightarrow DK^-$

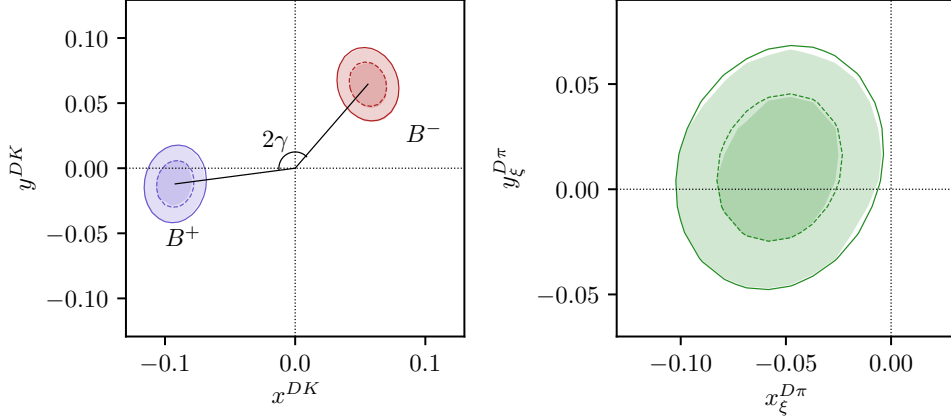


Figure 5.40: The 68 % and 95 % confidence regions for the fitted observables. The lines show the regions estimated from the covariance matrix returned by the default fit. The shaded areas are obtained in a likelihood scan, where the binned fit is run many times with all observables held at fixed values, scanning pairs of observables over the relevant ranges. The scan is made separately for the three pairs (x_-^{DK}, y_-^{DK}) , (x_+^{DK}, y_+^{DK}) , and $(x_\xi^{D\pi}, y_\xi^{D\pi})$, holding the four other parameters fixed at their default-fit central values during a given scan. Then the minimum log-likelihood is related to a χ^2 via $\mathcal{L}_{\min} = \frac{1}{2}\chi^2$ (discarding an irrelevant constant), and the confidence region limits placed at $\chi^2 = 2.30$ and $\chi^2 = 6.18$, yielding the relevant percentiles for a χ^2 distribution with 2 degrees of freedom.

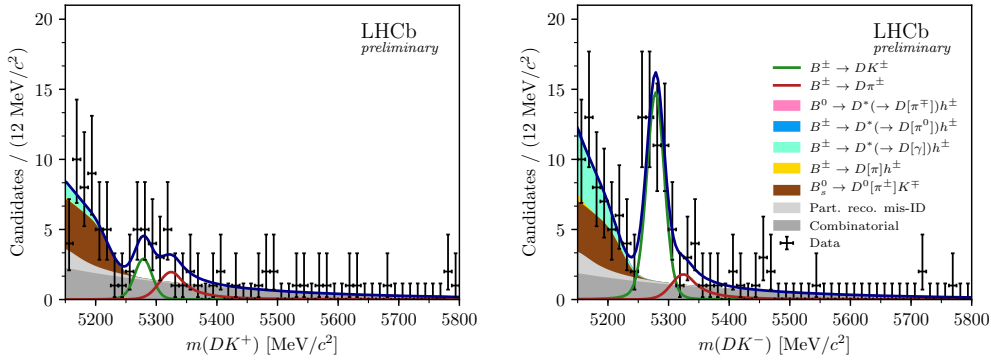


Figure 5.41: The invariant mass distribution for the (left) $B^+ \rightarrow DK^+$ candidates in bin -2 and (right) the $B^- \rightarrow DK^-$ candidates in bin +2, where $D \rightarrow K_S^0\pi^+\pi^-$ and the K_S^0 is reconstructed in the DD category.

decays in bin -2 of the $D \rightarrow K_S^0\pi^+\pi^-$ Dalitz plot are compared. The presence of CP violation is clearly visible.

The obtained F_i parameter values are shown in Table 5.10. These parameters can be useful in other BPGBS measurements made within the LHCb collaboration: it is expected that the systematic uncertainty due to differences between the Dalitz-plot acceptance profile in $B^\pm \rightarrow Dh^\pm$ decays and, say, $B \rightarrow D^*K$ or $B \rightarrow DK^*$ decays is smaller than the systematic arising from extracting the

Table 5.9: Statistical uncertainties and correlation matrix for the fit to data.

Uncertainty ($\times 10^{-2}$)						
	$x_-^{DK^\pm}$	$y_-^{DK^\pm}$	$x_+^{DK^\pm}$	$y_+^{DK^\pm}$	$x_\xi^{D\pi^\pm}$	$y_\xi^{D\pi^\pm}$
σ	0.96	1.14	0.96	1.20	1.99	2.34

Correlations						
	$x_-^{DK^\pm}$	$y_-^{DK^\pm}$	$x_+^{DK^\pm}$	$y_+^{DK^\pm}$	$x_\xi^{D\pi^\pm}$	$y_\xi^{D\pi^\pm}$
$x_-^{DK^\pm}$	1.000	-0.125	-0.013	0.019	0.028	-0.165
$y_-^{DK^\pm}$		1.000	-0.011	-0.009	0.105	0.030
$x_+^{DK^\pm}$			1.000	0.088	-0.099	0.038
$y_+^{DK^\pm}$				1.000	-0.076	-0.141
$x_\xi^{D\pi^\pm}$					1.000	0.146
$y_\xi^{D\pi^\pm}$						1.000

efficiency profile from simulated decays. Therefore, the obtain central values and uncertainties have been made public [?], including a set of systematic uncertainties discussed in Section 5.6.12.⁷

5.5.3 Cross checks

A series of cross checks are performed to verify that the fit to data is behaving as expected.

Comparison to results of earlier analyses

It is confirmed that the results obtained in fits of the Run 1 or 2015+16 data sets in isolation are compatible with the results obtained in the original LHCb analyses of those data sets [?, ?]. In order to do so, the whole analysis procedure is carried out using only the relevant subset of data, and the strong-phase inputs from the CLEO collaboration are used in the fit. Two effects need to be taken into account when comparing the central values.

Firstly, the overlap between the data samples is not 100 % due to changes in the candidate selection. The overlap between the new selection and the data set of the original analysis of Run 1 data is about 70 %, whereas is it about 90 % for the 2015+16 data set. In order to determine the expected difference between the observables fitted from data sets with significant overlap, a large number of toy data

⁷In practice, it is the obtained \mathcal{R}_i values that are made public, related to the F_i parameters via Eq. (5.23).

Table 5.10: The fitted F_i values including statistical uncertainties. The associated systematic uncertainties are negligible, as discussed in Section 5.6.12.

F_i values: $D \rightarrow K_S^0 \pi^+ \pi^-$		
bin	LL	DD
-8	0.024 ± 0.001	0.024 ± 0.000
-7	0.127 ± 0.001	0.133 ± 0.001
-6	0.062 ± 0.001	0.056 ± 0.001
-5	0.046 ± 0.001	0.042 ± 0.001
-4	0.095 ± 0.001	0.095 ± 0.001
-3	0.160 ± 0.001	0.160 ± 0.001
-2	0.153 ± 0.001	0.153 ± 0.001
-1	0.095 ± 0.001	0.097 ± 0.001
1	0.022 ± 0.001	0.020 ± 0.000
2	0.005 ± 0.000	0.005 ± 0.000
3	0.004 ± 0.000	0.004 ± 0.000
4	0.055 ± 0.001	0.056 ± 0.001
5	0.027 ± 0.001	0.022 ± 0.000
6	0.004 ± 0.000	0.003 ± 0.000
7	0.055 ± 0.001	0.057 ± 0.001
8	0.067 ± 0.001	0.072 ± 0.001

F_i values: $D \rightarrow K_S^0 K^+ K^-$		
bin	LL	DD
-2	0.207 ± 0.004	0.202 ± 0.003
-1	0.222 ± 0.004	0.230 ± 0.003
1	0.290 ± 0.005	0.296 ± 0.003
2	0.281 ± 0.005	0.271 ± 0.003

sets were generated in sets of two, where 70 (90) % of decays were shared between the data sets. Both data sets were fitted and the difference between the obtained central values for each observable tabulated; the standard deviation of these distributions are used to calculate the pulls between the old analysis results and the new fits to data. This check does not take into account that the semi-leptonic PID cuts were introduced to remove a potential peaking background, which may have had a small systematic effect on the earlier measurement results. Thus the expected differences are likely to be slightly underestimated and the check is conservative.

Furthermore, the F_i parameters were determined in a semi-leptonic control channel in the earlier analyses. Therefore, the expected difference obtained above is adjusted by adding the F_i -related systematic uncertainty of the original analysis in quadrature, when comparing the old results to those in new fits to the Run 1

Table 5.11: Comparison between the results on the Run 1 analysis [?] and the central values obtained when fitting the Run 1 dataset with the selection and fit setup described in this note. The pull is calculated using the 1σ expected difference, which takes the sample overlap and the systematic uncertainty on the F_i parameters in the previous analysis into account, but assumes all other systematic uncertainties to be perfectly correlated. The new fits are performed using the CLEO strong-phase inputs.

Observable	Run 1 result [?] (central value $\times 10^{-2}$)	New Fit (central value $\times 10^{-2}$)	Pull
x_-^{DK}	2.50	4.04	0.85
y_-^{DK}	7.50	9.14	1.02
x_+^{DK}	-7.70	-9.40	-0.91
y_+^{DK}	-2.20	0.80	1.77
<i>p</i> -value: 0.057			

Table 5.12: Comparison between the results on the 2015+16 analysis [?] and the central values obtained when fitting the 2015+16 dataset with the selection and fit setup described in this note. The pull is calculated using the 1σ expected difference, which takes the sample overlap and the systematic uncertainty on the F_i parameters in the previous analysis into account, but assumes all other systematic uncertainties to be perfectly correlated. The new fits are performed using the CLEO strong-phase inputs.

Observable	15+16 result [?] (central value $\times 10^{-2}$)	New Fit (central value $\times 10^{-2}$)	Pull
x_-^{DK}	9.00	8.36	-0.50
y_-^{DK}	2.10	1.16	-0.62
x_+^{DK}	-7.70	-8.58	-0.56
y_+^{DK}	-1.00	-2.82	-1.39
<i>p</i> -value: 0.239			

and 15+16 data sets. No further corrections have been made to the expected differences, which effectively assumes all other systematic uncertainties to be 100 % correlated. Also for this reason can the check be considered conservative. As can be seen in Tables 5.11 and 5.12, neither the Run 1 and 2015+16 comparisons show unreasonable differences in central values.

2691 Directly fitting the signal yields

As a cross-check, the fit is run in an alternative mode, in which the signal yields of each bin are independent parameters. The obtained yields are compared to those predicted from the results of the default fit in Fig. 5.42. The yields are shown for each "effective bin", where effective bin i is defined as bin $+i$ for B^+ decays and bin

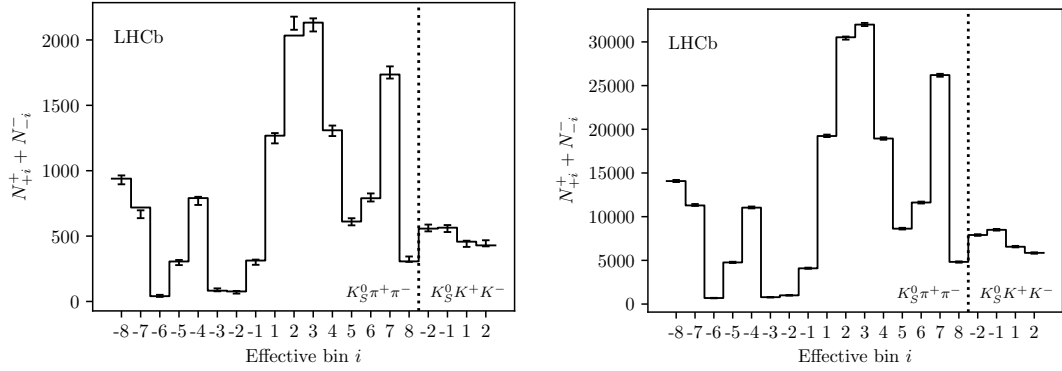


Figure 5.42: Comparison of (lines) the predicted yield given the determined CP observables and (error bars) the yield obtained in fits to data where each yield is an independent parameter. The yields are shown for (left) $B^\pm \rightarrow DK^\pm$ decays and (right) $B^\pm \rightarrow D\pi^\pm$ decays. The LL and DD categories have been combined, as has the B^+ and B^- yields for each effective Dalitz bin, defined as bin $+i$ for B^+ decays and bin $-i$ for B^- decays.

— i for B^- decays; in the CP symmetric case, these bins are expected to have equal yields (modulo production and detection asymmetries). The agreement between the two fit set-ups is seen to be excellent. The normalised yield asymmetries, defined as

$$A^i \equiv \frac{N_{-i}^- - N_i^+}{N_{-i}^- + N_i^+} \quad (5.25)$$

are shown in Fig. 5.43 for all decay channels. Again, the agreement between the nominal fit and the alternative fit with independent yields is found to be excellent for both $B^\pm \rightarrow Dh^\pm$ decays. It is also clear how, in the case of $B^\pm \rightarrow DK^\pm$ decays, the asymmetry is significantly different from zero for a number of bin pairs. The reason that the yield asymmetry is not zero in the fit that does not allow for CP violation, is that the overall yield of B^+ and B^- decays are allowed to differ in this fit; only the phase-space distribution of the decays is enforced to be CP -symmetric. The observed asymmetry is due to a combination of production and detection asymmetries, CP -violation and material interaction of the K_S^0 meson, and CP violation in the $B^\pm \rightarrow Dh^\pm$ decays, but no attempt is made to disentangle the effects.

2709 Fitting subsets of the data separately

2710 One cross check is carrying out, by determining the CP observables using a number
2711 of independent sub samples of the data set separately. This is done for the
2712 following following data splits

- 2713 • Fig. 5.44a shows the same plots, comparing the fits to the data set split by
2714 K_S^0 track type.

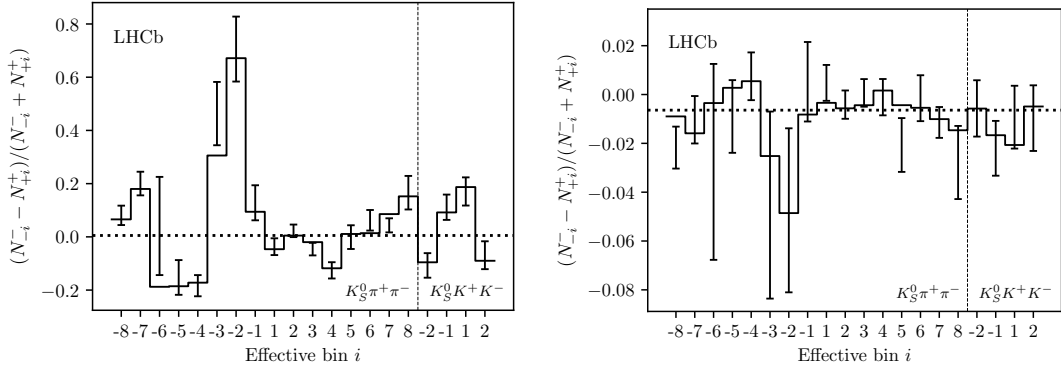


Figure 5.43: The bin-by-bin asymmetries $(N_{-i}^- - N_{+i}^+) / (N_{-i}^- + N_{+i}^+)$ for each Dalitz-plot bin number for (left) $B^\pm \rightarrow DK^\pm$ decays and (right) $B^\pm \rightarrow D\pi^\pm$ decays. The prediction from the central values of the CP -violation observables is shown with a solid line and the asymmetries obtained in fits with independent bin yields are shown with the error bars. The predicted asymmetries in a fit that does not allow for CP violation are shown with a dotted line.

- Fig. 5.44b shows the same plots, comparing the fits to the data set split by whether the D meson decays to the $K_S^0\pi^+\pi^-$ or $K_S^0K^+K^-$ final state.
 - Fig. 5.45a shows the two dimensional log likelihood contours for the observables for fits to the Run 1, 2015+16, 2017 and 2018 datasets separately
 - Fig. 5.45b shows the same plots, comparing the fits to the data set split by whether the candidate event was triggered by one of the signal particles at the hardware level (TOS), or by another particle in the underlying event (TIS).
 - Fig. 5.45c shows the same plots, comparing the fits to the data set split the magnet polarity during data taking.
- All figures show the Gaussian likelihood contours corresponding to the statistical uncertainties. There is good agreement between the results in all cases, given that in each cases the sub datasets are independent and therefore the statistical errors are uncorrelated.

Constraints from a subset of bins

An alternative way to subdivide the data is to examine the constraints from a subset of bins individually; this forms as a cross check because the observables favoured by each sub set should be compatible, and also serves as a useful illustration of the features of the BPGBGSZ method. Likelihood contours for (x_\pm^{DK}, y_\pm^{DK}) are shown in Fig. 5.46, obtained using the binned yields in the $D \rightarrow K_S^0\pi^+\pi^-$ bins, determined

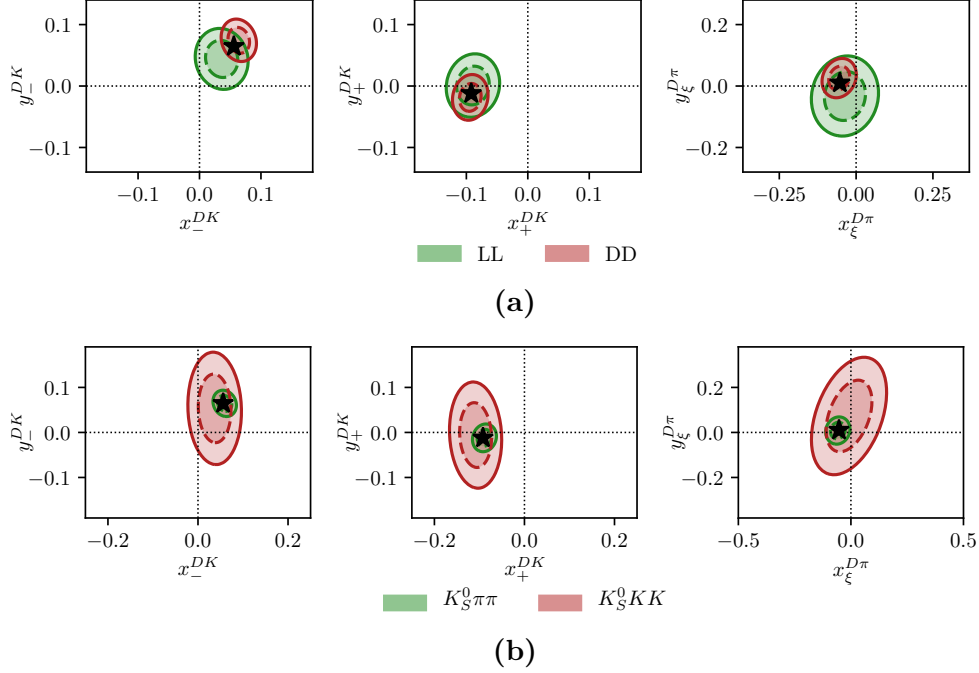


Figure 5.44: Comparison of the 68 % and 95 % confidence regions for (left) (x_-^{DK}, y_-^{DK}) , (centre) (x_+^{DK}, y_+^{DK}) , and (right) $(x_\xi^{D\pi}, y_\xi^{D\pi})$ obtained from fits to sub sets of the data set. The uncertainties are statistical only. The central values of the default fit are shown with a black star. The dataset is split by (a) LL and DD K_S^0 types and (b) D decay mode.

in the fits of individual bin yields described in Section 5.5.3. The bins are split by whether they are ADS-like, GLW-like, or Odd-even according to the classification in Section 2.3.5. It is clear that the likelihood regions show a reasonable overlap, and also how it is the GLW bins that constrain the x_\pm parameter, while the Odd-even and ADS-like bins provide the ability to constrain the y_\pm parameters.

2739 Significantly reducing the $B^\pm \rightarrow D\pi^\pm$ to $B^\pm \rightarrow DK^\pm$ cross feed

2740 One of the dominant backgrounds in the signal region of the $B^\pm \rightarrow DK^\pm$ channel is
 2741 from partly reconstructed $B \rightarrow D\pi X$ decays where the bachelor pion is misidentified
 2742 as a kaon. The background mode is well described by the included shape component,
 2743 and included in all relevant systematic studies. Nevertheless, an additional cross
 2744 check is carried out to ensure that it is not having a significant effect on the fit: the
 2745 analysis is repeated with PID requirement of $PIDK > 12$ required to place a candidate
 2746 in the $B^\pm \rightarrow DK^\pm$ category, instead of $PIDK > 4$. With this requirement 99.7 %
 2747 of $B^\pm \rightarrow D\pi^\pm$ decays are correctly identified, making the cross-feed component
 2748 in the $B^\pm \rightarrow DK^\pm$ channels significantly smaller than in the default fit. This
 2749 is clearly visible in Fig. 5.47, where the fit projections for the global fit of the

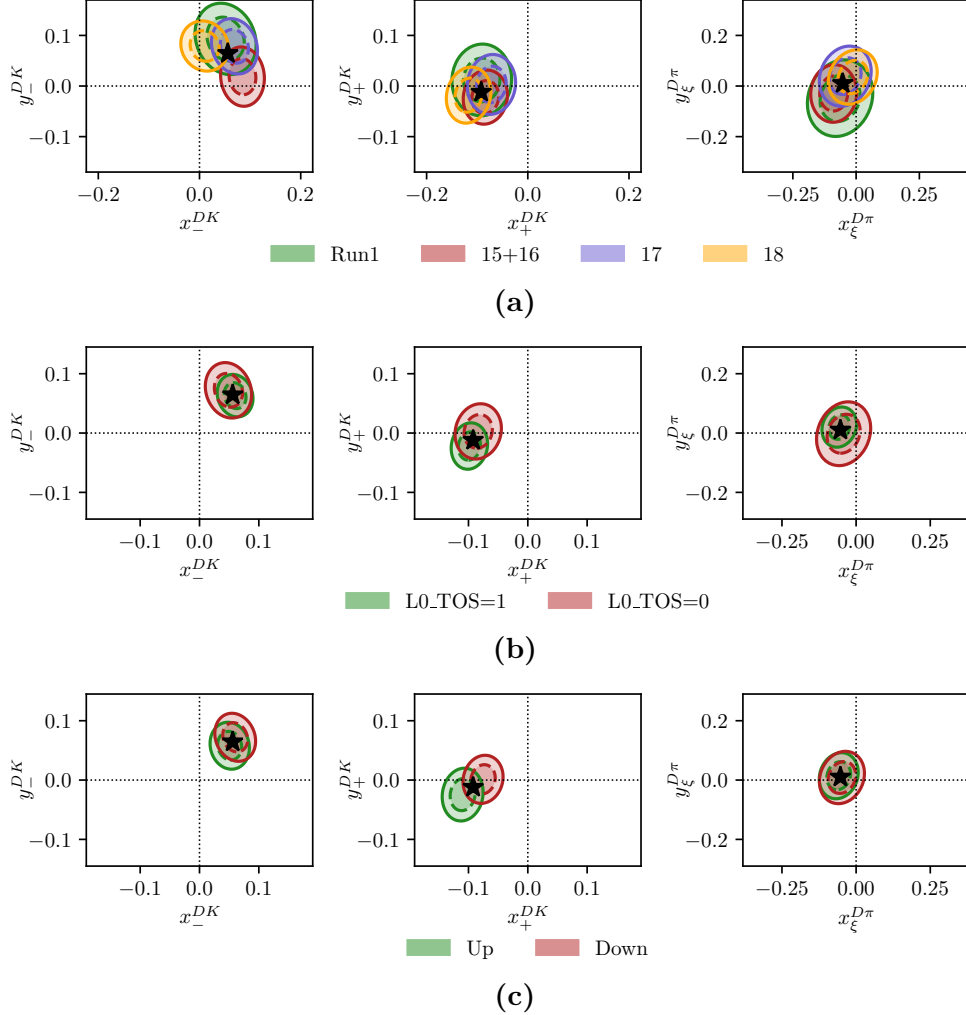


Figure 5.45: Comparison of the 68 % and 95 % confidence regions for (left) (x_-^{DK}, y_-^{DK}) , (centre) (x_+^{DK}, y_+^{DK}) , and (right) $(x_\xi^{D\pi}, y_\xi^{D\pi})$ obtained from fits to sub sets of the data set. The uncertainties are statistical only. The central values of the default fit are shown with a black star. The dataset is split by (a) data taking year, (b) trigger category, and (c) magnet polarity.

2750 $D \rightarrow K_S^0 \pi^+ \pi^-$ modes are shown. In return, the probability of correctly identifying a
 2751 kaon companion drops to about 68–69 %, resulting in a smaller effective signal yield.

2752 The measurement results are compared in Table 5.13, where the differences
 2753 in central value are seen to be reasonably small. It is not trivial to determine
 2754 whether the difference is statistically significant or not: the same candidates are
 2755 analysed in both cases, the difference being that a number of candidates that are
 2756 placed in the $B^\pm \rightarrow DK^\pm$ category in the nominal fit are placed in the $B^\pm \rightarrow D\pi^\pm$
 2757 category in the alternative fit. The uncertainty will not be 100 % correlated because
 2758 signal events that move from the DK to $D\pi$ category are placed in a region with
 2759 high background; however, this is somewhat compensated for by candidates that

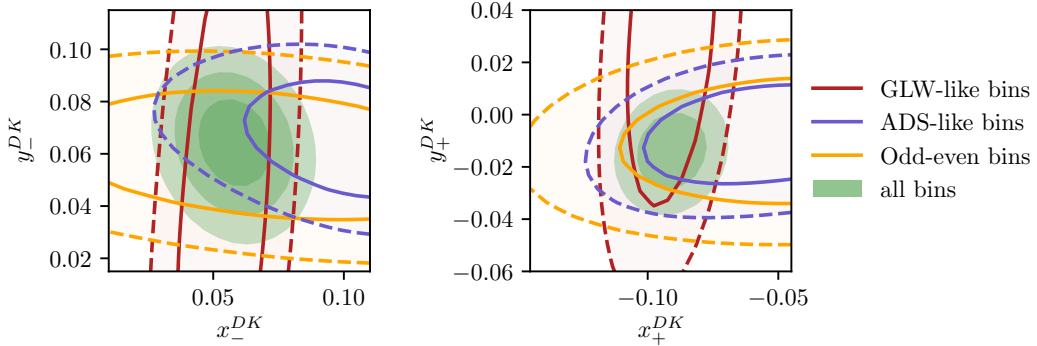


Figure 5.46: Constraints on the $B^\pm \rightarrow DK^\pm$ observables from the signal yields of different subsets the $D \rightarrow K_S^0\pi^+\pi^-$ Dalitz bins, using the bin categorisation developed in Section 2.3.5.

Table 5.13: Results of running the measurement with the default PIDK cut at 4 used to separate $B^\pm \rightarrow DK^\pm$ and $B^\pm \rightarrow D\pi^\pm$ candidates, as well as with an alternative PIK cut at 12, resulting in much lower cross-feed from misidentified $B^\pm \rightarrow D\pi^\pm$ decays. We also show the pulls, defined as $\Delta x / \sqrt{|\sigma_{PIDK>12}^2 - \sigma_{PIDK>4}^2|}$ as described in the main text body. The comparison was made before the BESIII measurement of the $D \rightarrow K_S^0 K^+ K^-$ strong-phase inputs became available; therefore the fits use the CLEO-only results [?] for this mode, which explains why the results quoted for $PIDK > 4$ differ slightly from the nominal fit results.

Parameter	PIDK > 4	PIDK > 12	$\sigma = \sqrt{\sigma_{PIDK>12}^2 - \sigma_{PIDK>4}^2}$	Pull
x_-^{DK}	5.59 ± 0.96	5.82 ± 1.01	0.30	0.77
y_-^{DK}	6.45 ± 1.14	6.86 ± 1.19	0.36	1.13
x_+^{DK}	-9.21 ± 0.96	-8.94 ± 1.01	0.30	0.93
y_+^{DK}	-1.21 ± 1.20	-0.94 ± 1.26	0.37	0.71
$x_\xi^{D\pi}$	-5.30 ± 1.99	-5.13 ± 2.02	0.32	0.52
$y_\xi^{D\pi}$	1.03 ± 2.34	1.71 ± 2.33	0.28	2.40

remain in the DK category gaining statistical power due to the increased purity.
An estimate of the expected statistical fluctuation can be determined by taking the difference of the statistical uncertainties in quadrature. Using this estimate, the observed shifts are found to be consistent with statistical fluctuation, and thus there is no sign of the background from $D\pi^\pm \rightarrow DK^\pm$ cross-feed causing issues.

Compare results obtained with different strong-phase inputs

It is interesting to compare the results obtained with different strong-phase inputs. This is done in Fig. 5.48, where the default fit results are compared to those obtained if the CP fit is done with the CLEO-only inputs [?], and with the model predictions from the 2018 Belle model [?] and the 2008 BaBar model [?]. For the

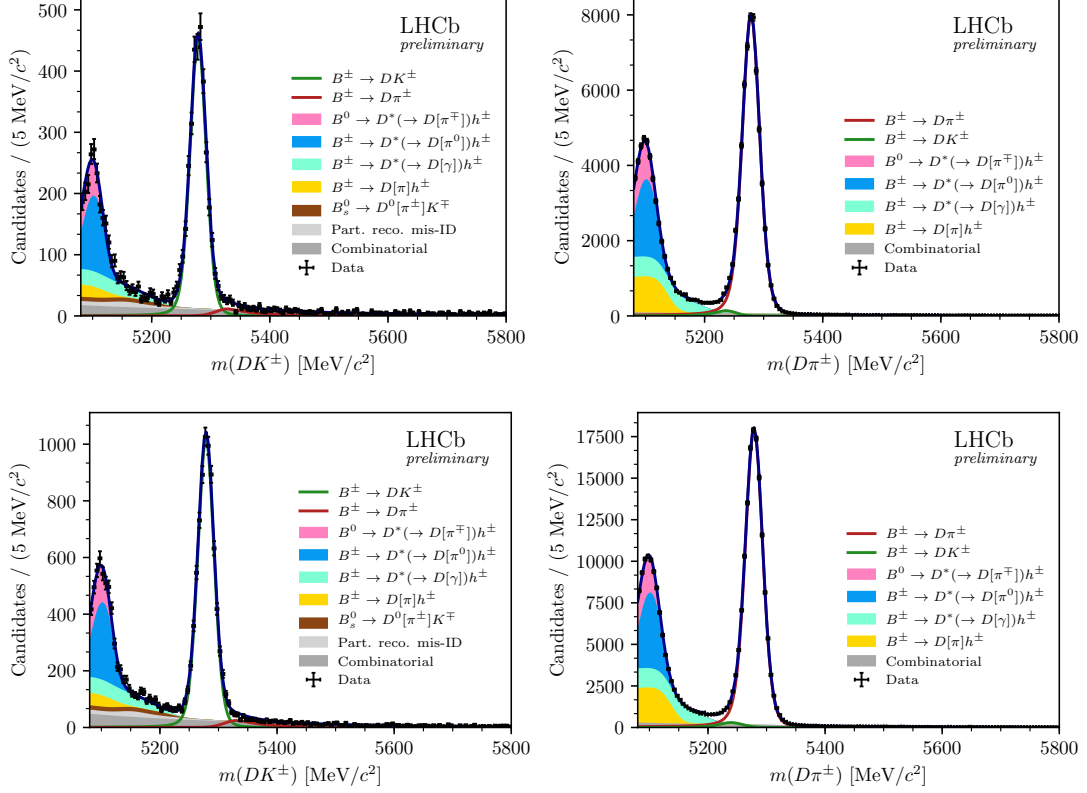


Figure 5.47: Fit projections for fits to the $D \rightarrow K_0^0 \pi^+ \pi^-$ candidates with a companion PIDK requirement at 12 instead of 4 used to split into (left) $B^\pm \rightarrow DK^\pm$ and (right) $B^\pm \rightarrow D\pi^\pm$ candidates, for the (top) LL and (bottom) DD categories.

2770 measurements, only the strong-phase-related uncertainties are included in the plot,
2771 since the statistical uncertainties are correlated. All results are found to agree well.

2772 5.6 Systematic uncertainties

2773 The following sections cover the suite of systematic uncertainties on the measurement
2774 that has been considered. All uncertainties are summarised in Section 5.6.12.

2775 5.6.1 Strong phase uncertainties

2776 The observables x_\pm^{DK} , y_\pm^{DK} , $x_\xi^{D\pi}$ and $y_\xi^{D\pi}$ are extracted using the central values of c_i
2777 and s_i from the BESIII–CLEO combinations [?, ?, ?]. Subsequently, the measurement
2778 uncertainty on these inputs is propagated to the observables by performing a large
2779 set of fits to data that use alternative values of c_i and s_i . The new c_i and s_i
2780 values are obtained by smearing the central values by their measured statistical
2781 and systematic uncertainties while taking into account their correlations. The use
2782 of different c_i and s_i values changes the extracted x_\pm^{DK} , y_\pm^{DK} , $x_\xi^{D\pi}$ and $y_\xi^{D\pi}$ values.

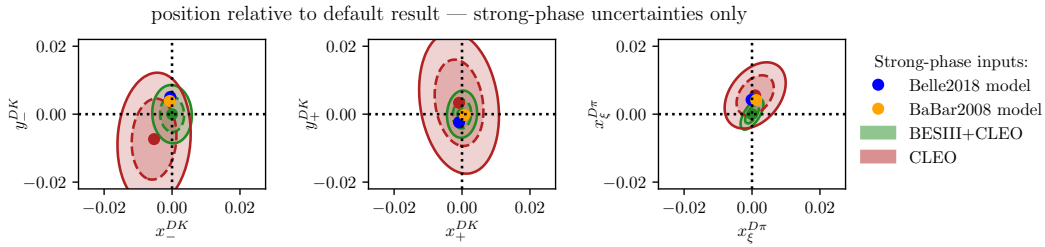


Figure 5.48: Fit results for (left) (x_-^{DK}, y_-^{DK}) , (centre) (x_+^{DK}, y_+^{DK}) , and (right) $(x_\xi^{D\pi}, y_\xi^{D\pi})$ depending on strong-phase inputs, shown relative to the default fit results. The included results are based on (green) the BESIII-CLEO combination, which is the default, (red) the CLEO-only results, (blue dot) the 2018 Belle model [?] and (orange dot) the 2008 BaBar model [?]. For the measurements, only strong-phase related uncertainties are included in the plotted confidence regions.

2783 The standard deviation of the distributions of central values extracted from 1000
 2784 data fits are assigned as a systematic uncertainty. The distributions are shown
 2785 in Fig. 5.49 and the assigned uncertainties are summarised in Table 5.14. The
 2786 correlation matrix related to the strong-phase uncertainty can be obtained from the
 2787 correlations observed between observables in the fits, and is also given in the table.

2788 The set of (c_i, s_i) that was employed in this analysis will be used in a series
 2789 of future BPGBGSZ measurements, both with additional B decay modes within
 2790 the LHCb collaboration and by the Belle II collaboration. This introduces some
 2791 correlation between the measurement results. In order to allow for an estimate
 2792 of the degree of correlation by future analysts, the 1000 samples (c_i, s_i) values
 2793 and the corresponding fit results for $(x_\pm^{DK}, y_\pm^{DK}, x_\xi^{D\pi}, y_\xi^{D\pi})$ have been made public
 2794 as supplementary material to Ref. [?].

2795 5.6.2 Efficiency-profile-related systematic uncertainties

2796 The non-trivial efficiency profile over the Dalitz plot can have a range of effects,
 2797 considered in the sections below.

2798 **The assumption that** $\eta^{DK}(s_-, s_+) = \eta^{D\pi}(s_-, s_+)$

2799 The assumption that the acceptance profile over the D -decay Dalitz plot is identical
 2800 between $B^\pm \rightarrow DK^\pm$ and $B^\pm \rightarrow D\pi^\pm$ decays was examined in detail in Section 5.2.2.
 2801 It was found that with signal yields similar to those in the data set, no statistically
 2802 significant difference between the efficiency profiles $\eta^{DK}(s_-, s_+)$ and $\eta^{D\pi}(s_-, s_+)$
 2803 was discernible, and no additional uncertainty due to this assumption is assigned.

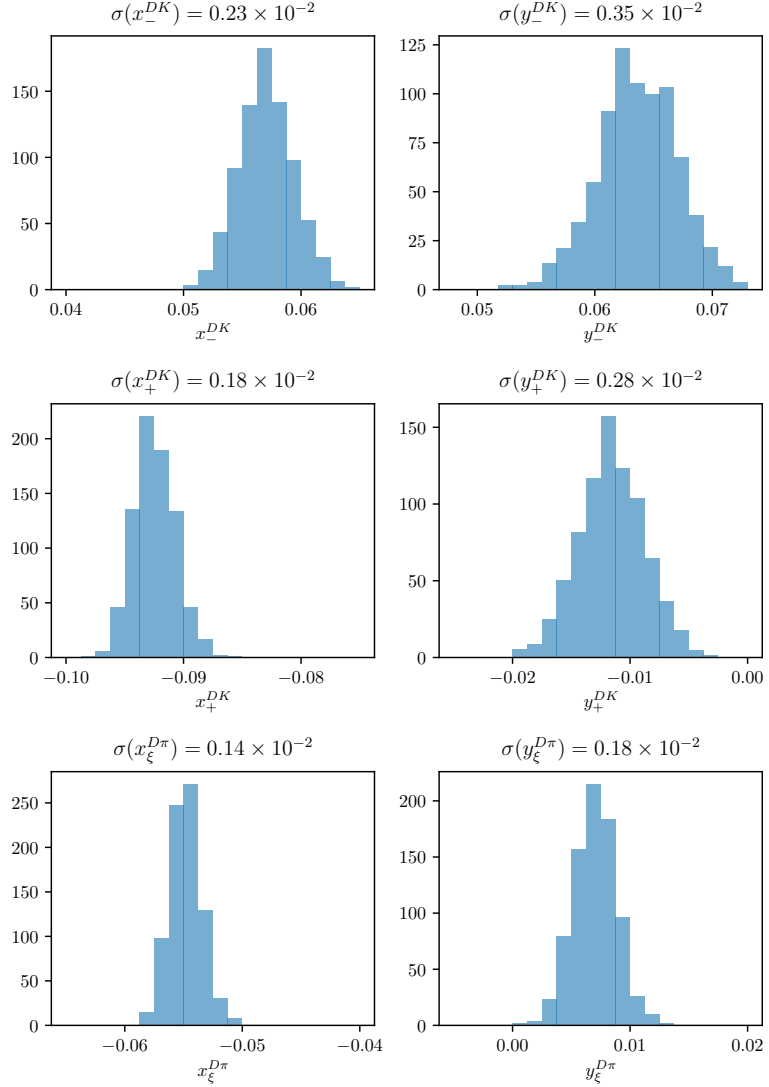


Figure 5.49: Spread of central values for the fitted observables when the input c_i and s_i from the BESIII+CLEO combination are varied according to their uncertainties and correlations.

2804 **The assumption that** $\eta(s_-, s_+) = \eta(s_+, s_-)$

2805 The measurement is sensitive to effects that break the assumption $\eta(s_-, s_+) =$
 2806 $\eta(s_+, s_-)$. Such a breakdown would mean that opposite points on the Dalitz plot
 2807 have different efficiencies and can only arise through a charge detection asymmetry
 2808 (e.g that it is more likely to detect a K^+ in the detector rather than a K^-).⁸

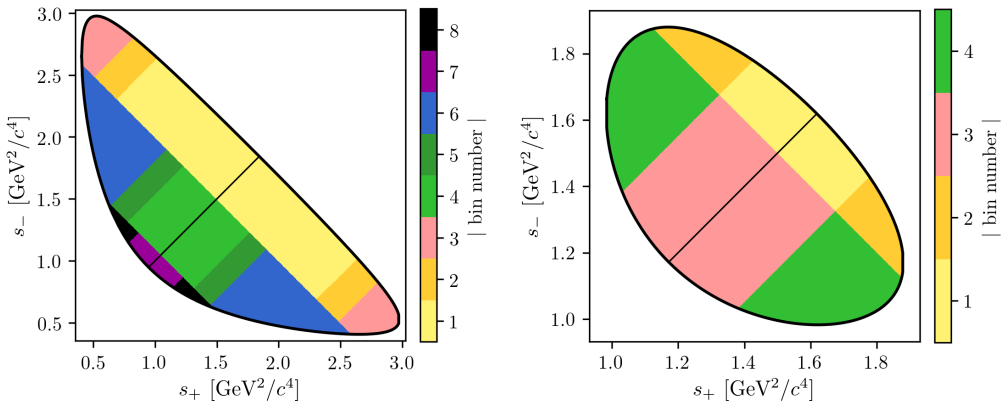
2809 The potential size size of such an asymmetry can be studied in simulation
 2810 where the D decay has a uniform distribution over the allowed phase space; in such
 2811 simulated samples, it would manifest itself as an observation different fractional

⁸Note that the measurement is insensitive to any asymmetry in the reconstruction of the companion track.

Table 5.14: Systematic uncertainties and correlation matrix due to strong-phase inputs.

Uncertainty ($\times 10^{-2}$)						
	$x_-^{DK^\pm}$	$y_-^{DK^\pm}$	$x_+^{DK^\pm}$	$y_+^{DK^\pm}$	$x_\xi^{D\pi^\pm}$	$y_\xi^{D\pi^\pm}$
σ	0.23	0.35	0.18	0.28	0.14	0.18

Correlations						
	$x_-^{DK^\pm}$	$y_-^{DK^\pm}$	$x_+^{DK^\pm}$	$y_+^{DK^\pm}$	$x_\xi^{D\pi^\pm}$	$y_\xi^{D\pi^\pm}$
$x_-^{DK^\pm}$	1.000	-0.047	-0.490	0.322	0.189	0.144
$y_-^{DK^\pm}$		1.000	0.059	-0.237	-0.116	-0.117
$x_+^{DK^\pm}$			1.000	0.061	0.004	-0.139
$y_+^{DK^\pm}$				1.000	0.127	-0.199
$x_\xi^{D\pi^\pm}$					1.000	0.638
$y_\xi^{D\pi^\pm}$						1.000

**Figure 5.50:** The rectangular binning schemes used to group candidates in (left) the $D \rightarrow K_S^0 \pi^+ \pi^-$ and (right) the $D \rightarrow K_S^0 K^+ K^-$ categories in a number of systematic uncertainty studies.

2812 yields of B^- decays in bin i and B^+ decays in bin $-i$. This effect has been looked for
 2813 using the large samples of $B^\pm \rightarrow D\pi^\pm$ decays that were generated for the analysis
 2814 of 2015 and 2016 data. The study is performed using the rectangular binning
 2815 schemes shown in Fig. 5.50, because this scheme is most sensitive to effects that vary
 2816 smoothly over phase space. The comparison plots are shown in Fig. 5.51, where it
 2817 can be seen that the p values for the hypothesis that there is no asymmetry all take
 2818 on reasonable values. Hence no further systematic uncertainty is considered.

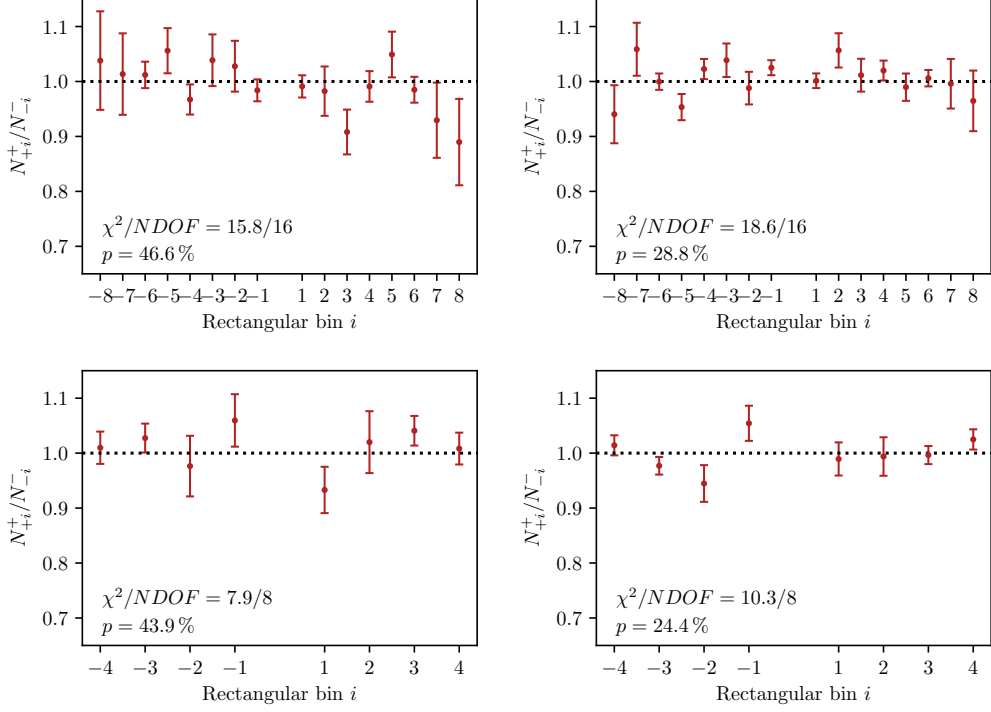


Figure 5.51: Comparison of the ratio of B^+ decays reconstructed in bin $+i$ to B^- decays reconstructed in bin $-i$ for simulated $B^\pm \rightarrow D\pi^\pm$ decays where (top) $D \rightarrow K_S^0\pi^+\pi^-$ and (bottom) $D \rightarrow K_S^0K^+K^-$, also split into (left) the LL and (right) the DD categories, using the rectangular binning schemes in Fig. 5.50. Calculated p values for the hypothesis that the ratio is flat are also shown, all of them being at least 20 %.

2819 Effect of phase-space efficiency profile on c_i and s_i

2820 As discussed in Section 2.4 there is a small bias, because the c_i and s_i values
 2821 that are used correspond to the definition

$$c_i = \frac{\int_i ds^2 |A_S^D(s_{-+})| |A_S^D(s_{+-})| \cos[\Delta\delta_D(s_{-+})]}{\sqrt{\int_i ds^2 |A_S^D(s_{-+})|^2} \sqrt{\int_i ds^2 |A_S^D(s_{+-})|^2}}, \quad (\text{and equivalent for } s_i,) \quad (5.26)$$

2822 whereas the non-flat efficiency profile in LHCb, $\eta(s_-, s_+) \equiv \eta(s_{-+})$, means that the
 2823 appropriate c_i' and s_i' entering the exact yield expressions are

$$c_i^{\text{eff}} = \frac{\int_i ds^2 \eta(s_{-+}) |A_S^D(s_{-+})| |A_S^D(s_{+-})| \cos[\Delta\delta_D(s_{-+})]}{\sqrt{\int_i ds^2 |A_S^D(s_{-+})|^2} \sqrt{\int_i ds^2 |A_S^D(s_{+-})|^2}}, \quad (\text{and equivalent for } s_i^{\text{eff}}.) \quad (5.27)$$

2824 The shifts $\Delta c_i = c_i^{\text{eff}} - c_i$, $\Delta s_i = s_i^{\text{eff}} - s_i$ can be estimated using the efficiency
 2825 profile in simulation and the latest amplitude models: the 2018 Belle model [?]
 2826 for $D \rightarrow K_S^0\pi^+\pi^-$ and the 2010 BaBar model [?] for $D \rightarrow K_S^0K^+K^-$. The strong-
 2827 phase parameters are first calculated assuming a uniform reconstruction efficiency

Table 5.15: The c_i and s_i values for $D \rightarrow K_S^0 \pi^+ \pi^-$ decays calculated via the 2018 Belle model [?] in two cases: assuming a uniform reconstruction efficiency over phase space, denoted $(c/s)_i^{\text{model}}$, and including the LHCb efficiency profile as obtained in simulation, averaged for LL and DD, denoted $(c/s)_i^{\text{eff}}$. The change due to including the efficiency is also tabulated.

Bin	c_i^{model}	c_i^{eff}	Δc_i	s_i^{model}	s_i^{eff}	Δs_i
1	-0.027	-0.007	0.019	0.812	0.794	-0.018
2	0.837	0.859	0.022	0.164	0.152	-0.012
3	0.163	0.163	-0.000	0.872	0.880	0.008
4	-0.914	-0.915	-0.001	0.076	0.082	0.006
5	-0.149	-0.170	-0.021	-0.856	-0.854	0.002
6	0.373	0.362	-0.011	-0.782	-0.805	-0.023
7	0.863	0.862	-0.000	-0.203	-0.202	0.002
8	0.860	0.862	0.002	0.330	0.336	0.006

Table 5.16: The c_i and s_i values for $D \rightarrow K_S^0 K^+ K^-$ decays calculated via the 2010 BaBar model [?] in two cases: assuming a uniform reconstruction efficiency over phase space, denoted $(c/s)_i^{\text{model}}$, and including the LHCb efficiency profile as obtained in simulation, averaged for LL and DD, denoted $(c/s)_i^{\text{eff}}$. The change due to including the efficiency is also tabulated.

Bin	c_i^{model}	c_i^{eff}	Δc_i	s_i^{model}	s_i^{eff}	Δs_i
1	0.738	0.735	-0.002	0.266	0.263	-0.003
2	-0.697	-0.744	-0.046	0.332	0.329	-0.003

over phase space according to Eq. (5.26), obtaining a set of values $\{c_i^{\text{model}}, s_i^{\text{model}}\}$. Then, an alternative set is calculated, $\{c_i^{\text{eff}}, s_i^{\text{eff}}\}$, using the same model, and the reconstruction efficiency profile found in full LHCb simulation. The LHCb reconstruction efficiency at a given point in phase-space is taken to be proportional to the yield in simulation, as the simulated decays were generated with a uniform distribution over phase space. The efficiency is averaged over the LL and DD categories in the calculation, according to the relative signal yields in these categories. The results, as well as their differences, are tabulated in Tables 5.15 and 5.16.

A systematic uncertainty due to employing the measured c_i and s_i directly in the fit is assigned by generating a large number of toy data sets where the signal yields are calculated using $(c_i^{\text{eff}}, s_i^{\text{eff}})$, and then fitting the data sets using $(c_i^{\text{model}}, s_i^{\text{model}})$. The mean bias of each observable in these toys is assigned as the systematic uncertainty, and is determined to be 0.1×10^{-2} or less for all observables. The smallness of the effect is the reason no effort is made to correct the c_i and s_i values in the nominal measurement.

2843 **5.6.3 Mass shapes**

2844 A number of uncertainties relate to the mass distributions that enter the fit model.

2845 Each is described in detail the sections below.

2846 **Determination of shape parameters**

2847 The statistical uncertainties on the shape parameters that are obtained in fits
 2848 to simulated decays and in the first stage fit to data need to be propagated to
 2849 the uncertainty on the obtained parameters. This is done via a bootstrapping
 2850 procedure, repeating these steps many times:

- 2851 • Each of the data sets used to determine parameters of the signal, crossfeed,
 2852 and lowmass shapes that are fixed in the first-stage fit to data of Section 5.4
 2853 are re-sampled with replacement, drawing a number of events equal to the
 2854 original data-set size. These are from simulation for signal and lowmass
 2855 shapes, and real data for the crossfeed shapes. All of the shapes are fit again,
 2856 on the re-sampled data sets.
- 2857 • The real dataset is re-sampled with replacement, drawing a number of events
 2858 equal to the original data-set size. Then, the first-stage fit of Section 5.4 is
 2859 repeated with the shapes obtained as described above, obtaining values for
 2860 the remaining shape parameters.
- 2861 • Finally, the CP fit is repeated using the shape parameters determined in the
 2862 preceding steps, but *without* re-sampling the dataset (to avoid a statistical
 2863 spread in the obtained central values that is independent of the shape
 2864 parameters).

2865 The uncertainty on each observable is taken to be the standard deviation of the
 2866 set of central values obtained as described above. This procedure propagates the
 2867 statistical uncertainty on the fixed parameters to the observables, in a way that
 2868 takes correlations into account, and which does not rely on the uncertainty estimates
 2869 in the preliminary fits being accurate. The uncertainties are less than 0.1×10^{-2}
 2870 for all DK^\pm observables and less than 0.2×10^{-2} for all $D\pi^\pm$ observables.

2871 A potential bias arises due the use of the sPlot method when obtaining the
 2872 mass distribution of decays where a $\pi \leftrightarrow K$ misidentification has taken place.
 2873 This is because the $m_{\text{swap}}(Dh^\pm)$ mass that is calculated while assuming a swapped
 2874 companion hypothesis and the nominal $m_{\text{default}}(Dh^\pm)$ mass are correlated (it is
 2875 always the case that $m_{\text{swap}} > m_{\text{default}}$ for a $\pi \rightarrow K$ misidentification ,for example).

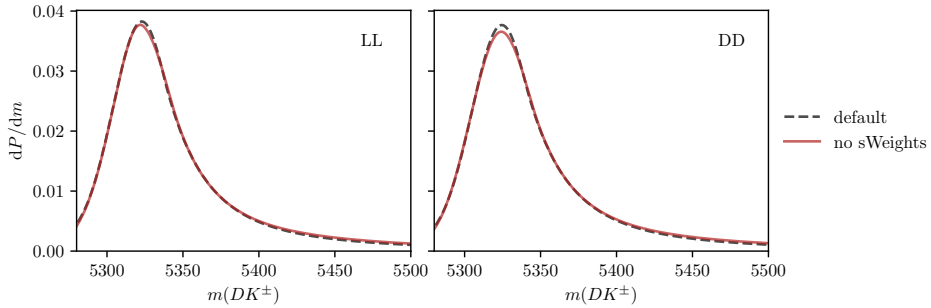


Figure 5.52: Comparison of the default and no-sWeights alternative shape for the $D\pi \rightarrow DK$ cross-feed component in the (left) LL and (right) DD categories where $D \rightarrow K_S^0 \pi^+ \pi^-$. The binned fit obtains essentially the same central values for the CP -violation observables, independently of which shape is used.

Thus, the assumptions of the sPlot method are not satisfied [?]. The correlation coefficient in the signal region is about 20 % for simulated signal decays. In order to assess the potential impact, an alternative mass distribution for $(B^\pm \rightarrow D\pi^\pm) \rightarrow (B^\pm \rightarrow DK^\pm)$ cross-feed is derived that does not rely on sWeights. Instead of fitting $B^\pm \rightarrow D\pi^\pm$ sample in the whole fit range and assigning sWeights before recalculating the B mass under the kaon companion hypothesis, the shape is obtained using $B^\pm \rightarrow D\pi^\pm$ candidates in the signal region. This is possible because the $B^\pm \rightarrow D\pi^\pm$ sample is very pure. The shapes are compared in Fig. 5.52 and are seen to be almost identical. Thus the sWeights do successfully subtract the contribution of combinatorial and partially reconstructed backgrounds in the default setup. The impact on the obtained CP -violation observables of using one or the other shape in the fits is negligible, and no further systematic uncertainty is assigned due to this effect.

Using the same mass shapes in all Dalitz bins

The mass shapes obtained the first-stage fit where all Dalitz bins are combined, are used in each individual bin of the subsequent binned fit. However, there could be some variation in the shape over the D -decay phase space, due to correlations between the phase-space coordinates and particle kinematics. The potential effect is investigated in pseudoexperiments, where toy data sets are generated with alternative signal, crossfeed, and combinatorial-background shapes that are allowed to differ between bins, and fitted with the default shapes. The partially reconstructed background is treated in a separate study, because further physics effects contribute to bin-by-bin variation, as described in the following section.

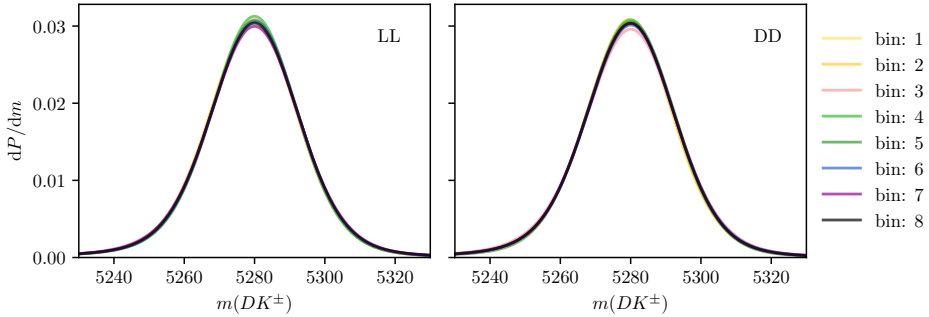


Figure 5.53: Signal shapes obtained in fits simulated $B^\pm \rightarrow D\pi^\pm$ decays for individual Dalitz bins in the optimal binning scheme, for (left) LL and (right) DD candidates in the $B^\pm \rightarrow D(\rightarrow K_S^0\pi^+\pi^-)\pi^\pm$ category.

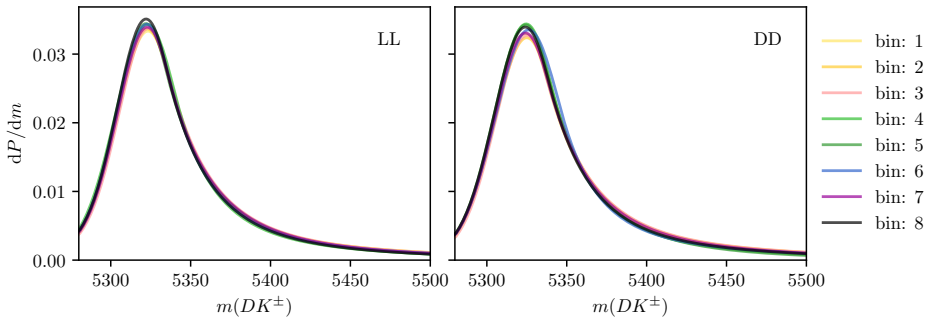


Figure 5.54: Mass shapes for $D\pi \rightarrow DK$ cross feed obtained for individual Dalitz bins in the optimal binning scheme, for (left) LL and (right) DD candidates in the $D \rightarrow K_S^0\pi^+\pi^-$ category.

2899 The alternative signal and cross-feed mass shapes are fitted independently in
 2900 each bin, following identical procedures to those outlined in Sections 5.4.1 and 5.4.2.
 2901 Examples of the obtained shapes are compared in Figs. 5.53 and 5.54.

2902 The shape of the combinatorial background can also vary over the D decay
 2903 phase-space; for example will the relative amount of fake D candidates versus real
 2904 D decays paired with a random bachelor certainly depend on the real D decay
 2905 amplitude for a given phase-space region. The effect is investigated in the high
 2906 B -mass sideband $m_B \in [5600, 6500] \text{ MeV}/c^2$, in which the $m(Dh^\pm)$ distribution is
 2907 fitted with a single exponential distribution, in bins of the Dalitz plot. The fits
 2908 combine B^+ and B^- candidates and merge bins $+i$ and $-i$, and are carried out
 2909 for both the *optimal* binning scheme of Fig. 2.7 (on page 21) and a *rectangular*
 2910 binning scheme, shown in Fig. 5.50, which better captures continuous trends over
 2911 the Dalitz plot. The study is done for $D \rightarrow K_S^0\pi^+\pi^-$ only due to available statistics.
 2912 The DD category of $B^\pm \rightarrow D\pi^\pm$ decays has the largest statistics and shows the
 2913 largest variation, and the fitted slopes for this channel are shown in Fig. 5.55. Two

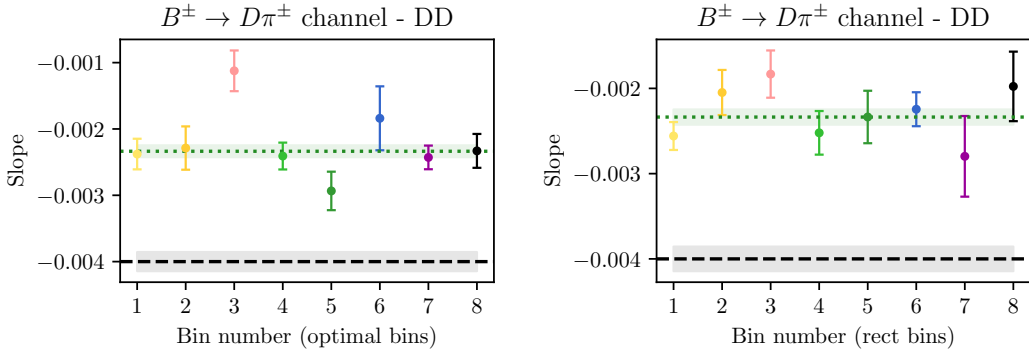


Figure 5.55: Plot of (dots) combinatorial slope in the high B mass background for each bin in the (left) the optimal binning scheme and (right) the rectangular binning scheme, for the DD $B^\pm \rightarrow D(\rightarrow K_S^0 \pi^+ \pi^-) \pi^\pm$ category. The slope when all bins are combined (green, dashed line) is also shown, and compared with (black dashed line) the slope in the default fit region.

effects are visible: 1) there is some variation in the slope as a function of the Dalitz bin, especially visible for the rectangular scheme, and 2) the exponential slope is larger in general in the high B -mass sideband. The latter effect does not pose a problem, since the employed exponential is found to provide an excellent fit in the default fit region. It does however need to be taken into account when deriving alternative, bin-dependent combinatorial slopes relevant for the default fit region. In order to do so, the alternative slope for bin i is defined

$$\alpha_{\text{default-range}}^i = \frac{\alpha_{\text{high-}m_B}^i}{\alpha_{\text{high-}m_B}^{\text{all-}DP}} \times \alpha_{\text{default-range}}^{\text{all-}DP}, \quad (5.28)$$

and used when generating the combinatorial-background component of the toy data sets for the study.

The average bias obtained for each observable in the ensemble of pseudo-experiments is assigned as a systematic uncertainty, found to be about 0.1×10^{-2} for each observable.

Ignoring physics effects in the lowmass background

In the CP fit, the same relative fractions of partly reconstructed B^\pm and B^0 backgrounds are used in each bin, as determined in the first-stage fit described in Section 5.4 (whereas the partly reconstructed $B_s^0 \rightarrow \bar{D}^0[\pi^+]K^-$ background is treated separately). However the distribution over the Dalitz plot depends on whether the partly reconstructed decays occur via an intermediate D^0 meson, a \bar{D}^0 meson, or an admixture of both. Consider a decay reconstructed as $B^- \rightarrow DK^-$ but which is actually a partially-reconstructed background. There are then four types of background that should be considered:

- Decays in which the D -meson in the true decay is a D^0 -meson. An example of this is $B^- \rightarrow D^{*0}(D^0\pi^0)\pi^-$ for which the π^0 from the D^{*0} decay is missed and the π^- is misidentified as the companion K^- . These are denoted ' D^0 -like'.⁹
- Decays in which the D -meson in the true decay is a \bar{D}^0 -meson. An example of this is $B_s^0 \rightarrow \bar{D}^0\pi^+K^-$ for which the π^+ is missed and the K^- is reconstructed as the companion K^- . These are denoted ' \bar{D}^0 -like'.
- Decays in which the D meson in the true decay can be either flavour, and both D flavours contribute to the decay amplitude. An example of this is $B^- \rightarrow D^*K^-$ for which the total decay amplitude into a D final state has contributions from both D^{*0} (decaying to D^0) and \bar{D}^{*0} (decaying to \bar{D}^0). The relative amplitude magnitude and phase between the two possible B decays are denoted $r_B^{D^*}$ and $\delta_B^{D^*}$ respectively. These are denoted ' r_B -like'.
- Decays that can be reconstructed as both D^0 - and \bar{D}^0 -like but where there is no quantum-mechanical interference. An example is $\bar{B}^0 \rightarrow D^0\pi^+\pi^-$ decays where either the π^+ or π^- can be reconstructed as the bachelor. These are denoted 50/50 D^0 -like and \bar{D}^0 -like.

For $B^+ \rightarrow DK^+$ decays everything is CP conjugated. The Dalitz-plot distribution for each of these cases is:

- D^0 decays (' D^0 -like')

$$\begin{aligned} N_{\pm i}(B^-) &\propto F_{\pm i} \\ N_{\pm i}(B^+) &\propto F_{\mp i} \end{aligned} \tag{5.29}$$

- \bar{D}^0 decays (' \bar{D}^0 -like'):

$$\begin{aligned} N_{\pm i}(B^-) &\propto F_{\mp i} \\ N_{\pm i}(B^+) &\propto F_{\pm i} \end{aligned} \tag{5.30}$$

- Decays with a quantum-mechanical admixture of D^0 and \bar{D}^0 (' r_B -like'):

$$\begin{aligned} N_{\pm i}(B^-) &\propto F_{\pm i} + (r_B^*)^2 F_{\mp i} + 2\sqrt{F_{+i}F_{-i}}[x_-^*c_{\pm i} + y_-^*s_{\pm i}] \\ N_{\pm i}(B^+) &\propto F_{\mp i} + (r_B^*)^2 F_{\pm i} + 2\sqrt{F_{+i}F_{-i}}[x_+^*c_{\pm i} - y_+^*s_{\pm i}] \end{aligned} \tag{5.31}$$

where (x_\pm^*, y_\pm^*) are defined analogously to the standard $B^\pm \rightarrow DK^\pm$ case.

⁹The naming convention is defined in terms of the D present in candidates reconstructed as B^- decays. For the charge conjugate case this decay would of course happen via a \bar{D}^0 , but is still denoted D^0 -like.

- 2957 • 50/50 D^0 -like and \bar{D}^0 -like:

$$\begin{aligned} N_{\pm i}(B^-) &\propto F_{\pm i} + F_{\mp i} \\ N_{\pm i}(B^+) &\propto F_{\pm i} + F_{\mp i} \end{aligned} \quad (5.32)$$

2958 The use of a single background shape across all bins may therefore introduce biases
 2959 because such a shape has no sensitivity to the bin-to-bin variations that will arise
 2960 if an admixture of these backgrounds is present.

2961 In the $D\pi$ channel, the dominant backgrounds are all D^0 -like ($\bar{B}^0 \rightarrow D^{*-}\pi^0$,
 2962 $B^- \rightarrow D^0\rho^-$, $B^- \rightarrow D^{*0}\pi^-$). There is a small contribution from $\bar{B}^0 \rightarrow D^0\rho(\rightarrow$
 2963 $\pi^+\pi^-$) decays where either the π^+ or π^- from the ρ^0 decay can be assigned as the
 2964 bachelor, and thus this background is 50/50 D^0 -like and \bar{D}^0 -like. The background
 2965 only corresponds to about 0.5 % of the total partially reconstructed background and
 2966 thus the impact is small. Nevertheless it is considered in the study described below.

2967 In the DK channel all categories of background appear. In the mass region
 2968 of the CP fit approximately 75.5% of backgrounds are D^0 -like ($\bar{B}^0 \rightarrow D^{*-}K^-$,
 2969 mis-identified $B^- \rightarrow D^{*0}\pi^-$, and mis-identified $B^- \rightarrow D^0\rho^-$), 7.5 % are \bar{D}^0 -like
 2970 ($B_s^0 \rightarrow \bar{D}^0\pi^+K^-$), 1% is 50/50 D^0 - \bar{D}^0 -like (mis-identified $B^0 \rightarrow D\rho^0$), and 16% are
 2971 r_B -like ($B^- \rightarrow D^*K^-$, $B^0 \rightarrow DK^{*0}$, and $B^- \rightarrow DK^{*-}$).

2972 In order to estimate the bias due to ignoring this effect, a large number of toy
 2973 data sets are generated using the default low mass shapes and total yields from
 2974 the first-stage fit in Section 5.4, but distributing each of them individually over
 2975 the Dalitz-bins according to Eqs. (5.29)-(5.31). When calculating the distribution
 2976 of $B^+ \rightarrow D^{*0}K^+$ decays over the Dalitz plot, the values [?]

$$r_B^{D^*} = 0.191 \quad \delta_B^{D^*} = 331.6^\circ \quad (5.33)$$

2977 are used. When calculating the distribution of $B^+ \rightarrow D^0K^{*+}$ decays over the
 2978 Dalitz plot the values [?]

$$r_B^{K^*} = 0.092 \quad \delta_B^{K^*} = 40^\circ. \quad (5.34)$$

2979 are used. The toy data sets are then fit with the default set up, and the observed
 2980 mean bias assigned as the corresponding uncertainty. The corresponding uncer-
 2981 tainties were found to be about 0.1×10^{-2} for all uncertainties. The variation in
 2982 the shapes is rather small in the mass range included in the fit, which explains
 2983 the small impact.

2984 If the B_s^0 background is *not* treated separately in the default fit, but instead
 2985 included in a single lowmass background shape along with the B^0 and B^\pm contribu-
 2986 tions, the systematic uncertainty is an order of magnitude larger when evaluated
 2987 as described above, and would be a dominating systematic. This motivates the
 2988 separate treatment of the B_s^0 background.

2989 5.6.4 CP violation and material interaction of the K_S^0

2990 A systematic uncertainty due to CP -violation effects and material interaction of
 2991 the K_S^0 is assigned using the results obtained in Section 4.3.7. In that section, the
 2992 expected bias on each of the observables in a combined $B^\pm \rightarrow Dh^\pm$ measurement
 2993 was evaluated for the detector geometry and particle kinematics of the LHCb
 2994 experiment. The calculation was made for $(r_B^{DK^\pm/D\pi^\pm}, \delta_B^{DK^\pm/D\pi^\pm})$ values close to
 2995 the world averages, and a number of γ values; the results were summarised in Fig. 4.8.
 2996 The systematic uncertainty is taken to be the largest absolute bias observed for each
 2997 parameter in the study. The largest uncertainty (on $y_\xi^{D\pi}$ where it is 0.46×10^{-2}) is
 2998 still an order of magnitude smaller than the statistical uncertainty.

2999 5.6.5 Impact of D mixing

3000 The effect of D -mixing is not accounted for in the measurement, which leads to
 3001 a small bias. Earlier studies have shown this to lead to a sub-degree bias on
 3002 measurements of γ in $B^\pm \rightarrow DK^\pm$ decays, in the case where the F_i parameters
 3003 are determined experimentally under the same experimental conditions as the γ
 3004 measurement [?]. A number of pseudoexperiments are carried out to verify that
 3005 this is also the case for the combined $DK^\pm-D\pi^\pm$ setup employed in the thesis.
 3006 They are performed following the same procedure described in Section 5.6.4 for
 3007 the case of neutral-kaon CP violation. The yields are calculated while taking D
 3008 mixing into account, using the mixing parameter values $x = (0.39^{+0.11}_{-0.12})\%$ and
 3009 $y = (0.65^{+0.06}_{-0.07})\%$ [?], and then fitted back assuming no D mixing. The biases are
 3010 found to be small, as expected, all of them smaller than 0.05×10^{-2} . The largest
 3011 relative biases are on the $B^\pm \rightarrow D\pi^\pm$ parameters, but even for those the relative
 3012 effect is less than 2 %. In agreement with Ref. [?], it is found that the biases increase
 3013 with an order of magnitude if the F_i parameters are fixed to the expected values
 3014 with no D -mixing, instead of being determined as part of the fit.

3015 5.6.6 PID efficiencies

3016 The uncertainty related to PID efficiencies is assessed by repeating the full two-stage
 3017 fit procedure a number of times, each time varying the PID efficiencies within
 3018 the uncertainties. The used uncertainty includes both a statistical and systematic
 3019 component, as described in detail in Section 5.1.3. The standard deviations of
 3020 the central values obtained for each observable are assigned as the systematic
 3021 uncertainty. The uncertainties come out below 0.1×10^{-2} for all observables.

3022 **5.6.7 Dalitz-coordinate resolution**

3023 There is a small systematic uncertainty related to Dalitz-plot-bin migration, where
 3024 the non-perfect resolution on the momentum measurement means that a candidate
 3025 is assigned to a different bin than it truly belongs to. This leads to non-negligible
 3026 net migration between bins that share a border in a region of phase space where
 3027 the amplitude varies rapidly. However, since the F_i are measured in the data
 3028 set, all leading order effects of migration are inherently taken into account. The
 3029 measurement is only sensitive to differences in migration between the DK^\pm and
 3030 $D\pi^\pm$ channels and the effect is small.

3031 The systematic uncertainty due to this effect is assigned using pseudoexperiments.
 3032 The study is made for the $D \rightarrow K_S^0 \pi^+ \pi^-$ mode only, which is sufficient since it
 3033 completely dominates the overall sensitivity.

- 3034 1. Signal $B^\pm \rightarrow DK^\pm$ and $B^\pm \rightarrow D\pi^\pm$ decays are generated continuously over
 3035 phase space, according to the expected distribution obtained with the latest
 3036 amplitude model from the Belle collaboration [?], assuming values of γ and
 3037 $(r_B^{DK^\pm/D\pi^\pm}, \delta_B^{DK^\pm/D\pi^\pm})$ close to the current world averages.
- 3038 2. The Dalitz coordinates of each candidate are then smeared using the experi-
 3039 ment resolution obtained in simulation. This is described further below.
- 3040 3. Finally, the generated candidates are binned and fitted back using the default
 3041 setup.

3042 The resolution is obtained via simulation, by comparing the reconstructed
 3043 phase-space coordinates with those calculated from the true momenta in samples of
 3044 simulated $D \rightarrow K_S^0 \pi^+ \pi^-$ decays. As can be seen in Fig. 5.56, the resolution is found
 3045 to vary over phase space and the distribution of shifts has significant exponential
 3046 tails. In order to take both effects into account, the smearing is done by shifting each
 3047 generated decay with a realised coordinate shift in full simulation, for a simulated
 3048 decay that took place at approximately the same place in the Dalitz plot. The
 3049 shift is multiplied with 120 % to take into account that the resolution is generally
 3050 better in simulation than data. If the shift results in Dalitz coordinates outside the
 3051 kinematically allowed region, a different shift is applied randomly instead.

3052 The average bias seen in the pseudoexperiments is assigned as the systematic
 3053 uncertainty. The uncertainties come out at about $(0.1 - 0.2) \times 10^{-2}$ for all parameters.
 3054 It is found that the bias is towards a smaller value of r_B^{DK} for all four DK^\pm
 3055 parameters ; this is to be expected, as bin migration washes out the asymmetries
 3056 in different areas of the Dalitz plot.

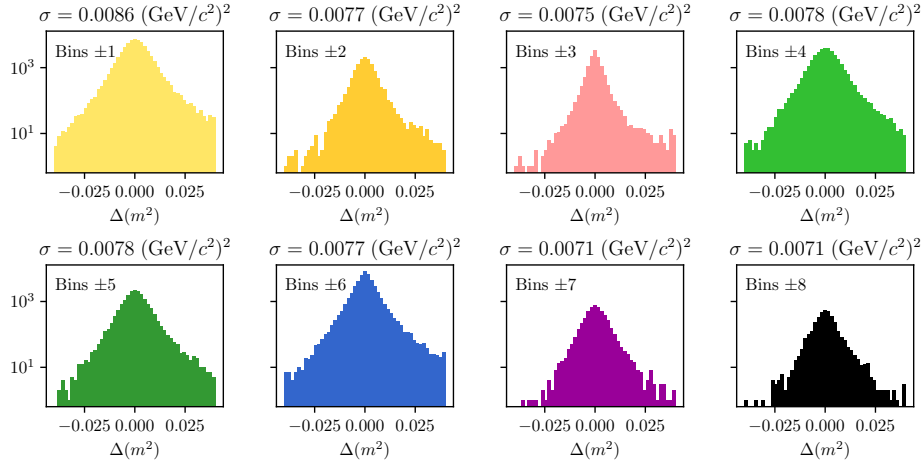


Figure 5.56: Distribution of the biases $\Delta(m^2) = m_{true}^2 - m_{reconstructed}^2$ in simulation for $m^2(K_S^0\pi^\pm)$ in bins of the rectangular binning scheme of Fig. 5.50.

5.6.8 The fixed yield fractions

A number of relative yields are fixed from efficiencies in simulation and branching fractions. In the DK^\pm modes, this is the case for all the relative yields of the partially reconstructed backgrounds, including partially reconstructed $B \rightarrow D\pi[X]$ decays where the pion is misidentified as a kaon, and the yield of the $B_s^0 \rightarrow DK\pi$ background relative to the $B \rightarrow D\pi$ yield. In the $B^\pm \rightarrow D\pi^\pm$ channel, the only fixed yield ratio is that of the partially reconstructed $B^\pm \rightarrow D^{*0}(\rightarrow D\pi^0)\pi^\pm$ and $B^0 \rightarrow D^{*\mp}(\rightarrow D\pi^\mp)\pi^\pm$ modes. The uncertainty on the observables due to uncertainties on these fixed fractions is assessed by repeating the two-stage fit procedure many times, each time shifting the yield ratios randomly within their uncertainties. The uncertainty on each observable is taken to be the standard deviation of the set of central values obtained in these fits. These are all smaller than 0.1×10^{-2} .

5.6.9 Systematic uncertainty due to backgrounds that are not modelled in fit

There are a number of backgrounds that are expected to be present at a small level, but which are not modelled in the fits to data because their impact on the fit results is minimal. Instead, a systematic uncertainty is assigned. Each contribution is described in the following sections and the related systematic uncertainties are summarised in Table 5.17.

Table 5.17: Summary of systematic uncertainties due to backgrounds that are potentially present with a small yield, but not included in the mass fit.

All uncertainties are quoted with implicit: $\times 10^{-2}$						
Mode	$\sigma(x_-^{DK^\pm})$	$\sigma(y_-^{DK^\pm})$	$\sigma(x_+^{DK^\pm})$	$\sigma(y_+^{DK^\pm})$	$\sigma(x_\xi^{D\pi^\pm})$	$\sigma(y_\xi^{D\pi^\pm})$
Λ_b^0 backgrounds	0.04	0.05	0.04	0.06	0.08	0.13
$B \rightarrow D\mu\nu X$	0.04	0.07	0.04	0.05	0.10	0.11
$B^\pm \rightarrow D(\rightarrow K_S^0\pi\mu\nu)h^\pm$	0.00	0.03	0.02	0.02	0.00	0.00
Swapped tracks	0.10	0.13	0.12	0.08	0.00	0.01
Total	0.11	0.16	0.13	0.12	0.08	0.13

Background from Λ_b decays

This section considers the possible impact of the two potential backgrounds from Λ_b^0 decays described in Section 5.4.3: $\Lambda_b^0 \rightarrow D^0 p\pi^-$ decays where the pion is not included in the candidate reconstruction and the proton assigned as the companion, and $\Lambda_b^0 \rightarrow \Lambda_c^+(\rightarrow pK_S^0\pi^+\pi^-)\pi^-$ decays where a pion in the Λ_c^+ decay is not reconstructed and the proton reconstructed as one of the D decay products. The impact of not including these in the default fit is assessed by generating toy data sets where the backgrounds are included in the generation step, which are then fitted back with default model. The former background is distributed over the Dalitz plot as \bar{D}^0 -like, cf. the terminology of Section 5.6.3, since a positive bachelor is produced along with a D^0 meson. The latter is also distributed as \bar{D}^0 -like in the study; the exact distribution is unknown, but a \bar{D}^0 -like background is likely to have the largest effect and thus this is a conservative choice. The total yields are taken relative to the signal yields, using the yield ratios discussed in Section 5.4.3. The $m(Dh^\pm)$ distributions are obtained using simulated samples, produced with **RapidSim**. The mean biases come out to be less than 0.1×10^{-2} for each CP -violation observable, which is assigned as a systematic uncertainty.

Semi-leptonic backgrounds

The impact of remnant $B \rightarrow D\mu\nu_\mu$ decays after requiring `isMuon=0` on the bachelor is assessed in pseudoexperiments. Toy datasets are generated where the background is added in the generation step, which are then fitted with the default model. The background yield relative to signal and the mass shape are obtained from a sample of fully simulated decays for conditions corresponding to the run conditions in 2012. The obtained bias in the toys is assigned as the systematic uncertainties: it is below 0.1×10^{-2} for all parameters.

3101 The systematic uncertainty relating to the presence of $D^0 \rightarrow K_S^0 \pi^- \mu^+ \nu_\mu$ is
 3102 estimated by repeating the bias studies of Section 5.3.3, but scaling the background
 3103 yields to 10% to take into account the lepton veto on the D decay products. All
 3104 biases are less than 0.05×10^{-2} in this case.

3105 **Swapped tracks**

3106 There is a peaking background present from $B^\pm \rightarrow D(\rightarrow K^\mp \pi^\pm) K_S^0 \pi^\pm$ decays where
 3107 the kaon is reconstructed as the companion and the K_S^0 is assigned to the D decay.
 3108 The yield of this background is determined to be 0.5% of the signal yield in the
 3109 $B^\pm \rightarrow DK^\pm$ channel in Section 5.3.5. The potential impact from the presence
 3110 of the background is estimated by

- 3111 1. Calculating the expected $B^\pm \rightarrow D\pi^\pm$ and $B^\pm \rightarrow DK^\pm$ signal yields in each
 bin for physics parameters similar to the world average values.
 - 3113 2. Then calculating the background bin yields in each $B^\pm \rightarrow DK^\pm$ bin, using
 a total yield equal to 0.5% of the signal yield, and the bin distribution
 from simulated samples of $B^\pm \rightarrow D(\rightarrow K^\mp \pi^\pm) K_S^0 \pi^\pm$ decays, produced via
 `RapidSim`. The study is carried out for multiple simulated samples, including
 decays where the $K_S^0 \pi$ pair in the B decay originate in different K^* resonances
 (generated with `EvtGen` and the proper resonance-spin models), as well as B
 decays that are evenly distributed over the allowed phase space.
 - 3120 3. For each sample, the signal and background yields are added, and the new
 $B^\pm \rightarrow D\pi^\pm$ and $B^\pm \rightarrow DK^\pm$ yields are fitted back with the default signal-
 yield expressions (including a fit of the F_i parameters).
- 3123 For each parameter, the most significant bias seen across the different `RapidSim`
 3124 samples is taken as the related systematic uncertainty. The uncertainty is below
 3125 0.15×10^{-2} for all parameters.

3126 **5.6.10 Bias correction**

3127 In the default sensitivity study, the bias was found to be compatible with zero.
 3128 However, the size of a potential bias can vary depending on the input parame-
 3129 ters. The size of the bias has been investigated with alternate input values of
 3130 $(\gamma, r_B^{DK^\pm}, \delta_B^{DK^\pm}, r_B^{D\pi^\pm}, \delta_B^{D\pi^\pm})$, obtaining the results in Table 5.18. A systematic
 3131 uncertainty due to a potential, small bias is calculated as the difference between
 3132 the maximum and minimum bias for a given parameter. The uncertainty assigned
 3133 in this way is very small in general, and less than 0.1×10^{-2} for all parameters.

Table 5.18: Biases observed with alternative input parameters and the systematic uncertainty assigned for the bias correction. All numbers are quoted with an implicit $\times 10^{-2}$.

Input ($\gamma, r_B^{DK^\pm}, \delta_B^{DK^\pm}, r_B^{D\pi^\pm}, \delta_B^{D\pi^\pm}$)	$x_-^{DK^\pm}$	$y_-^{DK^\pm}$	$x_+^{DK^\pm}$	$y_+^{DK^\pm}$	$x_\xi^{D\pi^\pm}$	$y_\xi^{D\pi^\pm}$
(72, 0.080, 117, 0.005, 288)	-0.02	-0.01	-0.02	-0.02	0.03	0.00
(75, 0.100, 130, 0.005, 300)	-0.03	-0.04	-0.00	0.02	0.01	-0.03
(82, 0.112, 144, 0.005, 330)	0.00	-0.01	0.00	0.03	-0.03	0.02
(71, 0.099, 129, 0.005, 300)	-0.02	-0.04	-0.00	-0.00	0.05	-0.00
Syst. uncertainty	0.04	0.03	0.02	0.04	0.09	0.05

3134 5.6.11 Charmless backgrounds

3135 As discussed in Section 5.3.1, a small number of charmless background decays
 3136 survive the D flight distance cut. In this section the systematic uncertainty related
 3137 to those is assessed, in a series of pseudoexperiments. Toy datasets are generated,
 3138 where a charmless background component is included, using the yields and shapes
 3139 obtained in the studies of Section 5.3.1. The Dalitz-bin distribution is obtained
 3140 by repeating the fits of that section for each bin individually. These datasets are
 3141 subsequently fitted back using the default model, which does not include a charmless
 3142 component. No statistically significant bias is observed.

3143 The study described above does not allow for charge-asymmetries in the charmless
 3144 backgrounds, in terms of overall yields and phase-space distributions. These
 3145 asymmetries are likely to be present, due to large local CP -violation in regions of
 3146 phase space in B^\pm decays to hadrons [?, ?]. The yields in the data-driven studies
 3147 of Section 5.3.1 are not large enough to assess asymmetries, let alone asymmetric
 3148 bin distributions with any degree of statistical precision. Instead, an extreme-case
 3149 scenario is investigated, where *all* the charmless background is added to either the B^+
 3150 or B^- data sample in generation. In both cases, no statistically significant biases are
 3151 observed, and it is concluded that the impact of charmless background is negligible.

3152 5.6.12 Summary of systematic uncertainties

3153 The complete set of included systematic uncertainties are summarised in Table 5.19.
 3154 It can be seen that the measurement is statistically limited. The correlation matrix
 3155 pertaining to the LHCb related systematics is given in Table 5.20. For studies where
 3156 the systematic uncertainty is obtained by repeating fits to data multiple times while
 3157 varying some input, the correlation matrix from the correlations of the fitted central
 3158 values. For studies that are based on generating a large number of toy datasets and

Table 5.19: Overview of all sources of uncertainty on the measurement.

Source	All uncertainties are quoted with implicit: $\times 10^{-2}$					
	$\sigma(x_-^{DK\pm})$	$\sigma(y_-^{DK\pm})$	$\sigma(x_+^{DK\pm})$	$\sigma(y_+^{DK\pm})$	$\sigma(x_\xi^{D\pi\pm})$	$\sigma(y_\xi^{D\pi\pm})$
Statistical	0.96	1.14	0.96	1.20	1.99	2.34
Strong-Phase inputs	0.23	0.35	0.18	0.28	0.14	0.18
Efficiency correction of (c_i, s_i)	0.11	0.05	0.05	0.10	0.08	0.09
Mass-shape parameters	0.05	0.08	0.03	0.08	0.16	0.17
Mass-shape bin dependence	0.05	0.07	0.04	0.08	0.07	0.09
Lowmass physics effects	0.04	0.10	0.15	0.05	0.10	0.09
CP violation of K_S^0	0.03	0.04	0.08	0.08	0.09	0.46
D mixing	0.04	0.01	0.00	0.02	0.02	0.01
PID efficiencies	0.03	0.03	0.01	0.05	0.02	0.02
Fixed yield ratios	0.05	0.06	0.03	0.06	0.02	0.02
Dalitz-bin migration	0.04	0.08	0.08	0.11	0.18	0.10
Bias correction	0.04	0.03	0.02	0.04	0.09	0.05
Small backgrounds	0.11	0.16	0.13	0.12	0.08	0.13
Total LHCb systematic	0.20	0.25	0.24	0.26	0.32	0.54
Total systematic	0.31	0.43	0.30	0.38	0.35	0.57

Table 5.20: Total LHCb-related systematic uncertainties and their correlation matrix.

Uncertainty ($\times 10^{-2}$)						
	$x_-^{DK\pm}$	$y_-^{DK\pm}$	$x_+^{DK\pm}$	$y_+^{DK\pm}$	$x_\xi^{D\pi\pm}$	$y_\xi^{D\pi\pm}$
σ	0.20	0.25	0.24	0.26	0.32	0.54

Correlations						
	$x_-^{DK\pm}$	$y_-^{DK\pm}$	$x_+^{DK\pm}$	$y_+^{DK\pm}$	$x_\xi^{D\pi\pm}$	$y_\xi^{D\pi\pm}$
$x_-^{DK\pm}$	1.000	0.864	0.734	0.897	0.349	0.318
$y_-^{DK\pm}$		1.000	0.874	0.903	0.408	0.362
$x_+^{DK\pm}$			1.000	0.771	0.563	0.447
$y_+^{DK\pm}$				1.000	0.507	0.451
$x_\xi^{D\pi\pm}$					1.000	0.484
$y_\xi^{D\pi\pm}$						1.000

³¹⁵⁹ determining the average bias, the correlation of a systematic on two observables
³¹⁶⁰ is taken to be +100 % if the biases are in the same direction, and -100 % if they
³¹⁶¹ are in opposite directions. The total systematic correlation matrix, including both
³¹⁶² LHCb-related systematics and that of the strong-phase inputs, is given in Table 5.21.

³¹⁶³ The studies described in this section also allow for an estimate of the systematic
³¹⁶⁴ uncertainties on the \mathcal{R}_i parameters of Eq. (5.23) or, equivalently the F_i parameters,
³¹⁶⁵ in a completely analogous manner to how the uncertainty on the CP -violation
³¹⁶⁶ observables was assigned. In all cases, however, the systematic uncertainty is found
³¹⁶⁷ to be much smaller than the statistical uncertainties that were given in Table 5.10.

Table 5.21: Total systematic uncertainties and their correlation matrix, including contributions due to strong-phase inputs as well as LHCb-related uncertainties.

Uncertainty ($\times 10^{-2}$)						
	$x_-^{DK\pm}$	$y_-^{DK\pm}$	$x_+^{DK\pm}$	$y_+^{DK\pm}$	$x_\xi^{D\pi\pm}$	$y_\xi^{D\pi\pm}$
σ	0.31	0.43	0.30	0.38	0.35	0.57

Correlations						
	$x_-^{DK\pm}$	$y_-^{DK\pm}$	$x_+^{DK\pm}$	$y_+^{DK\pm}$	$x_\xi^{D\pi\pm}$	$y_\xi^{D\pi\pm}$
$x_-^{DK\pm}$	1.000	0.301	0.156	0.576	0.265	0.231
$y_-^{DK\pm}$		1.000	0.437	0.218	0.183	0.170
$x_+^{DK\pm}$			1.000	0.445	0.414	0.310
$y_+^{DK\pm}$				1.000	0.353	0.243
$x_\xi^{D\pi\pm}$					1.000	0.502
$y_\xi^{D\pi\pm}$						1.000

³¹⁶⁸ The central values, statistical, and systematic uncertainties of the \mathcal{R}_i parameters
³¹⁶⁹ have been made public in Ref. [?] because they can be employed in future LHCb
³¹⁷⁰ measurements, as discussed in Section 5.5.2.

³¹⁷¹ 5.7 Obtained constraints on γ

³¹⁷² The measured values of $(x_\pm^{DK}, y_\pm^{DK}, x_\xi^{D\pi}, y_\xi^{D\pi})$ can be used to put constraints on the
³¹⁷³ possible values of the CKM angle γ and the hadronic nuisance parameters $r_B^{DK\pm}$,
³¹⁷⁴ $\delta_B^{DK\pm}$, $r_B^{D\pi\pm}$, and $\delta_B^{D\pi\pm}$. This is handled using the `gammacombo` package, which is
³¹⁷⁵ also used to combine all measurements of γ made by the LHCb collaboration [?, ?].

³¹⁷⁶ 5.7.1 Statistical approach

³¹⁷⁷ The optimal central values determined in a maximum likelihood fit. The set of
³¹⁷⁸ all observables for which a measurement has been made is denoted A , and the set
³¹⁷⁹ of underlying physics parameters is denoted θ . The physics parameters of course
³¹⁸⁰ determine the probability density function of measurement results of A , $f(A|\theta)$.
³¹⁸¹ Given a specific set of measurement results, A_{obs} , a likelihood function is defined

$$\mathcal{L}(\theta|A_{\text{obs}}) = f(A_{\text{obs}}|\theta) \quad (5.35)$$

³¹⁸² and the estimate of θ is the set of parameters that maximize the likelihood

$$\hat{\theta} = \arg \max_{\theta} \mathcal{L}(\theta|A_{\text{obs}}). \quad (5.36)$$

3183 In practice, a χ^2 function is defined

$$\chi^2(\theta|A_{\text{obs}}) = -2 \ln \mathcal{L}(\theta|A_{\text{obs}}) \quad (5.37)$$

3184 and minimized instead. In the specific case where the likelihood profile is Gaussian,
3185 it can be described by the simple expression

$$\chi^2(\theta|A_{\text{obs}}) = (A_{\text{obs}} - A(\theta))^T \Sigma_{A_{\text{obs}}}^{-1} (A_{\text{obs}} - A(\theta)) + c, \quad (5.38)$$

3186 where $\Sigma_{A_{\text{obs}}}$ is the *measured* covariance matrix for the observables (used as an
3187 estimate of the true, underlying covariance matrix), $A(\theta)$ denotes the value of the
3188 observables expressed in terms of the underlying physics parameters, and c is a
3189 constant that is independent of θ . In the specific case considered here

$$\begin{aligned} A &= (x_-^{DK}, y_-^{DK}, x_+^{DK}, y_+^{DK}, x_\xi^{D\pi}, y_\xi^{D\pi}) \\ \theta &= (\gamma, r_B^{DK\pm}, \delta_B^{DK\pm}, r_B^{D\pi\pm}, \delta_B^{D\pi\pm}). \end{aligned} \quad (5.39)$$

3190 The likelihood scan presented in Section 5.5.2 proved that the Gaussian expression
3191 in Eq. (5.38) provides an excellent description of the likelihood profile of the
3192 measurement, when $\Sigma_{A_{\text{obs}}}$ is taken to be the covariance matrix obtained in that
3193 section. Thus, the χ^2 function defined in Eq. (5.38) is minimised to determine
3194 the best estimate of γ .

3195 Two different methods are employed to construct confidence regions for the
3196 observables of interest, known within the `gammacombo` framework as the PROB and
3197 PLUGIN methods. Both methods aim to construct confidence regions for some
3198 subset, ϕ , of the full parameter set θ . The remaining parameters, dubbed nuisance
3199 parameters below, are denoted $\eta = \theta \setminus \phi$. In practice, ϕ most often denotes a single
3200 parameter, and of special interest is of course the case where $\phi = \gamma$. Both methods
3201 aim to solve the problem that due to the number of parameters in θ (five in the case
3202 considered here, but up to 40 in the latest LHCb combination [?]), it is not feasible
3203 to derive the confidence regions from a full-fledged Neumann construction [?]. Under
3204 assumptions discussed below, the methods achieve reasonable coverage nonetheless,
3205 ie. had the measurement been repeated many times, the confidence region is
3206 expected to cover the true parameter(s) with a probability at least at large as
3207 the quoted confidence level (CL), independently of the true parameter value. The
3208 presentation follows the `gammacombo` manual [?].

3209 The PROB method is a simple profile-likelihood method. The minimum value
3210 of the χ^2 function is denoted $\chi^2_{\min} \equiv \chi^2(\hat{\theta}|A_{\text{obs}})$. To evaluate the CL for a specific
3211 value (set of values) of ϕ_0 , the χ^2 function is again minimised, this time under

the constraint that $\phi = \phi_0$, resulting in a new minimum $\hat{\theta}' = (\phi_0, \hat{\eta}')$. In the approximation that all likelihoods are exactly Gaussian, the variable

$$\Delta\chi^2(\phi_0|A_{\text{obs}}) = \chi^2(\hat{\theta}'|A_{\text{obs}}) - \chi^2_{\min} \quad (5.40)$$

follows a χ^2 distribution with n degrees of freedom, where n is the number of parameters in ϕ [?]. This can be used to evaluate CL at that point as

$$CL(\phi_0|A_{\text{obs}}) = F_n(\Delta\chi^2(\phi_0|A_{\text{obs}})) \quad (5.41)$$

where F_n is the cumulative distribution function of a χ^2 distribution with n degrees of freedom. The method takes its colloquial name from the fact that this function is named `Prob` in the `ROOT` package. Confidence regions can be defined by scanning the values of ϕ_0 over a region of interest. These confidence regions assume that the estimates $\hat{\theta}$ follow a Gaussian distribution centred on the true values, which is the case for maximum likelihood estimates in asymptotically large samples [?]; in other cases they may not have good coverage properties. Given the Gaussian shape obtained in the likelihood scan of Section 5.5.2 the confidence regions are likely to be well behaved in the case considered here.

However, for the purpose of comparing to the combination of several LHCb measurements in Section 5.5.3 below, the `PLUGIN` method is necessary. The method is described in Ref. [?], based on the hybrid resampling method presented in Ref. [?]. It foregoes the assumption that $\Delta\chi^2$ follows a χ^2 distribution, and instead estimates the distribution in a bootstrapping scheme. The procedure is as follows: the values of $\hat{\theta}$, $\hat{\theta}'$, and $\Delta\chi^2(\phi_0|A_{\text{obs}})$ are determined as described above; then the following steps are carried out a number, N_{toys} , of times

- 3232 1. Generate a "toy" result, A_{toy}^i , following the distribution $f(A|\hat{\theta}')$
- 3233 2. Determine $\Delta\chi^2(\phi_0|A_{\text{toy}}^i)$ by minimising the χ^2 function for the results A_{toy}^i twice, once where all parameters in θ are free, and once where $\phi = \phi_0$ is enforced

3236 Then the CL is defined by

$$CL(\phi_0) = 1 - \frac{N(\Delta\chi^2(\phi_0|A_{\text{obs}}) < \Delta\chi^2(\phi_0|A_{\text{toy}}^i))}{N_{\text{toys}}} \quad (5.42)$$

3237 While the coverage properties are not proven, evidence is presented in terms of
 3238 asymptotic results and simulation studies in Refs. [?, ?]. The coverage properties
 3239 have also been investigated in relation to LHCb combinations, and the intervals
 3240 were found to perform well in most cases [?].

3241 **5.7.2 Interpretation results**

3242 The central values and confidence regions obtained for the physics parameters are

$$\begin{aligned} \gamma &= (68.7^{+5.2}_{-5.1})^\circ, \\ r_B^{DK^\pm} &= 0.0904^{+0.0077}_{-0.0075}, \\ \delta_B^{DK^\pm} &= (118.3^{+5.5}_{-5.6})^\circ, \\ r_B^{D\pi^\pm} &= 0.0050^{+0.0017}_{-0.0017}, \\ \delta_B^{D\pi^\pm} &= (291^{+24}_{-26})^\circ, \end{aligned} \quad (5.43)$$

3243 where the quoted uncertainties are obtained via the **PLUGIN** method. The one-
3244 dimensional CL plots are shown in Fig. 5.57. It is also clear that the **PROB** and
3245 **PLUGIN** confidence regions agree well; this is expected given the Gaussian likelihood.
3246 A series of two-dimensional confidence regions are shown in Fig. 5.58, where it
3247 can be seen that the observables define a single solution for γ as expected. It
3248 is worth noticing that the uncertainty of this measurement alone is on par with
3249 the current world average, due to the increased data sample, and the significant
3250 reduction of systematic uncertainties due to the new measurement strategy and
3251 updated inputs from BESIII.

3252 The contribution to the uncertainty on γ from each of the statistical, strong-
3253 phase-related, and LHCb-related uncertainties in isolation can be estimated by
3254 repeating the interpretation while only including subsets of the uncertainties on
3255 the input parameters. Such studies have been performed using the **PROB** method.
3256 Running with statistical uncertainties only yields an uncertainty on γ of 5.05° .
3257 Including only the statistical and LHCb-related systematic uncertainties yields an
3258 uncertainty on γ of 5.08° , suggesting that the LHCb-related systematics contribute
3259 an uncertainty of 0.6° . This is a reduction compared to earlier analyses, where
3260 the contribution was about 2° . A significant contribution to the improvement is
3261 the efficiency-related systematic that has been avoided by promoting $B^\pm \rightarrow D\pi^\pm$
3262 to a signal channel. Including only the statistical and the strong-phase-related
3263 uncertainties leads to an uncertainty on γ of 5.09° , showing the strong-phase-related
3264 uncertainty to be 0.6° , somewhat lower than the expectation of 1.2° presented in
3265 Ref. [?]. This is partly because the uncertainty estimate of that paper does not
3266 take into account the use of the $D \rightarrow K_S^0 K^+ K^-$ channel, and partly because the
3267 uncertainty estimate depends on the specific central values.

3268 The obtained statistical uncertainty on γ is in excellent agreement with the
3269 expectation from pseudoexperiments. The interpretation procedure outlined above
3270 has been performed for each of the pseudoexperiments performed to establish the

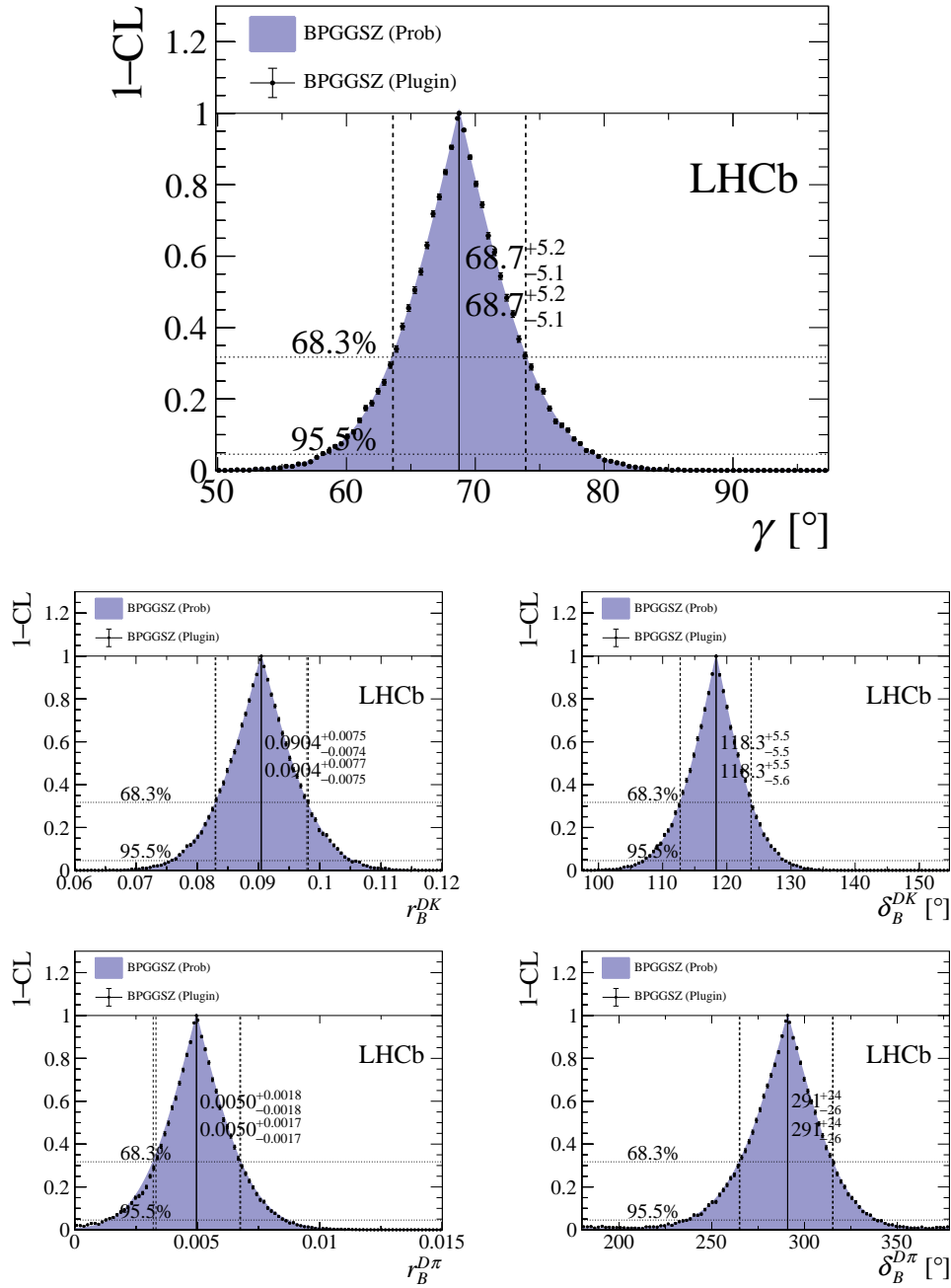


Figure 5.57: Confidence levels for the physics parameters of interest. The solutions are written on the plots, where the top number is given with PROB uncertainties and the bottom number with PLUGIN uncertainties.

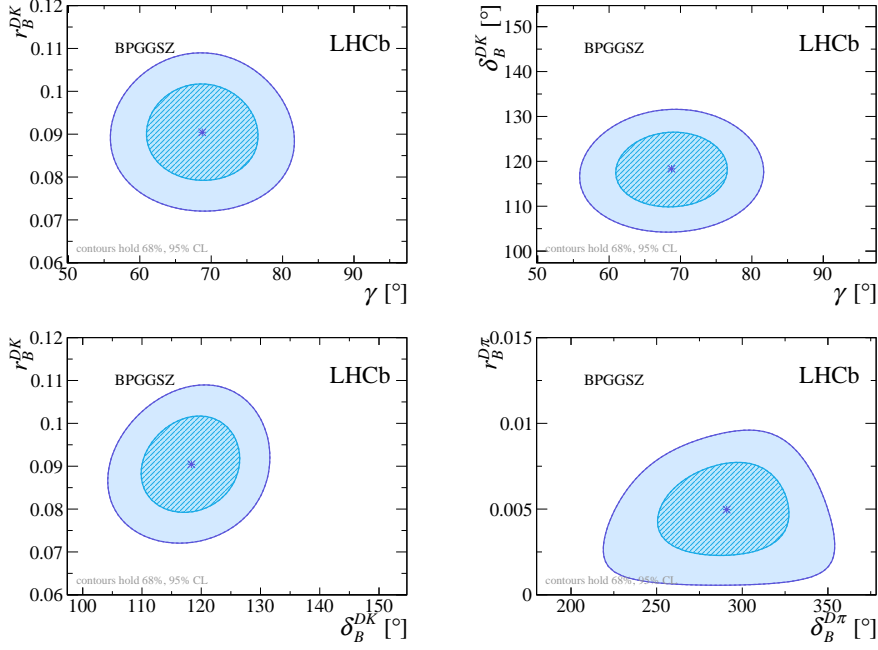


Figure 5.58: The 68 % and 95 % confidence regions for combinations of the physics parameters of interest, as obtained from the results of this measurement. The regions are calculated via the PROB method of `gammacombo`.

3271 feasibility of the CP fit in Section 5.5.1 (including only statistical uncertainties on the
 3272 observables) and the central 90 % interval of the obtained uncertainties is $[4.4^\circ, 6.0^\circ]$.
 3273 Similar studies have been carried out where no background decays are included in the
 3274 generated toy data sets. In this case, the precision on γ is improved by about 30 %.

3275 5.7.3 Compatibility with other measurements

3276 It is worth comparing the obtained constraints on the physics parameters with the
 3277 information available from other measurements, made at the B factories and by
 3278 the LHCb collaboration using other decay channels. This comparison is made for γ
 3279 and the hadronic parameters in the $B^\pm \rightarrow DK^\pm$ decay in Fig. 5.59, comparing to
 3280 the results of the combinations of γ measurements by the Belle [?] and BaBar [?]
 3281 collaborations presented in 2013, and the 2018 combination of LHCb results [?]. For
 3282 this purpose, the LHCb combination is re-performed, removing the input from earlier
 3283 BPGBGSZ measurements that use $B^\pm \rightarrow DK^\pm$ decays, because they were made
 3284 using data that is re-analysed in the present thesis; thus they need to be excluded
 3285 to make the results that are compared independent. The combination employs the
 3286 same statistical method outlined above, with the exception that the likelihood now
 3287 depends on observables measured in a number of different analyses. The included
 3288 measurements are summarised in Table 5.22. It can be seen in Fig. 5.59 that the

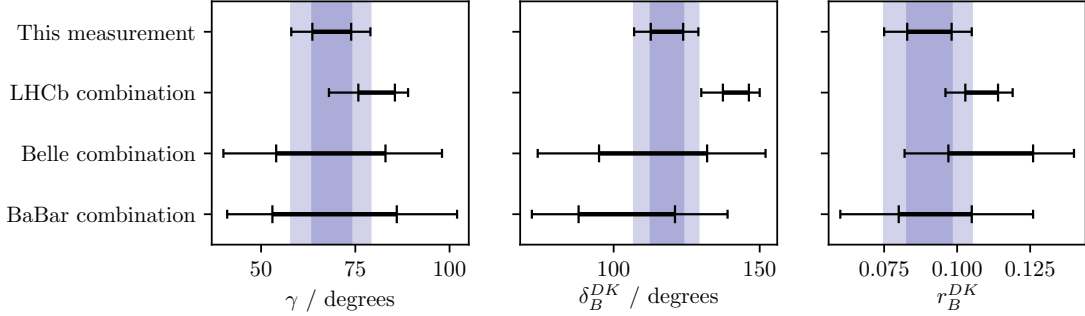


Figure 5.59: Comparison of the 1σ and 2σ confidence intervals obtained results for γ and the physics parameters relating to $B^\pm \rightarrow DK^\pm$ decays, with those from the combinations of γ measurements by the Belle [?] and BaBar [?] collaborations, and the 2018 combination of LHCb results [?] where the BPGGSZ measurements have been excluded.

3289 results obtained in this thesis agree well with the Belle and BaBar results, but are in
 3290 some tension with the 2018 LHCb combination, especially for the δ_B^{DK} parameter.

3291 The level of compatibility can be quantified by calculating the three-dimensional
 3292 χ^2 of the BPGGSZ results and those of the LHCb combination (without the earlier
 3293 BPGGSZ measurements), with respect to the best fit values of $(\gamma, r_B^{DK\pm}, \delta_B^{DK\pm})$
 3294 when all measurements are combined. The two-dimensional confidence regions
 3295 obtained in these three cases are compared in Fig. 5.60, where some tension in $r_B^{DK\pm}$
 3296 and $\delta_B^{DK\pm}$ is visible again. The calculation is based on the PLUGIN uncertainties; for
 3297 the LHCb combination these uncertainty estimates are slightly larger than the ones
 3298 obtained via the PROB method. One obtains $\chi^2 = \chi_{GGSZ}^2 + \chi_{LHCb}^2 = 0.7 + 9.1 = 9.8$,
 3299 which for 3 degrees of freedom correspond to a p -value of 2 %, or a 2.3σ deviation.
 3300 However, this tension is expected to be reduced when other measurements in the
 3301 LHCb combination are updated to include results based on the full Run 1 and 2 data
 3302 set. The most important update is that of the two-body ADS/GLW measurement
 3303 in $B^\pm \rightarrow DK^\pm$ decays because that measurement, and the BPGGSZ measurement
 3304 presented in this thesis, have the largest impact in the combination.

3305 The latest LHCb combination in which $B^\pm \rightarrow D\pi^\pm$ parameters were determined
 3306 is from 2016 [?]. Two solutions existed for $(r_B^{D\pi^\pm}, \delta_B^{D\pi^\pm})$ which made the interpreta-
 3307 tion problematic. As can be seen in Fig. 5.61, the measurement presented in this
 3308 thesis picks out one of these solutions, with which it is in excellent agreement. This
 3309 solution agrees with the theoretically expected value of $r_B^{D\pi^\pm} \sim 0.005$ [?]. Thus,
 3310 the inclusion of the results presented here are expected to lead to a much less
 3311 problematic inclusion of the $B^\pm \rightarrow D\pi^\pm$ channel in future LHCb combinations.

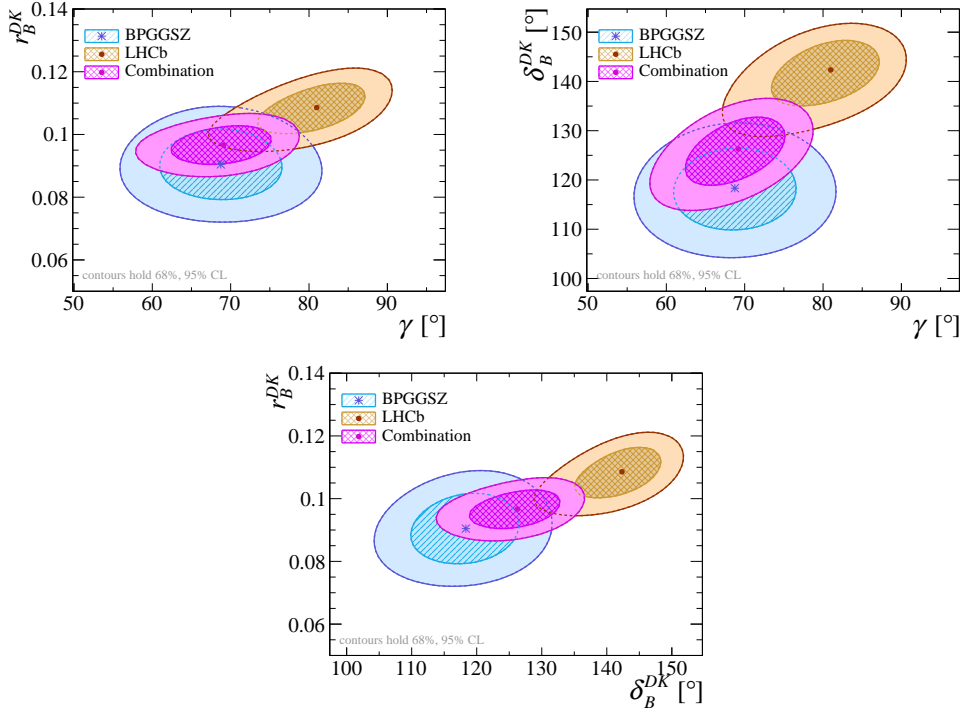


Figure 5.60: The 68 % and 95 % confidence regions for $(\gamma, r_B^{DK\pm})$, $(\gamma, \delta_B^{DK\pm})$, and $(\delta_B^{DK\pm}, r_B^{DK\pm})$ for this measurement, the 2018 LHCb combination [?] where the BPGBGSZ results have been excluded, and the combination thereof, calculated via the PROB method of `gammacombo`.

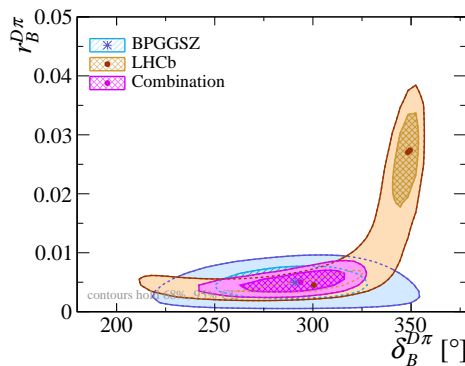


Figure 5.61: The 68 % and 95 % confidence regions for $(\delta_B^{D\pi\pm}, r_B^{D\pi\pm})$ obtained from the results of this measurement, in the 2016 LHCb combination [?], and the combination thereof, calculated via the PROB method of `gammacombo`.

Table 5.22: List of the LHCb measurements used in the combination that the results obtained in the present thesis is compared to. These correspond to the 2018 LHCb combination [?], except that the earlier BPGBS results made with $B^\pm \rightarrow DK^\pm$ decays have not been included in the comparison. In the method column, TD stands for "time-dependent".

B decay	D decay	Method	Ref.	Data set
$B^+ \rightarrow DK^+$	$D \rightarrow h^+h^-$	GLW	[?]	2011-16
$B^+ \rightarrow DK^+$	$D \rightarrow h^+h^-$	ADS	[?]	2011-12
$B^+ \rightarrow DK^+$	$D \rightarrow h^+\pi^-\pi^+\pi^-$	GLW/ADS	[?]	2011-12
$B^+ \rightarrow DK^+$	$D \rightarrow h^+h^-\pi^0$	GLW/ADS	[?]	2011-12
$B^+ \rightarrow DK^+$	$D \rightarrow K_S^0 K^+ \pi^-$	GLS	[?]	2011-12
$B^+ \rightarrow D^*K^+$	$D \rightarrow h^+h^-$	GLW	[?]	2011-16
$B^+ \rightarrow DK^{*+}$	$D \rightarrow h^+h^-$	GLW/ADS	[?]	2011-16
$B^+ \rightarrow DK^{*+}$	$D \rightarrow h^+\pi^-\pi^+\pi^-$	GLW/ADS	[?]	2011-16
$B^+ \rightarrow DK^+\pi^+\pi^-$	$D \rightarrow h^+h^-$	GLW/ADS	[?]	2011-12
$B^0 \rightarrow DK^{*0}$	$D \rightarrow K^+\pi^-$	ADS	[?]	2011-12
$B^0 \rightarrow DK^+\pi^-$	$D \rightarrow h^+h^-$	GLW-Dalitz	[?]	2011-12
$B^0 \rightarrow DK^{*0}$	$D \rightarrow K_S^0 \pi^+\pi^-$	BPGBS	[?]	2011-12
$B_s^0 \rightarrow D_s^\mp K^\pm$	$D_s^+ \rightarrow h^+h^-\pi^+$	TD	[?]	2011-12
$B^0 \rightarrow D^\mp\pi^\pm$	$D^+ \rightarrow K^+\pi^-\pi^+$	TD	[?]	2011-12
Measurements included in Ref. [?] but not in the present comparison				
$B^+ \rightarrow DK^+$	$D \rightarrow K_S^0 h^+h^-$	BPGBS	[?]	2011-12
$B^+ \rightarrow DK^+$	$D \rightarrow K_S^0 h^+h^-$	BPGBS	[?]	2015-16

6

3312

3313

Summary and outlook

3314 Say something clever

Appendices

A

3316

3317

Projections of the main fit to data